NASA Technical Memorandum 105211

The Structure and Development of Streamwise Vortex Arrays Embedded in a Turbulent Boundary Layer

Bruce J. Wendt and Isaac Greber
Case Western Reserve University
Cleveland, Ohio

and

Warren R. Hingst
Lewis Research Center
Cleveland, Ohio

September 1991

NASA

THE STRUCTURE AND DEVELOPMENT OF STREAMWISE VORTEX ARRAYS EMBEDDED IN A TURBULENT BOUNDARY LAYER

Bruce James Wendt and Isaac Greber
Case Western Reserve University
Cleveland, Ohio 44106

and

Warren R. Hingst
National Aeronautics and Space Administration
Lewis Research Center
Cleveland, Ohio 44135

Abstract

An investigation of the structure and development of streamwise vortices embedded in a turbulent boundary layer was conducted in the test facility CW-22 at NASA Lewis Research Center. The vortices were generated by a single spanwise row of rectangular vortex generator blades. A single embedded vortex was examined, as well as arrays of embedded counter-rotating vortices produced by equally spaced vortex generators.

Measurements of the secondary velocity field in the crossplane provided the basis for characterization of vortex structure. Vortex structure was characterized by four descriptors. The center of each vortex core was located at the spanwise and normal position of peak streamwise vorticity. Vortex concentration was characterized by the magnitude of the peak streamwise vorticity, and the vortex strength by its circulation.

Measurements of the secondary velocity field were conducted at two crossplane locations to examine the streamwise development of the vortex arrays. Large initial spacings of the vortex generators produced pairs of strong vortices which tended to move away from the wall region while smaller spacings produced tight arrays of weak vortices close to the wall.

The crossplane structure of embedded vortices is observed to be very similar to that exhibited by the two dimensional Oseen vortex with matching descriptors. Quantitative comparisons are established.

A model of vortex interaction and development is constructed using the experimental results. The model is based on the structure of the Oseen vortex. Vortex trajectories

are successfully modelled by including the convective effects of neighbors, and images to represent the wall. The streamwise decay of circulation is successfully modelled for the single vortex, and for large initial spacings, by accounting for the effects of wall friction. An additional mechanism associated with the turbulent stress field in the near vicinity of the vortex cores is postulated to explain the large losses in circulation obtained for the smaller initial spacings. The streamwise decay of vortex circulation at the smaller spacings is successfully modelled by summing wall friction losses and "proximity" losses. These proximity losses are found to be proportional to the gradient in streamwise vorticity occurring between an embedded vortex and its adjacent counter-rotating neighbors.

Acknowledgements

This work was funded by NASA Grant NAG 3-520, under the supervision of project monitor Warren R. Hingst. It was submitted by the author, Bruce James Wendt, as a thesis in partial fulfillment of the requirements for a Doctor of Philosophy Degree from Case Western Reserve University. Serving as thesis advisor was Isaac Greber.

The author is indebted to many NASA-Lewis workers and associates for their extensive assistance during the long course of this project.

In particular, I would like to give special thanks to Arthur Sprungle for his assistance in the design and drawing of the many parts used in this project. Warren Hingst, of NASA-Lewis, was largely responsible for obtaining the five hole probe used in this study. His assistance during the calibration procedure is greatly appreciated. I would also like to thank the Facilities Operation Division engineers; Frank Behning (now retired) and Richard Brokopp. The many mysteries of ESCORT services were timely solved in a professional fashion by electrical engineer Robert Gronski of Sverdrup. Dedicated lab assistance and facility operation was provided by Testing Installation Division's Bruce Wright and assistant Dennis Brown.

Finally, a special thanks to David Rigby of Sverdrup, for his insights into the workings of LaTeX, the document preparation system used to produce the text in this report.

Page intentionally left blank

Contents

Nomenclature

a_{ie}	vortex ellipticity coefficient
A	surface area of heater element
B_i	vortex concentration, $(B_i = \pi\omega^i_{max}/\Gamma_i)$
c	vortex generator chord length
C_f	skin friction coefficient
C_p	specific heat at constant pressure
C_{prox}	proximity loss coefficient for vortex circulation
C_{wf}	wall friction loss coefficient for vortex circulation
C_τ	shear stress scaling constant
h	height of vortex generator
h_x	heat transfer coefficient
H	vortex angular momentum, boundary layer shape factor
I	power circuit current (heater element)
k	thermal conductivity
L	streamwise location of heater trailing edge
L_{ts}	streamwise length of test section
M	wall friction moment
N_v	number of embedded vortices in an array
Pr	Prandtl number
P_s	static pressure
P_t	total pressure
q_w	surface heat flux
r	radial coordinate

Re_x	plate length Reynolds number
R_i	radial position (Oseen model)
R_{ie}	radial position (elliptical model)
R_{0i}	radial position where vorticity changes sign
S	spacing between adjacent vortex generators
St_x	Stanton number
t	time
T	temperature
$\overline{T_f}$	integrated film temperature
T_r	recovery temperature
T_{wx}	calibrated color temperature of liquid crystal
u	streamwise velocity component
U_e, U_∞	freestream velocity
u_τ	friction velocity
v	normal velocity component
v_r	secondary velocity - radial component
v_θ	secondary velocity - azimuthal component
w	spanwise velocity component
W	wake parameter function of Coles
x	streamwise coordinate
x_L	x location of upstream data grid
x_0	x location of vortex generator trailing edge
x_R	x location of downstream data grid
x_s	x location of boundary layer separation
x_t	x fitting constant for core velocity deficit

x^*	streamwise length of vortex development, $(x^* = x - x_0)$
y	normal coordinate
y_c	model estimate of vortex core normal location
y_i	vortex core normal location descriptor
z	spanwise coordinate
z_c	model estimate of vortex core spanwise location
z_{L1}, z_{L2}	spanwise location of stagnation points in wall w velocity
z_i	vortex core spanwise location descriptor
α	vortex generator angle of attack
α_p	flow pitch angle
β	boundary pressure gradient parameter
β_p	flow yaw angle
Γ	circulation
Γ_i	vortex circulation descriptor
Γ_{ie}	elliptical vortex model circulation
δ	boundary thickness at vortex generator mounting location
δ^*	displacement thickness
ϵ	turbulent eddy viscosity of Squire
Θ	momentum thickness
μ	dynamic viscosity
ν	kinematic viscosity
ν_i	vortex turbulent eddy viscosity
ξ	peak vorticity decay rate parameter
Π	wake parameter of Coles
ρ	air density

τ_i	local value of wall shear stress - spanwise component
τ_w	wall shear stress
τ_{2Dx}	wall shear stress - flat plate boundary layer
ω^i_{Lmax}	vortex peak vorticity at Station 74
ω^i_{max}	vortex peak vorticity descriptor
ω^i_{Rmax}	vortex peak vorticity at Station 150
ω^{ie}_{max}	peak vorticity - elliptical model
ω^{ie}_x	streamwise vorticity - elliptical model
ω^i_{xc}	model estimate of peak vorticity

Chapter 1

Introduction and Background

A small flow obstruction protruding from a smooth surface will generate a streamwise vortex in much the same way as a trailing vortex is shed from the wing tip of an aircraft. The purposeful design and implementation of such flow obstructions or "vortex generators" to obtain some degree of boundary layer control is now an established engineering practice.

Vortex generators are often mounted upstream of a rapidly thickening boundary layer in a region of pressure rise. Such a flow situation commonly occurs on the trailing edges of wing surfaces, or in the interior flow surfaces of a diffuser. Figure 1.1 diagrams such a case. In Figure 1.1 the boundary layer separates from the surface at a downstream location x_s. To enhance the performance of the diffuser or airfoil, the designer wishes to delay separation or move the point x_s downstream as far as possible. There are a variety of ways of accomplishing this, and each technique has its benefits as well as its drawbacks.

If the incoming boundary layer is laminar, it is possible to "trip" it turbulent. In doing so, the rate of momentum transfer is increased between the freestream and boundary layer thus energizing the fluid in the boundary layer and forestalling separation. Momentum transfer is enhanced because turbulent flow provides a "mixing" mechanism more efficient

than that available from laminar molecular diffusion alone. In most cases of engineering interest the boundary layer is already turbulent. If this is the case, and x_s is still too far upstream to satisfy design requirements, additional means of delaying separation are sought.

Partial removal of the boundary layer fluid at the surface, or energizing the boundary layer fluid by blowing at the surface, are two ways to delay separation. The additional design complexity and cost such systems incur is considerable.

Another approach is to increase the rate of mixing beyond that occurring in turbulent flow alone. The vortex generator is a device which accomplishes this. Figure 1.2 illustrates how the vortex generator works. In Figure 1.2 the vortex generator is a small rectangular blade-like fin mounted perpendicularly to the flow surface (here being the surface of a wing) at an angle of attack α with respect to the direction of the freestream. The trailing vortex shed from the tip of the vortex generator entrains the high momentum fluid of the freestream and mixes it with the boundary layer fluid through the helical motion of the vortex flow. Thus the vortex acts as a large scale mixer, increasing the rate of momentum transfer between the freestream and boundary layer to a greater extent than that offered by natural turbulence alone. The details of the peculiar helical pattern of the vortex flow is referred to here as the vortex "structure". The penalty paid for the presence of the vortex is the additional drag force occurring on each vortex generator. This drag force is responsible for an increase in the average momentum thickness of the boundary layer downstream of such a device.

The effective mixing action of a vortex generator is a function of the strength of the resulting vortex, and its position relative to the boundary layer. These, in turn, are determined from the vortex generator geometry (height h, aspect ratio h/c, and angle of attack α). The mixing properties of the vortex change as its structure and position in the boundary layer develop downstream.

Vortex generators are often mounted in array configurations which run perpendicularly to the streamwise direction of the flow. This direction is referred to as the *spanwise* coordinate. Figure 1.3 shows an array of vortex generators. The thickness of the boundary layer at the mounting location of the vortex generators is δ. The mixing performance of an array of embedded streamwise vortices is also a function of streamwise position and depends, of course, on the characteristics of the individual vortices in the array. Interaction between vortices in an array occurs if the distance between adjacent vortices is small enough. This interaction modifies their subsequent downstream development, affecting both structure and position in the boundary layer. For a given vortex generator geometry, vortex interaction is a function of the vortex generator array spacing parameter characterized in Figure 1.3 by the nondimensional spacing ratio (S/δ).

Figure 1.4a illustrates an application of an array of delta wing vortex generators on the wing surface of a small aircraft. Figure 1.4b illustrates a similar use of rectangular blade vortex generators in a subsonic diffuser. The designer wishing to maximize the mixing performance of such systems will need to consider the interrelated complexities of vortex structure, path, development, and interaction as well as the connection of these variables to the design parameters of the vortex generator arrays. Tackling the problem by numerical modelling may prove difficult as fully turbulent three dimensional boundary layer flows remain mostly outside of current computational capabilities.

In the present study an alternate approach based on mean flow modelling is explored. When the mean flow variables of velocity and vorticity are examined in the plane of the secondary flow field (the "crossplane" as diagrammed in Figure 1.3), embedded vortex structure is observed to bear close resemblance to simple two dimensional vortex models. The question addressed here is : "Can a three dimensional model of embedded vortex interaction and development be constructed from two dimensional models of vortex structure?"

Three dimensional mean flow modelling of vortex array structure based on the properties of a two dimensional model requires careful characterization of vortex structure as well as additional assumptions about the relevant physical processes involved in vortex interaction and development. It is an iterative procedure requiring a detailed experimental description of embedded vortex structure and development. The experimental results provide the "constraint" which the model must match if it is constructed correctly.

The objectives of this study are summarized as follows :

- Provide a detailed and highly resolved experimental description of vortex array structure in the crossplane, covering enough relevant changes in the vortex generator array to characterize vortex to vortex and vortex to boundary layer interactions. Examine the vortex arrays in the crossplane at two or more locations downstream of the vortex generators to characterize the streamwise development of the array.

- Construct two dimensional vortex models and compare the structure of these to that obtained in the crossplane data. Quantify these comparisons. Develop a three dimensional model of vortex array structure and streamwise development based on the two dimensional models. This model should include the representation of relevant physical processes affecting the development of the embedded vortex array.

In connection with the second objective of this study, the following question will be addressed : "What assumptions about these processes are necessary to obtain a working model that provides a good representation of the mean flow data?" Finally, the limitations of this approach are explored and the implications of the model to the present understanding of embedded vortex structure and development are discussed.

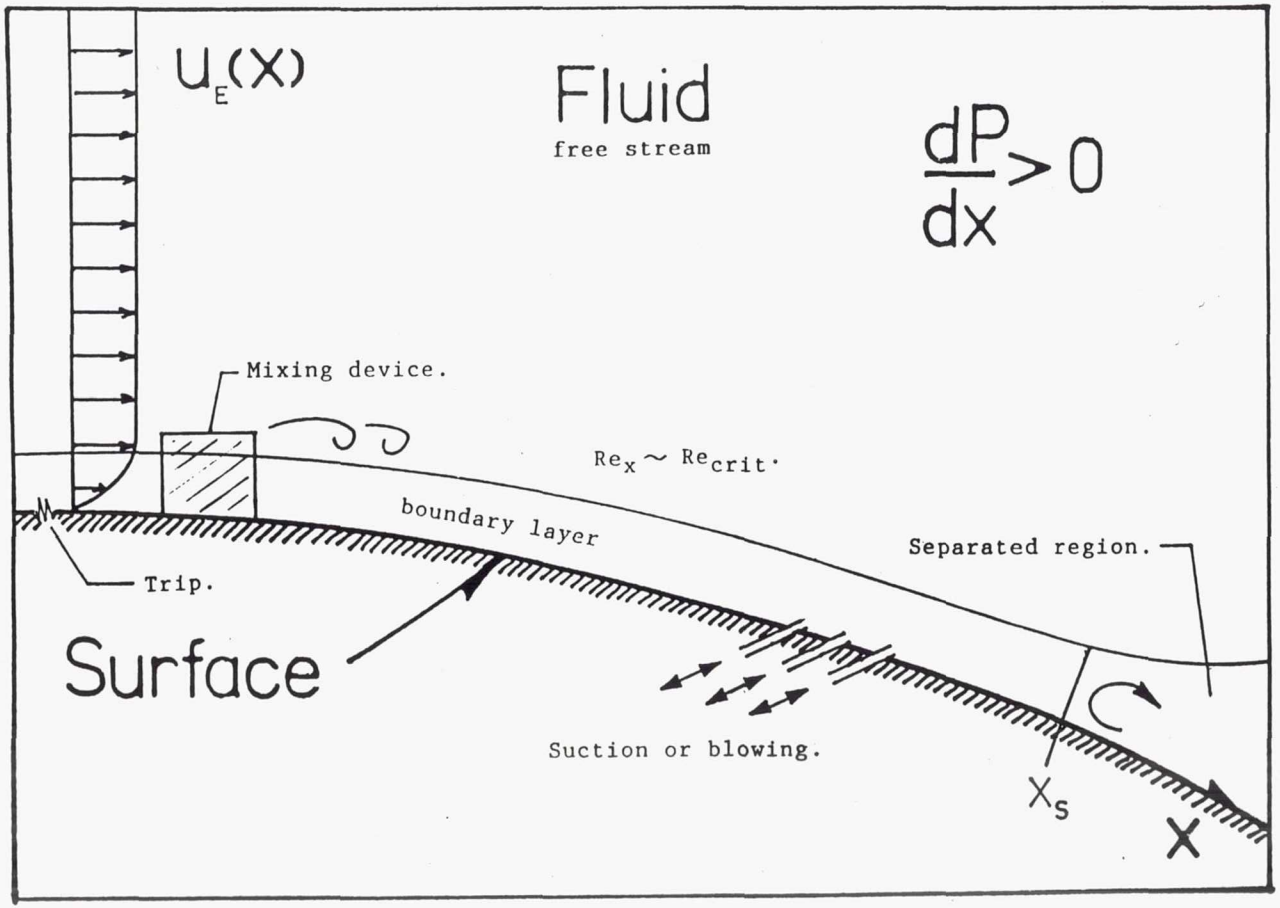

Figure 1.1 - A variety of techniques are employed to forestall the boundary layer separation at x_s. These include tripping, blowing or suction through the surface, and mixing devices (vortex generators).

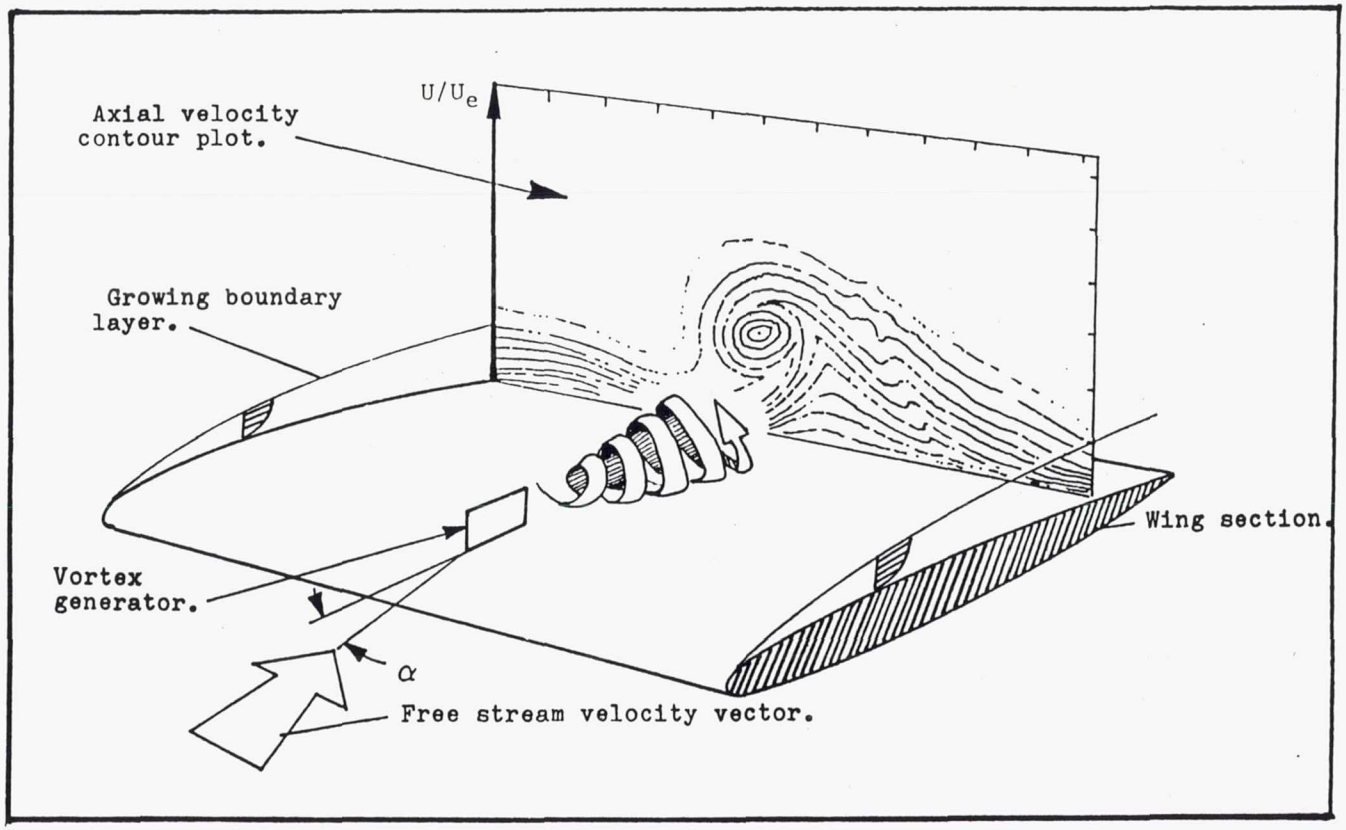

Figure 1.2 - A vortex generator mounted on a flow surface at an angle of attack sheds a single vortex which embeds itself in the boundary layer downstream. Contours of the axial velocity ratio, U/U_∞, provide a clear depiction of the vortex-boundary layer interaction.

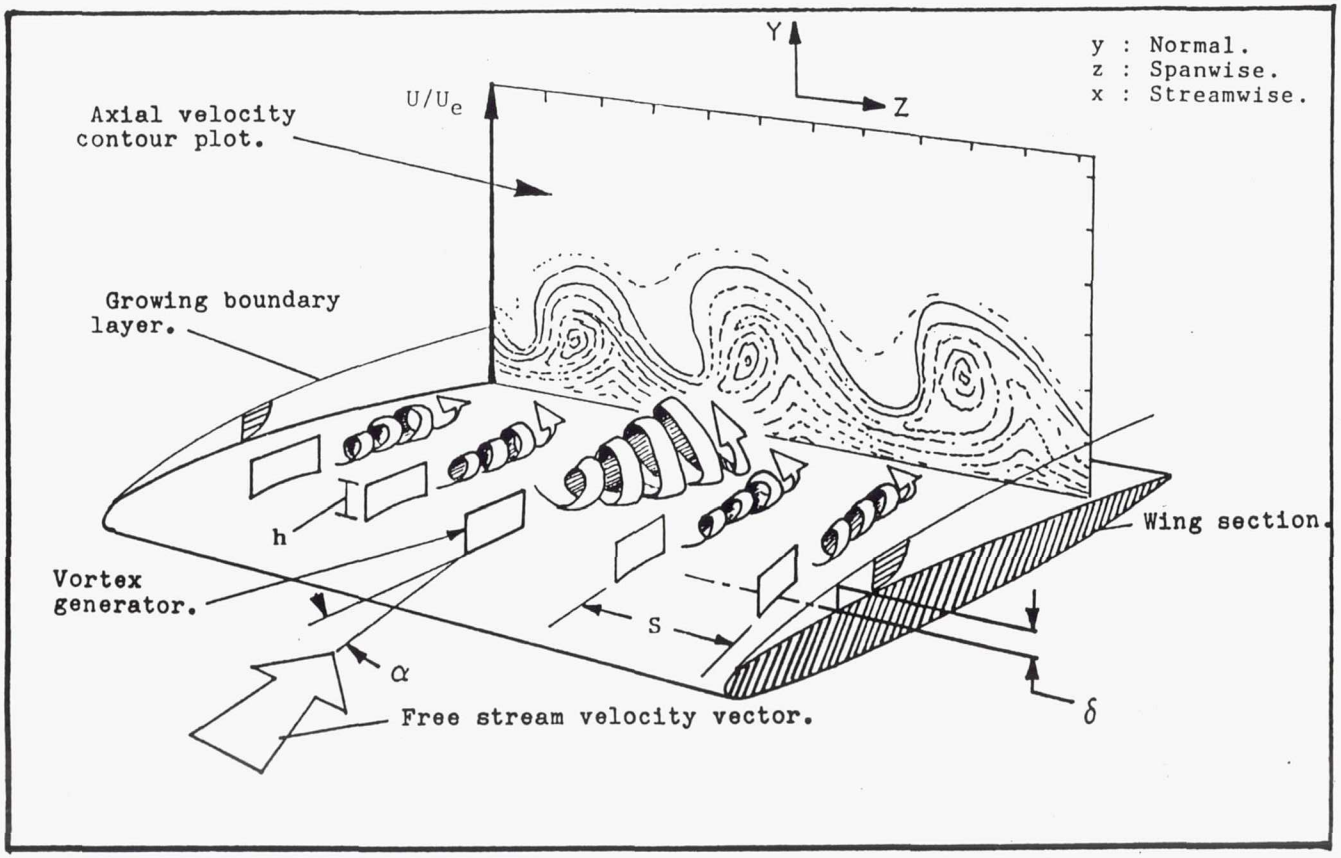

Figure 1.3 - An array of vortex generators is characterized by the nondimensional spacing ratio, S/δ, the hieght ratio, h/δ, and the angle of attack α.

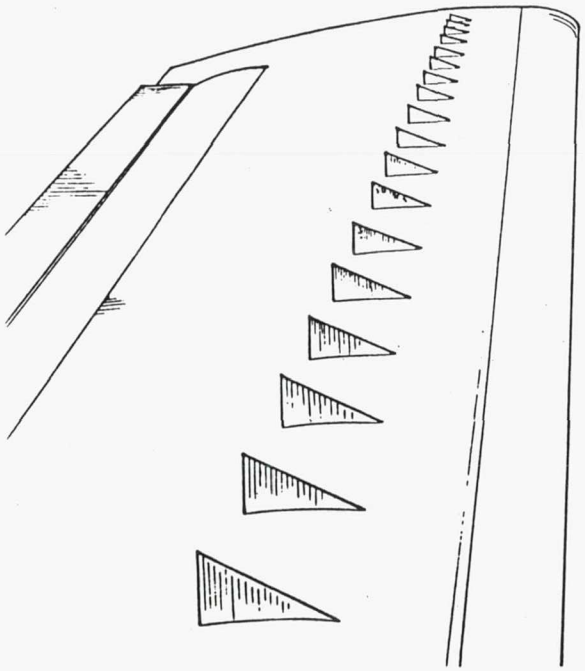

1.4a

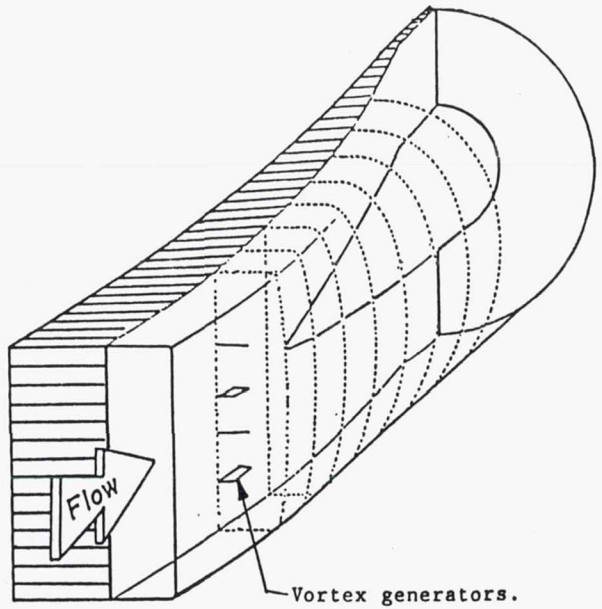

1.4b

Figure 1.4a (left) - Delta wing vortex generators mounted on the canard wing of a small aircraft (Aviation Week and Space Technology, 6/86).

Figure 1.4b (right) - A row of rectangular blade vortex generators inside a subsonic diffuser (from Brown et. al. (1968)).

Chapter 2

Literature Survey

Many studies, both theoretical and experimental in nature, have been conducted on the flow structure, development, and practical uses of streamwise vortices in turbulent boundary layer flows. From this large body of available literature are selected those studies bearing similarities to the present one. Studies providing similarities in the overall flow geometry, the generated vortex flow structures, and the parametric designs of the vortex generator arrays provide the information needed to design a useful experiment. The studies selected serve as a standard of comparison to which the results of the present study will be gauged.

Attention will first focus on experimental performance studies of vortex generator arrays mounted to produce streamwise vortices in or near the vicinity of a boundary layer. "Performance" in this case refers to some measurable gain of boundary layer control or heat transfer enhancement. The range of vortex generator types, mounting configurations, and flow conditions will be examined.

The connection between fundamental vortex flow structure and the mixing ability of an embedded array of streamwise vortices is examined by considering the structure and development of isolated vortices, i. e. those vortices occurring far from boundaries, boundary

layers, and other vortices.

Studies selected for the final portion of the review purposefully generate an embedded vortex or vortex array to resolve, in detail, the resulting flow structures. Here the differences in structure and development of isolated vortices versus embedded vortices is explored. The influences of adjacent wall and neighboring vortices are considered.

2.1 Performance Studies

Taylor and Bruynes of the United Aircraft Corporation were the first workers to recognize the potential of vortex generators as a means of controlling boundary layer flows. Early investigations at UAC were concerned with improving diffuser performance with arrays of flat plate type vortex generators similar to the type used in this study. Taylor (1950) summarized this work. These early studies were followed by work of a more fundamental nature in which the flow structure and behavior of embedded vortices was related to the design characteristics of the individual vortex generators and the parameters of the array configurations in which these were mounted.

Taylor and Grose (1954) modelled the behavior of an embedded vortex array with an array of two dimensional potential vortices with images to represent the bounding wall. The streamlines produced by the model were used to judge the mixing effect of the array. The results were mostly qualitative but firmly established the importance of vortex spacing and location in the boundary layer to the mixing properties of the array. The model also revealed some of the basic flow characteristics of the counter and co-rotating array configurations.

An experimental portion of the same study examined the mixing performance of a variety of vortex generator arrays. A boundary layer was formed on a vertically mounted splitter plate inside the test and diffuser section of a wind tunnel. The vortex generators were

mounted in a single long spanwise row where the local Reynolds number was roughly 9×10^6 and the boundary layer thickness was about 5 cms. The streamwise velocity profile of the boundary layer downstream of the vortex generators was measured with a pitot rake. The mixing performance criteria was taken to be the spanwise averaged ratio of streamwise velocity 1.9 cms from the surface to the local freestream velocity. This ratio was evaluated at the streamwise position of the rake. A variety of vortex generator designs were tested but the study concluded that the simple flat plate or *vane* type vortex generator was as effective or more effective a mixing device than the others. Figure 2.1 diagrams some of the devices used by Taylor and Grose. The study found that optimum performance was obtained with a counter-rotating array of vane type generators having $S/\delta \approx 2.5$, and $h/\delta \approx 1.3$. The mixing performance of this array increased with vortex generator angle of attack until $\alpha \approx 8°$. For α greater than about 8° no increase in mixing was seen.

Schubauer and Spangenberg (1960) concluded that forced mixing by arrays of vortex generator devices has much the same effect on boundary layers as reductions in an adverse pressure gradient. Their study was conducted on the flat bottomed wall of a wind tunnel test section. Here a nominally two dimensional boundary layer could be produced and subjected to a variety of adverse pressure gradients by the opening of adjustable slats on the test section top wall. The adverse pressure rise began roughly at the streamwise mounting location of the vortex generator array where the local Reynolds number was 1.9×10^6, freestream velocity was 25 m/sec, and the boundary layer was about 2.5 cms thick. The same adverse pressure gradient was applied to the boundary layer for a variety of vortex generator devices mounted in various single row array patterns. Some of the devices used are illustrated in Figure 2.2. The mixing performance criterion was based on the streamwise distance between the start of the pressure rise and the location of boundary layer separation on the wall. (The location of separation was revealed by chalk dust patterns.) The best

performance was obtained by the "triangular plow" with a spacing ratio of 6.0. However, the authors noted that this particular device was also subject to a relatively high drag penalty. Close in mixing performance to the triangular plow were the "simple plow" at a spacing ratio of 8.0 and the conventional vortex generator with $S/\delta = 7.0$; both with a drag force considerably less than that obtained on the triangular plow.

To maintain its mixing action on the fluid of a boundary layer an embedded vortex must remain properly situated with respect to the boundary layer. A variety of factors can cause motion of the vortex with respect to the boundary layer. Primary among these factors are wall and neighboring vortex proximity. Figures 2.3a-d diagram the possible motions of embedded vortices in the crossplane. In Figure 2.3a a single embedded vortex is convected along the wall in the same direction as the crossflow underneath the core of the vortex. The closer the vortex is to the wall, the stronger the resulting crossflow which, in turn, implies a greater convective velocity on the vortex core. Figure 2.3b represents an embedded array of co-rotating vortices. Here all vortices possess the same convective velocity and the entire array moves along the wall in the same direction as the crossflow at the wall. Note that there is no tendency for for vortices in such an array to move outside of the boundary layer. In Figure 2.3c two counter-rotating vortices are in close proximity to each other and to the wall. The flow between the vortices is directed towards the wall. The velocity field of each vortex convects the other vortex towards the wall and the wall, in turn, convects each vortex away from the other. In this case, again, there is no tendency for the vortices to move out of the boundary layer. In Figure 2.3d another counter-rotating pair of vortices is in close proximity to each other and the wall. This time the flow between vortices is directed up, away from the wall. Each vortex convects the other up and out of the boundary layer region. Keeping the vortex properly situated with respect to the boundary layer is thus a matter of balancing the strength, rotation, spacing, and distance from the wall for all vortices in the

array. This is achieved by proper design and placement of the vortex generators.

Pearcy (1961) recognized the importance of vortex to wall and vortex to vortex interactions on the mixing performance of embedded arrays of streamwise vortices. Theoretical models were developed to explain and predict the resulting motions of vortices based on the initial strengths (angle of attack α), and the spacing and hieght ratios of the vortex generator arrays that produced them. Although these results were based on potential flow models and did not take into account the damping influences of viscosity and turbulence, they did provide good qualitative agreement with a corresponding set of experiments at the National Physics Laboratory. In the experiments the influences of viscous and turbulent stresses could be observed. From these results a set of guidelines on vortex generator array designs were developed.

For arrays of co-rotating vortices good performance was obtained only when the vortex generators were set to produce equal strength vortices with an initial spacing ratio of 3.0 or more. For spacing ratios less than this, the low momentum fluid swept away from the wall by one vortex would be ingested by the downflow of its neighbor, thereby reducing mixing performance. Unequal strength vortices tended to push neighbors out of the boundary layer. The vortices produced by vortex generators on the boundary of the array (the "exterior" vortices) tended to merge with the neighboring interior vortices and lift out of the boundary layer. Taking into account the drag induced by the presence of the vortex generators, an optimum performance spacing ratio of 5.0 or 6.0 was determined by Pearcy for the co-rotating configuration.

Vortices in counter-rotating arrays exhibit a tendency to draw together and lift each other out of the boundary layer. Motion away from the boundary layer can be delayed, however, by suitably spacing and sizing the vortex generators. Figure 2.4 diagrams such an array of vortex generators producing counter-rotating vortices. The curved lines represent the path

of the vortices in the crossplane. Using vortex 2 as an example, we see that it is initially convected down to the wall by the velocity field of its near neighbor, vortex 1. Vortex 2 is then convected along the wall until it finds itself in the proximity of vortex 3 whereby it is then lifted up, away from the surface. To maximize the mixing performance of the counter-rotating array we need to maximize the time spent near the wall by the vortices. Pearcy found that a ratio of $D/S = 4.0$ and $S/h = 2.5$ maximized the mixing performance of the counter-rotating array over the greatest streamwise distance. If the streamwise extent of the required mixing is not critical then increased mixing may be obtained by slight adjustments to these values.

Subsonic diffuser performance is enhanced by the application of forced mixing by vortex generators. Brown et. al. (1968) applied the design principles of Pearcy to establish the proper placement of counter-rotating vortex generators around the mouth of a subsonic diffuser inlet. Tests were conducted on the inlet with the vortex generators mounted, at an inlet Mach number of 0.5 ($U_\infty \approx 175$ m/sec, $\delta \approx 0.6$ cms). Results were compared to the performance of a conventional trumpet-shaped diffuser. It was found that the diffuser with vortex generators mounted reduced pressure recovery losses by about 40 percent.

By bringing the higher momentum fluid of the freestream closer to the wall, the action of vortical mixing effectively thins the boundary layer in certain regions underneath the embedded vortices. Here the skin friction and heat transfer (which are now functions of both streamwise and crossplane coordinates) are increased.

Spangler and Wells (1964) examined crossplane profiles of skin friction resulting from a turbulent boundary layer with embedded streamwise vortices. The study was carried out along the walls of a tubular test section in a boundary layer tripped turbulent. The Reynolds number of the channel flow, based on the diameter of the test section, was roughly 2×10^5. A row of vane type vortex generators were mounted where the local boundary layer thickness

was $\delta = 6.3$ cms, and the freestream velocity about 14 m/sec. Height ratios of $h/\delta =$ .02, .1, and .2 were examined for counter-rotating arrays arranged in an unequal spacing pattern appropriate for optimum mixing as defined by Pearcy (1961); i. e. $D/S = 4.0$. Measurements of streamwise velocity profiles and crossplane skin friction profiles were taken with and without the vortex generators mounted. The drag force on the vortex generators was measured as well. It was found that the embedded vortices increased and decreased skin friction locally but that the integrated effect (over the crossplane coordinate) was an increase in skin friction. The manner in which the skin friction profiles persisted with streamwise distance indicated that the responsible mechanism was vortical mixing, and not any effect associated with the "form" drag on the vanes. The mixing benefit of the array was gauged by the measured maximum crossplane velocities. The penalty paid was gauged by the form drag. The ratio of crossplane velocity to form drag was found to be a maximum for $\alpha = 8°$.

Increased heat transfer results from the mixing action of embedded vortices. Russel et. al. (1982) used vortex generators to enhance the heat transfer from flat plate fins in heat exchanger devices. A large scale model of ten fins was constructed with vane type vortex generators mounted on the fin surfaces in a configuration set to produce counter-rotating vortices. Transient heat transfer visualization tests were conducted in a heated airstream. Local coefficients of heat transfer on the fin surface varied in a manner consistent with the placement of the vortex generators and the action of the resulting vortices. Secondary velocities directed towards the fin surface produced high rates of heat transfer, velocities away from the surface produced low rates of heat transfer. The net effect, however, was an increase in the overall heat transfer coefficient of the plate fins.

Rao and Mehrotra (1983) also examined the effect of embedded vortices on the streamwise component of skin friction occurring downstream of a spanwise row of vortex generators set to produce counter-rotating vortices. The integrated result was obtained experimentally

by measuring the drag force on a downstream section of the flow surface. The flow surface was flat and the boundary layer which formed over it was turbulent. Freestream velocity was varied between 12 and 40 m/sec yielding plate length Reynolds numbers between 3×10^5 and 8×10^5. The boundary layer thickness at the vortex generator mounting station was approximately 1.5 cms. Three vortex generator devices were tested. Two were vane type vortex generators, and the third an obstacle device in the form of a circular disc. Figure 2.5 indicates how this device was mounted to produce a pair of counter-rotating vortices. The vortex generators could be mounted either upstream of, or directly on, the drag force sensitive surface. The latter case was done to obtain the form drag on the vortex generators themselves. A variety of spacing ratios were tested with the intention of producing a configuration which would reduce the drag force suffered by the surface due to skin friction effects alone. It was found, however, that all configurations of the vane type vortex generators increased the skin friction drag above the flat plate results. Arrays of the obstacle device, curiously, reduced the drag force. The authors attributed this result to the deficit in the streamwise velocity field (resulting in a corresponding drop in the primary wall shear stress component) present in the considerable wake region generated by these devices.

Turk and Junkhan (1986) correlated heat transfer augumentation with the characteristics of the vortex generator array. The study was conducted in an initially laminar boundary layer formed over a flat plate. Surface heating elements with attached thermocouples were used to measure the local heat transfer coefficients behind a single spanwise row of vane type vortex generators set to produce counter-rotating vortices. Freestream velocities were varied between 2.5 and 9.0 m/sec. The thickness of the laminar boundary layer at the vortex generator mounting station was about 0.25 cms. Spanwise profiles of the heat transfer coefficient were recorded at a variety of downstream locations for arrays of vortex generators differing either in spacing or hieght ratios. The profiles observed were similar in shape to

the ones recorded by Russell et. al. (1982). The spanwise averaged heat transfer coefficient at the streamwise position x was nondimensionalized by the value obtained for the nominal two dimensional boundary layer at the same location. It was found that this nondimensional ratio was greater than one over the entire measurement domain and increased as x increased. This ratio was also a function of array spacing and hieght ratios. In general, it was found that tightly spaced arrays of large blades produced the greatest heat transfer enhancement.

Crossplane profiles of skin friction coefficient were obtained by Johnston and Nishi (1990) for a turbulent boundary layer with embedded streamwise vortices. The experiments were conducted in a low speed wind tunnel where a boundary layer was formed over a flat surface and tripped turbulent. The freestream airspeed was approximately 15 m/sec. The embedded vortices were created by jets of air issuing from a spanwise row of holes in the wall surface. When the axis of the jet was aligned with the air stream a pair of counter-rotating vortices was formed. Figure 2.6 diagrams the vortex generator jet (VGJ). The thickness of the boundary layer at the jet location was about 1.5 cms and the jets were positioned 10.2 cms apart. The presence of embedded streamwise vortices was verified by measurements of streamwise velocity profiles. With the jets off nominal two dimensional boundary layer behavior was observed. By varying the ratio of jet velocity to freestream velocity, VR, vortices of differing strengths could be obtained. Spanwise profiles of skin friction coefficient, C_f, were recorded at two positions downstream of the vortex generators. Increasing VR above about 0.4 drastically increased the spanwise variation of C_f. The location and action of the embedded vortices could be inferred from the spanwise behavior of C_f as follows. Embedded vortex downflow increased C_f above the value observed in the nominal two dimensional boundary layer. The center of the vortex was located near the peak in C_f. A rapid drop in C_f occurred where the secondary flow of the vortex moved away from the wall. The minimum value of C_f was below the value obtained in the two

dimensional boundary layer. These results for C_f are qualitatively similar to the results obtained for the heat transfer coefficient in the experiments of Turk and Junkhan (1986).

A close relationship exists between the secondary flow structure of a vortex and the distortion of the boundary layer in which it is embedded. To better understand this, an examination of vortex structure in general is helpful. The structure and development of a vortex removed from the influences of walls and neighboring vortices (an "isolated" or "free" vortex) provides such a general description.

2.2 The Structure and Development of Isolated Vortices

As noted previously, the helical or "swirling" pattern of vortex flow is mostly responsible for the effectiveness of streamwise vortices as mixing devices. The vortex is best characterized in the crossplane where the pattern of secondary flow properties provides a graphical depiction of the vortex structure. Two dimensional models are most often used to describe this structure, the most fundamental being the potential vortex. The potential vortex consists of an axisymmetric flow field with the following properties :

$$\text{Streamlines: } \psi = -\frac{\Gamma}{2\pi} \ln r, \tag{2.1}$$

$$\text{Radial velocity component: } v_r = 0, \tag{2.2}$$

$$\text{Azimuthal velocity component: } v_\theta = \frac{\Gamma}{2\pi r}, \tag{2.3}$$

where r is measured from the vortex center, and Γ is the vortex circulation :

$$\Gamma = \oint_{path} \vec{V} \cdot d\vec{s}, \tag{2.4}$$

where "path" refers to any closed path around the vortex center and $\vec{s}$ refers to the path coordinate. $\vec{V}$ represents the secondary velocity vector. The $1/r$ behavior of the azimuthal velocity component is typical of most vortex flows in regions removed far enough from the center. The potential vortex is an inviscid flow; real vortices are observed to have central regions of viscous flow referred to as "cores". The flow field of the viscous core roughly approximates a body in solid rotation.

A two dimensional vortex model with a viscous core is referred to as an "Oseen" vortex. The laminar Oseen vortex represents the time dependant decay of a potential vortex whose velocity at the origin ($r = 0$) is forced to zero at time $t = 0$. The model equations are developed by a solution of a simplified form of the Navier-Stokes momentum equation with appropriate boundary conditions. Chapter 5 contains the details of this solution procedure. The model velocities are found to be :

$$\begin{aligned} \text{Radial velocty} : v_r &= 0, \\ \text{Azimuthal velocity} : v_\theta &= \frac{\Gamma_\infty}{2\pi r}\left[1 - \exp\left\{-\frac{r^2}{4\nu t}\right\}\right], \end{aligned} \tag{2.5}$$

where ν is the coefficient of kinematic viscosity. The unsteady solution can be transformed to a steady solution through a transformation relating the decay time t to a convective displacement, $(x - x_0)$, along the axis of streamwise motion where x_0 represents the vortex origin (a wing tip for example) :

$$t = \frac{x - x_0}{U_\infty}, \tag{2.6}$$

where U_∞ is the velocity of the convecting freestream. Near the center of the vortex (where $r \approx 0$) the velocity varies linearly with r. In the far field, away from the vortex center, the vortex flow field is potential. The circulation of the Oseen model is a function of radius r

measured from the origin and is given by :

$$\Gamma = \Gamma_\infty \left(1 - \exp\left\{-\frac{r^2}{4\nu t}\right\}\right), \tag{2.7}$$

where Γ_∞ is the result as $r \rightarrow \infty$.

A patchwork model consisting of the outer flow region of a potential vortex and a core in solid body rotation is known as the "Rankine" model. Like the potential vortex, the radial velocities of the Rankine model are zero. The azimuthal velocities are given by :

$$\begin{aligned} v_\theta &= \frac{\Gamma r}{2\pi r_0^2}, \; r \leq r_0, \\ v_\theta &= \frac{\Gamma}{2\pi r}, \; r \geq r_0, \end{aligned} \tag{2.8}$$

where r_0 is the radius of the viscous core and Γ is the circulation of the Rankine vortex determined on a path of radius $r \geq r_0$.

An important connection to three dimensional flow occurs when considering the downstream development of an isolated vortex. Following the initial roll-up of the vortex sheet into a vortex structure with a core of concentrated vorticity, the vortex grows by diffusion of the core vorticity into the surrounding inviscid field. As the core grows the azimuthal velocities drop off. The radial pressure gradient required to balance the centrifugal force of rotation becomes less steep as the azimuthal velocities tail off downstream. This leads to a positive axial pressure gradient ("axial" meaning streamwise in this case) and a resulting loss of streamwise momentum in the region of the vortex core. Thus the streamwise velocity $u(r)$ in the region of the core will be less than the surrounding freestream velocity U_∞. The difference $(u - U_\infty)$ is referred to as the streamwise "velocity deficit" of the core.

The velocity deficit of a trailing vortex core was systematically analyzed by Batchelor

(1964). In the analysis Batchelor assumed that the trailing vortex was in a full stage of development and the formative processes associated with the roll-up of the vortex sheet were complete. At this far downstream position the vortex core was assumed to be in a state of diffusive growth due to the action of viscosity. The equation of motion along the azimuthal coordinate yielded the Oseen profile of Eq. (2.5). By assuming that $|u - U_\infty| \ll U_\infty$ Batchelor was able to obtain a similarity solution of the streamwise momentum equation. The maximum streamwise velocity deficit was found to occur at the core center and varied with x following the relationship :

$$(U_\infty - u) \sim \frac{\Gamma^2}{\nu x} \ln\left[\frac{x U_\infty}{\nu}\right].$$

Early development of the theories concerning the structure of isolated vortices was motivated by the problems associated with trailing vortices shed from the surfaces of large commercial aircraft. The flow fields created by such vortices are amazingly persistent in time and create flight hazards for smaller airplanes happening upon these wake regions. The trailing vortices generated in these cases (as well as in most cases of engineering interest) are turbulent in nature, and possess three dimensional developmental characteristics. Modifications of the two dimensional models described above have been proposed by researchers to account for these characteristics.

To account for turbulence in the structure of a trailing vortex Squire (1965) proposed that the coefficient of viscosity ν in the Oseen model of Eqs. (2.5)-(2.7) be replaced by :

$$(\nu + \epsilon),$$

where ϵ is a turbulent "eddy" viscosity having a value proportional to the vortex circulation :

$$\epsilon = a_0 \Gamma. \tag{2.9}$$

Hoffman and Joubert (1963) developed a model of the circulation profile of a turbulent trailing vortex based on an empirical fit to experimental data and dimensional analysis. Hoffman and Joubert's vortex consisted of :

1. An "inner" or core region of flow such that :

$$\frac{\Gamma}{\Gamma_1} = 1.83 \left(\frac{r}{r_1}\right)^2, \quad \frac{r}{r_1} \lesssim 0.4, \tag{2.10}$$

   where r_1 is the radial position of maximum azimuthal velocity, and Γ_1 is the circulation contained in the region of radius r_1. The inner flow region behaves as if it were an "eye" in solid body rotation.

2. A transition region between the inner and an "outer" region.

3. The outer region of flow where circulation varies logarithmically with radial position :

$$\frac{\Gamma}{\Gamma_1} = 2.14 \log_{10}\left(\frac{r}{r_1}\right) + 1, \quad 0.6 \lesssim \frac{r}{r_1} \lesssim 3.0. \tag{2.11}$$

This profile was found to hold true regardless of the particular value of viscosity, provided :

$$\frac{U_\infty x}{\Gamma} > 150,$$

where x is the distance downstream from the vortex origin.

McCormick, Tangler, and Sherrieb (1968) correlated data collected in the wake of air-

craft to an Oseen model having an eddy viscosity following Eq. (2.9). The constant of proportionality, a_0, was found to vary with the strength and radius of the measured viscous core. A better fit to the data was obtained with the profile of Hoffman and Joubert (1963) above.

The high levels of turbulence present in the core of trailing vortices may originate from the locations where the vortices roll up. When a trailng vortex is shed from an aircraft, for example, turbulence may be entrapped in the core from boundary layers occurring on the flow surfaces. Flight experiments indicate that turbulence levels in the core remain high, even at far downstream locations. This suggests that some mechanism exists to sustain core turbulence.

Owen (1970) proposed a model of a turbulent vortex in which the core turbulence is sustained by viscous diffusion of eddies across a core boundary region of small but finite thickness. The Owen model of a turbulent vortex is diagrammed in Figure 2.7. The model consists of a core of radius r_c in solid body rotation separated from an outer irrotational flow by an irregular boundary "sheath" of thickness δ_0. The vortex turbulence is confined to the core region of radius r_c and vanishes across the sheath. Assuming that the core boundary propagates outward like $(\text{time})^{1/2}$ (characteristic of viscous diffusion) Owen was able to obtain a relationship for the eddy viscosity similar to the model proposed by Squire :

$$\epsilon = \alpha_0 \Gamma,$$

where α_0 was found to be proportional to the vortex Reynolds number :

$$\alpha_0 \sim \left(\frac{\Gamma}{\nu}\right)^{-1/2}.$$

Wind tunnel and flight data are better correlated with Owen's result of a variable eddy

viscosity (see, for example, Iversen (1976)).

Uberoi (1978) argues that pre-existing studies of turbulent vortex growth and development neglect the radial and axial convection of angular momentum. Uberoi (1977) establishes the dominance of the terms representing these quantities, particularly in the early stages of vortex development. Uberoi (1978) further postulates that core turbulence is sustained by the streamwise velocity deficit present in the vortex core. Accepting the Owen model of the turbulent vortex, but including the influence of the terms representing the radial and axial convection of angular momentum on the growth of the viscous core, Uberoi was able to obtain a circulation profile for a turbulent trailing vortex in a general stage of development :

$$\frac{\Gamma}{\Gamma_\infty} = 1 - \left[1 + \frac{a}{b}\left(\exp\{b\eta\} - 1\right)\right]^{-1},$$

where :

$$\eta = \left(\frac{rU_\infty}{\Gamma_\infty}\right)^2 \left(\frac{\Gamma_\infty}{xU_\infty}\right)^n.$$

a, b, and n are constants. The circlation profile of Uberoi provides excellent correlation to the data of Singh (1974), Iversen (1976), and Phillips and Graham (1984), as well as others.

2.3 The Structure and Development of Embedded Vortices

The presence of a bounding wall and associated turbulent boundary layer substantially influence the structure and development of streamwise vortices. The interaction between the turbulent boundary layer and the embedded vortex creates a complex three dimensional flow field. In the studies reviewed below the focus is generally on the resulting distortions of the turbulent boundary layer. Examinations of heat transfer, skin friction, and secondary

flow structure are conducted in the presence of embedded vortices and compared to the two dimensional boundary layer results obtained in the absence of embedded vortices. In the present study we are interested in approaching the problem from the opposite direction, or in other words; to focus attention on the embedded vortices themselves, and ask : What influence does the turbulent boundary layer have on the structure and development of the embedded vortices? Embedded vortex structure and development may be compared to the structure and development of isolated vortices to measure the effect of wall and boundary layer. This approach requires a careful characterization of vortex structure. Our review of isolated vortex structure indicates the following general characterization :

1. **Strength** : The vortex circulation, Γ, or vortex Reynolds number, Γ/ν, provides a characterization (or "descriptor") of vortex strength.

2. **Location** : The point about which the core is centered on provides a descriptor of vortex location. Conveniently, this point coincides with the location of peak streamwise vorticity in the crossplane.

3. **Stage of Diffusive Development** : The radius of the viscous core, or the magnitude of peak streamwise vorticity provide possible descriptors for the diffusive state of the vortex.

Attention will focus on how the embedded vortices in various studies have been characterized. If "structure" is characterized in terms of vortex descriptors then "development" is the change in these descriptors as the flow proceeds downstream. The influence of the wall, boundary layer, and neighboring vortices on the downstream development of the descriptors will also be examined.

Eibeck and Eaton (1985) extensively examined the interaction between a turbulent boundary layer and a single embedded vortex. Their study was one in a series of simi-

lar studies conducted under the auspices of the Department of Mechanical Engineering at Stanford University. A flat plate boundary layer was tripped turbulent along one wall of a test section in a low speed wind tunnel. A single delta wing vortex generator set at an angle of attack was used to produce a single embedded vortex. The local Reynolds number at the streamwise mounting location of the vortex generator was 5.1×10^5. The boundary layer thickness here was 1.3 cm, and the height ratio of the vortex generator was varied in the range $0.77 \leq h/\delta \leq 2.31$. The freestream velocity was held to a nominal value of 16.0 m/sec. Vortices of differing strengths were created by adjusting the angle of attack α or hieght ratio h/δ.

Measurements of secondary velocities in the crossplane allowed computation of the vortex descriptors. The descriptor of vortex strength was taken to be the vortex circulation, the diffusive state of the vortex was measured by the radius of the viscous core. These descriptors were determined by curve fitting the secondary velocity data in the crossplane to a Rankine model (Eqs. (2.8)) of the vortex following a four parameter least squares procedure. (The four parameters being circulation, core radius, and the z and y locations of the core center.) In the model curve fit an image vortex was used to represent the influence of the wall.

A total of 5 different embedded vortex test conditions were examined. Results included the measurement of the secondary velocity field in the crossplane at four streamwise locations downstream of the vortex generator, and measurements of streamwise velocities through the distorted boundary layer at a variety of spanwise and streamwise locations. Contours of streamwise velocity viewed in the crossplane allowed for a graphical depiction of the interaction between vortex and boundary layer. A constant heat flux surface heater was installed 23 cms downstream of the vortex generator mounting station. Thermocouples mounted on the flow surface allowed for a determination of the local heat transfer coefficient. A thermocouple probe determined the crossplane structure of the distorted thermal bound-

ary layer at several downstream locations. Measurements of skin friction were obtained with surface fence gauges.

The heat transfer results indicated increases of up to 25 percent over flat plate results for heat transfer coefficient. Comparing the spanwise behavior of heat transfer coefficient to the crossplane flow structure it was seen that the areas of increased heat transfer corresponded to the region of vortex downflow. The stronger vortices produced larger increases in heat transfer at the same crossplane location. Decreases in heat transfer down to about 15 percent under flat plate results occurred at spanwise locations coinciding with the upflow region of the vortex. Measurements of skin friction produced similar results.

The measured boundary layer profiles indicated a thinned boundary layer present in the vicinity of the vortex downwash and a thickened boundary layer in the vicinity of the vortex upwash. The boundary layer profiles suggested that the heat transfer and skin friction behavior of the distorted boundary layer could be obtained from two dimensional results provided that these results were correlated to the local thickness of the boundary layer with embedded vortex present.

When the downstream development of the single embedded vortex was compared to the development of an isolated vortex, several interesting points were observed :

1. Circulation of an isolated vortex does not decrease as the vortex develops downstream. The circulation of an embedded vortex does decrease. This is explained by the presence of the wall. A spanwise component of the wall shear stress gives rise to a torque opposing the rotation of the vortex.

2. The core vorticity profile of an isolated vortex is always circular in shape. In contrast, the observed downstream profiles of core vorticity of the embedded vortex were *elliptically* shaped. In the study it was not decided whether this ellipticity was due to the presence of the wall or whether it indicated an unsteady effect - a vortex oscillating

or "meandering" from side to side during examination.

3. The downstream growth of the core radius of the embedded vortex was found to be much greater than the growth observed for an isolated turbulent vortex having the same vortex Reynolds number. Two possible explanations were given :

   - The turbulent nature of the boundary layer surrounding the vortex core may contribute to the diffusion taking place within the core.
   - The presence of a streamwise velocity deficit (or wake) in the study contributed to the turbulence intensity inside the core region thereby increasing the rate of diffusive growth.

A study of the structure and development of a single embedded vortex was carried out by the Stanford team of Westphal, Pauley, and Eaton (1987). The flow geometry and test conditions covered were similar to the Eibeck and Eaton study described above with some differences. The freestream velocity was somewhat higher ($U_\infty \approx 25$ m/sec), and an additional adverse pressure gradient condition was applied to the boundary layer in the test section of the wind tunnel to observe its effect on the development of the embedded vortex. Measurements of secondary velocities in the crossplane were taken at several streamwise positions. When plotted out, this data provided a graphical depiction of the vortex structure. The velocity data was converted to streamwise vorticity data; the spatial derivatives of the secondary velocities being obtained by fitting cubic splines to the velocity data profiles. Crossplane contour plots of the streamwise vorticity also provide a graphical illustration of the vortex core structure. In addition to mean flow measurements in the crossplane, the turbulent properties of the embedded vortex were probed by measuring five of six independant components of the Reynolds stress tensor with a X-wire. In addition, skin friction was measured by the application of a Preston tube, and visualized by using an oil film technique.

Six vortex descriptors were used to characterize vortex structure. All six were obtained from the streamwise vorticity data. These are as follows :

1) Strength - Circulation, Γ.

2-3) Location - z, y location of peak streamwise vorticity, (z_c, y_c).

4) State of Development - Peak streamwise vorticity, $\omega_{x,max}$.

5-6) State of Development - z, y dimensions of the core, (R_z, R_y).

The circulation was obtained by integrating the vorticity over the region of the core. Descriptors 2-6 were obtained by examining the streamwise vorticity field in the crossplane.

Vortex circulation was observed to decay slowly, following a pattern similar to that observed in the earlier study. After 2 meters of streamwise development a 20 percent loss of upstream circulation was typical. In contrast, the peak vorticity dropped by an order of magnitude over the same streamwise distance. With the addition of an adverse pressure gradient the peak vorticity was observed to decay even further, and at a faster initial rate upstream. The decay rate of peak vorticity closely paralleled the growth rate of the viscous core. When the y dimension of the viscous core (R_y) became a significant fraction of the vortex position in the boundary layer (y_c) the core took on an elliptical shape. At the downstream station it was found that $R_y/R_z \sim 2.0$ for the case of a constant pressure gradient. When an adverse pressure gradient was applied the ellipticity of the core became even greater; R_y/R_z was observed to be about 3.0 at the downstream station.

Sharp peaks in spanwise skin friction profiles were a strong indication that the vortex ellipticity was not due to any quasi-steady meander. The distortion of the Reynolds stress field in the vicinity of the embedded vortex was found to be more pronounced under the influence of the adverse pressure gradient.

To quantify the effects of vortex to vortex interaction on the structure and development of embedded vortices Pauley and Eaton (1988) conducted an experimental study of embedded vortex pairs. The flow geometry was identical to the earlier Stanford study of Eibeck and Eaton (1985). The vortices were again generated by delta wing vortex generators set at an angle of attack. Three types of vortex to vortex interaction were extensively studied : A counter-rotating configuration producing a region of downflow between vortices (a "common downflow" pair), a counter-rotating configuration producing a region of upflow between vortices (a "common upflow" pair), and a pair of co-rotating vortices. Crossplane measurements of vortex structure by means of hot wire and pitot probes were performed at resolutions exceeding those of the earlier studies. Surface measurements of heat transfer and skin friction aided in defining the vortex to vortex and vortex to boundary layer interactions. The turbulent flow field of the embedded vortices was explored by conducting extensive crossplane measurements of all six components of the turbulent Reynolds stress.

Vortex structure was quantified as follows :

1. Strength - Vortex circulations were determined from integration of streamwise vorticity over the region of the vortex cores.

2. Location - The location of the vortex center was taken to be the crossplane coordinates of the location of peak streamwise vorticity in the cores.

3. The state of vortex development was taken to be the magnitude of the peak streamwise vorticity in the core.

Comparison of the velocity and vorticity data in the crossplane to the velocity and vorticity structure exhibited by an Oseen model with matching descriptors revealed striking similarities between the two.

Motion of the vortex cores was observed to follow the general characteristics of potential flow theory as outlined by Pearcy (1961). A downflow pair of counter-rotating vortices was observed to push along the wall away from each other. The downflow pair exhibited no tendency to move away from the wall and so the resultant interaction with the boundary layer was strong. An upflow pair of counter-rotating vortices was observed to draw together and convect each other up and out of the boundary layer. The resultant interaction with the boundary layer was therefore weak. A co-rotating pair of vortices was observed to merge rapidly into a single embedded vortex. At the downstream measurement station little trace of the original vortex pair was evident in the combined vortex structure.

The streamwise decay of vortex circulation was correlated to the proximity of the vortex to the wall. When the vortex was close to the wall the strong crossflows generated a correspondingly strong torque opposing the rotation of the vortex. This frictional torque originated from the spanwise component of the wall shear stress. This explains why the rate of circulation decay observed for the downflow vortex pair was higher than that observed for the upflow pair; the downflow pair of vortices remained closer to the wall during their downstream development.

The streamwise decay of peak vorticity was dependant on the proximity of neighboring vortices. A close neighbor would strongly perturb and "spread" the vorticity field of an embedded vortex core thereby increasing the rate of decay of peak vorticity beyond levels observed for single embedded vortices. Vorticity spreading and the rate of peak streamwise vorticity decay were observed to be proportional to the proximity *and* strength of the neighboring vortex.

Conclusive evidence on the responsible factor behind the ellipticity of the core structure was discovered. The streamwise vorticity field of the core was distorted by the convection of the secondary flow field. To show this, terms representing the mean convection of streamwise

vorticity due to the secondary flow were evaluated from the data in the vicinity of the embedded vortex core. Evaluation of the turbulent Reynolds stress field also revealed the following :

- A region of enhanced turbulent kinetic energy appears in the core as a result of the velocity deficit there. The velocity deficit strongly affects the behavior of the normal Reynolds stresses in the vicinity of the core, but does not strongly affect the turbulent shear stress field there.

- The interaction between vortices in close proximity is accompanied by elevated levels and distorted distributions of the Reynolds stresses occurring in the cores. The region between vortices in close proximity is characterized by high turbulence production and diffusion.

Streamwise development of vortex structure in the absence of a substantial core velocity deficit has been conducted by Shabaka, Mehta, and Bradshaw (1984). To reduce the influence of the velocity deficit on the turbulence structure of the core, the vortex generators were mounted in the settling chamber, far upstream of the test section. Resulting mean flow structure was similar to that obtained at the far downstream measurement station in the Stanford studies.

Sankaran and Russell (1990) have carried out a computational study of vortices embedded in a turbulent boundary layer. The mathematical model used is based on the steady incompressible Navier-Stokes equations, neglecting the streamwise viscous derivatives. A $\kappa - \epsilon$ turbulence model was used in conjunction with the partially parabolized equations. Many features of vortex structure, interaction, and development were qualitatively reproduced by this model. These features included downstream distortion of the core, spanwise behavior of the skin friction coefficient, and the relationship between vortex

proximity and peak vorticity decay.

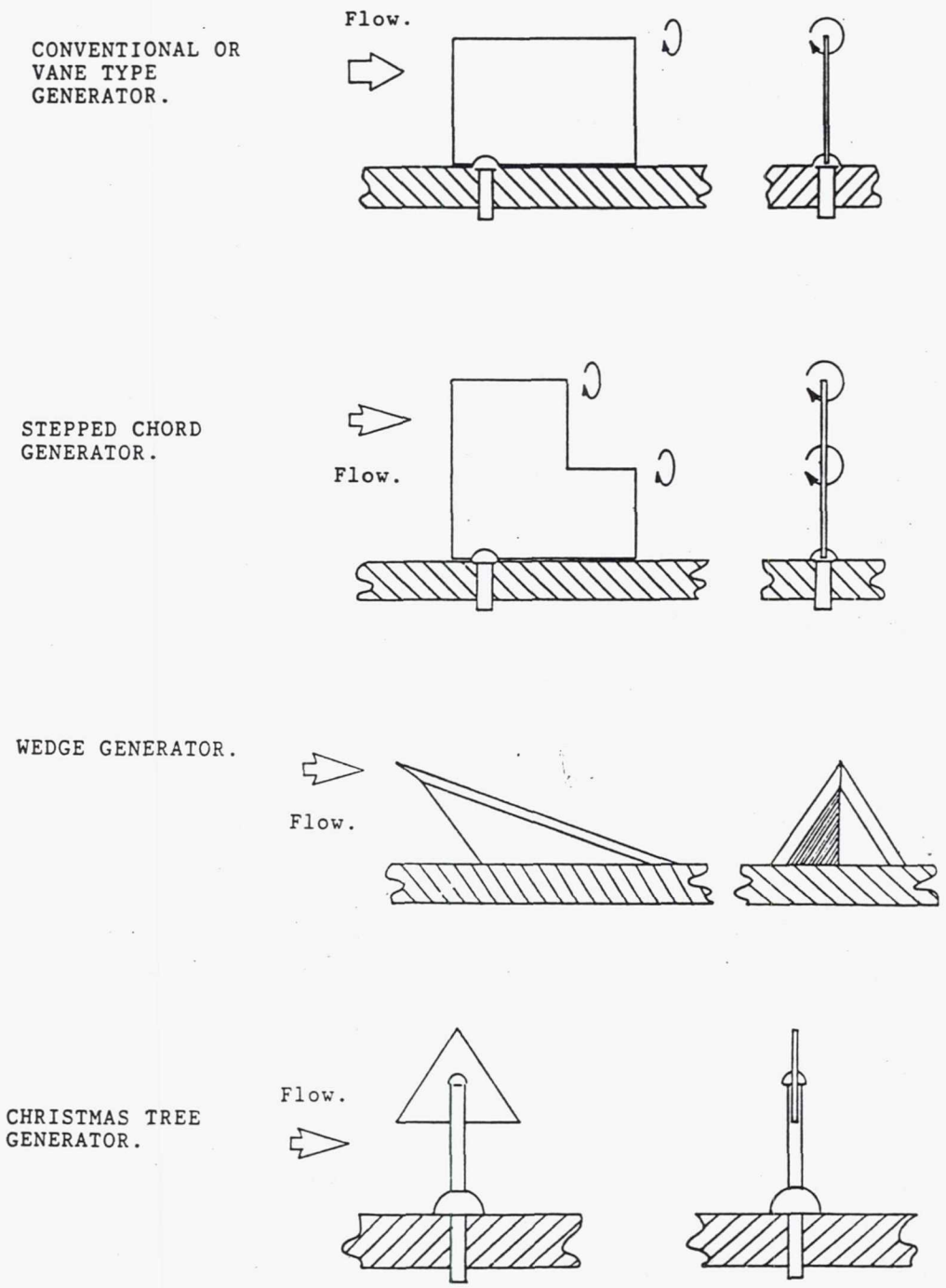

Figure 2.1 - Vortex generator devices used by Taylor and Grose (1954).

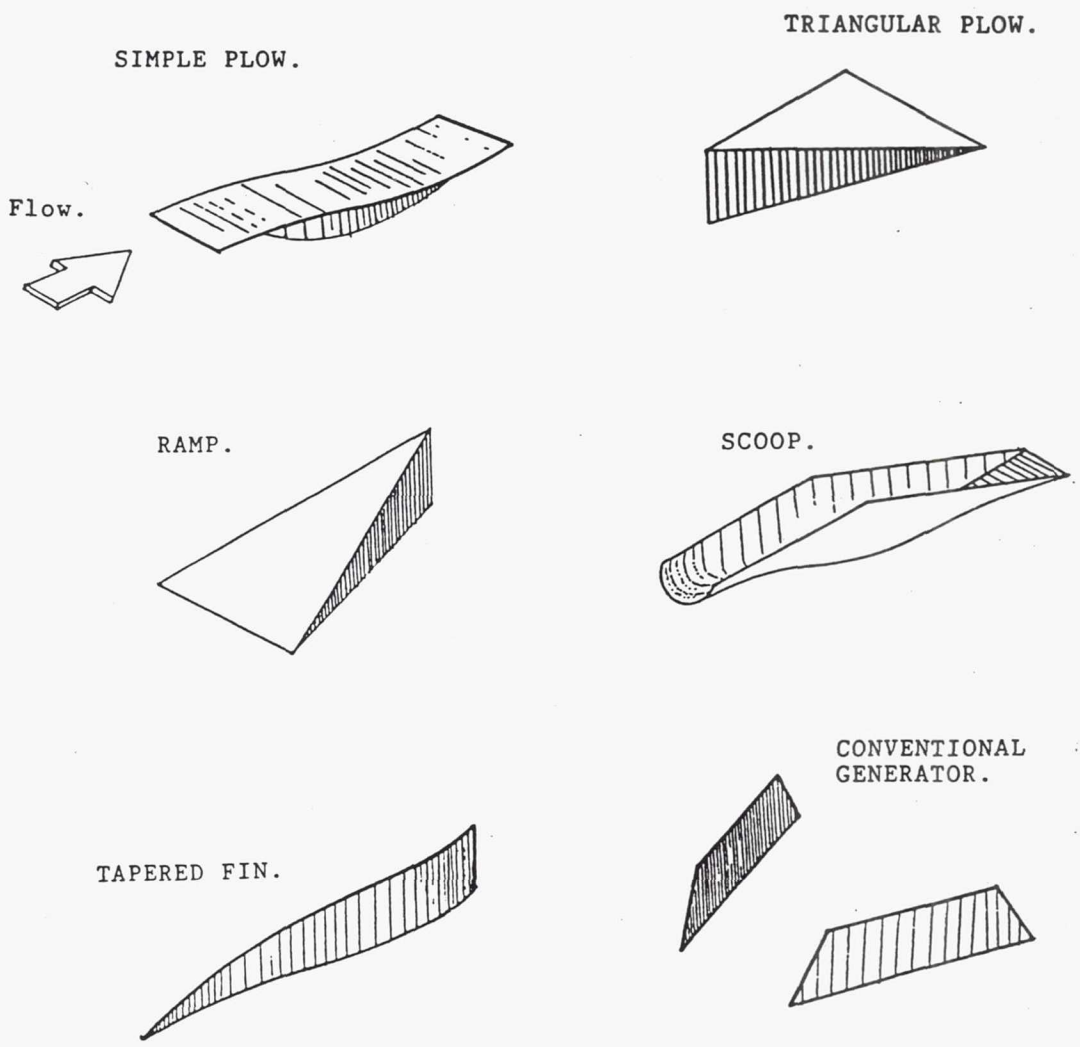

Figure 2.2 - The vortex generator devices of Schubauer and Spangenburg (1960).

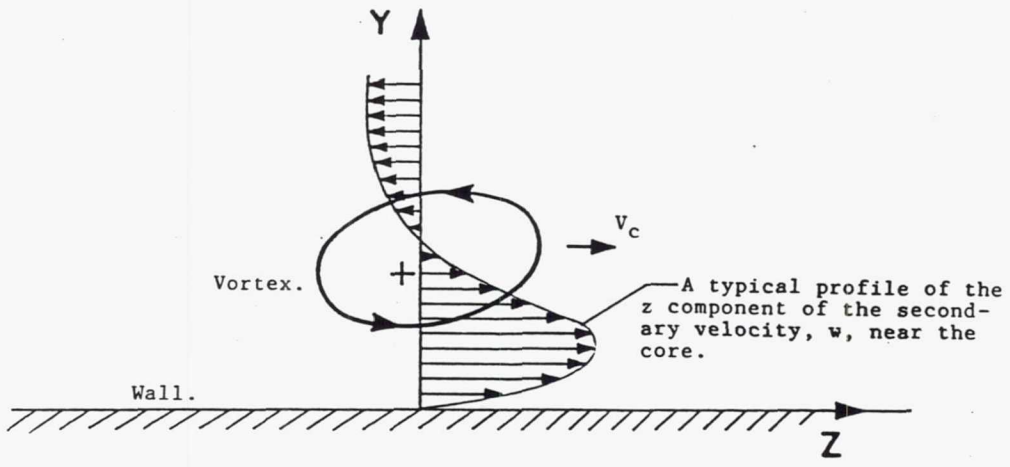

2.3a

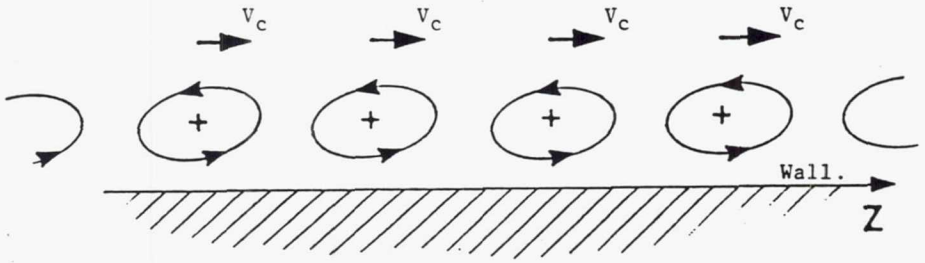

2.3b

Figure 2.3a (top) - A vortex in close proximity to the wall is convected along the wall by the strong secondary flows occurring near the wall and under the vortex. The core central location proceeds along the wall at velocity V_c.

Figure 2.3b (bottom) - An array of equal strength co-rotating vortices. The entire array moves to the right at velocity V_c.

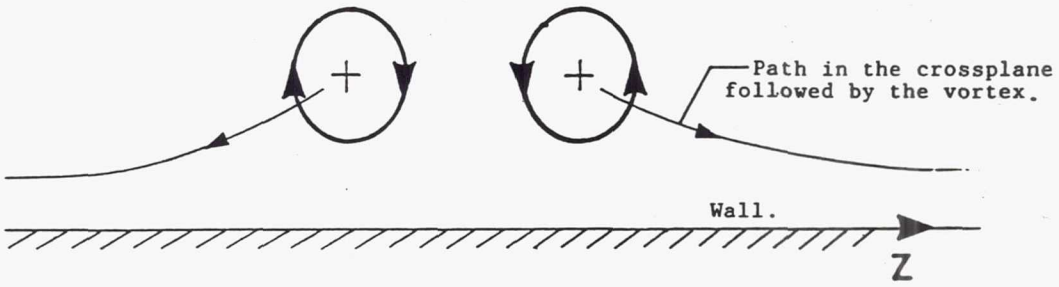

2.3c

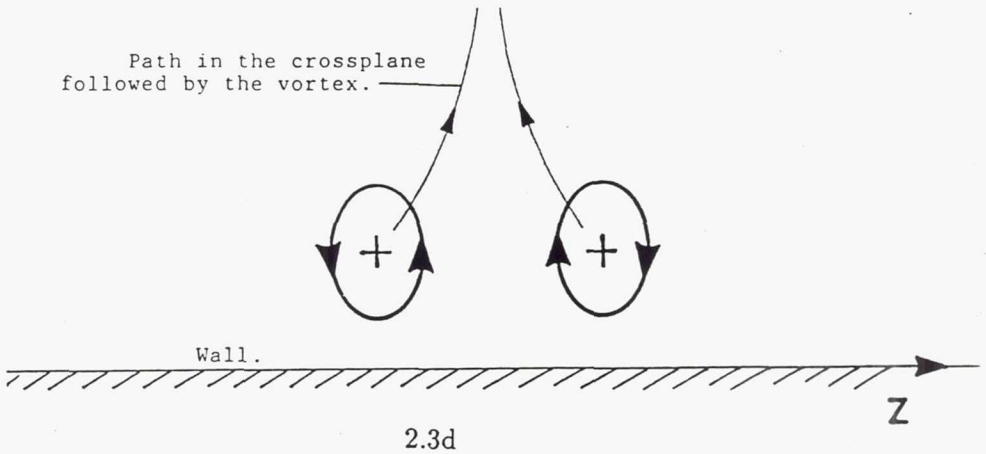

2.3d

Figure 2.3c (top) - Two counter-rotating vortices in close proximity to each other and the wall. The secondary flow between the vortices is directed towards the wall. As the flow proceeds downstream the vortices follow divergent paths in the crossplane but do not move out of the boundary layer region.

Figure 2.3d (bottom) - Two counter-rotating vortices in close proximity to each other and the wall. The secondary flow between the vortices is directed up away from the wall. As the flow proceeds downstream the vortices come together and lift away from the boundary layer region.

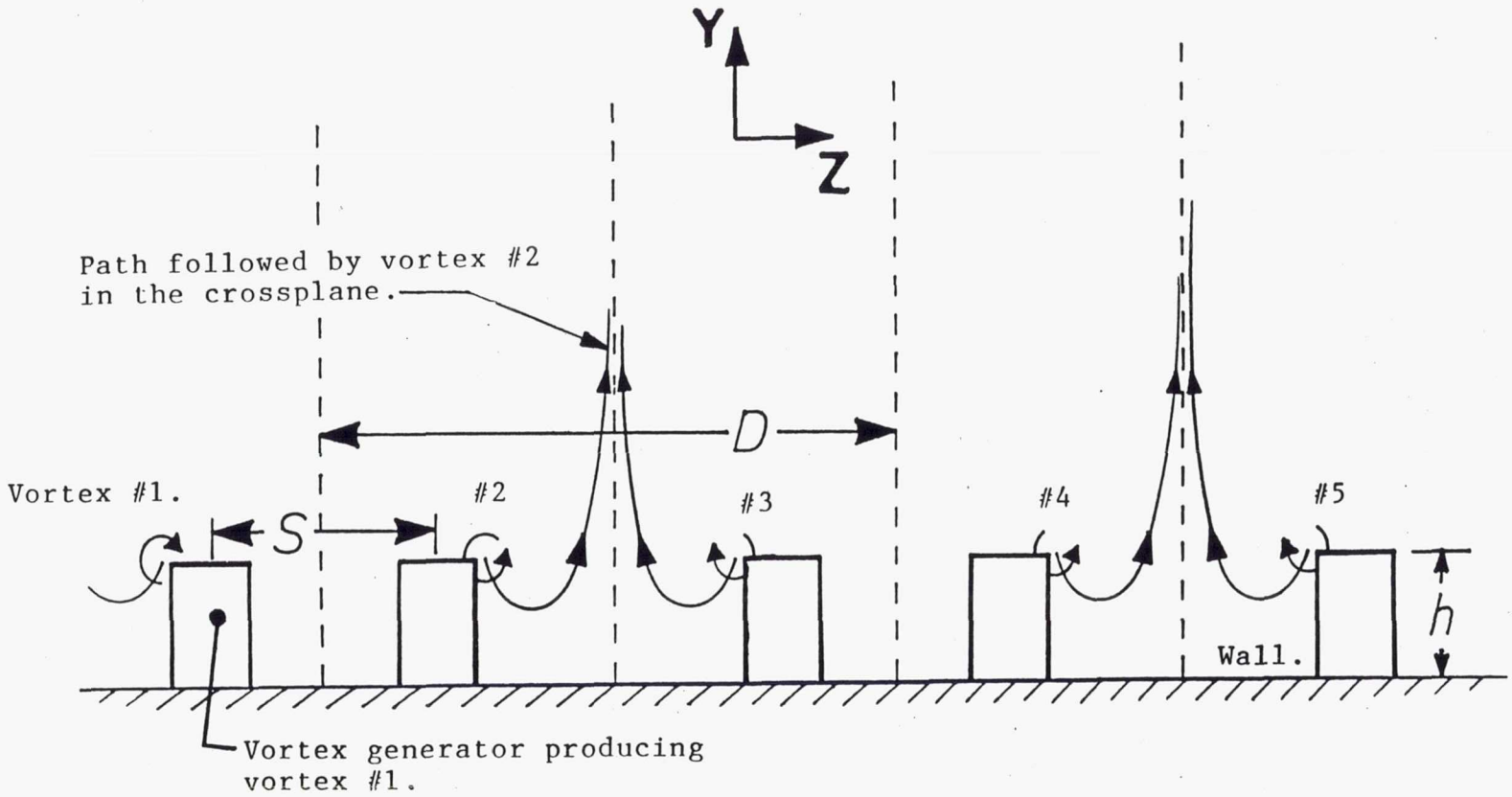

Figure 2.4 - Crossplane trajectories of counter-rotating vortices produced by an unequally spaced array of vortex generators.

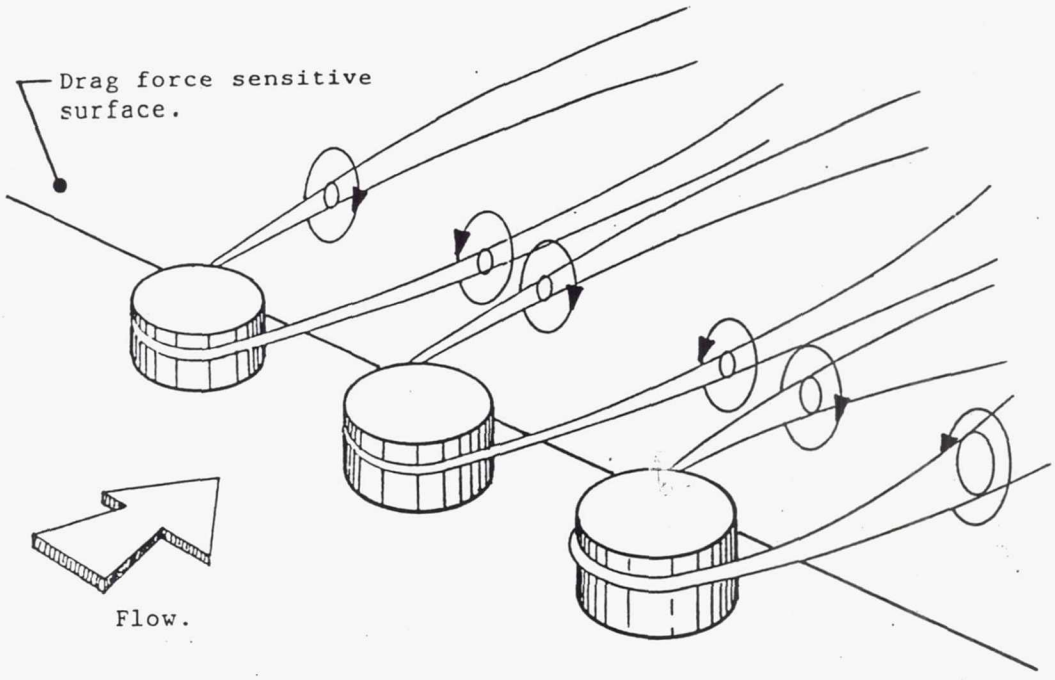

Figure 2.5 - The obstacle device of Rao and Mehtra (1983).

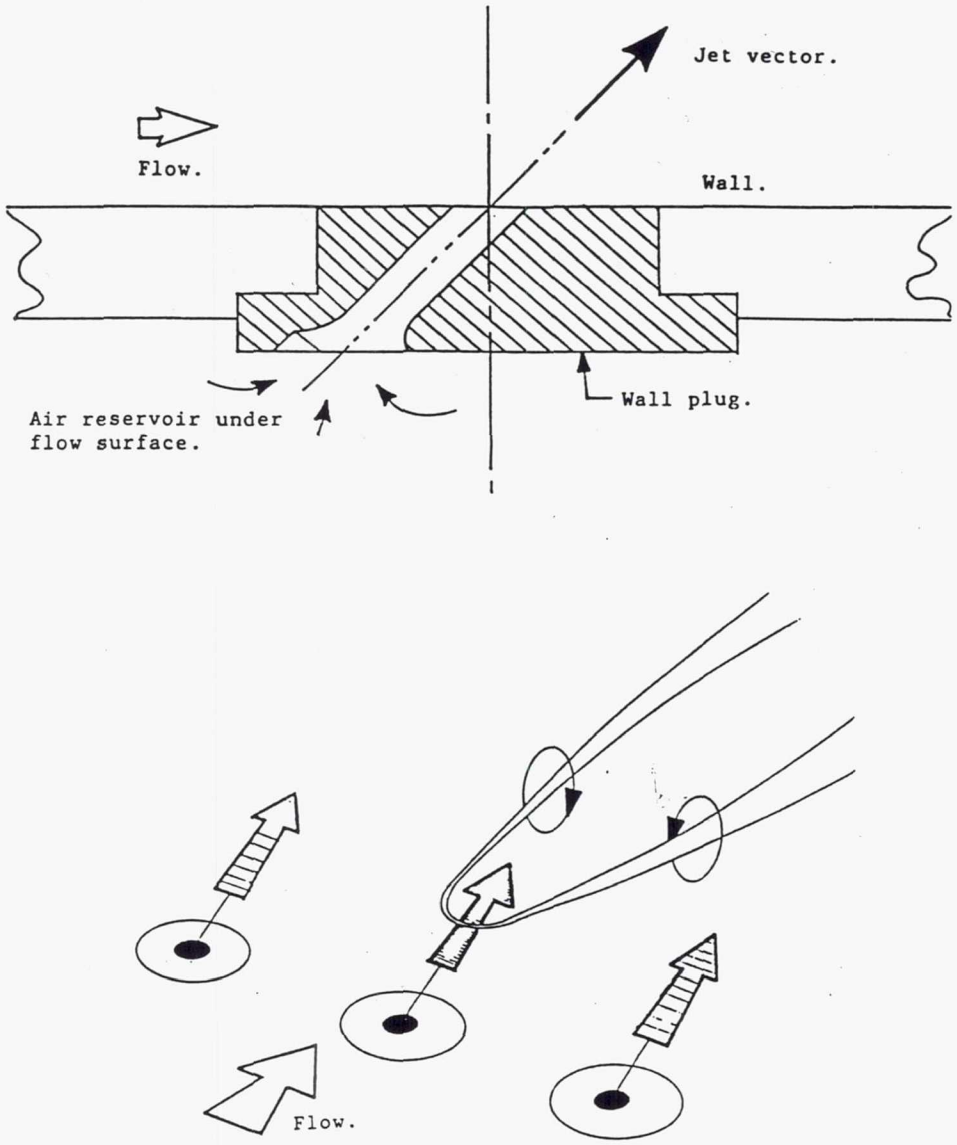

Figure 2.6 (top) - Geometry of the vortex generator jet (VGJ) of Johnston and Nishi (1990). The bottom diagram indicates how the streamwise vortices were generated from an array of VGJs.

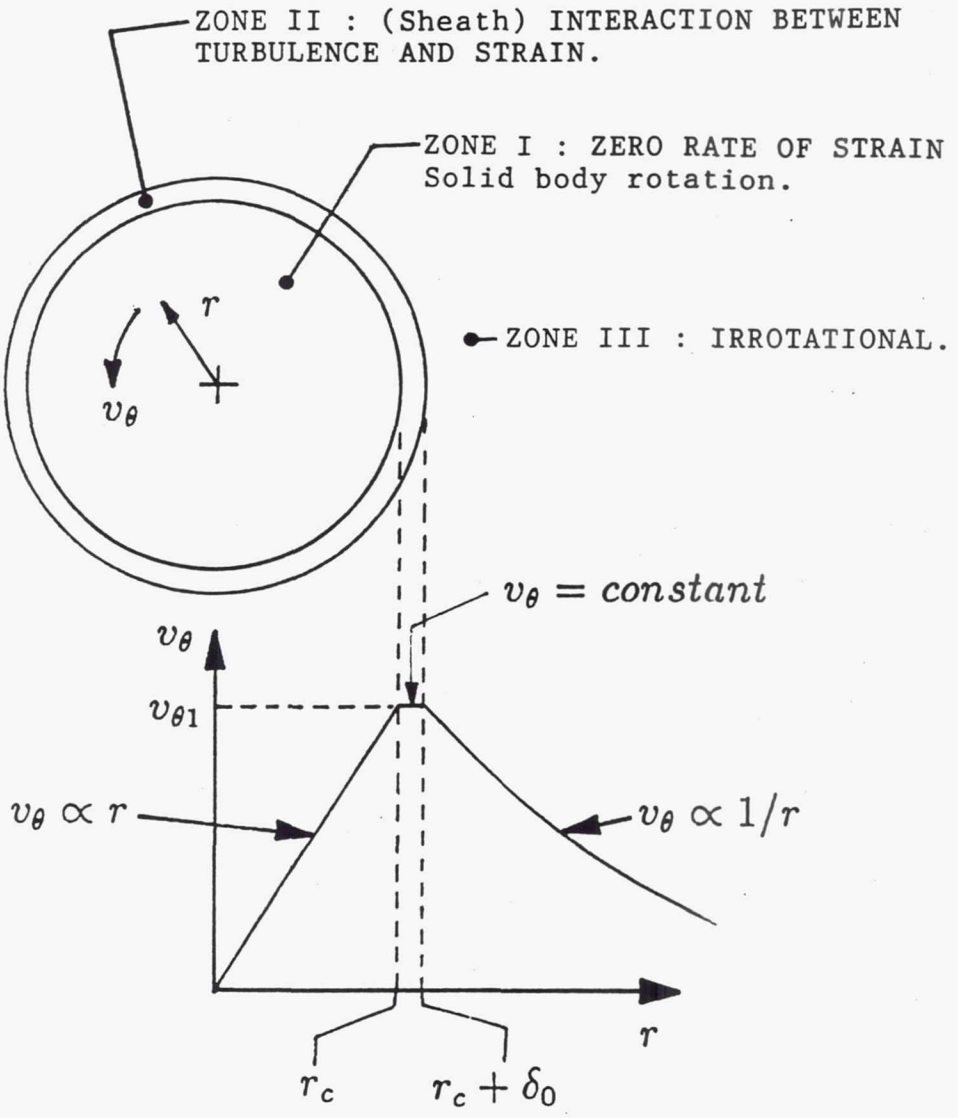

Figure 2.7 - The Owen model of an isolated turbulent vortex.

Chapter 3

Facilities and Procedures

3.1 The Test Facility

This investigation was conducted in the CW-22 test facility at the NASA Lewis Research Center. The test facility in CW-22 consists of a subsonic wind tunnel originally built to test design modifications proposed for the Altitude Wind Tunnel (AWT), an enormous facility also located at Lewis. The facility in CW-22 is a 1/10 scale model of the proposed high speed leg of the AWT. The test section and diffuser assemblies are currently in storage at Plumbrook Station. Figure 3.1 is a photograph of the CW-22 test facility. A schematic diagram of this test facility appears in Figure 3.2. Refer now to Figures 3.2 and 3.3 for the following discussion of the wind tunnel's design and operation.

The NASA Lewis air supply service provided dry air pressurized to 275.8 Kps (40 psig) at the upstream end of the facility. At the downstream end the airflow exited to a vacuum exhaust. The air entered the facility through a vertical inlet pipe located at the far upstream end of a large plenum tank. The air supply pipe entered the plenum tank through the top and extended down to the plenum tank floor. Inside the plenum tank the pipe contained

an interior grid of porous baffles attached at right angles to the pipe centerline and was perforated around its outer surface. These features aided in turning the airflow to the horizontal, and dispersing it evenly in the plenum tank. To reduce the large noise levels generated by the perforated pipe, the plenum tank was insulated all around with 15 cms of compressed Kevlar. The large tank aided in reducing the turbulence of the incoming airflow. To further this end, 4 screens of 34-mesh and 60 percent porosity were placed at the downstream exit of the plenum tank. These screens also aided in providing a uniform flow to the contraction sections that followed.

After exiting the screens the airstream entered a bellmouth contraction, where the flow area was reduced by about 60 percent. The flow then entered a constant area settling chamber and was forced through a 30 cm thick honeycomb flow straightening grid. Upon leaving the settling chamber the airstream underwent its final contraction to the test section. This contraction section had an inlet to exit area ratio of 6.5 and was designed to make the transition from a flow area of circular geometry present in the settling chamber to the octagonal flow area of the test section.

The test section consisted of 8 one inch thick aluminum plates (or "sidewalls") arranged to form a cross sectional flow area in the shape of an octagon[1]. The flow area at the entrance to the test section was equivalent to the area of a 61 cm diameter circle and increased linearly by one percent over the 168 cms of test section length. This was to account for the growth of boundary layers in the contraction section and on the test section sidewalls. Figures 3.4–3.7 diagram the relevant test section geometry. The sidewalls did not touch at the vertices of the octagon but formed open slots running parallel to the test section centerline. These slots could be filled, to some extent, by the addition of slot inserts. By changing the slot inserts the test section "porosity" was varied. The test section porosity is defined as the ratio of

[1]Hence the facility's alternate name "Mach 1 Octagonal Wind Tunnel".

circumference length of open space (resultant slot width × 8) to circumference length of closed space (sidewall width × 8). This definition is valid after the first 30 cms of test section length (due to a linearly varying sidewall width to this point). For this investigation the test section porosity was kept at 11 percent.

During normal operation a portion of the airstream flowing through the test section could exit through the open slots. At the downstream end of the test section flaps were located at the slot positions to reingest this air or some portion of it. Covering the contraction section, test section, and a portion of the diffuser, was a large diameter plenum shell. This feature allowed the operation of a "Plenum Evacuation System" or PES. This PES could bleed airflow from the test section through the slots. This combination of open slots, flaps, plenum shell, and PES exhaust allowed for a uniform Mach number distribution over the length of the test section for a wide variety of flow blockages (models) and flow conditions. The large plenum shell also allowed for a variety of instrumentation to be mounted around the test section.

Following the test section the airstream entered a transition duct (octagonal to circular) and then to a conical diffuser. After two 90 degree turns the airstream exited the facility through a valve to the altitude exhaust. The inlet for the PES pipeline was located near the flaps at the downstream end of the test section. The PES pipeline was then routed to the altitude exhaust and the PES flow was controlled by a separate valve connected to this exhaust.

3.1.1 Instrumentation Overview

After following a standard manual start-up routine the operation of the wind tunnel in CW-22 was fully automated. Each flow measuring device, whether operational or research, was assigned a specific channel and monitored by Lewis's ESCORT II operating system.

The voltage signals from thermocouples and several pressure transducers, as well as other instrumentation were digitized by a NEFF A/D multichannel digitizer. Most pressure measurements were made by an ESP (Electro Scanning Pressure) measurement subsystem. This system consisted of a number of modules, each containing 32 individual PSI piezo-electric transducers. The ESCORT system provided the conversions to engineering units for all of these signals. The ESCORT system consisted of a standard network of minicomputers on which a specifically tailored control program was run. The operational program on the ESCORT service provided a dual purpose. During the test run the program provided active control allowing the operator and researcher to monitor and change flow and test conditions. In post run data analysis the program used the recorded channel outputs to recreate the tunnel flow conditions (Mach number, total pressure, etc.) as well as the particular test conditions determined by all research instrumentation in use at the time. Using this data, the program could provide a hardcopy printout of tunnel flow and test conditions, or create a VAX data file. At any time during the test run a recording (data reading) of all channels could be manually implemented by the researcher or operator. In ESCORT terms this is known as a "contact closure". These contact closures could also be implemented automatically by supporting research instrumentation in the control room. The use of either approach to the data aquisition depended, in part, on the particular research instrumentation mounted inside the tunnel.

Uncertainties in the measured quantities are summarized in Table 3.1.

3.1.2 Operational Instrumentation

A standard ASME sharp edged orifice plate mounted in the inlet pipe far upstream of the test section monitored the tunnel mass flow rates. Another similar orifice plate mounted in the PES piping network monitored PES mass flow rates. The orifice plate pressures

were measured by individual transducers; orifice plate temperatures by copper-constantan thermocouples.

Settling chamber total temperature probes, contraction section total pressure probes, and test section sidewall static pressure taps aided in setting and controlling the test section flow conditions. The total temperature probes were mounted on 4 circumferentially distributed rakes in the settling chamber at an axial location of $x_{ts}/L_{ts} = -1.474$. Refer to Figures 3.3 and 3.8. The total pressure probes were mounted on 4 circumferentially distributed rakes axially located at the entrance to the contraction section, $x_{ts}/L_{ts} = -.851$. Refer to Figures 3.3 and 3.9. Static pressure instrumentation for the test section is diagrammed in Figure 3.10.

The tunnel mass flow rates could range between 21.0 and 66.5 kg/sec. This corresponded to test section Mach numbers of 0.2 and 0.9 respectively. PES mass flow rates ranged between 0.0 and 4.0 kg/sec.

For this investigation the tunnel total pressure was held roughly to atmospheric condition. The total temperature was approximately room temperature ($15°C, 59°F$). Except for a portion of the boundary layer qualification study, the test section Mach number was held to $M_{ts} = 0.2$. This corresponded to a free stream velocity of roughly 70 m/sec in the test section. PES flow was not needed to maintain uniform test section conditions at this low value of M_{ts}.

More information concerning the design and operation of the Mach 1 Octagonal Wind Tunnel may be found in the reports of D. Harrington, R. Burley, and R. Corban (1986); and R. Burley and D. Harrington (1987).

3.2 Research Instrumentation and Experimental Procedures

3.2.1 Overview of the Experimental Program

A large flat plate mounted vertically inside the test section equally divided the cross sectional flow area. It was on this vertical plate that a boundary layer developed and encountered the vortex generators. This experimental study took place in three parts :

1. A boundary layer qualification study done in the absence of vortex generators investigated the two dimensionality of the "base" flow and ensured the proper functioning of flow probes, traversing mechanisms, and other measurement systems.

2. A velocity flow field study to capture all three components of the velocity vectors produced by the embedded vortices. A five hole pressure probe was traversed in a regular grid running perpendicular to the streamwise coordinate at two axial locations on the vertical plate. The plate used for this study was instrumented with a static pressure tap grid.

3. A flow visualization and heat transfer study to capture contours of constant temperature on the surface of the plate underneath the vortices. This particular plate contained a constant heat flux surface heater on which a layer of liquid crystal was applied.

3.2.2 Splitter Plate and Vortex Generators

The bottom and top test section sidewalls ran parallel and equidistant over the total streamwise length of the test section and so provided convenient anchoring surfaces for the splitter plate. Figure 3.11 is a downstream view of the test section with the splitter plate

installed.

Both splitter plates were fabricated from 1.91 cm thick aluminum slabs and were machined to the dimensions illustrated in Figure 3.12. A parabolic profile was cut into the leading edge of each splitter plate and the surface of the plate facing sidewall no. 3 (refer to Figure 3.11) was polished smooth. The boundary layer of interest, with or without embedded vortices, was developed on this side of the splitter plate.

Figure 3.13 is a cutaway view of the test section with splitter plate mounted, showing the test section coordinate system in use. The vortex generators were mounted at a single streamwise location, $x = 64.0$ cms. 41 equispaced vortex generator mounting holes symmetrically placed about the splitter plate centerline ran parallel to the spanwise (z) coordinate. These mounting holes were spaced 1 cm apart. The mounting holes were filled with flush fitting pins in the absence of vortex generators.

The vortex generators were rectangular blade-like fins fabricated from a single piece of stainless steel stock. Two different sizes were used. The vortex generator top profile was similar to that of a symmetric airfoil. Figure 3.14 is a drawing indicating the dimensions of the vortex generators and mounting hole pins.

3.2.3 Velocity Field Study

The static pressure tap grid built into the splitter plate used in the velocity field study is diagrammed in Figure 3.15. The tap holes were 0.051 cm in diameter at the plate flow surface. Shallow channels machined into the back of the plate provided the routing for the tap tubing. After the tubing was installed these channels were filled with Devcon epoxy and sanded smooth. The static pressure tap grid was designed to serve two purposes :

1. Record the spanwise surface static pressure variation induced by the embedded vortices. To serve this end there were 5 spanwise rows of taps at 5 different streamwise

locations on the plate as diagrammed in Figure 3.15. The tap holes were spaced closer together near the vortex generator mounting station in the expectation of a narrower vortex structure there.

2. Record the streamwise gradient of surface static pressure. The gradients were expected to be slight along the streamwise coordinate. To capture these gradients three streamwise rows of taps were included into the grid design diagrammed in Figure 3.15.

Probe Traversing Mechanism

The velocity probes used in this study were positioned by a two axis traversing mechanism. The probes were traversed in spanwise-normal ($z - y$) grids to capture the crossflow structure of the embedded vortices. In addition, the probe could be rotated about its stem axis. Figure 3.16 is a diagram of the traversing mechanism installed above sidewall no. 3 in the test section.

Probe motion along the y-axis was implemented by a stepping motor and a lead screw. Probe rotation was implemented by another stepping motor and gears. These component parts were contained within an actuator device (BBR) manufactured by L.C. Smith Co.

The limit switches for the y motion were set to provide a 17.8 cm traverse. The stepping motor and lead screw combination could provide an increment of y motion as small as 0.018 cm. A 10 turn potentiometer recorded the probe y position. As was typical of any research quantity of interest, the y position of the probe was assigned an ESCORT channel and was available to the researcher on a display in the control room. A calibration procedure determined that positional accuracy along the y-axis of motion was $\pm$ 0.006 cm.

The limit switches for the probe angular motion were set to provide 180 degrees of rotation. The smallest increment of angular motion provided by the stepping motor was 0.20 degrees. A 10 turn potentiometer tracked the probe angular position. A separate

calibration procedure determined that the probe angular displacement was certain to within $\pm 0.15°$.

The y traversing upper platform of the BBR actuator was fitted with a solid brass airfoil strut. This strut provided the probe stem with additional stiffness. The strut had a symmetric cross section through which a 0.64 cm diameter hole was bored over the 30 cm length of the strut. The probe stem was fitted into this bore when mounted in the actuator. The probe could be rotated inside the strut (the strut itself did not rotate), but no y motion of the probe relative to the strut was possible. Thus the distance from the probe tip to the freestream end of the airfoil strut remained constant at 10.5 cms. This distance was sufficient to prevent the wake of the strut from interfering with either the boundary layer structures near the splitter plate surface, or the probe tip itself.

To provide motion along the spanwise component of the traverse, the BBR actuator was attached to a Thomson platform mounted above sidewall no. 3. The platform consisted of ball bushings on a cylindrical stainless steel track and was powered by a Dayton linear actuator. The z position of the probe was recorded by a potentiometer mounted to the linear actuator. Positional accuracy was determined to be ± 0.012 cm.

Figure 3.17 is a diagram of sidewall no. 3 showing the streamwise locations where the z traversing slots were cut. The three upstream slots were cut into a small aluminum plate which fit into a corresponding window at this location. The span of the z traverse was limited by the requirement that slots not breach or weaken the sidewall. To prevent a significant structural weakening of the sidewall it was determined that a minimum of 1.5 cms of stock on either side of the traversing slots (or windows) was necessary. Limit switches kept the z actuator within the slot dimensions indicated on Figure 3.17. A covering which moved with the z traverse of the probe and strut sealed the slot during experimental operations. When another streamwise location was desired, the apparatus in Figure 3.16 was disassembled and

moved. Recalibration of the actuators was performed before resuming research.

Boundary Layer Pitot Probe

A pitot probe was constructed by the instrumentation shop at NASA-Lewis. It was specifically designed to resolve the profile of the thin boundary layer occurring in this study. Figure 3.18 is a drawing of the pitot probe. The probe tip was constructed out of 0.05 cm OD stainless steel tubing. This probe was mounted inside the traversing mechanism and used in conjunction with a "touch control" circuit. This circuit allowed the probe to locate the plate surface by gently making contact with it at the end of its y traverse. Use of the touch control circuit permitted accurate location of the probe tip (with respect to the flow surface) under operating conditions where the possibility of deflections was present.

Five Hole Probe

A five hole pressure probe was used to measure the three components of the mean velocity field vector. The probe tip is diagrammed in Figure 3.19. The probe was constructed of 5 silver brazed stainless steel tubes, each one being 0.05 cm OD. The tip diameter of the probe was 0.152 cms.

The calibration of the five hole probe followed a procedure outlined by Pauley and Eaton (1988). A detailed description of this procedure is given in the Appendix. In short, since the measured maximum flow angles fell into the range of ± 20 degrees, the pitch correlation was independant of the yaw angle. Likewise, the yaw correlation was independant of the pitch angle. This behavior was verified during the calibration procedure where it was possible to simultaneously pitch and yaw the probe. The independant calibrations of the pitch and yaw behavior were carried out in the open jet facility (CE-12) at NASA-Lewis.

For each streamwise location where crossflow data was collected, a location above the

splitter plate centerline (z=0.00 cm, y=10.00 cms) was chosen as the location of the reference flow angle measurement. The reference pitch and yaw angle were measured at this location in the absence of vortex generators. All flow angles recorded in subsequent data collection at this particular streamwise survey station were measured with respect to these reference angles. In practice it was possible to yaw the probe to obtain a reference yaw angle of 0.0 degrees. The probe then remained "frozen" in this angular position in subsequent use. It was not possible to pitch the probe with the mechanism used in this study.

Probe pressures for both the five hole probe and the boundary layer probe were monitored by the ESP $\pm 34.5 \mathrm{KN/m^2}$ transducers. These transducers had an accuracy of $\pm 0.015 \mathrm{KN/m^2}$. At each $(z-y)$ crossplane grid point the five probe pressures were recorded along with the tunnel total pressure and local wall static pressure. The probe calibration equations were subsequently used in the conversion to velocities.

Wall proximity effects on the five hole probe were small enough to be neglected in this study. The five hole probe was sensitive to large mean velocity gradients, however, and a correction scheme was necessary. This scheme is outlined in the Appendix.

Supporting Control Room Equipment

The L.C. Smith BBR actuator was traversed automatically through a L.C. Smith actuator controller receiving commands from a control program running on a Fluke instrument controller. The z traverse was accomplished manually from the control room. The operator referred to a LED readout of the z actuator position on either the ESCORT display or a Fluke digital multimeter while handling the motion switch for the z actuator. In the few cases where the yaw position of the probe was adjusted, it was done manually through the L.C. Smith controller by referring to an LED display on another Fluke digital multimeter.

Procedural Notes on Data Aquisition

Before starting an experimental run, and after a run was finished,the ESCORT barometer was verified by comparison to the lab barometer reading.

Two contact closures were taken at set points during the tunnel start-up procedure. Three others were taken as part of the shut-down procedure. These data readings were used to verify that all instrument channels were working properly.

Five hole probe angular position was held constant during the run. To verify this, reference readings in the free stream were taken before and after the probe was traversed over the crossplane grid. Data aquisition consisted of automated contact closures at every grid point. All channels were recorded. Data aquisition was interrupted periodically by the need to recalibrate the ESP transducers. This was done automatically by a program running on a Leading Edge minicomputer.

About 600 grid points per run were covered. In the cases where the whole grid could not be covered in one run, a portion of the grid was redone on the following run. The grid data which was "overlapped" could then be compared for repeatibility. In all such cases the corresponding data agreed to within 5 percent. This was due, in part, to the high degree to which tunnel flow conditions could be established and controlled.

3.2.4 Heat Transfer Visualization

By using a layer of heat activated liquid crystal, lines of constant temperature could be recorded on the heated splitter plate surface downstream of the vortex generators. Surface heat transfer behavior produced by any given configuration of vortex generators was deduced from a series of surface temperature contours, recorded by camera, and made possible by varying the power supplied to the heated plate.

The Heated Plate

The heated splitter plate is diagrammed in Figure 3.20. In the middle of the plate, symmetrically positioned with respect to the plate centerline, was a rectangular pit. This pit was machined to a depth of 1.14 cms below the flow surface. A piece of NC Proofboard was machined to fit inside this pit, where it was epoxied in place. Figure 3.21 is a diagram of this inlay. NC Proofboard is a hard, porous material with heat insulating properties. The two horizontal slots machined into the inlay at the top and bottom held the inlay copper bus bars needed to carry the large currents to the heating element. A shallow recessed area between the inlay copper bus bars held the heating element and liquid crystal laminate. The heating element was a piece of Inconel foil 0.0025 cm thick. The NC Proofboard surface was hardened with a coat of epoxy and sanded smooth before the heating element was attached with a layer of double tape. Figure 3.22 is a diagram of the heater composite. The inlay bus bars were plated with a layer of nickel. The Inconel foil was then tack welded to the surface of both bus bars after they were epoxied in place. The Inconel foil received a coating of flat black paint. The final coating was the liquid crystal itself. The heater composite, when finished, was flush with the splitter plate flow surface.

The inlay bus bars were attached to another pair of copper bus bars. Shallow channels machined into the back side of the splitter plate held these bus bars in place. Refer to Figure 3.23a. Outside of the test section the bus bars were connected by heavy cable to a 300 amp DC power supply. The electrical circuit consisting of heating element, bus bars, cables, and power supply is diagrammed in Figure 3.23b. Over 98 percent of the resistance in this circuit was due to the heating element. The circuit provided equal paths of resistance between the inlay bus bars. The resistance of the heating element was measured at 0.0391 ± 0.0002 ohms. The uniformity in foil thickness and the relative insensitivity of foil resistance to temperature gradients allowed for the generation of a uniform surface heat

flux. The magnitude of the surface heat flux could be varied through the power supply by a manual potentiometer dial in the control room. The current in the circuit, the voltage drop across the heating element, and the power dissipated in the heating element were available on the ESCORT display in the control room. A typical current required during operation at Mach 0.2 was about 100 amperes. This occurred with a voltage drop of about 4 or 5 volts over the heating element. The power generated at the surface was constant over the surface and was typically equal to about 5000 watts/m^2.

The temperature activated liquid crystal used in this study is a type known as "cholesteric" and is described in detail by S.A. Hippensteele, L.M. Russel, and F.S. Stepka, (1981). The liquid crystal turned a bright yellow at a temperature of $42.8 \pm 0.2°C$. This was determined by a calibration procedure using an Omega type E thin foil thermocouple mounted on the trailing edge surface of the heating element. The thermocouple response was used to activate an ESCORT safety circuit which cut power to the plate if the surface temperature exceeded $75°C$. The mounted thermocouple also made it possible to check the color-temperature response of the surface at any time during the test.

Under steady flow conditions the heat generated in the resistive element was transferred to the immediate surroundings as follows :

- Convected to airstream ($U_e = 70\, m/sec$) : $\approx$ 97%.
- Radiated to airstream and tunnel walls : $\approx$ 2.5%.
- Conducted through Proofboard inlay : $\approx$ 0.5%.

Supporting Hardware Elements

Figure 3.24 diagrams all the remaining hardware elements used in this phase of the study. Color slides of the surface isotherm patterns were taken by an Olympus 35 mm camera

mounted above sidewall no. 3. The camera pointed down through a plexiglas window. This window replaced the aluminum plate with traversing slots from the velocity field study. The strobe light used for this camera was mounted above another plexiglas window in the angled sidewall no. 2. The strobe was positioned here to prevent the reflected glare from interfering with the exposures. A color video camera was mounted alongside the still camera over sidewall no. 3. The video camera provided backup pictures in the event the still camera malfunctioned during the test. Two fluorescent lights mounted in the bleed slots provided the necessary illumination for the video camera. The radiative spectrum of the fluorescent lighting includes ultraviolet frequencies which tend to degrade the liquid crystal. To prevent this, the fluorescent tubes were fitted with plexiglas shields which absorbed nearly 100 percent of the harmful radiation.

Procedural Notes on Data Aquisition

Once the set points for test section flow conditions were achieved by the tunnel operator, the researcher sent power to the plate heating element. The power was increased until the calibrated yellow band reached the leading edge of the heating element (laminate). The position of the yellow band could be followed by referring to a video monitor in the control room. Power input to the heating element was greatest when the yellow band reached the laminate leading edge. The current required for this condition was noted and the power was decreased in fairly large intervals until the yellow band disappeared completely from the surface. The current at this minimum power condition was also noted and the approximate current range covered from maximum to minimum power was divided by the number of remaining exposures. At the minimum power setting an exposure was taken and a manual contact closure recorded data on all ESCORT channels. The power was increased by the appropriate increment and the procedure repeated. A settling time of roughly 3 minutes

was needed between pictures. After this time interval no unsteady effects in the isotherm pattern could be detected. This was verified through a calibration procedure in which time intervals of up to 25 minutes were examined.

INSTRUMENT	MEASURAND	TYPICAL VALUE	UNCERTAINTY δ	%
ESP Pressure Transducer	P_s, P_t, Probe Pressures.	96500 Pa	±150	<1%
Boundary Layer Probe	u	40-70 m/sec	±0.5	1%
Five Hole Probe	u	40-70 m/sec	±0.5	1%
	v,w	0-15 m/sec	±0.3	2%
Actuator Position	x	1.50 m	±0.001	<1%
	y	0-2 cms	±0.006	<1%
	z	0-6 cms	±0.012	<1%
Liquid Crystal Band	T_{wx}	316 K	±0.2	<1%
Thermocouple (Type E)	T_{wx}	320 K	±1.0	<1%
Heater	q_w	5000 W/m^2	±100	2%

TABLE 3.1 - Measurement uncertainties.

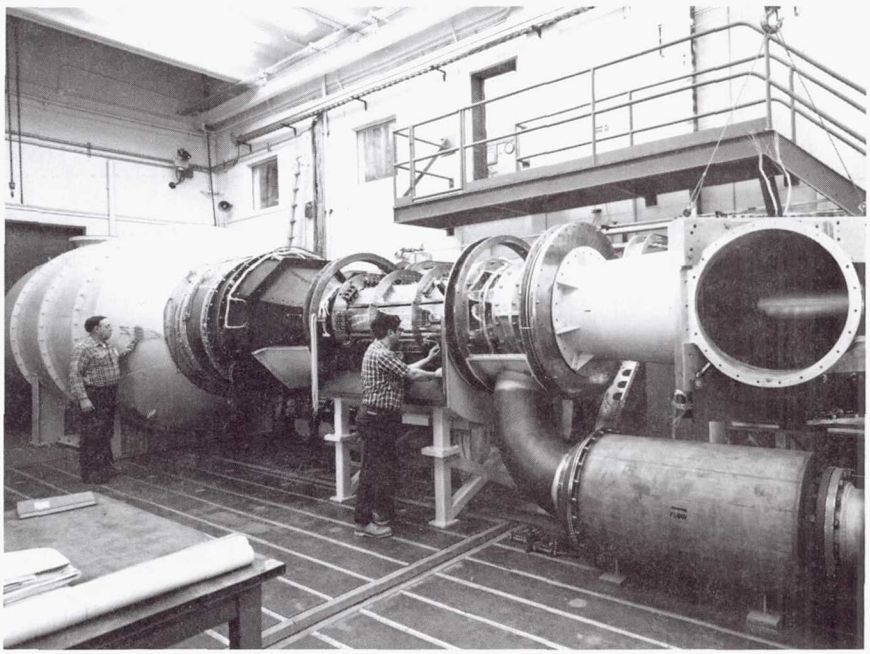

Figure 3.1– The test facility in CW-22.

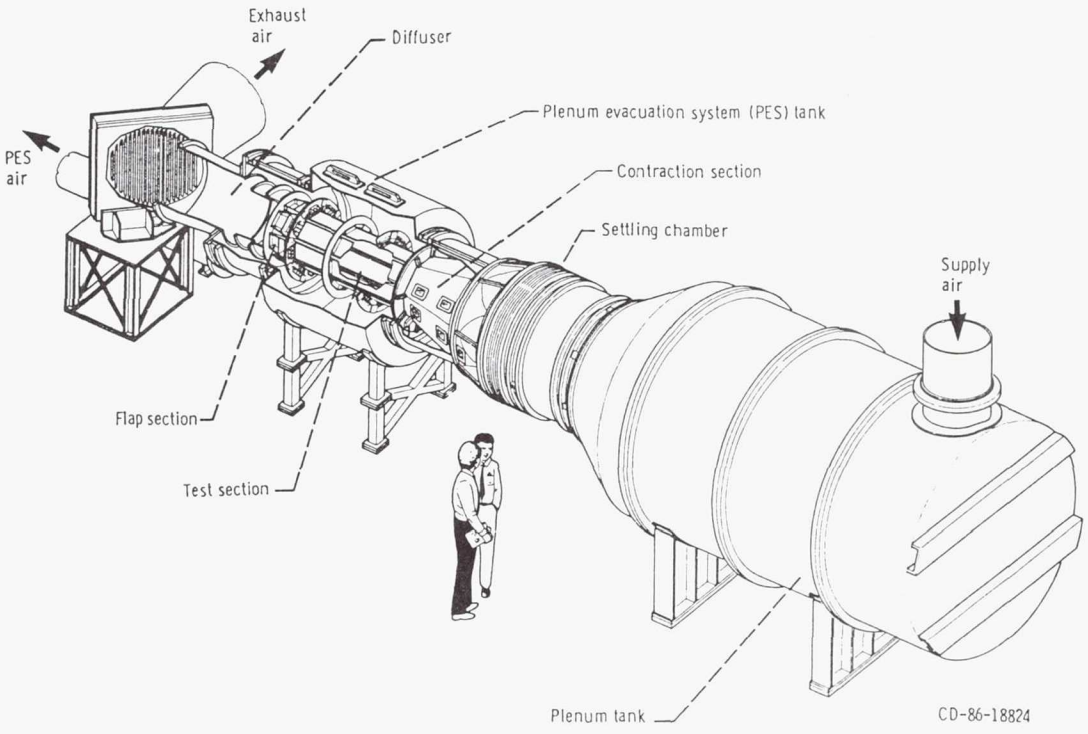

Figure 3.2– Schematic diagram of the test facility as seen from the opposite side.

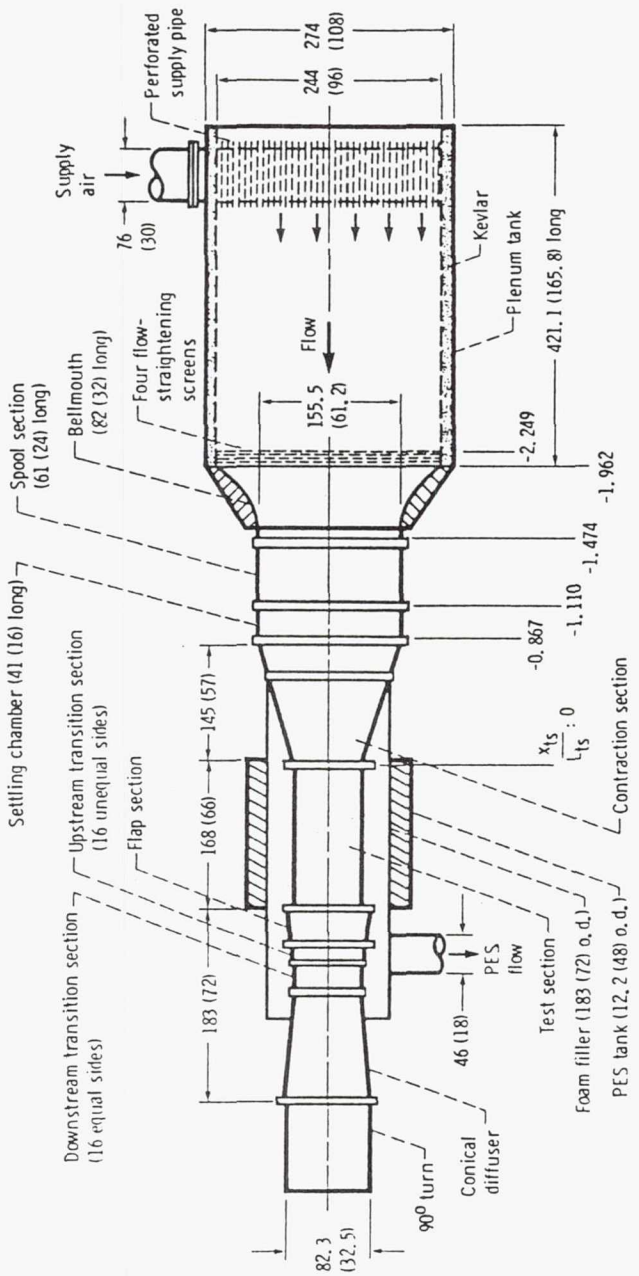

Figure 3.3- Geometric details of the test facility. All dimensions are in centimeters (inches).

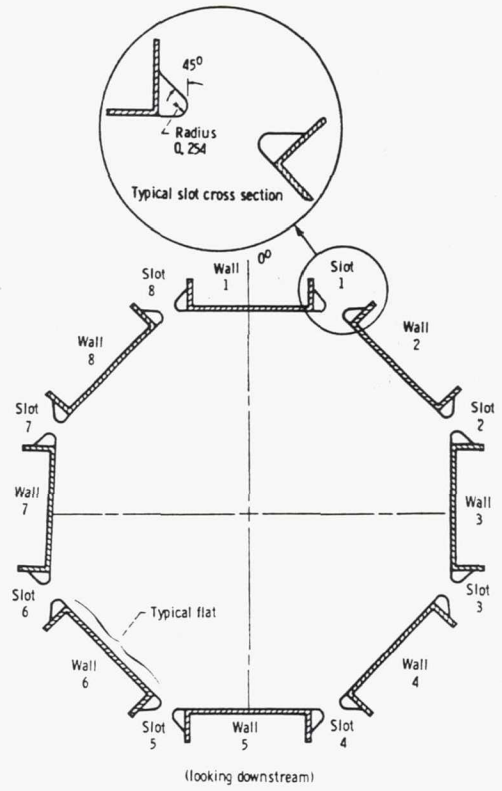

Figure 3.4– Typical cross section of the slotted, octagonal test section. All dimensions are in centimeters.

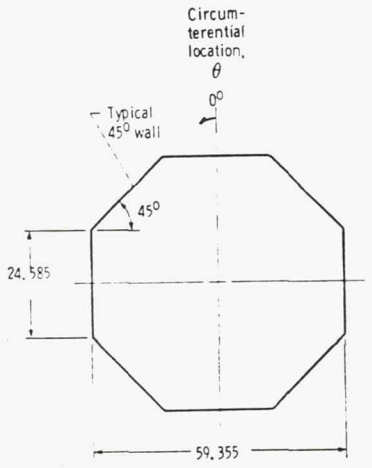

Figure 3.5– Cross section of the entrance to the test section ($X_{ts}/L_{ts} = 0$). Dimensions are in centimeters.

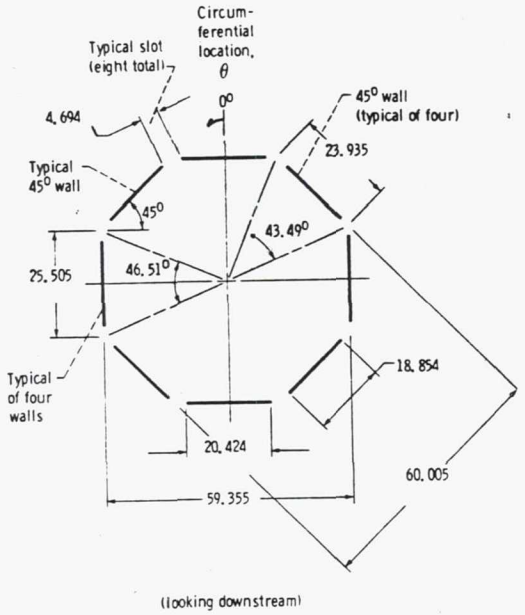

Figure 3.6– Cross section of the test section exit ($X_{ts}/L_{ts} = 1.0$). Dimensions are in centimeters.

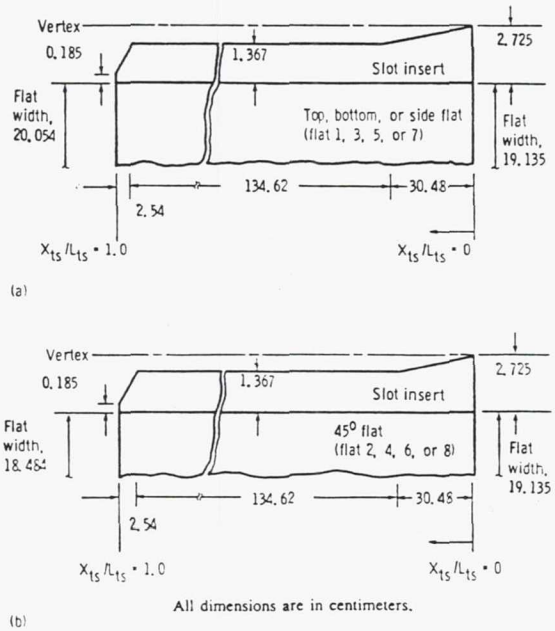

a) Top, bottom, left, or right sidewall.

b) 45° (angled) sidewall.

Figure 3.7– Geometric details of the test section sidewalls. Each sidewall consists of a flat and two slot inserts.

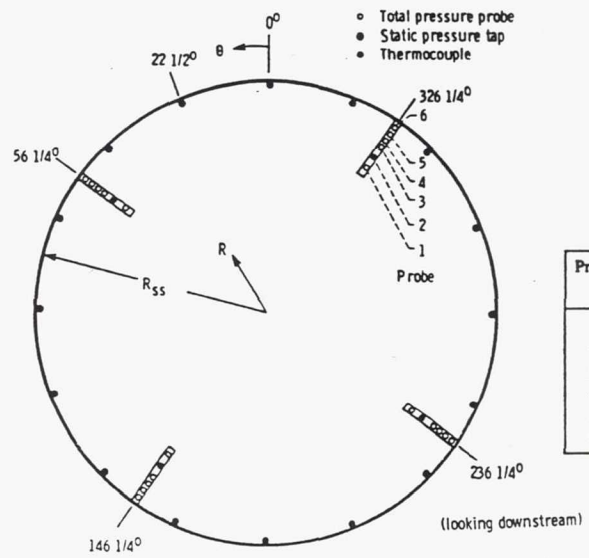

Probe	Radial location R/R_{ss}
1	0.877
2	.910
3	.935
4	.951
5	.967
6	.984

Figure 3.8– Pressure and temperature instrumentation at the entrance to the settling chamber ($X_{ts}/L_{ts} = -1.474$).

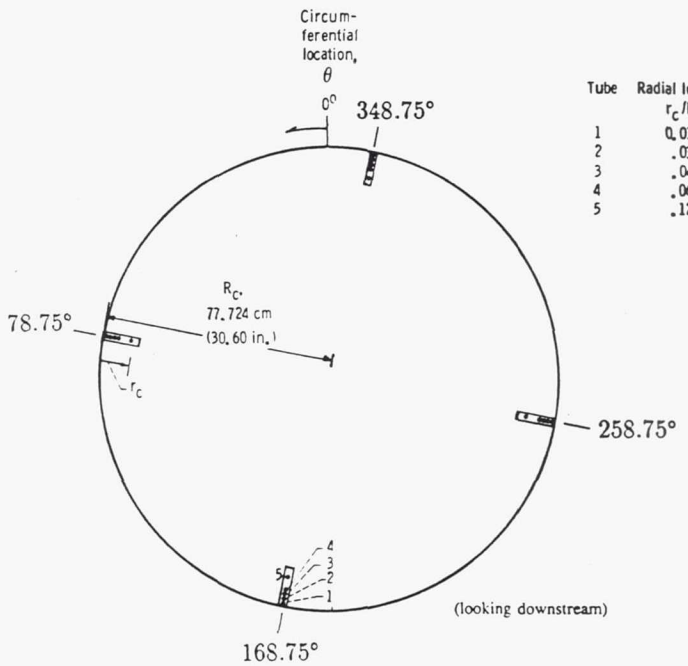

Tube	Radial location, r_c/R_c
1	0.016
2	.033
3	.049
4	.065
5	.123

Figure 3.9– Total pressure instrumentation at the nominal entrance to the contraction section ($X_{ts}/L_{ts} = -0.851$).

Static-pressure tap number	Test-section static-pressure axial location, X_{ts}/L_{ts}	Static-pressure tap number	Test-section static-pressure axial location, X_{ts}/L_{ts}	Static-pressure tap number	Test-section static-pressure axial location, X_{ts}/L_{ts}
1	0.008	10	0.348	19	0.689
2	.045	11	.386	20	.727
3	.083	12	.424	21	.765
4	.121	13	.462	22	.803
5	.159	14	.500	23	.841
6	.197	15	.538	24	.879
7	.235	16	.576	25	.917
8	.273	17	.614	26	.955
9	.311	18	.652	27	.992

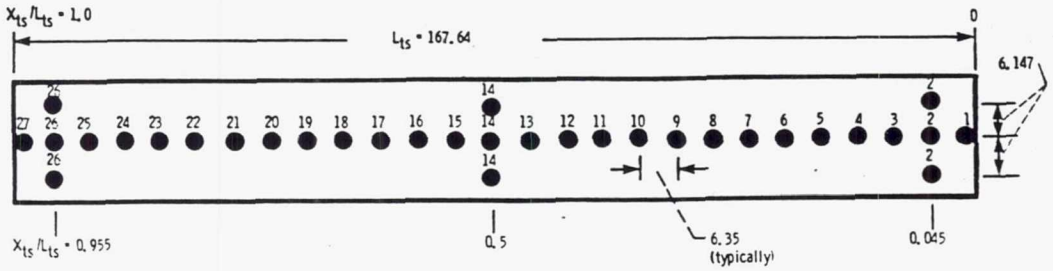

Flat 1 instrumentation (typical of all eight flats).

Figure 3.10– Test section static pressure instrumentation. All dimensions are in centimeters.

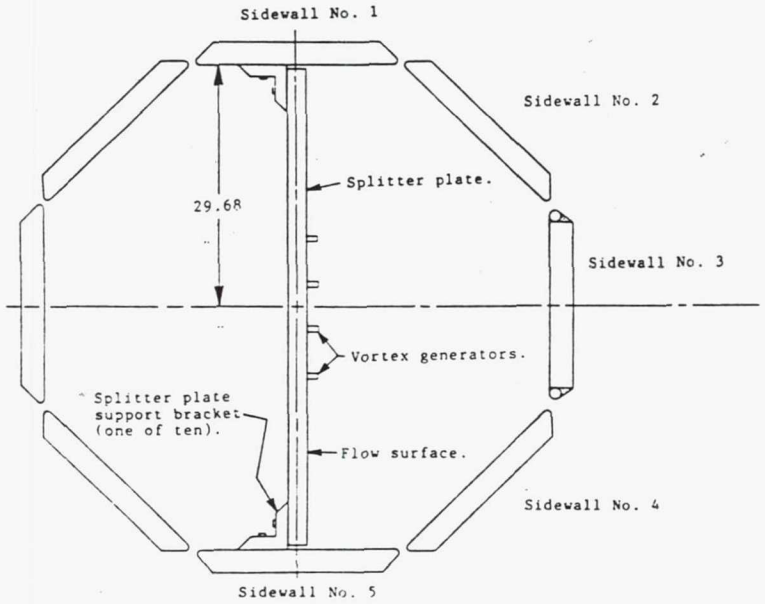

Figure 3.11 - The octagonal test section with splitter plate installed, looking downstream. Dimensions are in centimeters.

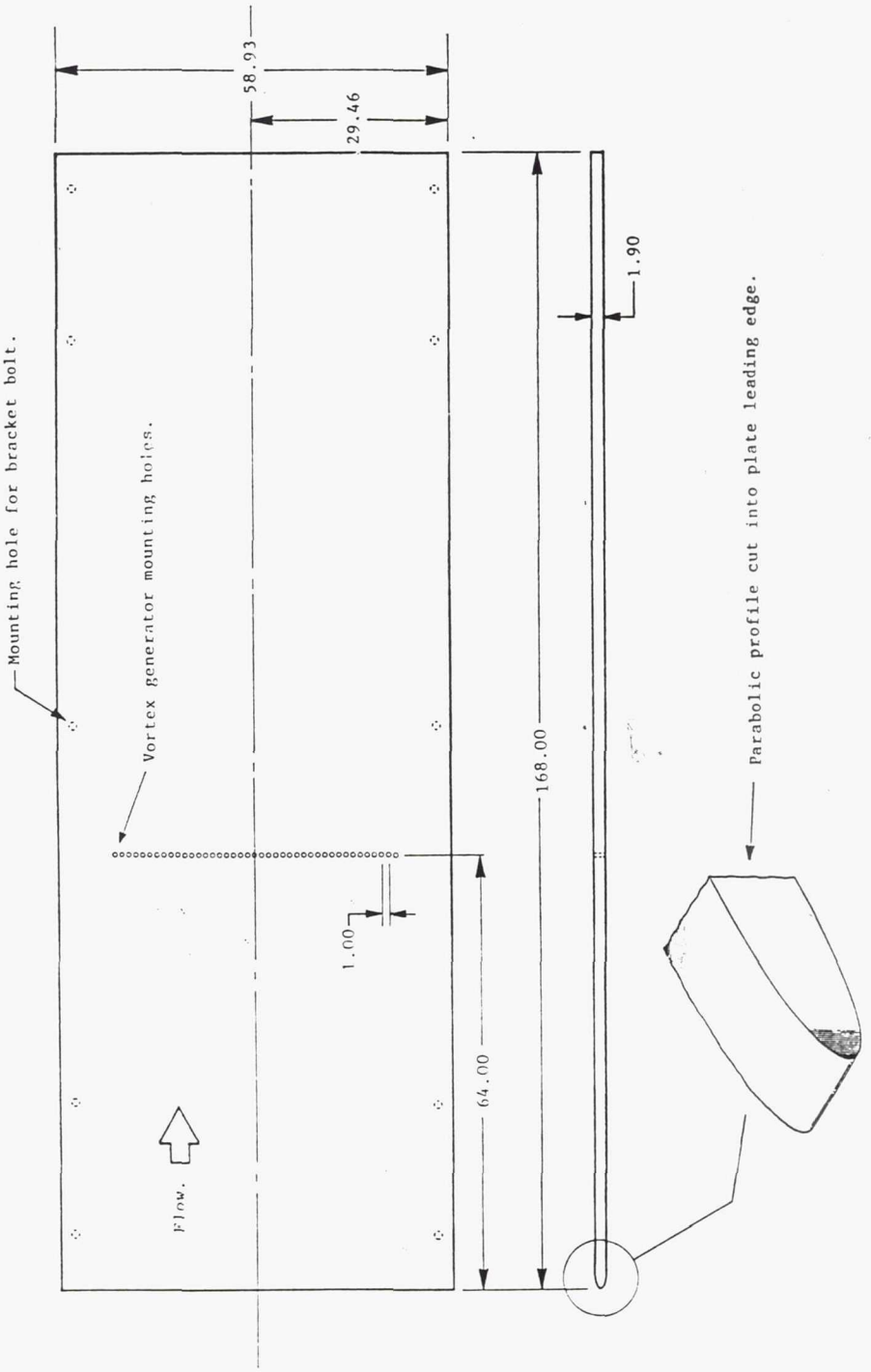

Figure 3.12 - Overall geometry of the aluminum splitter plates. The top view is looking down on the flow surface. Dimensions are in centimeters.

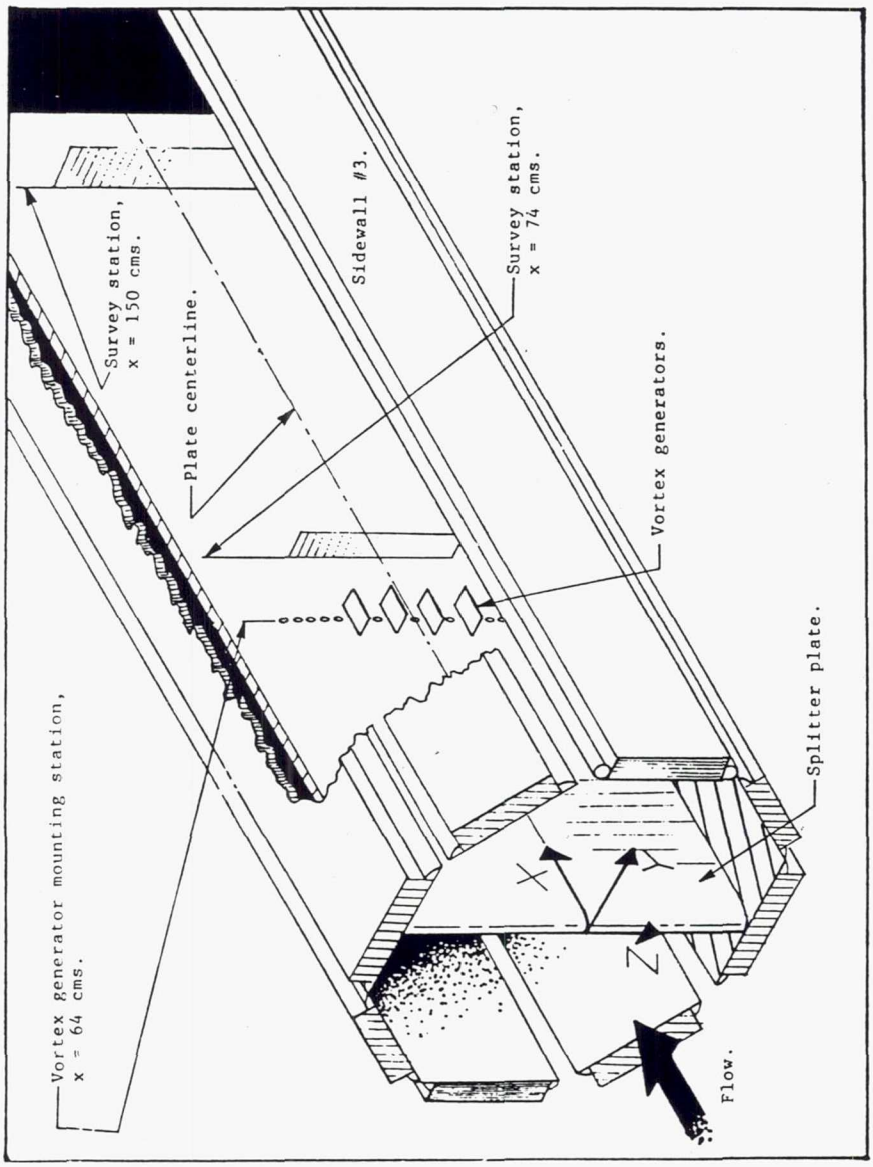

Figure 3.13 - Cutaway view of the octagonal test section with splitter plate installed. Coordinate system is centered on the plate leading edge.

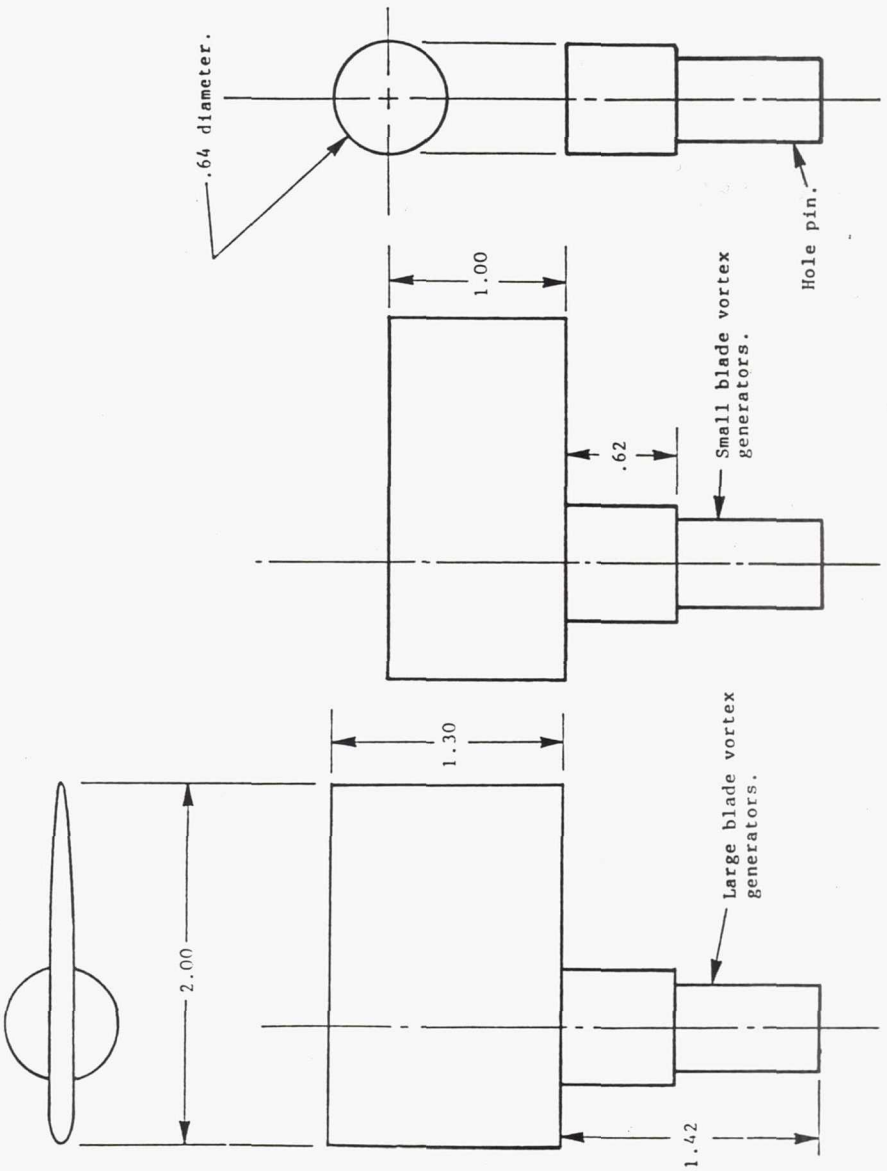

Figure 3.14 - Vortex generator and hole pin geometry. Vortex generators are constructed from stainless steel; hole pins from an aluminum alloy. Dimensions are in centimeters.

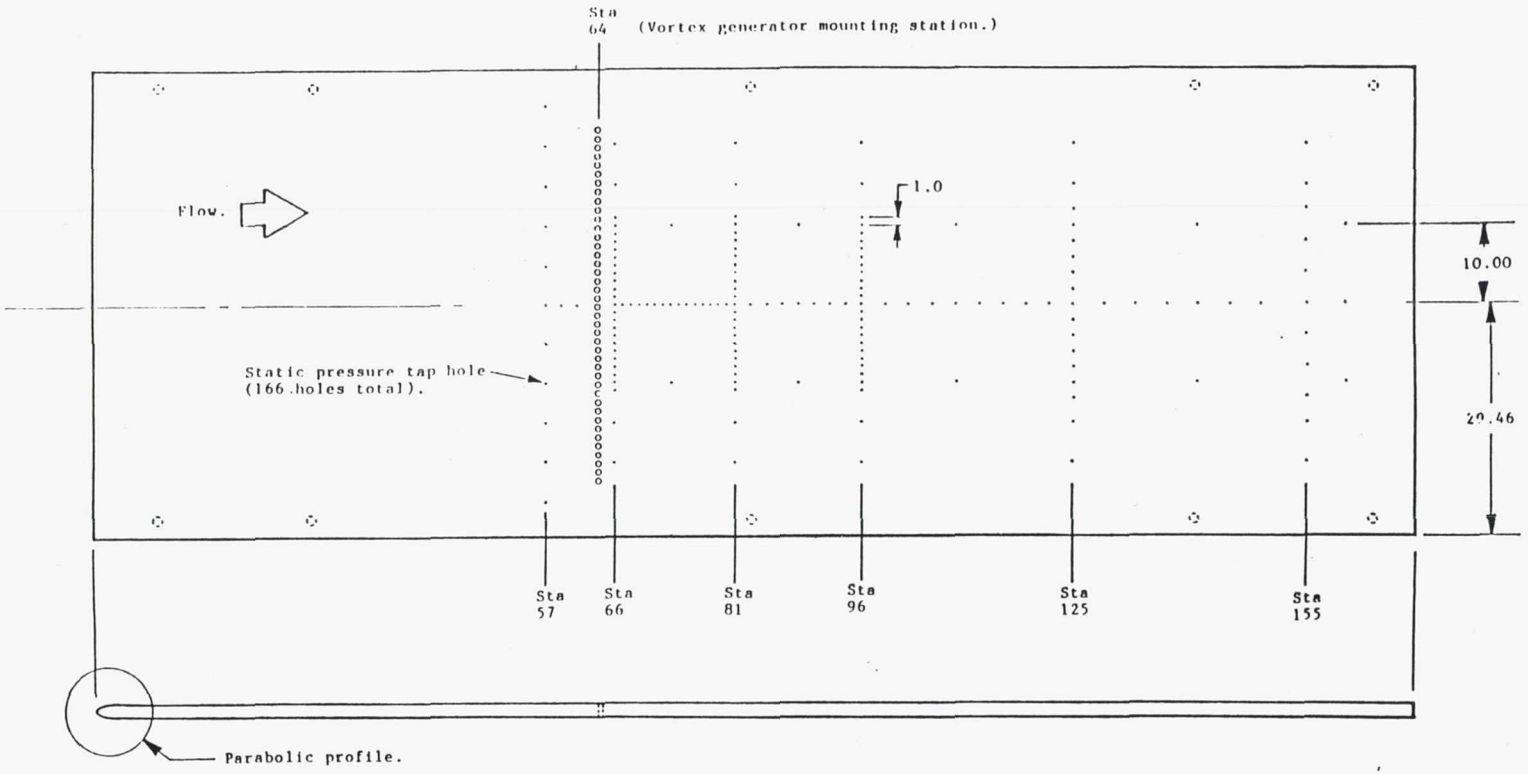

Figure 3.15 - Top view of the surface static pressure tap instrumented splitter plate. The tap grid geometry is indicated. Dimensions are in centimeters.

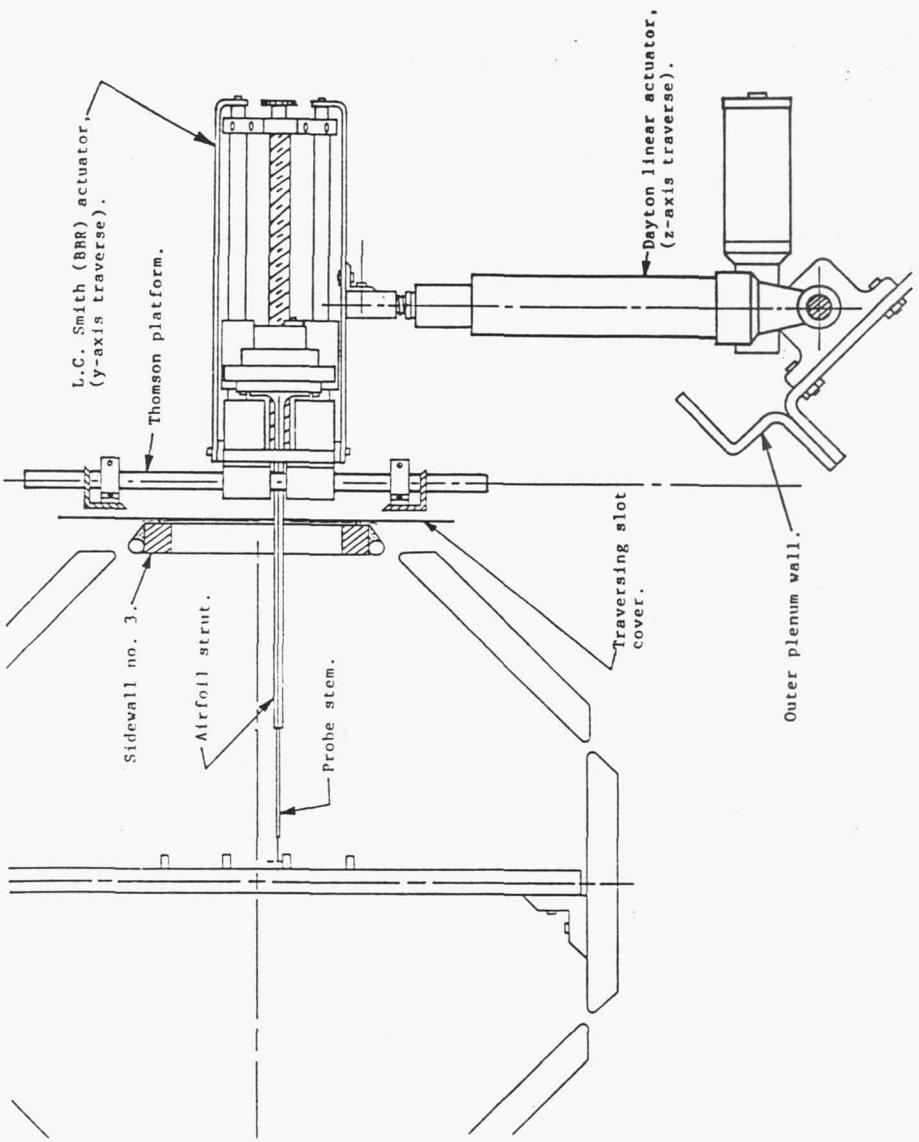

Figure 3.16 - The velocity probe traversing mechanism. Dimensions are in centimeters.

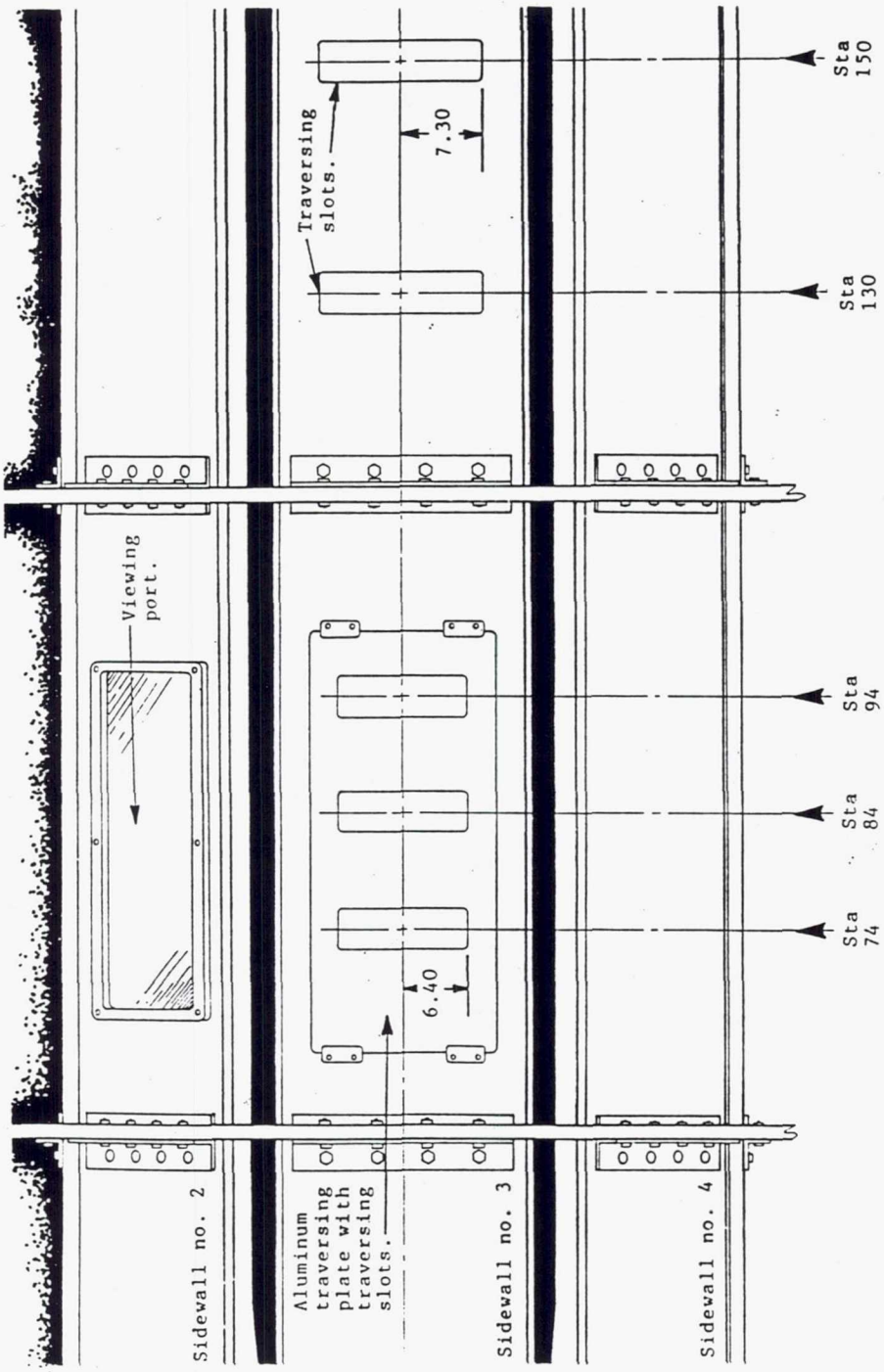

Figure 3.17 - Top view of sidewall no. 3 showing the streamwise locations of the traversing slots. Dimensions are in centimeters.

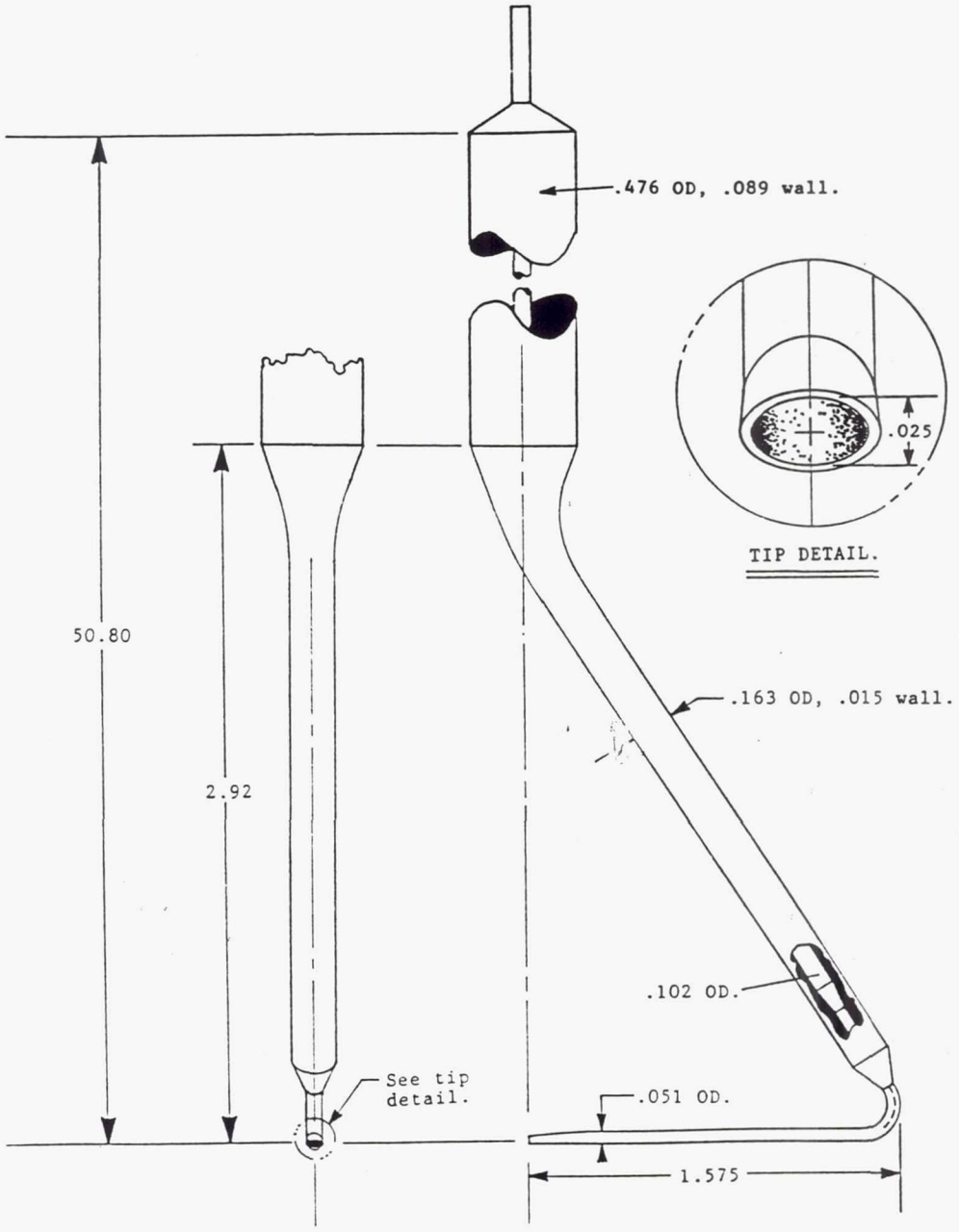

Figure 3.18 - Geometry of the boundary layer pitot probe. Probe is constructed from silver brazed stainless steel tubing. Dimensions are in centimeters.

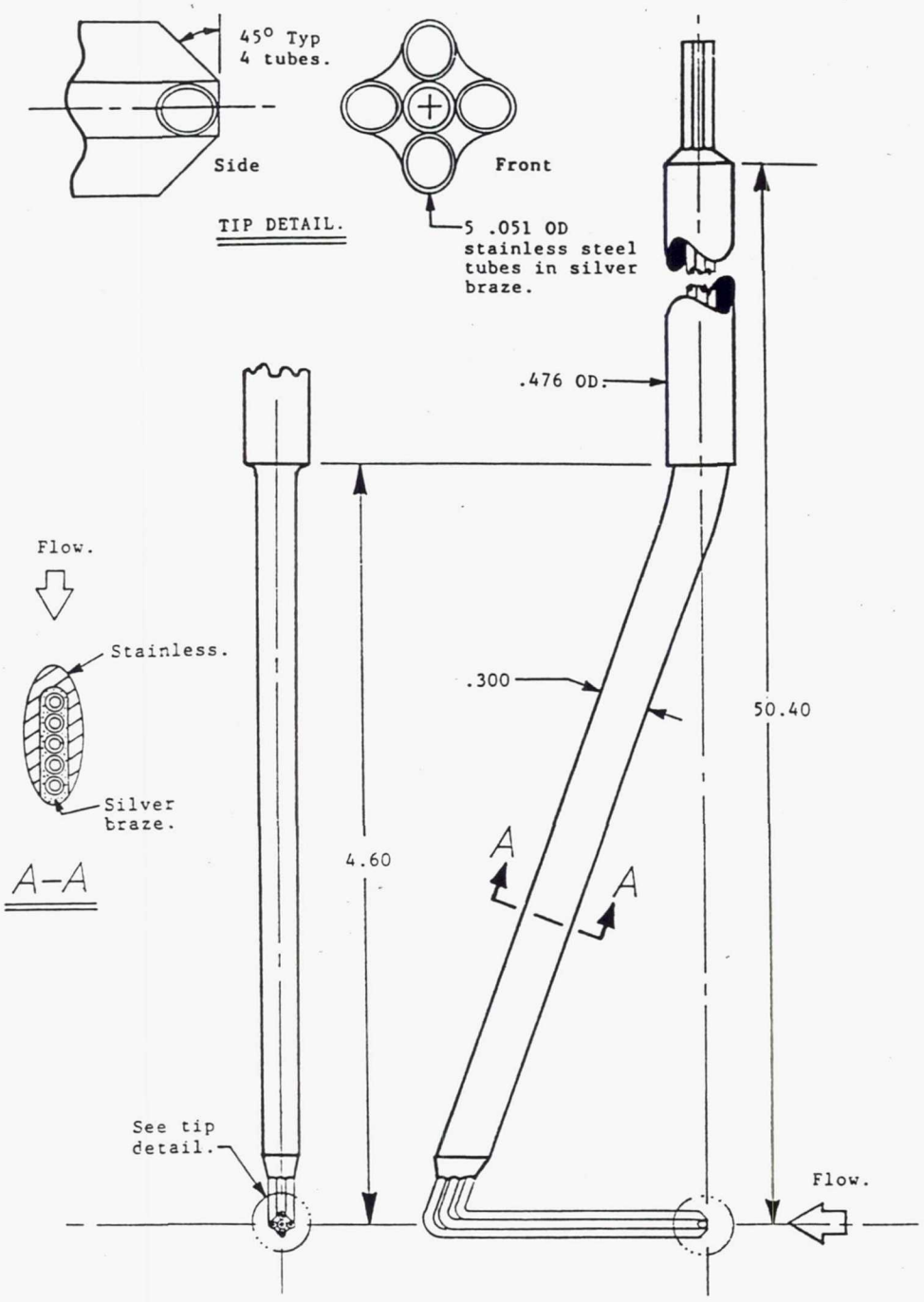

Figure 3.19 - Geometry of the five hole probe. Probe is constructed from silver brazed stainless steel parts. Dimensions are in centimeters.

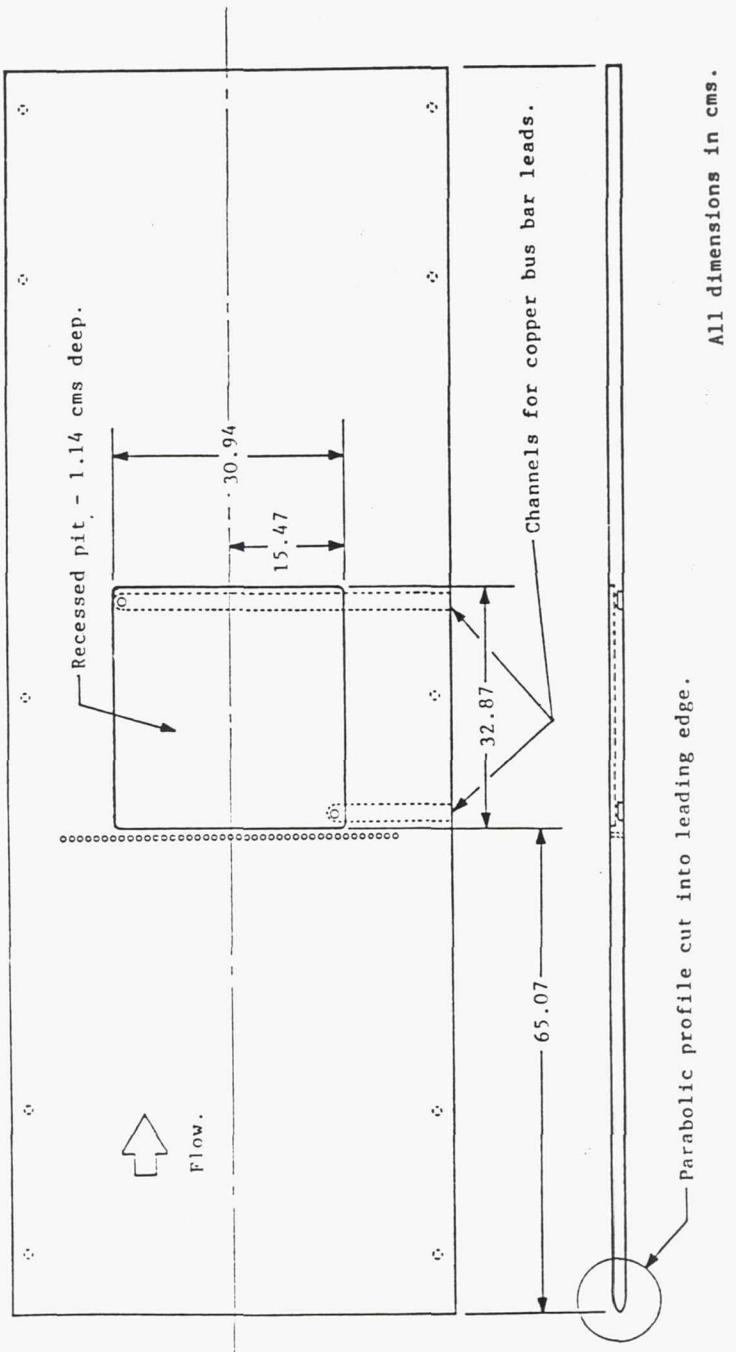

Figure 3.20 - Top view of the heated splitter plate. The recessed area in the center of the plate holds the insulated inlay base and heater element.

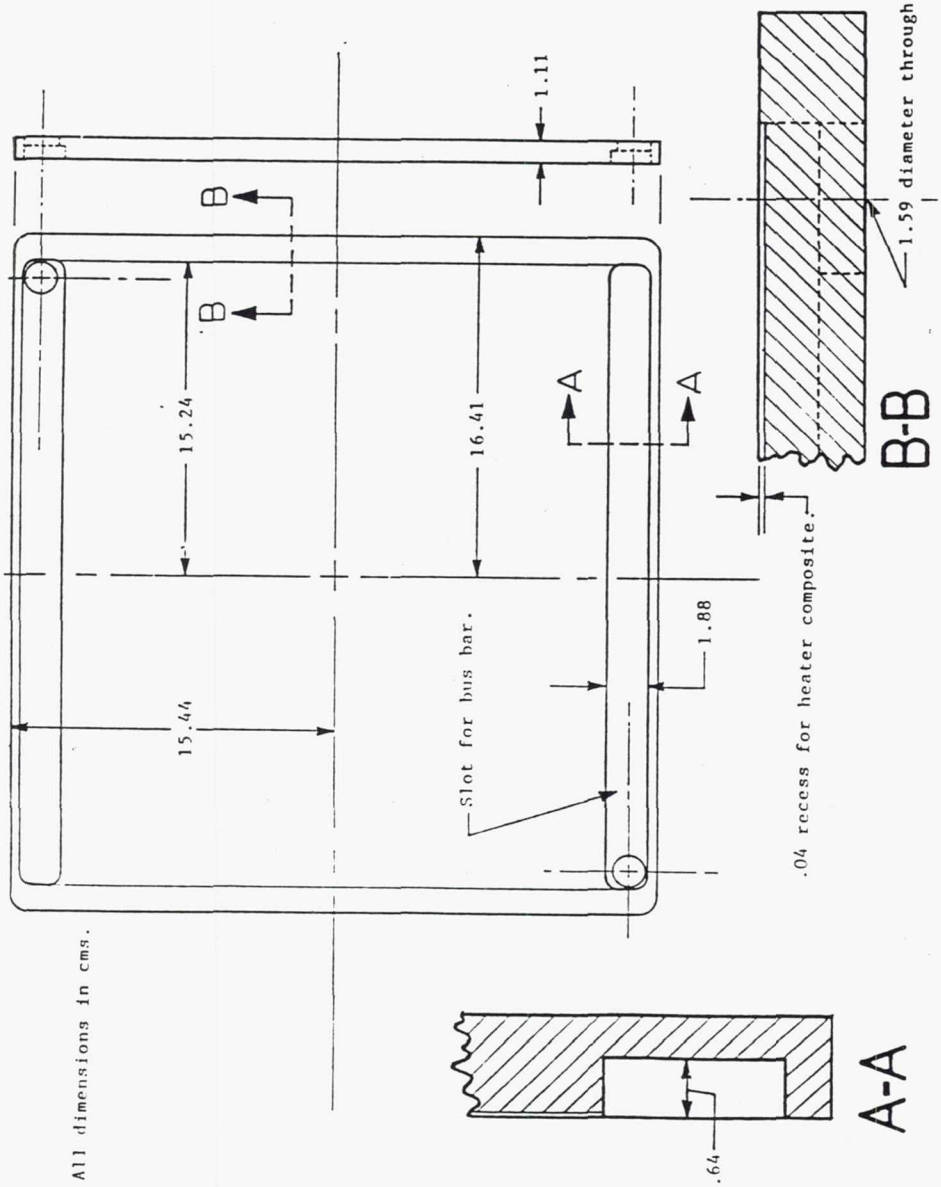

Figure 3.21 - The geometry of the insulated inlay on which the heater composite is mounted. The material is N.C. Proofboard.

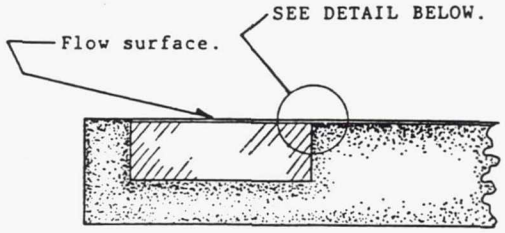

Cross section A-A of Figure 3.21 with
bus bar and heater installed.

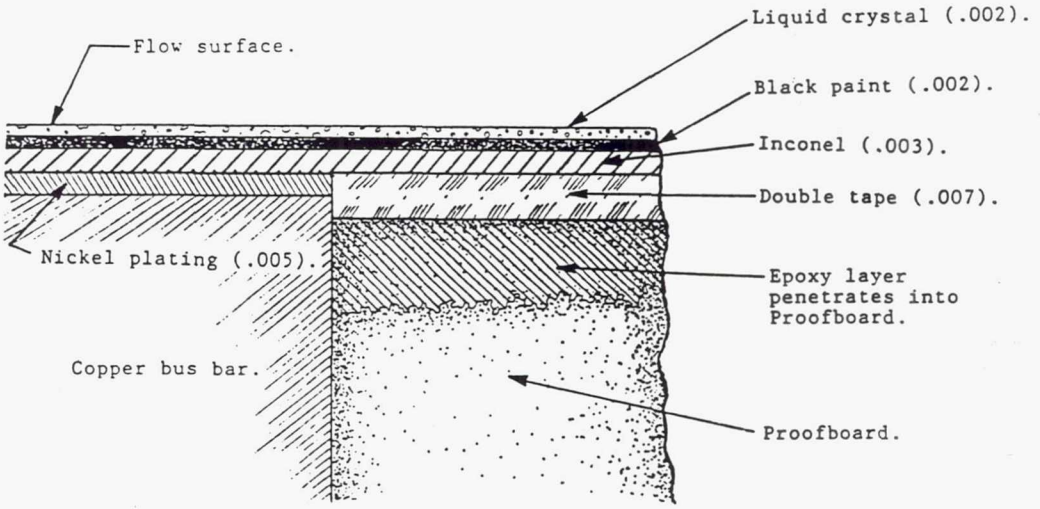

DETAIL OF HEATER COMPOSITE CONSTRUCTION.
Thickness dimensions in cms.

Figure 3.22 - A detailed schematic view of the heater composite showing constuction details and dimensions.

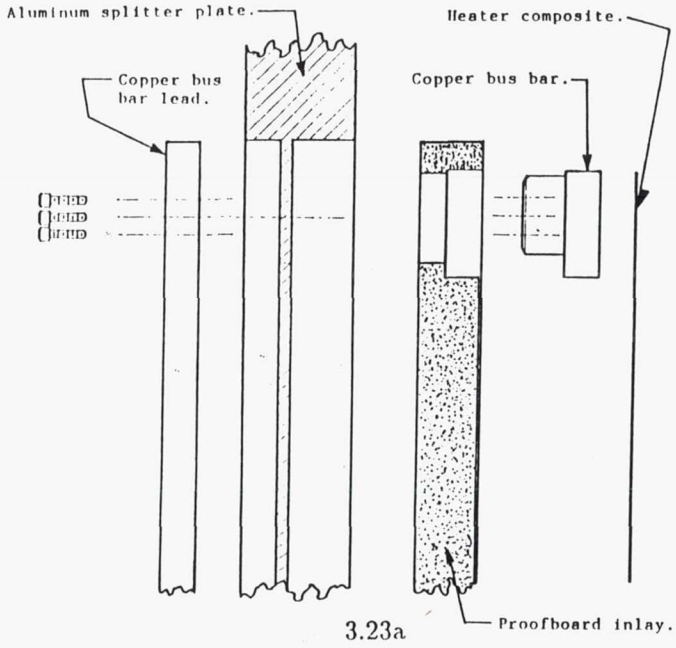

3.23a

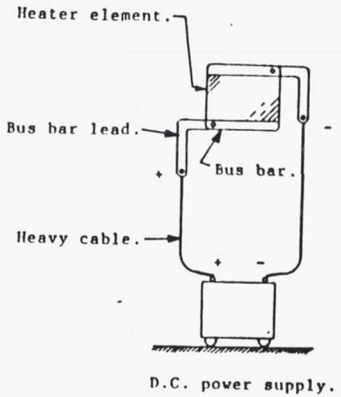

3.23b

Figure 3.23a - Assembly drawing of the heater showing plate, heater composite, insulated base, and copper bus bars.

Figure 3.23b - Simplified circuit diagram of the heater. In response to the voltage applied across the resistance element the surface heater provides a fixed uniform heat flux of magnitude q_w.

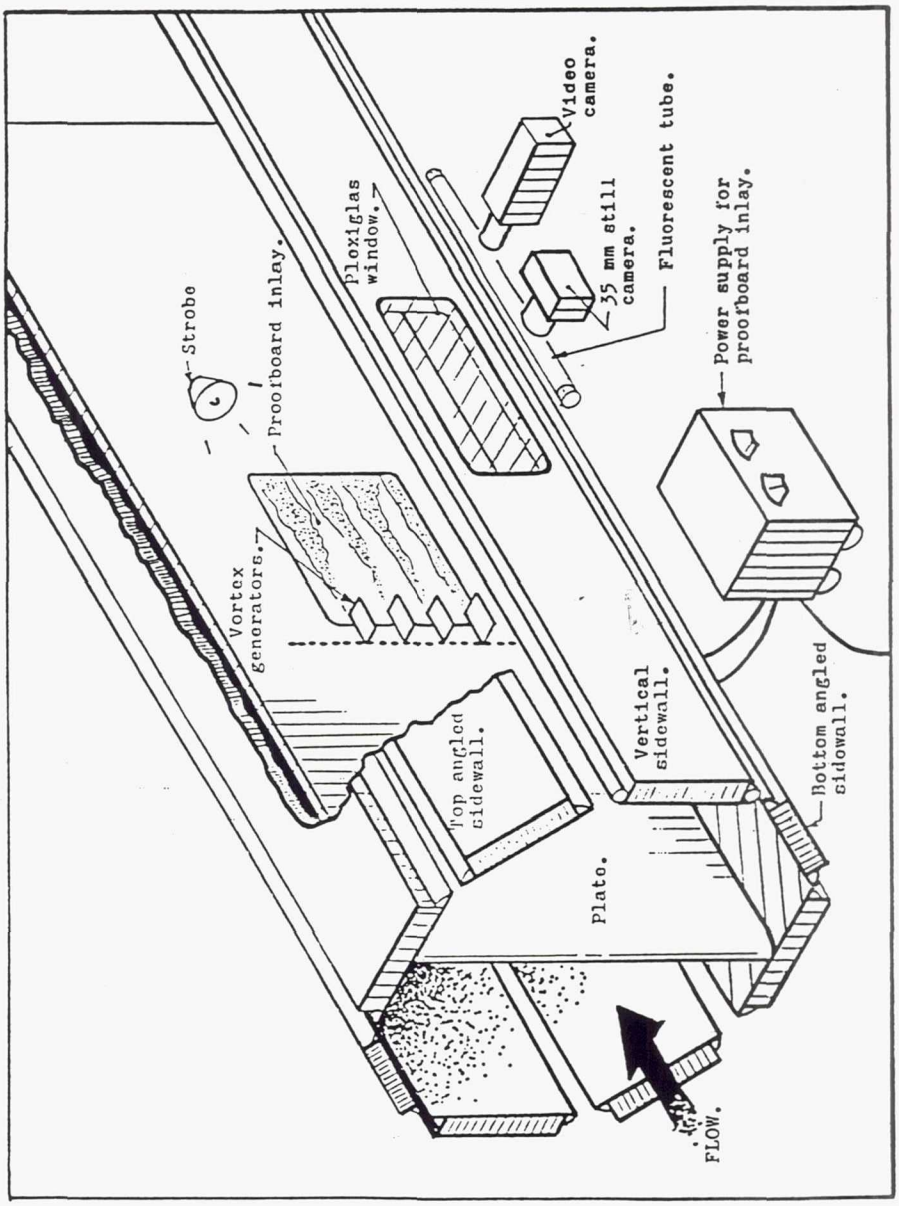

Figure 3.24 - Additional hardware elements used in the heat transfer portion of the study.

Chapter 4

Experimental Results

4.1 Two Dimensional Boundary Layer Definition

The splitter plates used in this study were carefully machined and installed. In the middle region of the splitter plate, away from the junction of flow surface and sidewall, the flow was two dimensional in character. The boundary layer that formed here was typical of flat plate turbulent boundary layers. This was confirmed by measurements taken with the full array of instrumentation described in Chapter 3.

4.1.1 Hydrodynamic Results

For the flow properties typically encountered in the CW-22 test facility a nominal Mach no. of 0.2 corresponded to a freestream velocity of about 70 m/sec. Preliminary analysis based on the splitter plate design indicated a laminar boundary layer forming over the flow surface for the first 7-10 cms of streamwise length x. At the vortex generator mounting station (x = 64.0 cms or "Station 64") the analysis indicated a fully turbulent boundary layer with a thickness of about 1.0 cm. The local Reynolds number at Station 64 was

3.0×10^6.

Spanwise uniformity of the flat plate boundary layer was gauged by traversing the five hole probe over a rectangular grid at Stations 74 and 150. The traversing grid at Station 74 is diagrammed in Figure 4.1a. Figure 4.1b is the resulting contour plot of the streamwise velocity. Use of the five hole probe also allowed for a survey of flow angularity at Stations 74 and 150. It was found that the magnitude of the secondary velocity vectors inside and outside the flat plate boundary layer were small enough to fall within the measurement uncertainty of the five hole probe. No coherent structure of this secondary flow was discernible. Figure 4.2a diagrams the survey grid used at Station 150. Figure 4.2b is the corresponding contour plot of streamwise velocity.

The near wall structure of the boundary layer could best be examined through the use of the boundary layer probe. Streamwise velocity profiles were taken with the boundary layer probe at various spanwise locations at Stations 129 and 150. Figure 4.3 diagrams the profiles taken on the plate centerline ($z = 0.0$ cms). Profiles taken with the five hole probe at Stations 74 and 150 (also with $z = 0.0$ cms) are included as well.

Workers investigating the structure of flat plate turbulent boundary layers have developed extensive data sets to which the present results may be compared. A set of scalar integral parameters outlined by Coles (1968) provides a convenient means of making this comparison. The integral parameters of Coles are defined as :

- Displacement Thickness : $\delta^* = \int_0^\infty (1 - \frac{\rho u}{\rho_\infty U_\infty}) dy$,
- Momentum Thickness : $\Theta = \int_0^\infty \frac{\rho u}{\rho_\infty U_\infty} (1 - \frac{u}{U_\infty}) dy$,
- Shape Factor : $H = \delta^*/\Theta$.

The boundary layer probe provided the velocity profiles used in this data reduction. A cubic spline was fit through the data and integrated. The results appear in Table 4.1 and

compare favorably with results obtained by Coles (1968) and J. Nikuradse (1942) as reported in Schlichting (1968).

Figure 4.4a is the centerline velocity profile at Station 129 plotted in wall coordinates. The straight line running through the plot represents the law of the wall relationship :

$$u^+ = 2.44 \ln y^+ + 5.0, \tag{4.1}$$

where

$$\begin{aligned} u^+ &= u/u_\tau, \\ y^+ &= y u_\tau/\nu, \\ u_\tau &= \sqrt{\frac{\tau_w}{\rho}}. \end{aligned}$$

The friction velocity, u_τ, was determined by an iterative procedure. A least squares regression routine based on Eq. (4.1) determined a value of u_τ for each data point in the range : $50 < y^+ < 350$. The average value of u_τ among these points was then used to plot the complete profile. The subset of points used to determine u_τ was then extended or restricted based on the positions of the plotted points relative to the line representing Eq. (4.1), and u_τ was recalculated. The resulting values of u_τ and wall shear stress τ_w are listed in Table 4.1. Figure 4.4b is the corresponding centerline profile at Station 150.

The boundary layer thickness, δ, is listed in Table 4.1. It comes from a curve fit routine suggested by Coles (1968). Coles combined law of wall-wake is :

$$u^+ = 2.44 \ln y^+ + 5.0 + 2.44 \Pi W(y/\delta), \tag{4.2}$$

where

$$W(y/\delta) = 2\sin^2(\frac{\pi y}{2\delta}).$$

A least squares procedure based on Eq. (4.2) determined the best values of δ and the wake parameter Π for each profile. The frictional velocity used in this routine comes from the procedure described in connection with Eq. (4.1).

Figure 4.5 is a plot of wall static pressure versus x on the plate centerline. A mildly favorable pressure gradient is present at Stations 129 and 150. A parameter used to gauge the effect of a pressure gradient on the boundary layer structure is β :

$$\beta = \frac{\delta^*}{\tau_w}\frac{dP}{dx}.$$

Estimates of β listed in Table 4.1 are small enough to exclude any significant pressure gradient effects.

4.1.2 Heat Transfer Results

As in the case of hydrodynamics, extensive theoretical and experimental work form a mostly complete picture of the thermal structure of the flat plate turbulent boundary layer. The element of thermal structure that is focused on here is the temperature behavior of the heated flow surface. Before moving onto the results, lets first use the background available to examine the expected surface temperature behavior of the heated plate. The following analysis is based on 2 dimensional boundary layer behavior. It is assumed to apply to the region of the heated surface away from the spanwise edges (bus bars).

Heat Transfer Behavior Based on a Constant Property Analysis

An equation developed by Kays and Crawford (1980) describes heat transfer in a flat plate turbulent boundary layer with a constant surface heat flux beginning at $x = \epsilon$:

$$St_x Pr^{2/5} = 0.0307 Re_x^{-1/5}(1 - (\epsilon/x)^{9/10})^{-1/9}, \tag{4.3}$$

where $St_x = h_x/(\rho C_p U_\infty)$ and $h_x = q_w/(T_{wx} - T_r)$. The quantity q_w is the wall heat flux. T_r is the recovery temperature of Eckart and Drake (1972). At a Mach number of 0.2, T_r is only slightly higher than the value of the freestream static temperature, T_∞.

Eq. (4.3) would be the answer to the problem except for one minor difficulty. At what temperature do we evaluate the properties of air? An integral mean temperature can be defined as a film temperature, $\overline{T}_f$:

$$\overline{T}_f = T_r + \frac{Pr^{2/5} q_w}{0.0307 \rho C_p U_\infty} \frac{(U_\infty/\nu)^{1/5}}{(L - \epsilon)} \int_\epsilon^L x^{1/5}(1 - (\frac{\epsilon}{x})^{9/10})^{1/9} dx. \tag{4.4}$$

This equation follows directly from Eq. (4.3). For this study, ϵ = 0.669 m, L = 0.961 m and the integral in Eq. (4.4) :

$$\frac{1}{L - \epsilon} \int_\epsilon^L x^{1/5}(1 - (\epsilon/x)^{9/10})^{1/9} dx$$

has a numerical value of 0.223. Thus the film temperature becomes a function of the wall heat flux q_w :

$$\overline{T}_f = \frac{7.756 q_w \mu^{1/5}}{(kT)^{2/5} \rho^{4/5} C_p^{3/5}} + T_r, \tag{4.5}$$

where a Mach number of 0.2 is assumed. The procedure to follow to get $\overline{T}_f$ as a function of q_w is straightforward :

1. Evaluate the air properties at T_r, solve Eq. (4.5) for $\overline{T}_f$.

2. Determine air properties at the new value $\overline{T}_f$. Recalculate $\overline{T}_f$. Repeat until convergence is obtained.

For the flow parameters described for this study, the wall heat flux needed to activate the liquid crystal fell into the range : $3200 \leq q_w \leq 8400$ watts/m^2. For this range of heat flux the iterative procedure desribed above yields the correlation :

$$\overline{T}_f - T_r \approx 0.0053\, q_w \text{ Kelvin}, \tag{4.6}$$

where q_w is measured in watts/m^2.

Eq. (4.3) along with Eq. (4.6) for the film temperature constitute the expected heat transfer behavior of the heated flow surface.

Test Results

The 35 mm slide camera recorded the streamwise position x of the calibrated yellow color on the heated surface. At the same time the test section flow conditions and wall heat flux q_w were recorded. Recall that $q_w = 0.97(I^2R/A)$, where I is the current in the power circuit, R and A are the resistance and area of the heating element, respectively.

The expected value of h_x at the location x was calculated through Eq. (4.3) by evaluating the air properties at the film temperature determined through Eq. (4.6). The heat flux range covered in this flat plate test was :

$$4010 \leq q_w \leq 7140 \text{ watts/m}^2.$$

In order to facilitate the comparison between the expected results and the data an "average"

value of the film temperature was determined through Eq. (4.6). This is done by simply choosing the heat flux q_w which split the covered range in half, $q_w = 5575$ watts/m^2. T_r drifted by about half a degree Kelvin during the test, and had an average value of about 291 K. Eq. (4.6) thus yields $\overline{T}_f \approx 321$ K. h_x in Eq. (4.3) (with $\overline{T}_f = 321$ K) is plotted versus x in Figure 4.6. The plotted points in Figure 4.6 are the data :

$$h_{xi} = q_{wi}/(T_{wx} - T_r),$$

where T_{wx} is the calibration temperature of the yellow band, 315.9 K. Near the trailing edge of the heated surface the yellow band had a noticeable width. Here the x location of the band was taken to be at its center.

The agreement between the expected results and the data is very good. The discrepancy is only about 2 % for the data points near the trailing edge. The discrepancy is somewhat higher for data points near the leading edge where Eq. (4.3) underpredicts h_x by about 3-4 %. This is most likely due to the assumed value of $\overline{T}_f$ being too high here.

Figure 4.6 verifies the two dimensional heat transfer behavior of the flat plate boundary layer. Although this behavior is based on the somewhat crude assumption of constant air properties, Figure 4.6 also clearly indicates that, at least for the power conditions covered in this study, this assumption is entirely adequate.

4.2 Boundary Layer with Embedded Vortices

The specific goals of this study, as outlined in Chapter 1, are met in large part by the experimental description of the embedded vortex array. To this end, the measurement systems described in the previous chapter are used in the following ways :

1. The flow structure of the embedded vortex array is well described by a fine resolution of the secondary velocity vector field in the crossplane. This data was aquired by the five hole probe traversing a rectangular grid in the crossplane. Other descriptions of the vortex array structure, such as contour plots of streamwise velocity or vorticity come either directly, or are derived from, the five hole probe data.

2. The growth and development of the embedded vortex array may be examined by using the five hole probe at two or more crossplanes, widely spaced along the streamwise coordinate. The trajectories of the individual vortices may also be inferred from the heat transfer data obtained through the use of the liquid crystal coated splitter plate.

4.2.1 Test Condition Parameters

Based on the objectives of this study and on the nature of the facility and research equipment involved, suitable restrictions were placed on the range of test parameters covered.

There were several factors involved in choosing a freestream Mach number of 0.2. A Mach number of 0.2 coincided with the lower end of the wind tunnel's calibrated range. At Mach numbers above 0.3 the vibration level inside the test section presented some cause for concern. This was a particular problem in the heat transfer test, where a vibrating mount could cause erratic operation of the slide camera. A range of Mach numbers between 0.2 and 0.3 presented little in the variation of the boundary layer thickness at Station 64, δ, and so a fixed Mach number of 0.2 was settled on.

Investigations of a single embedded vortex, and embedded counter-rotating vortex pairs were well documented by the Stanford workers, Eibeck and Eaton (1985), and Pauley and Eaton (1988). The case of the single embedded vortex was re-examined in this study, to take advantage of the higher resolutions employed.

Investigations of an embedded vortex array involved an even number of nominally equal

strength vortices (typically 4 vortices, sometimes more), arranged in counter-rotating pairs :

- A vortex array consisting of an even number of embedded vortices was chosen to take advantage of the flow symmetry involved. As an example, consider Figure 4.7. Figure 4.7 represents an array of 4 embedded, counter-rotating vortices. The line of symmetry is marked. (Note the number convention for the vortices, proceeding from left to right). Much survey time could be saved if only half of the embedded array needed to be examined. Of course, symmetry can only apply to those cases where the vortex generators are set to produce identical vortices in an initially symmetric arrangement. This assumption of symmetry was tested in several cases.

- To produce vortices of equal strength, the vortex generators were set at the same absolute value of angle of attack, α. The relationship between α and resulting vortex strength was not a subject for this investigation. H.D. Taylor (1954) investigated the relationship between mixing performance (related to vortex strength) and α for blade-like rectangular vortex generators similar to the ones employed here. He reported that for $\alpha \approx 10°$, optimum mixing was obtained.

- Pauley and Eaton (1988) observed that counter-rotating vortices maintained individual identities in the boundary layer while vortices in co-rotating arrays of limited size (2-6 embedded vortices) often did not. Co-rotating pairs by themselves and on the spanwise ends of an array often merged together. For this reason the counter-rotating configuration was chosen.

The desire to keep the vortex in the vicinity of the boundary layer translates to a height ratio $h/\delta \approx 1.0$. For this study $h/\delta = 1.3$, except for two cases where $h/\delta = 1.0$.

Figure 4.8 summarizes the test condition parameters covered at the vortex generator mounting station. The boundary layer thickness here is $\delta = 1.0$ cm. The vortex generators

are set to produce two counter-rotating pairs of vortices with $\alpha = \pm 10°$ and $h/\delta = 1.3$. The spacing ratio in Figure 4.8 is $S/\delta = 2.0$. Spacing ratios were varied in the range : $2.0 \leq S/\delta \leq 7.0$. The spacing between adjacent vortex generators was the same *at the vortex generator mounting station*. The distance between the vortex generator tips at the trailing edges was offset somewhat. This offset did not affect the resulting array symmetry.

As the rest of this chapter and the next will show, the data collected for this limited range of test conditions provides a sufficient basis for the understanding of the behavior of embedded vortex arrays of a much more general composition.

4.2.2 Flow Structure of Embedded Vortices

Survey Grid Parameters

Velocity data on crossplane grids provide a detailed picture of the flow field structure of embedded vortices. The two crossplane grids employed here were located at Station 74 and Statio 150 (refer to Figure 3.13). Of the survey stations available, these two were the most widely separated in x.

Survey grid size and resolution was determined at each spanwise station by balancing the following factors :

- Grid point spacing $\Delta z = \Delta y$ (or "resolution") was to be *as fine as possible* given the time constraints of the study. To cover the desired number of test conditions (vortex generator array sizes and spacings) it was determined that each four hour test run would need to cover at least half a test condition. The primary factor limiting the number of grid points covered per test run was the settling time needed for the probe pressures. Other factors included the speed of the probe traversing mechanism, and the need to periodically recalibrate the ESP pressure transducers. A calibration procedure using the five hole probe in an embedded vortex array at both survey

stations determined that a settling time of at least 6 seconds was required between grid points. This worked out to a little over 600 grid points per four hour test run given the other constraints.

- As mentioned in Chapter 3, the maximum spanwise extent of the survey grids was limited by the geometry of the sidewall traversing slots. The normal (y) extent of the survey grid was set by considering the normal extent of the boundary layer and embedded vortex structure at each station. Figures 4.1b and 4.2b indicate the y extent of the flat plate boundary layer. The secondary flow due to embedded vortices could thicken the boundary layer by as much as three to four times the flat plate result. This was true at both streamwise stations. In this study, the focus is primarily on the structure of the embedded vortices themselves, and not on their interaction with the boundary layer. An important description of this structure lies in the vorticity field created. The y extent of the survey grid was therefore set to capture this vorticity field. Although the y extent of the survey grid was set in this way, it proved sufficient to capture a major portion of the thickened boundary layer as well. This was true for all test conditions covered.

Figure 4.9a is a diagram of the survey grid employed at Station 74. Grid point spacing is $\Delta z = \Delta y = 0.127$ cm. There are a total of 1215 grid points in this grid. Figure 4.9b is a diagram of the survey grid employed at Station 150. Grid point spacing here is $\Delta z = \Delta y = 0.203$ cm. There are a total of 1260 grid points in this grid. The Station 74 survey grid has a finer resolution to capture a more condensed vortex structure there.

Descriptive Elements of Vortex Structure

Secondary velocity vector fields, contours of streamwise vorticity, and contours of streamwise velocity provide a graphical representation of vortex structure in the crossplane. A

quantitative description of vortex structure is also useful, especially when making comparisons between the individual vortices in an array, as well as when making comparisons between vortices from different arrays or test conditions. Four quantitative descriptors classify vortex structure at a particular streamwise location and so provide a natural framework for understanding vortex streamwise development. Following the work of Westphal, Eaton, and Pauley (1985) four descriptive elements of vortex structure are employed. For each vortex i in the array they are :

1. Peak streamwise vorticity : ω^i_{max}.
2. Spanwise location of ω^i_{max} : z_i.
3. Normal location of ω^i_{max} : y_i.
4. Circulation : Γ_i.

In the list above a subscript or superscript i denotes the descriptor quantity of vortex i. y_i and z_i may be thought of as the location of the center of the vortex, the point around which the vortex "spins". ω^i_{max} is an indication of the extent to which the vortex core has diffused in its downstream development. The circulation, Γ_i, is a measure of the vortex "spinning power", i. e. its strength.

The descriptors of the embedded vortices originate from the velocity data in the cross-plane. Following convention, the three components of the velocity vector are u, w, and v. These are the streamwise (x), spanwise (z), and normal (y) components, respectively. Figure 4.10a is a vector plot of the secondary velocities (w and v) induced by a single embedded vortex at Station 74. Determination of the four quantitative descriptors for this vortex first requires a conversion of the velocity field to a vorticity field. The component of vorticity

required here is the streamwise vorticity, ω_x :

$$\omega_x = (\frac{\partial w}{\partial y} - \frac{\partial v}{\partial z}). \tag{4.7}$$

Since velocities are known at the grid points a finite difference formula is a natural choice to represent the spatial derivatives in Eq. (4.7). Another choice, preferred by the Stanford workers, is to determine the derivatives from a spline fitted curve of the v and w velocity profiles. To decide between the two approaches an analytical velocity field was constructed from the equations for an embedded vortex model. This model is composed of two "Oseen" vortices. The Oseen vortex model is discussed in detail in Chapter 5. The model velocities were evaluated at (z,y) locations corresponding to the grid points at the survey stations. A random velocity component less than or equal in magnitude to the uncertainty in the five hole probe measurement was added to the secondary velocities produced by the model. Finite difference and cubic spline derivative formulas were used to determine $\partial w/\partial y$ and $\partial v/\partial z$ for the model w and v velocity profiles. These were compared to the analytical derivatives. A fourth order finite difference formula with second order accuracy on the grid boundaries most closely matched the analytical derivatives, outperforming both the cubic spline routine and second order finite difference formulas. Significant improvement over the fourth order results was not achieved with finite difference formulas of order higher than four.

Using finite differences, the velocity data was converted to streamwise vorticity data. Figure 4.10b is a plot of streamwise vorticity contours at Station 74, corresponding to the velocity field in Figure 4.10a. The contours define the extent of the viscous core and are, as expected, circular in shape. This core region of vorticity is often referred to as "primary" vorticity. A region of "secondary" vorticity of opposite sign is produced at the wall. This

region of secondary vorticity is induced by the viscous interaction between the primary vortex and the wall and tends to grow in size as the vortex develops downstream. Roll up of this region of secondary vorticity into an identifiable vortex structure was not observed in this study. The region of induced secondary vorticity is along the wall and to the right of the vortex in Figure 4.10b

Evaluation of the quantitative descriptors of vortex structure proceeds from the vorticity field. ω^i_{max} is located at some grid point having coordinates (z_i, y_i). For the vortex illustrated in Figure 4.10a :

$$\begin{aligned} \omega^i_{max} &= 29640\,\mathrm{sec}^{-1}, \\ z_i &= 1.52\,\mathrm{cm}, \\ y_i &= 1.02\,\mathrm{cm}. \end{aligned}$$

It must be emphasized that this is a grid estimate; the chance that a grid point would precisely coincide with the vortex center is remote. A refinement of these estimates will be discussed in connection with a vortex model developed in Chapter 5. Circulation, Γ_i, was calculated by first isolating the region of primary vorticity in the data field. This was done by simply referring to a contour plot such as Figure 4.10b. Then it was possible to proceed in two ways. First, a direct integration of the vorticity :

$$\Gamma_i = \int\int_{region} \omega_x \, dy \, dz,$$

where "region" refers to the region of primary vorticity, excluding the opposite sign induced vorticity at the wall. Secondly, a closed path about the vortex was defined. Again, this path

enclosed the region of primary vorticity and excluded the region of induced vorticity :

$$\Gamma_i = \oint_{path} \vec{V} \cdot d\vec{s},$$

where $\vec{V}$ is the secondary velocity vector and $\vec{s}$ refers to the path coordinate. By using closed rectangular paths, or closed paths composed of line segments in the z or y coordinate directions, the circulation was easily determined. Circulation was calculated in both ways and the agreement was always within 5 percent, most often within 2 percent. By using both grid techniques for vortex circulation on the velocity and vorticity field created by the model vortex, an estimate of the uncertainty in determining the vortex circulation from the data was obtained. The vortex model's circulation could be determined to within 1 percent of its input value. It was found that the circulation of the region of induced secondary vorticity was less than or equal (in magnitude) to about 4 percent of the corresponding primary circulation at Station 74, and about 10 percent (or less) at Station 150. The circulation of the vortex illustrated in Figure 4.10a is $\Gamma_i = .281\ \mathrm{m}^2/\mathrm{sec}$. The corresponding quantitative descriptors of vortex structure are listed on each crossplane plot in Figures 4.10a-b and on the crossplane plots to follow.

Contours of streamwise velocity illustrate the interaction of the vortex and boundary layer. Figure 4.10c is a plot of the streamwise velocity ratio (U/U_∞) contours for the single embedded vortex at Station 74. The thinning of the boundary layer under the downwash side of the vortex is evident, as is the thickening of the boundary layer on the upwash side. The streamwise velocity deficit in the vortex core is also graphically illustrated.

Figures 4.11a-c are the corresponding results for the single embedded vortex at Station 150. At this streamwise location the vortex has diffused considerably. ω^i_{max} is reduced to about 5 percent of its value at Station 74. Figures 4.12a-b are the secondary velocity

vector fields of Figures 4.10a and 4.11a replotted with the same velocity and length scale to emphasize the extent to which secondary flows of the embedded vortex have weakened and diffused. Note the flattening of the vorticity contours in Figure 4.11b. The vortex has moved along the wall by about 3 cms in the positive z direction between Stations 74 and 150. A reduction in circulation of about 15 percent between survey stations may be attributed to the effects of wall friction.

Four Element Array Results at Station 74

Figure 4.13 is a schematic depiction of an embedded array of N_v counter-rotating vortices. Such an array results from a particular setting of the vortex generators at Station 64 and as such, constitutes a *single test condition*. For reference purposes the vortices are numbered from left to right and can also be identified as either rotating clockwise (CW) or counterclockwise (CCW). A pair of vortices can be identified by the direction of the secondary flow between them. For example, vortices 3 and 4 are referred to as an "upflow pair" since the secondary flow between them is directed up, away from the wall. Vortices 4 and 5 are a downflow pair. Table 4.2 is a summary of the test conditions examined at Station 74. Individual vortices are identified and the corresponding descriptors are given. There are a total of five test conditions examined at Station 74. These include 4 vortex generator arrays of different spacing ratios and the results of the single vortex generator.

Having the structure of the single embedded vortex at Station 74 allows us to address the following question : When does the structure of the vortex array become simply a sum of vortices whose individual structure is identical to the single embedded vortex? Naturally, this behavior is expected when the distances between vortices is large enough. Consider Figures 4.14a-c which show the right half upflow pair from a four element vortex array. The vortex generator spacing ratio is 5.0. Vortex 3 clearly is similar in appearance and

structure to the single embedded vortex in Figures 4.10a-c. Vortex 4 is merely its mirror image. Figures 4.15 - 4.17 reveal a similar pattern. The velocity vector and vorticity patterns indicate the vortex retains its circular core shape regardless of the distance between vortices. Apparently each vortex is so strongly condensed that its shape can withstand the distortional convective forces of its neighbors.

Figures 4.14b - 4.16b also reveal that the relative displacement of vortex core with respect to generator tip is similar to the case of the single embedded vortex. In the case of the single embedded vortex it is assumed that proximity to the wall and vortex strength most strongly influences this displacement. Figures 4.17a-c reveal something not seen in the results produced from the larger spacing ratios. Vortex 3 is lower in the boundary layer than vortex 4 is, indicating that the vortices are now close enough for noticeable convective displacement to occur along the y axis. Although the vortices in this proximity resist noticeable distortional effects, the displacement effects or *trajectories* are no longer merely influenced by proximity to the wall, but are influenced by proximity of the neighboring vortices as well. The streamwise velocity ratio contours in Figure 4.17c also indicate a boundary layer thickening greater than a simple summation of the single vortex result.

There are a range of vortex circulations listed in Table 4.2. This range is considerably larger than would be expected from the uncertainty in determining the circulation. On the assumption that differences in vortex circulation due to various downstream developments should be small at the upstream station, this range of vortex circulations would have to originate at the vortex generators themselves. A small misalignment of the blades or small differences in blade tip thicknesses and curvatures could explain the range of resulting vortex circulation in Table 4.2. The implication of this is that although the circulation of each vortex is known to within a few percent, the uncertainty in the *initial* value of circulation is considerably higher. From Table 4.2 this uncertainty would be about 12 percent. It is

important to keep this in mind when considering the downstream results.

Four Element Array Results at Station 150

Table 4.3 summarizes the test conditions examined at Station 150. The core locations of the vortices encountered at Station 150 indicate trajectories that are strongly influenced by both the wall and neighboring vortices. Contours of streamwise vorticity show the vortex cores as diffuse and distorted elliptical shapes, unlike the condensed circular shapes encountered at the upstream measurement station. Here again, it is the influence of the wall and neighboring vortices, to varying degrees, which account for these distortions.

Refer again to the structure of the single embedded vortex at Station 150, Figures 4.11a-c. Note the elliptical shape of the vortex core in Figure 4.11b. The major axis is more or less parallel to the wall. This particular shape results from the close proximity of the core to the wall. How is this explained? The answer lies in a general result, evident in the illustrations to follow : *The secondary velocity field c[illegible]tes distortional effects through the transport of primary and secondary streamwise vorticity.*

We've already noted that secondary vorticity is created from the viscous interaction of the secondary flow with the wall. In the case of the single embedded vortex the secondary velocities are strongest along the wall, underneath the vortex core. It is here where the production of secondary vorticity is greatest. However, Figure 4.11b indicates no discernible secondary vorticity is present here. The secondary vorticity created along the wall accumulates in the upwash region of the vortex, being convected there by the strong secondary flows along the wall. Figure 4.11b clearly indicates this. In like fashion, the primary vorticity field responds to the convection of the secondary flow; core vorticity is drawn out into an elliptical shape following the wall.

Figures 4.18a-c illustrate the RIIS upflow vortex pair produced from a four element

vortex generator array of spacing ratio 7.0. Relative displacement of core location with respect to the vortex generator tip indicate that the vortices in this pair were moving towards each other along the wall. Because of the relatively large initial spacing of the vortex generators, the vortices in Figure 4.18 follow trajectories in the secondary flow plane that are influenced primarily by proximity to the wall. This would seem to be true for most of their streamwise development to Station 150. It may be that at Station 150 and beyond the vortices in Figure 4.18 are close enough to start convecting each other away from the wall. The influence of neighboring vortex proximity on the trajectories subsequent to Station 150, however, would likely be small due to the weak secondary flows present here.

The shape of the vortices in Figure 4.18b is similar to that of the single embedded vortex. This again indicates that proximity to the wall was the larger of the two influences in the downstream development of the vortices in this array. There is one significant difference between the structures of the spacing ratio 7 vortices and the single vortex at Station 150. In Figure 4.18b the region of opposite sign secondary vorticity for each vortex is considerably smaller than the corresponding region for the single vortex. In fact, accumulated opposite sign vorticity has effectively vanished between the vortices. As the vortices approach each other along the wall, the strength of the secondary flow between them increases. The accumulated secondary vorticity in this upwash region is swept up away from the wall between the vortices. Figure 4.18b shows several weak and indistinct "chunks" of streamwise vorticity floating above the wall between the two vortices. These most likely are the remnants of the secondary vorticity generated by both vortices.

Figures 4.19 through 4.22 illustrate the structure of the RHS vortex pair (like the pair in Figure 4.18) produced from a four element array of vortex generators set at spacing ratios of 6.0, 5.0, 4.0, and 3.0. Figures 4.23a-c illustrate the structure of the entire array of four vortices produced by vortex generators set at an initial spacing ratio of 2.0.

In Figure 4.19b the vortex cores are butted up against each other alongside the wall. Although the cores retain an elliptical shape, there is some evidence that the touching core ends are moving up away from the wall. As in the case of the vortex pair in Figure 4.18b no distinct region of secondary vorticity is discernible.

The vortex cores in Figure 4.20b, while still close to the wall, are surely in the process of convecting each other away from the wall. The distinct "quartered circle" shape results from secondary flow of roughly equal magnitude both along the wall and between the vortices. Figure 4.20b also offers the first evidence of secondary vorticity in association with its parent core in a vortex array at Station 150. The "tongue" of vorticity extending down from the base of each vortex core towards the wall represents the secondary vorticity produced by the opposing parent vortex. This secondary vorticity, being opposite in sign to the parent vortex, has merged (to some extent) with the same sign primary vorticity of the neighbor vortex. It is likely, though, that this tongue represents only a remnant, the balance of the secondary vorticity having been convected up between the vortices and out of the measurement domain.

The vortex cores in Figure 4.21b have convected each other to a significant distance away from the wall. The vortices are elliptical in shape, but now the major axis runs perpendicular to the wall. This shape may be attributed to the distortional influence of the secondary flow, now much stonger between the vortices themselves than between the wall and the vortices.

Making an intrusion into the illustrated flow field of Figures 4.21a-c is vortex no. 2 from the LHS upflow pair. Vortices 1 and 2 play an influential role in the resulting trajectories of vortices 3 and 4 in arrays produced with initial spacing ratios less than 4.0. This is evident in Figures 4.22a-c where the RHS upflow pair illustrated is produced with an initial spacing ratio of 3.0. Here the motion away from the wall is dramatically reduced. The convective influence of vortex 2 (whose core vorticity can be seen on the left side of Figure 4.22b) is

now being felt on vortex 3. The result is that vortex 3 is being pulled in opposite directions, towards the wall by vortex 2, and away from the wall by vortex 4. Where vortex 3 ends up depends on the strength and the distance between the individual vortices. A stagnation point in the secondary flow field above vortices 3 and 4 in Figure 4.22a indicates that vortex 2 is somewhat stronger than either vortex 3 or 4. The fat "wedge" shape seen in Figure 4.22b results, in part, from a secondary flow field of roughly equal strength on three sides (left, bottom, and right) of each vortex.

Figures 4.23a-c illustrate the entire array of four embedded vortices at Station 150. Note the high degree of symmetry between the LHS and RHS vortex pairs. The initial spacing ratio is 2.0. The downflow pair consisting of vortices 2 and 3 convect each other against the wall and are held in proximity by the "pushing" of the exterior vortices 1 and 4. Vortices 1 and 4 are most strongly influenced by their upflow partners and so tend to move up away from the wall. The peculiar secondary flow field that results produces the highly elliptical "lung" shaped interior vortex pair seen in Figure 4.23b. The exterior vortices, being relatively unconfined, are mostly circular in shape.

In addition to the observations made above, there are several other trends in the structural development of the embedded vortices that should be mentioned.

In particular, the relatively large decrease in vortex circulation between Stations 74 and 150 for vortices produced in arrays with initial spacing ratios of 2.0 or 3.0 warrants a closer look. Refer to Figure 4.24. Although this decrease may be due, in part, to the confinement of some vortices near the wall (where circulation loss by wall friction occurs), comparison with the case of the single embedded vortex suggests that some other loss mechanism is involved. This may be a proximity effect associated with the neighboring vortices. This idea is explored in Chapter 5.

The convective effects of the secondary velocity field on the primary vorticity is some-

times referred to as "vorticity spreading". The peak vorticity, like the primary vorticity field in which it is embedded, is affected by vorticity spreading. The spreading of the primary vorticity field enhances the decay of the peak vorticity; the amount of decay increasing with the proximity and strength of the neighboring vortices. This is indicated in the listing of the descriptive parameters in Table 4.2 and 4.3 where the amount of decay of the peak vorticity between Stations 74 and 150 increases with decreasing initial spacing ratio.

Contours of streamwise velocity ratio u/U_∞ at Station 150 (Figures 4.18c-4.23c) show that the streamwise velocity deficit in the vortex core, which was strongly evident at Station 74, has nearly disappeared at the downstream measurement station. As was the case at Station 74, a strong correlation exists between the strength of the downwash or upwash regions between vortices and the local thickness of the boundary layer.

Other Array Results at Station 150

Table 4.3 lists descriptive parameters for vortices produced in counter-rotating arrays with N_v greater than 4. The objective here is to examine how the presence of additional vortices influences the structure of the two interior pairs as illustrated in Figures 4.18-4.23.

Figures 4.25a-c illustrate an upwash vortex pair produced from a six element vortex generator array with an initial spacing ratio of 6.0. This pair corresponds to the pair illustrated in Figures 4.19a-c. Now, however, there is an additional counterclockwise vortex to the right of this pair, out of the measurement domain in Figure 4.25. The relative displacement and shapes of the vortices in Figure 4.25 are very much like the ones illustrated in Figure 4.19. The vortices in this pair are somewhat fatter than their counterparts from the four element array indicating that the additional vortices may exert a slight "packing" effect which forces the interior pairs to a closer proximity. For the most part, though, the additional vortices on the array exterior do not influence the development of the interior

pairs to any great extent. This is mainly because these exterior vortices do not come into close proximity to the interior pairs during any stage of downstream development. The wall convects vortices 2, 3, 4, and 5 together in upflow pairs, but drives vortices 1 and 6 along the wall away from these interior pairs.

The implications for arrays with N_v greater than 6 are evident. When the initial spacing ratio is between 4.0 and 7.0 the vortices pair off as they develop downstream. Regions of upflow between adjacent vortices in the pair are strengthened as the vortices draw together under the convective influence of the wall. Downflow regions between pairs weaken as the vortex pairs separate from each other. The smaller the initial spacing ratio (in this range) the further the vortices in the upflow pairs convect each other away from the wall as they move downstream.

The effect of additional counter-rotating vortices on the pair illustrated in Figure 4.22 (initial spacing ratio 3.0) can be seen in Figures 4.26 and 4.27. Figure 4.26 shows both interior pairs. A additional vortex exists to the left and right of these pairs, just outside of the measurement domain. Vortex no. 3 is stronger than either vortex 4 or 5 and a stagnation point in the secondary velocity appears above the RHS upflow pair in Figure 4.26a just as it does in Figure 4.22a. Vortex 5 in Figure 4.26 is slightly closer to the wall than vortex 4 in Figure 4.22. The addition of 3 counter-rotating vortices to the left and right of the two interior pairs results in the array illustrated in Figures 4.27a-c. The distance between the upflow vortex pairs in Figures 4.27a-c is less than the corresponding distance in Figures 4.26a-c. The increased proximity between pairs seems to be the only significant result of increasing N_v for arrays with an initial spacing ratio of 3.0. The vortex shapes and positions relative to the wall are not dramatically changed by increasing N_v. Although the vortices still pair off into identifiable upflow pairs, neighboring pairs of vortices are close enough so that the strength of the downflow regions between vortex pairs is similar in

magnitude to the upflow regions between the vortices in any such pair. In spite of the close proximity between vortices in an upflow pair, the vortices do not convect each other to the same distance away from the wall that occurs for initial spacing ratios of 4.0 or 5.0. Again, this is a result of the nearby convective influences of the neighboring pairs.

Dramatic losses in peak vorticity and circulation were observed at the downstream station for vortices in arrays produced with initial spacing ratios of 2.0 or 3.0. If the vortex generators were set to produce initially weak vortices in an array with a spacing ratio of 2.0 or 3.0, would observations at the downstream station reveal definable vortex structures? If not, what would be the nature of the vorticity field? To investigate these questions a set of 4 vortex generators was cut down to the size diagrammed in Figure 3.14. The height ratio is $h/\delta = 1.0$. These 4 smaller blades were mounted in a counter-rotating configuration and data was collected at Station 150. The results appear in Figures 4.28a-c and 4.29a-c.

Figures 4.28a-c illustrate the resulting vortex array produced with an initial spacing ratio of 3.0. The entire array of 4 vortices is captured. Each vortex in this array maintains a distinct identity and is similar in appearance to the arrays produced with the larger blades and $S/\delta = 3.0$.

Figures 4.29a-c illustrate the small blade vortex array produced with an initial spacing ratio of 2.0. Three vortices and a part of the fourth are visible in the measurement domain in Figures 4.29a-b. A stagnation point in the secondary flow appears between the two stronger CCW vortices in Figure 4.29a. Below this stagnation point is what appears to be a "lump" in the secondary flow field. Examination of Figure 4.29b reveals this lump to be a remnant of the interior CW vortex, vortex no. 2. It appears as if vortex 1 (or possibly both vortices 1 and 3) has distorted and spread the core vorticity of vortex 2 to the extent that no discernible vortex structure for no. 2 now exists at the downstream measurement station. The measurement domain of Figures 4.29a-c was origially intended to show all four

vortices, however the apparent breakup of the interior CW vortex has given the entire array a convective shift (due to the stronger CCW vortices) to the right, taking vortex 4 partially out of the picture.

Surface Static Pressure Results

Static pressure variation on the splitter plate flow surface occurred in both the x and z coordinate directions. The streamwise variation in surface static pressure was the same with or without the embedded vortices. Refer to Figure 4.5. Measurable spanwise gradients in surface static pressure occurred at only two streamwise locations and only in the presence of vortex generators and/or embedded vortices. At the spanwise row of taps located at Station 66 sharp peaks in static pressure were recorded. Refer to Figure 4.30. Figure 4.30 is a plot of the surface static pressure variation at Station 66 for the case of a single embedded vortex. The spanwise region affected is very narrow, surrounding surface static pressure is identical to the flat plate value. The z location of the peak pressure coincides with the location of the vortex generator trailing edge. This spanwise variation in surface static pressure is likely the result of a wake effect occurring in the immediate downstream vicinity of the blade. If it were due to the secondary flows of an embedded vortex, a corresponding drop in static pressure below flat plate values would also be expected and would coincide with the location of the strongest surface crossflow. At the spanwise row of taps located at Station 81 a slight spanwise variation in static pressure occurs. Refer to Figure 4.31. These variations in surface static pressure are most likely due to the presence of a vortex, the dip in pressure coinciding with the expected location of the vortex crossflow. The rapid decay in strength of the vortex secondary flow is apparently the reason that spanwise variations in the surface static pressure are not recorded downstream subsequent to Station 81.

Heat Transfer Results

Contour lines of heat transfer coefficient, h_x, are presented for four test conditions in Figures 4.32-4.35. Each contour line i represents a different value of h_x :

$$h_{xi} = q_{wi}/(T_{wx} - T_r),$$

where T_{wx} is the color calibrated temperature of the wall, 315.9 K, and q_{wi} is the wall heat flux required to generate the contour line.

Figure 4.32 is the heat transfer coefficient plot for a single embedded vortex. The vortex tracks across the heated surface, following a slightly curved trajectory in the (x, z) plane. The path of the vortex is visualized most easily by following the high density region of contour lines eminating from the location of the vortex generator trailing edge. This high density region represents a steep, mostly spanwise, gradient in heat transfer coefficient, steeper than the streamwise gradient imposed near the leading edge of the heated surface by the effect of the unheated starting length. (Compare Figure 4.32 to Figure 4.6). The steep spanwise gradient in h_x corresponds to (roughly) the track of the vortex, and as such, represents the boundary between a "hot zone" (below the track in Figure 4.32) and a cool zone (above the track) on the heated surface. The hot zone results from relatively low values of h_x occurring in the upwash region of the vortex. Here, as noted before, the local boundary layer is thickened. Heat transfer coefficient peaks in the downwash region of the vortex where the boundary layer is correspondingly thinner.

The sharp waviness in the contours in the immediate downstream vicinity of the vortex generator trailing edge is a peculiar feature of the plot that is not easily explained in terms of a vortex-boundary layer interaction. Note that the large "dip" in the wavy shape seems to coincide in location and orientation to the vortex generator blade. This may be an

indication that it represents some sort of wake phenomena. This also was the implication of the surface static pressure results at Station 66.

The observations made above for the case of the single embedded vortex apply also to the other three cases. Figure 4.33 is a contour map of h_x for a vortex array produced with an initial spacing ratio of 4.0. The four vortex tracks visible in Figure 4.33 draw together as they proceed downstream, the corresponding vortices forming two upflow pairs as expected. The two hot zones formed in Figure 4.33 are indicative of the thickened boundary layer between the two vortices in each upflow pair. Figure 4.34 is formed with an initial spacing ratio of 3.0 and Figure 4.35 with an initial spacing ratio of 2.0.

Summary Remarks

Equally spaced vortex generator blades were used to produce arrays of counter-rotating vortices embedded in an otherwise flat plate turbulent boundary layer. The effect of the vortices on the boundary layer depends on the strength and direction of the vortical secondary flows. The strength and direction of the vortical flows depends, in turn, on the manner in which the array of vortices is structured; vortex proximity to other vortices and to the wall, and individual vortex strength and concentration are important structural parameters.

At the upstream crossplane the vortex array was composed of nearly identical vortices. The highly condensed circular cores were widely separated and equidistant from the wall.

At the downstream station the structure of the array depended on the spacing of the vortex generators. Large spacings produced vortices that tended to pair off and move out of the boundary layer. These vortices kept a large portion of their original circulation since their motion away from the wall reduced circulation lost to wall friction effects. Although the vortices still formed upflow pairs at the smaller spacings, motion away from the wall was restricted by the close proximity of neighboring upflow pairs. The vortices in these tighter

arrays tended to be weaker since they were held in close to the wall and were more strongly spread or distorted by neighboring vortices.

Peak streamwise vorticity decayed rapidly and vortex secondary flows distorted the initially circular vortex cores into the variety of elliptical shapes seen at the downstream station. Vortex and wall proximity control the strength of the secondary flows which in turn determine the extent of the distortions suffered by the vortex cores in the array.

Study	X (cm)	U_∞ (m/sec)	δ (cm)	δ^* (cm)	θ (cm)	H	u_τ (m/sec)	τ_w (Nt/m^2)	Π	Re_θ	β
Present	129	70	2.01	0.276	0.203	1.35	2.497	7.41	.52	9420	-.05
Present	150	70	2.15	0.289	0.219	1.32	2.522	7.56	.41	10370	-.15
Nikuradse	129	70	-	0.255	0.197	1.30	-	-	-	9300	-
Nikuradse	150	70	-	0.290	0.224	1.30	-	-	-	10600	-
Coles	-	-	-	-	-	1.38	-	-	-	3000	-
Pauley	66	16	1.59	0.249	0.176	1.41	0.669	-	-	1790	-

Table 4.1 - The descriptive parameters of the two dimensional flat plate boundary layer.

Vortex array initial spacing ratio.	Vortex number	Circulation (m^2/sec)	Grid estimate of peak vorticity. (sec^{-1})	Grid estimate of core center. (cms) z_c	y_c
(single)	1	0.281	29640	1.52	1.02
2.0	3	0.287	27800	1.14	1.02
	4	-0.266	-26060	2.79	1.27
3.0	3	0.269	27750	0.25	1.02
	4	-0.262	-25860	2.79	1.14
4.0	3	0.280	30280	-0.64	1.02
	4	-0.262	-23810	2.79	1.14
5.0	3	0.279	27880	-0.64	1.02
	4	-0.268	-25500	3.81	1.02

Table 4.2 - Vortex descriptors at Station 74.

Vortex array initial spacing ratio.	N_v	Vortex number	Circulation (m^2/sec)	Grid estimate of peak vorticity. (sec^{-1})	Grid estimate of core center. (cms) z_c	y_c
(single)	1	1	0.228	1440	4.06	1.22
2.0	4	1	0.112	471	-1.22	2.64
		2	-0.104	-554	0.20	1.42
		3	0.100	527	2.24	1.02
		4	-0.120	-422	3.66	2.44
3.0	4	3	0.151	536	2.84	1.02
		4	-0.146	-515	4.47	1.22
4.0	4	2	-0.223	-739	-5.49	2.44
		3	0.227	857	0.20	2.84
		4	-0.228	-902	2.03	2.64
5.0	4	3	0.239	1170	1.22	1.83
		4	-0.221	-792	3.05	1.83
6.0	4	3	0.207	693	-0.61	1.02
		4	-0.217	-902	2.24	1.22
7.0	4	3	0.201	726	-0.41	1.22
		4	-0.206	-774	3.66	1.02
3.0	6	2	0.157	538	-3.66	2.23
		3	-0.186	-841	-1.83	2.23
		4	0.153	620	3.05	1.22
		5	-0.151	-619	4.67	1.22
3.0	10	4	0.166	729	-2.64	1.42
		5	-0.145	-486	-0.81	1.42
		6	0.157	573	3.05	1.83
		7	-0.165	-670	4.67	1.83

Table 4.3 - Vortex descriptors at Station 150.

Vortex array initial spacing ratio.	N_V	Vortex number	Circulation (m^2/sec)	Grid estimate of peak vorticity. (sec^{-1})	Grid estimate of core center. (cms) z_c	y_c
6.0	6	4	0.233	1068	2.03	1.63
		5	-0.233	-978	4.67	1.63
(small blades)						
2.0	4	1	0.125	477	1.02	1.42
		2	-0.025	-299	3.05	0.81
		3	0.080	403	4.88	1.42
3.0	4	1	0.144	484	-3.66	2.03
		2	-0.134	-456	-1.83	2.03
		3	0.116	369	1.63	2.44
		4	-0.177	-629	3.25	2.44

Table 4.3 (continued) - Vortex descriptors at Station 150.

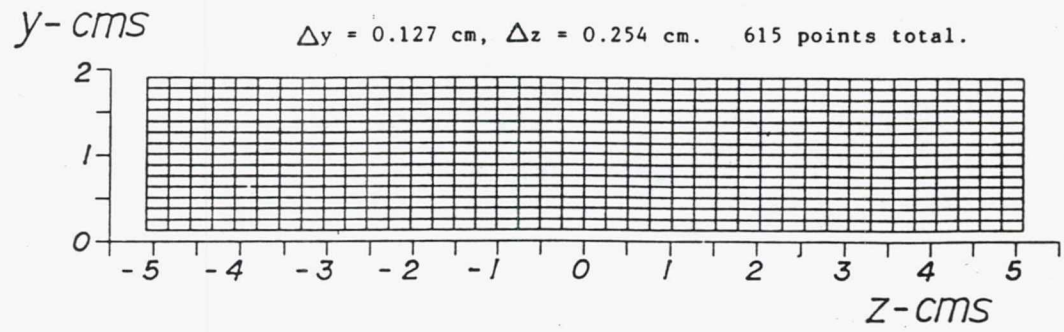

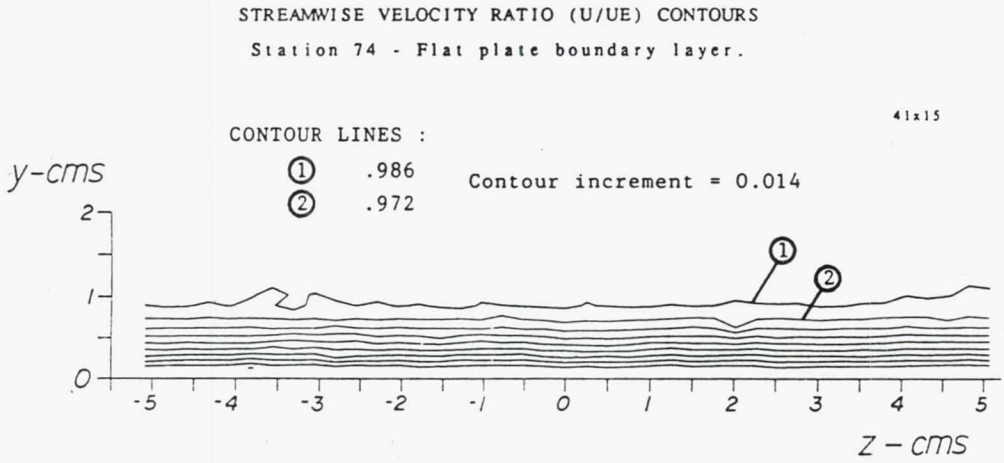

Figure 4.1a (top) - The traversing grid in use at Station 74 for probing the flat plate boundary layer. The five hole probe was used over this grid.

Figure 4.1b (bottom) - The resulting plot of streamwise velocity ratio, U/U_∞, of the flat plate boundary layer at Station 74. The freestream Mach no. is 0.2.

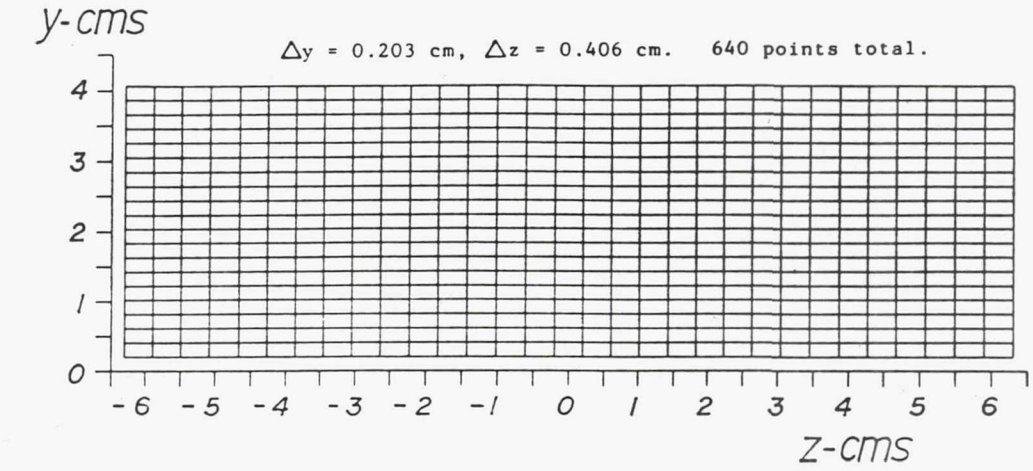

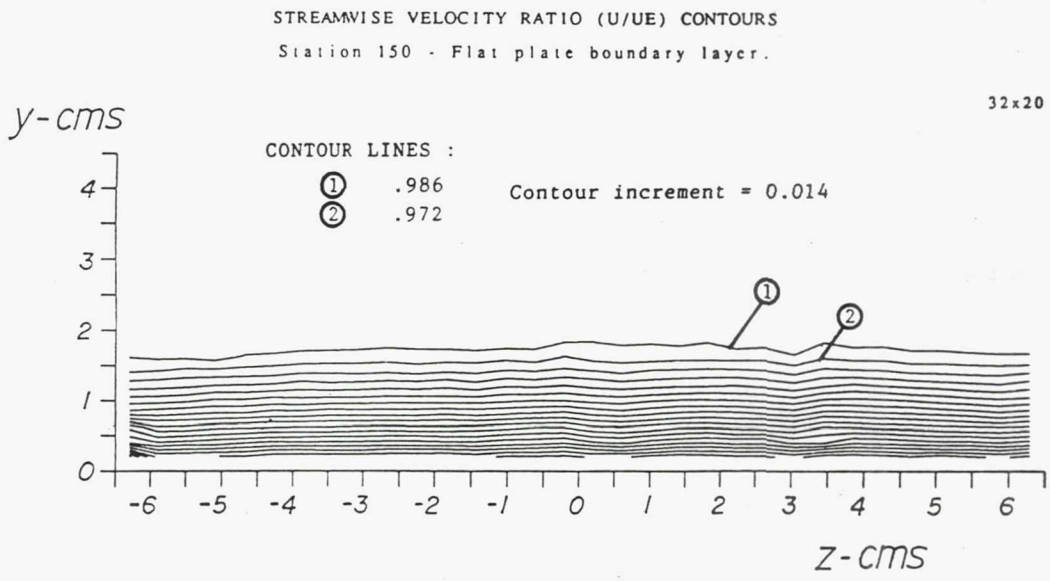

Figure 4.2a (top) - The traversing grid in use at Station 150 for probing the flat plate boundary layer. The five hole probe was used over this grid.

Figure 4.2b (bottom) - The resulting plot of streamwise velocity ratio, U/U_∞, of the flat plate boundary layer at Station 150. The freestream Mach no. is 0.2.

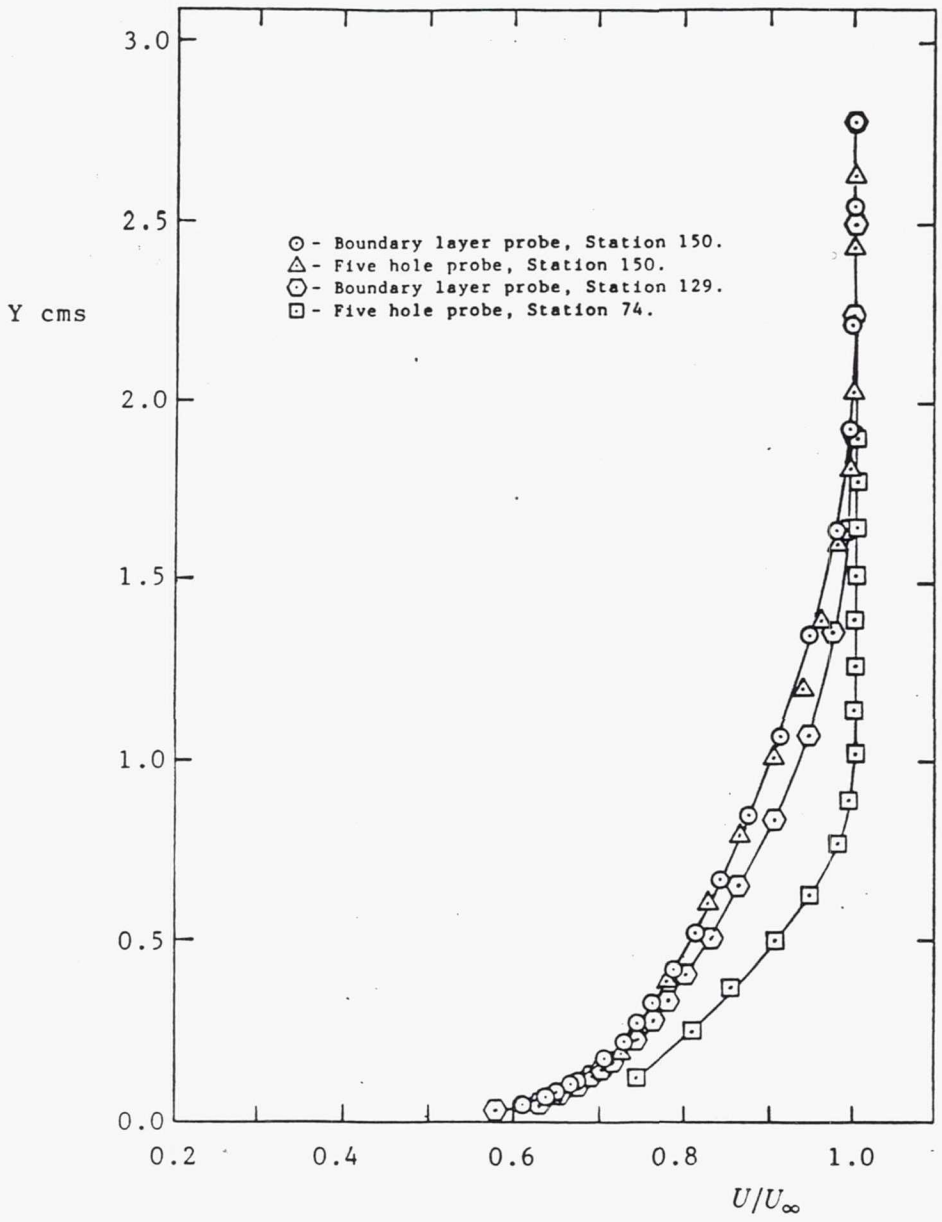

Figure 4.3 - Profiles of U/U_∞ versus y of the flat plate boundary layer. Profiles were obtained with the boundary layer and five hole probes at various streamwise locations on the splitter plate centerline (z = 0.0 cms).

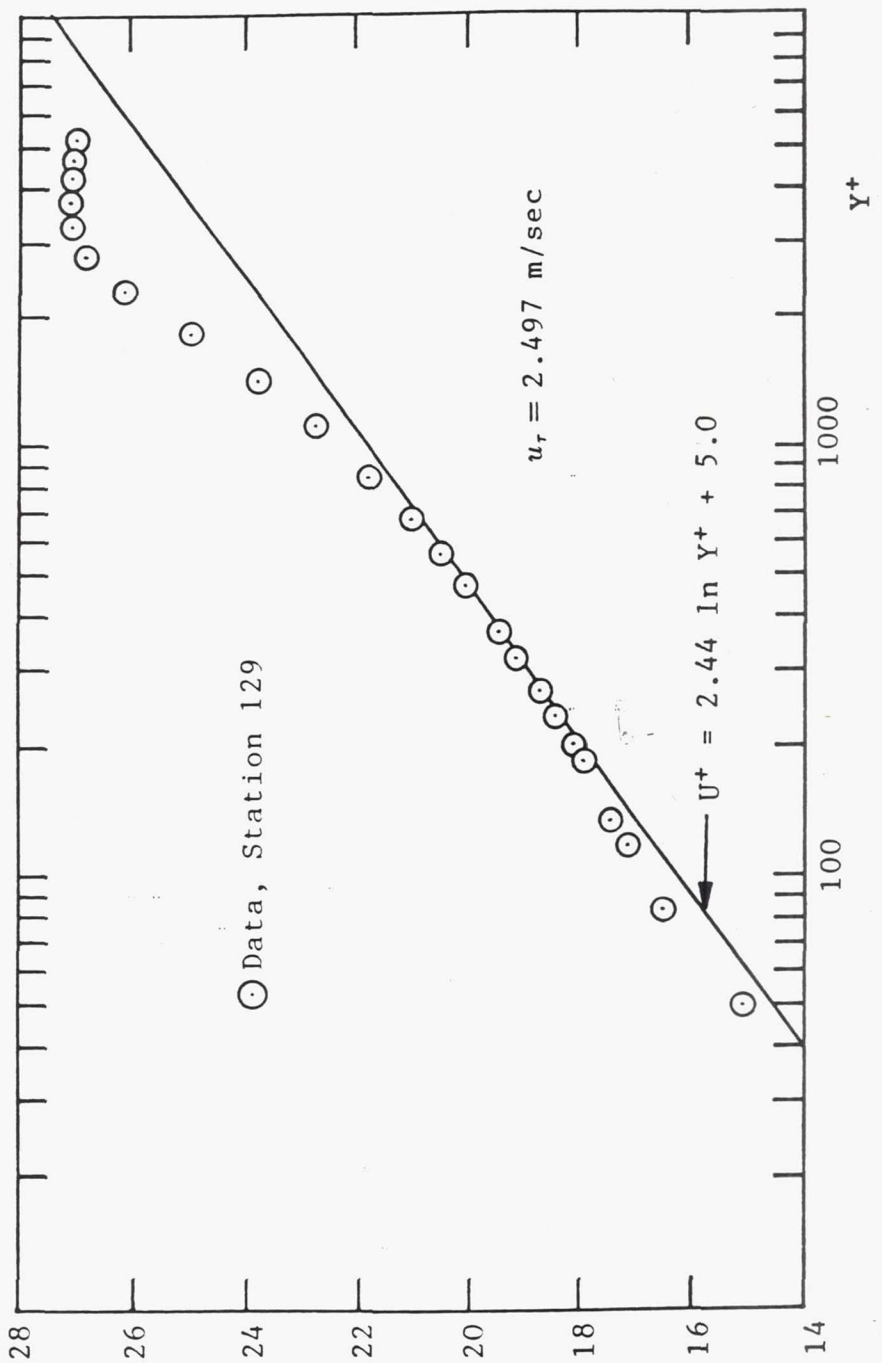

Figure 4.4a - The centerline (z = 0.0 cms) streamwise velocity profile of the flat plate boundary layer at Station 129 plotted in wall coordinates.

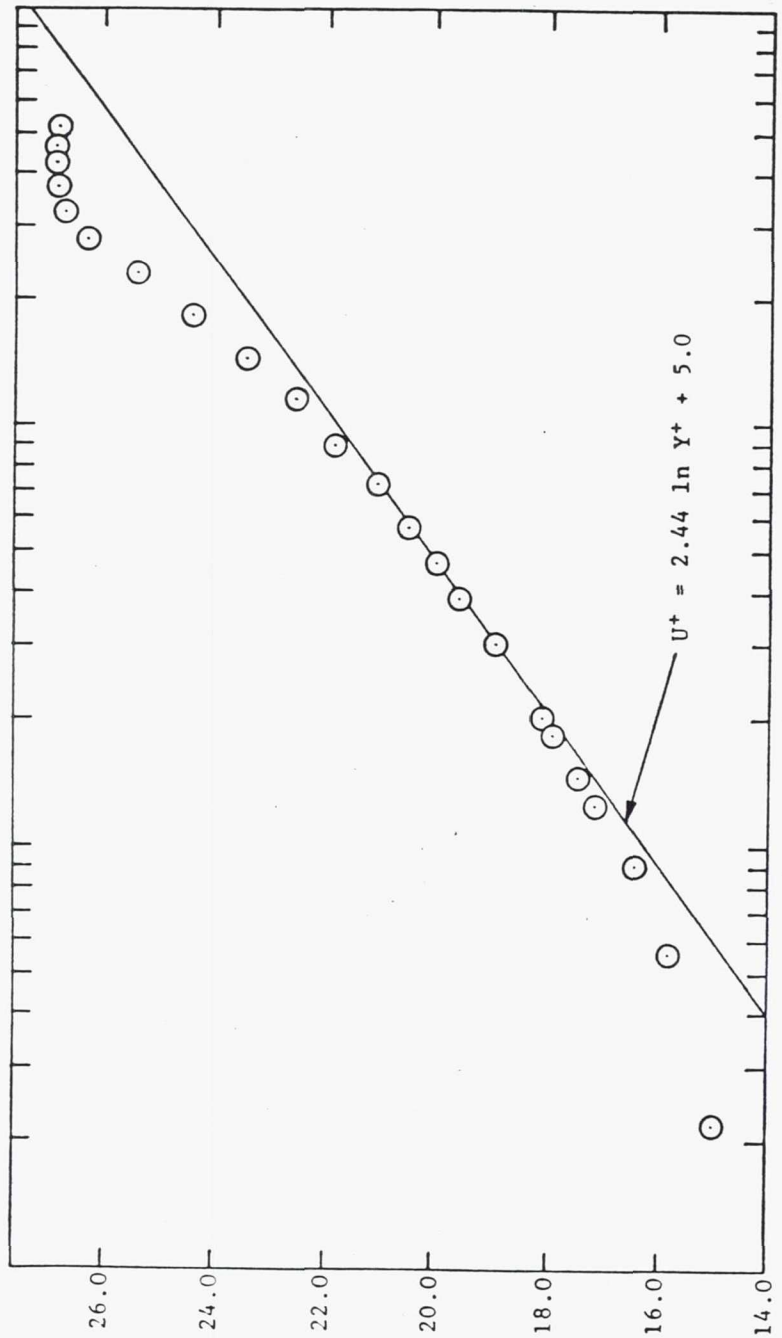

Figure 4.4b - The centerline (z = 0.0 cms) streamwise velocity profile of the flat plate boundary layer at Station 150 plotted in wall coordinates. u_τ = 2.52 m/sec.

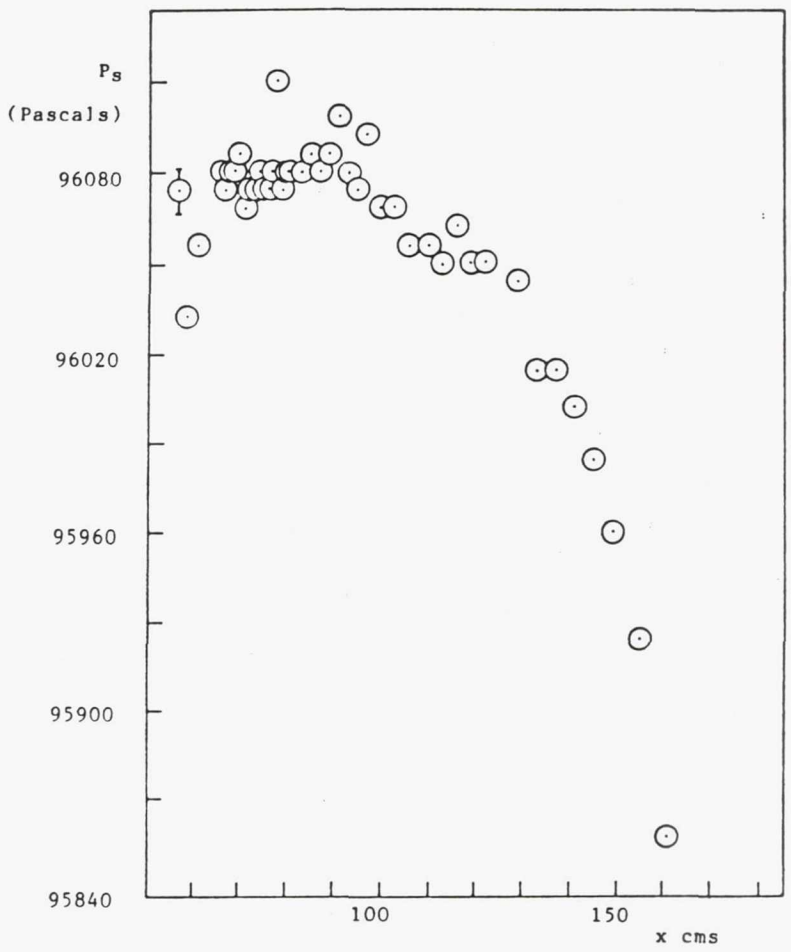

Figure 4.5 - The streamwise variation of surface static pressure along the splitter plate centerline. The Mach number is 0.2.

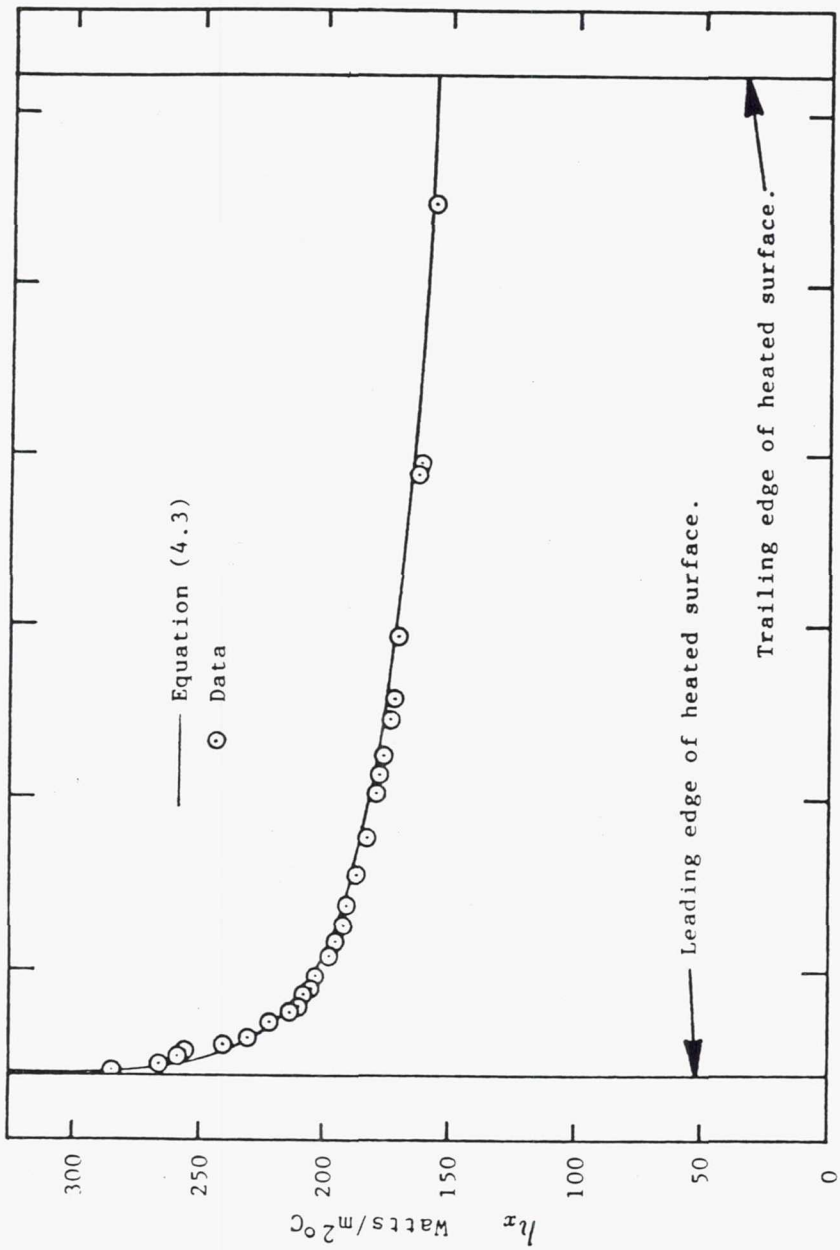

Figure 4.6 - Heat transfer coefficient, h_x, versus x over the heated flow surface. Eq. (4.3) provides the predicted behavior shown by the curved line. The small circles are data points from the flat plate test of the heated surface.

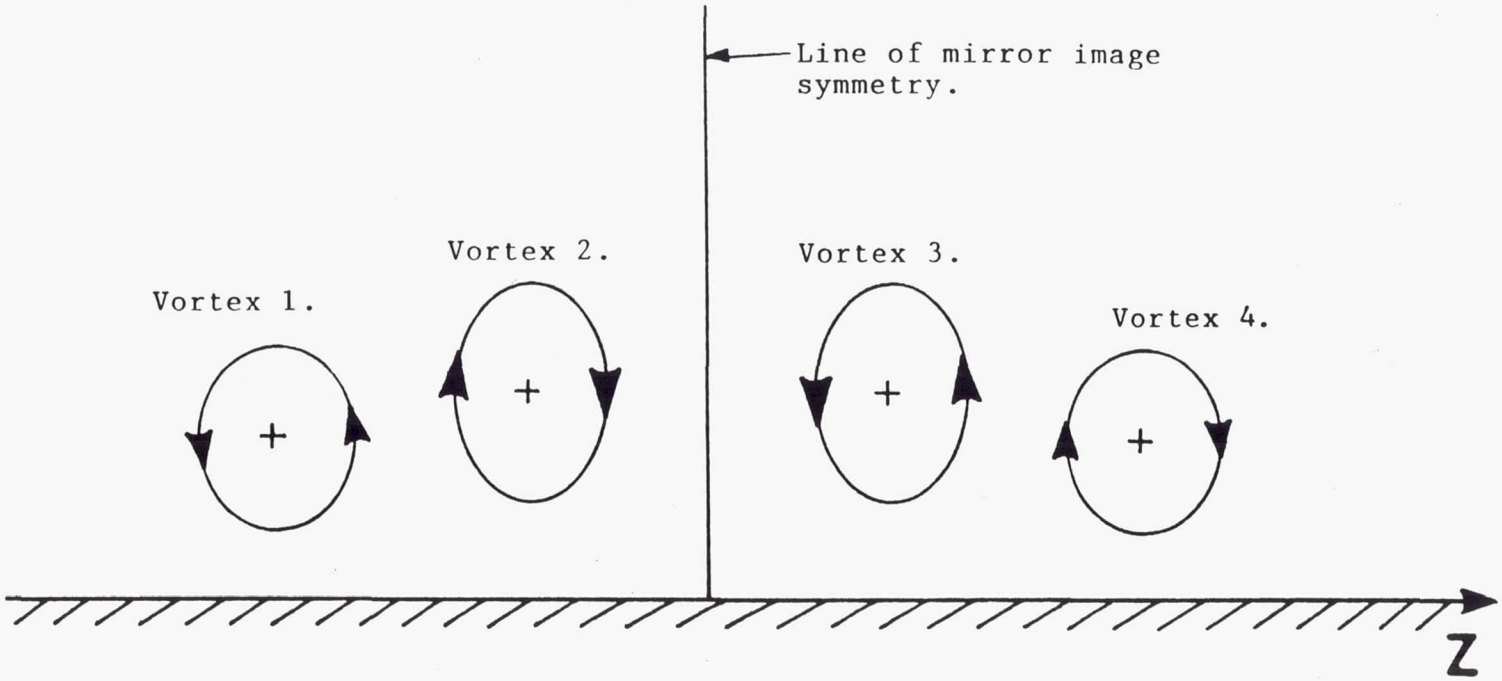

Figure 4.7 - A diagram of four embedded, counter-rotating vortices in the crossplane. This array was produced by 4 identical vortex generators set in an initially symmetric arrangement. The array has mirror image symmetry with respect to the line indicated.

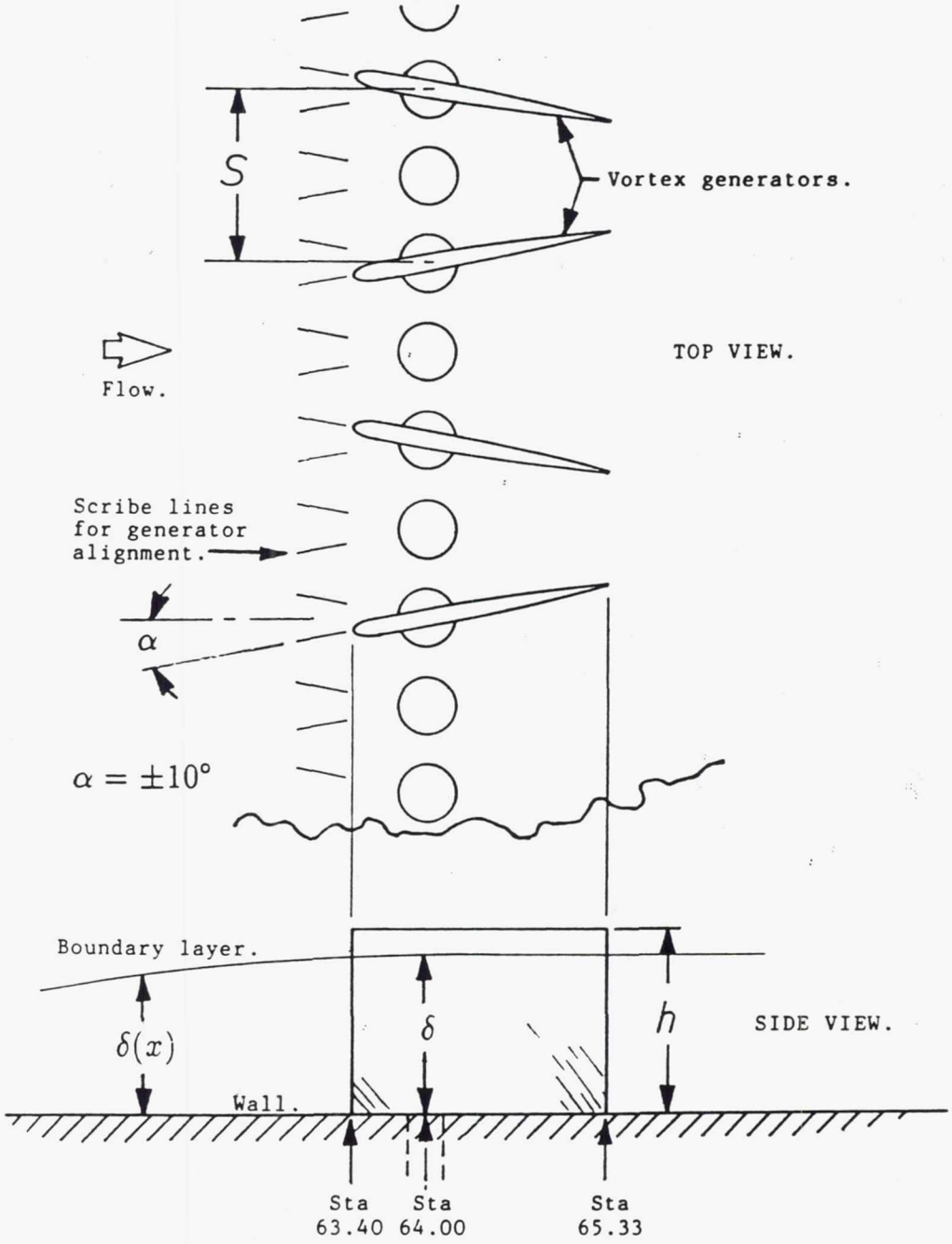

Figure 4.8 - Test condition parameters of the vortex generator array at the mounting station.

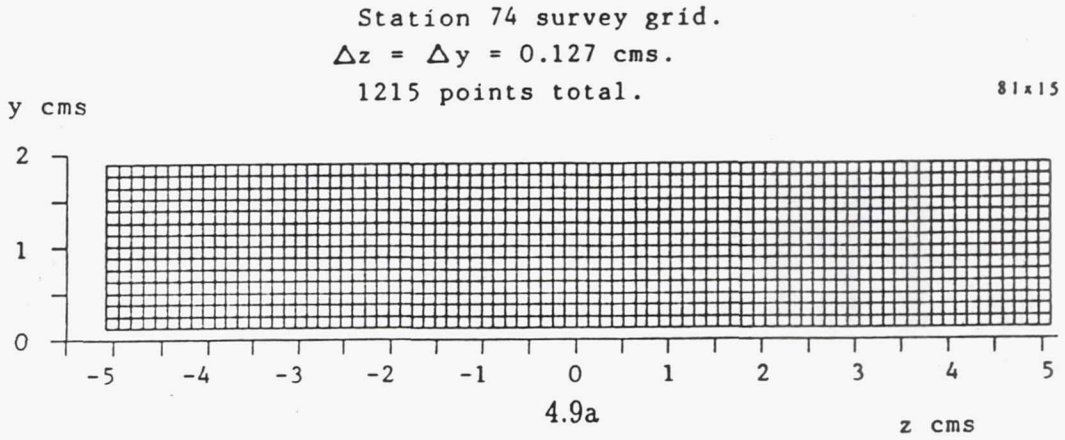

4.9a

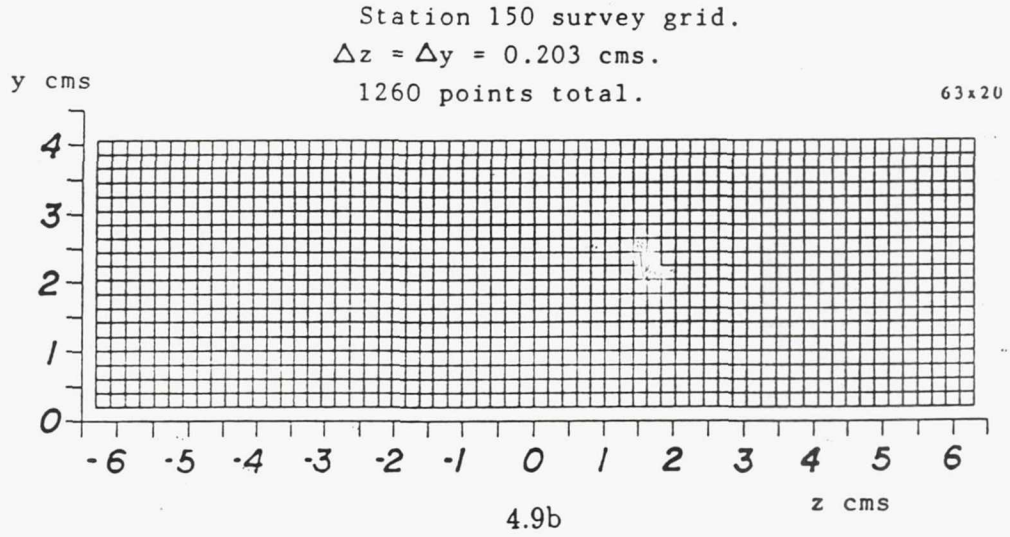

4.9b

Figure 4.9a (top) - The survey grid at Station 74.

Figure 4.9b (bottom) - The survey grid at Station 150.

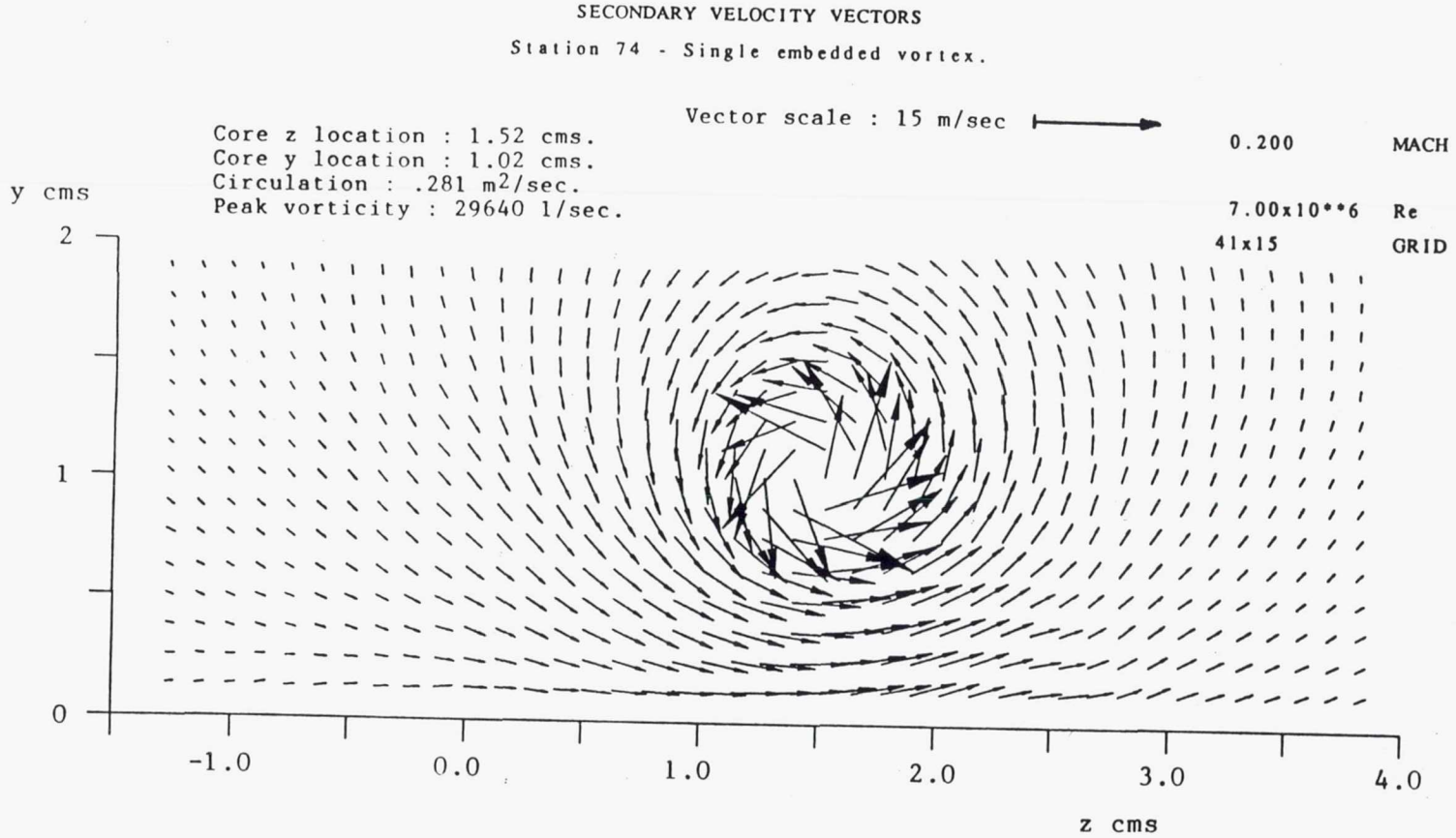

Figure 4.10a - The measured secondary velocity vectors of the single embedded vortex at Station 74.

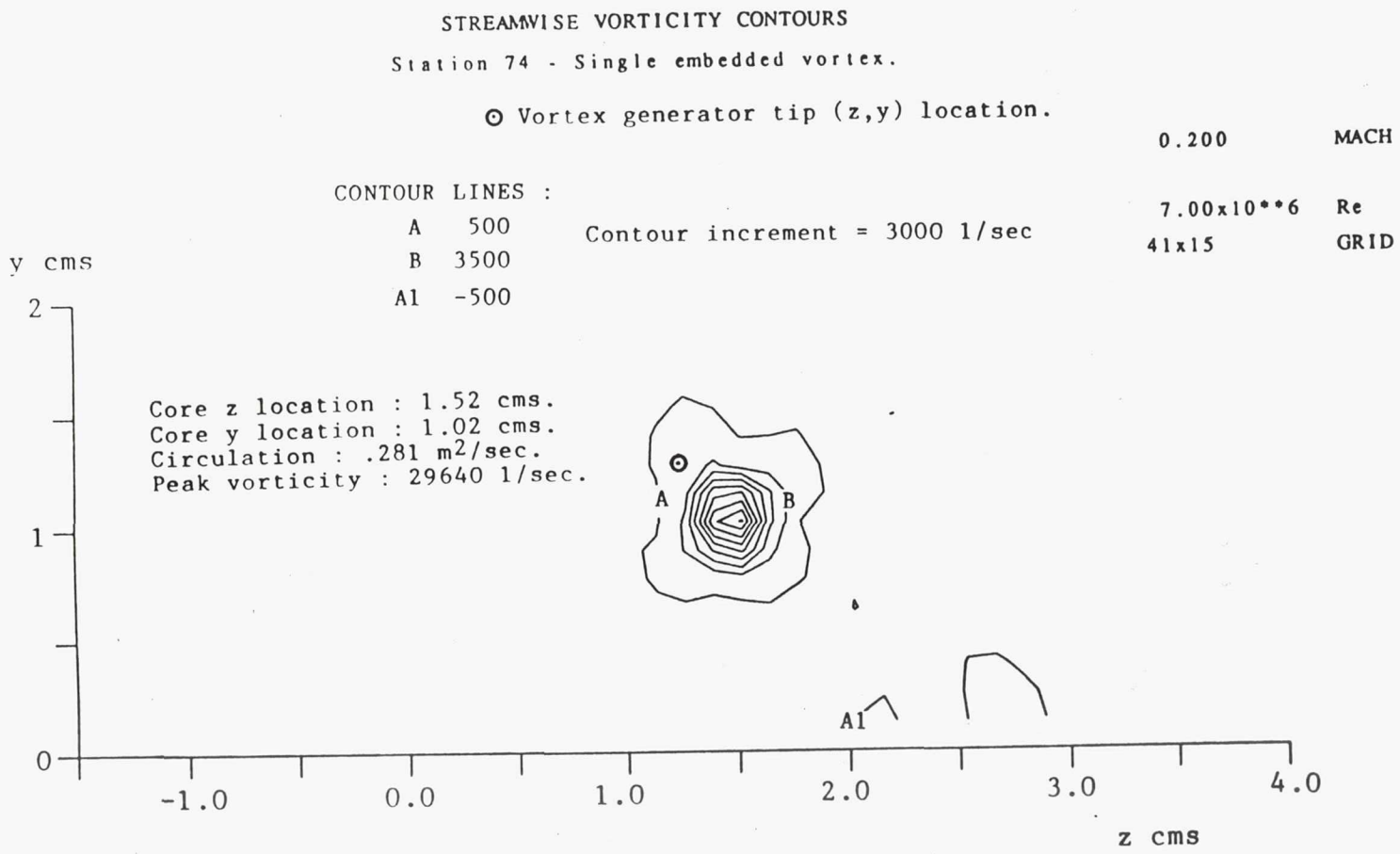

Figure 4.10b - The streamwise vorticity contours of the single embedded vortex at Station 74.

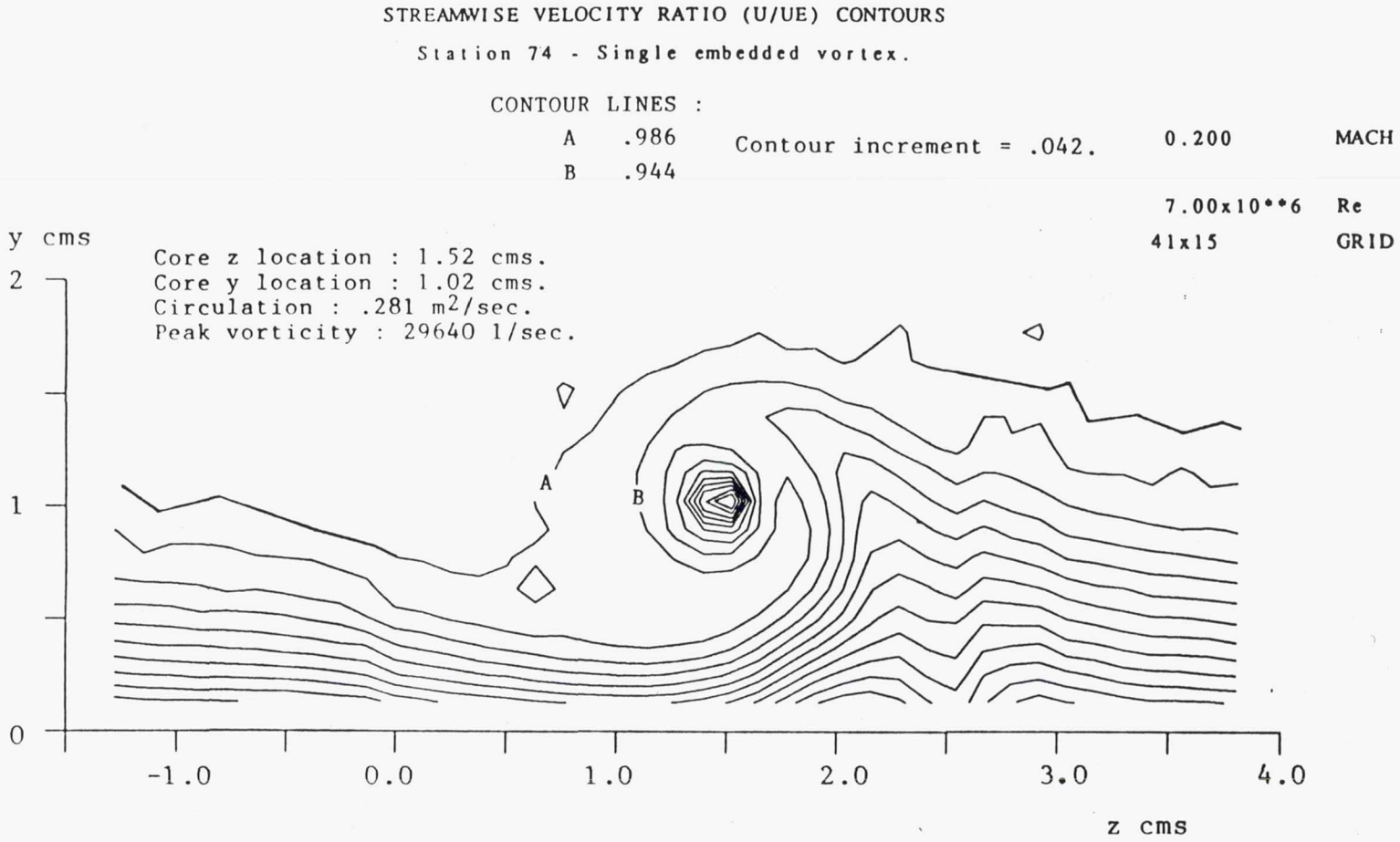

Figure 4.10c - Contours of the streamwise velocity ratio U/U_∞ of the single embedded vortex at Station 74.

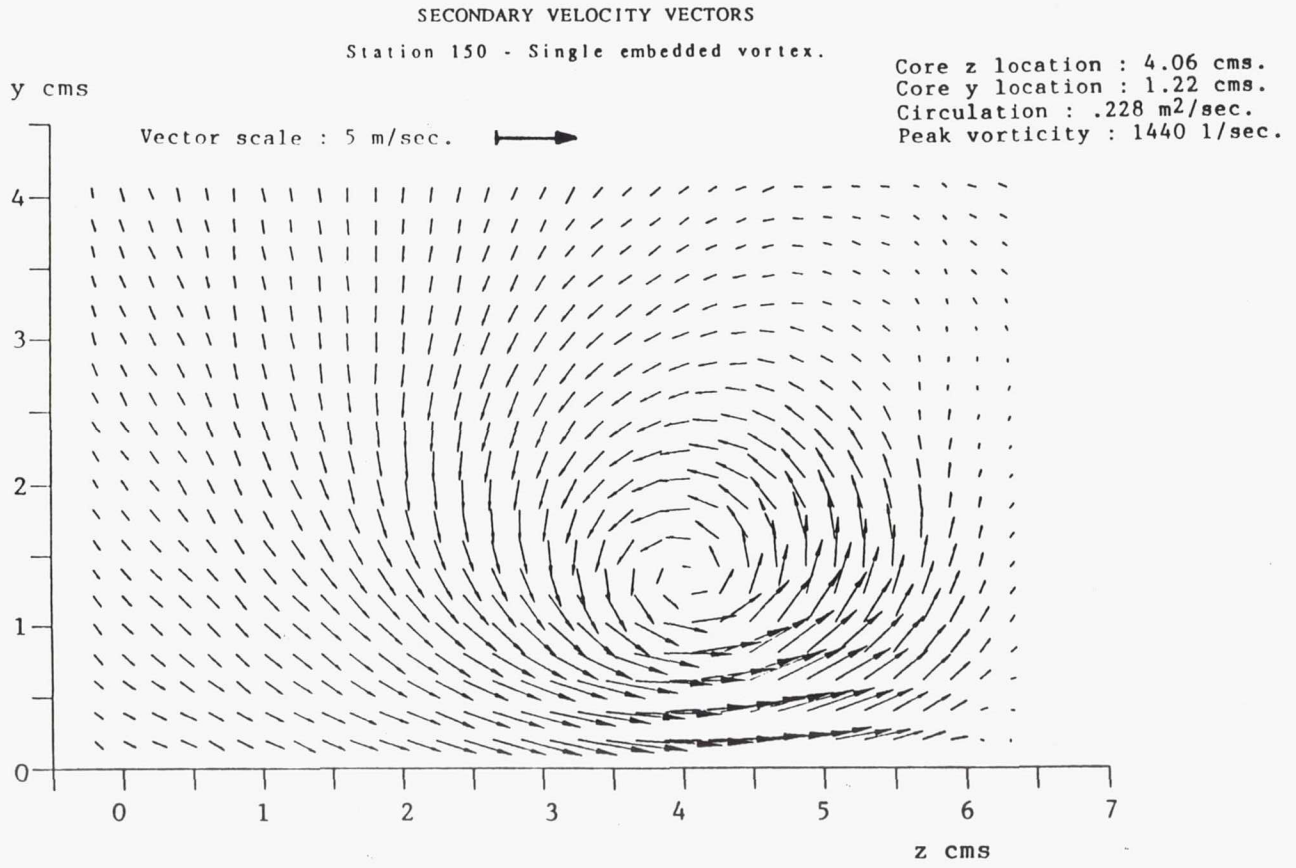

Figure 4.11a - The measured secondary velocity vectors of the single embedded vortex at Station 150.

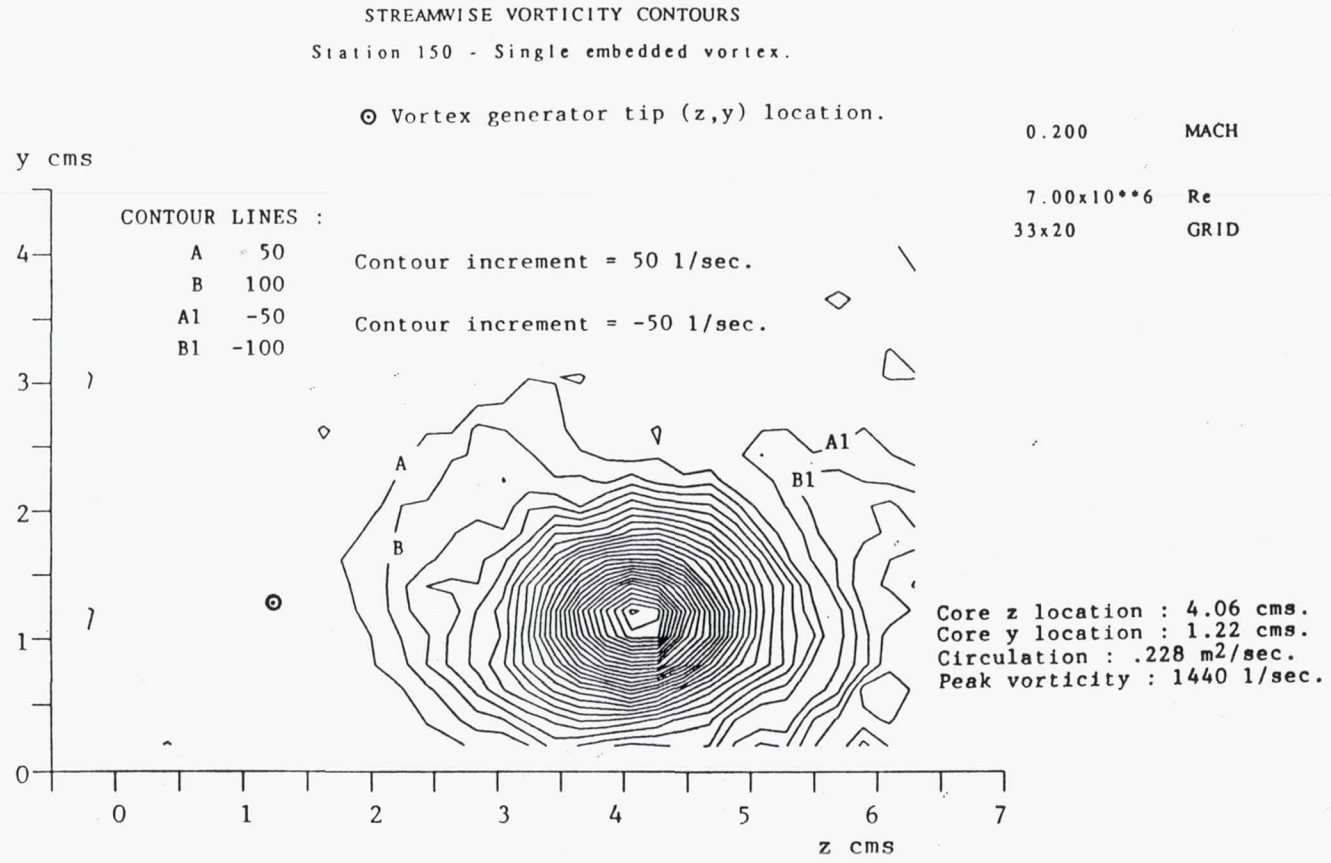

Figure 4.11b - The streamwise vorticity contours of the single embedded vortex at Station 150.

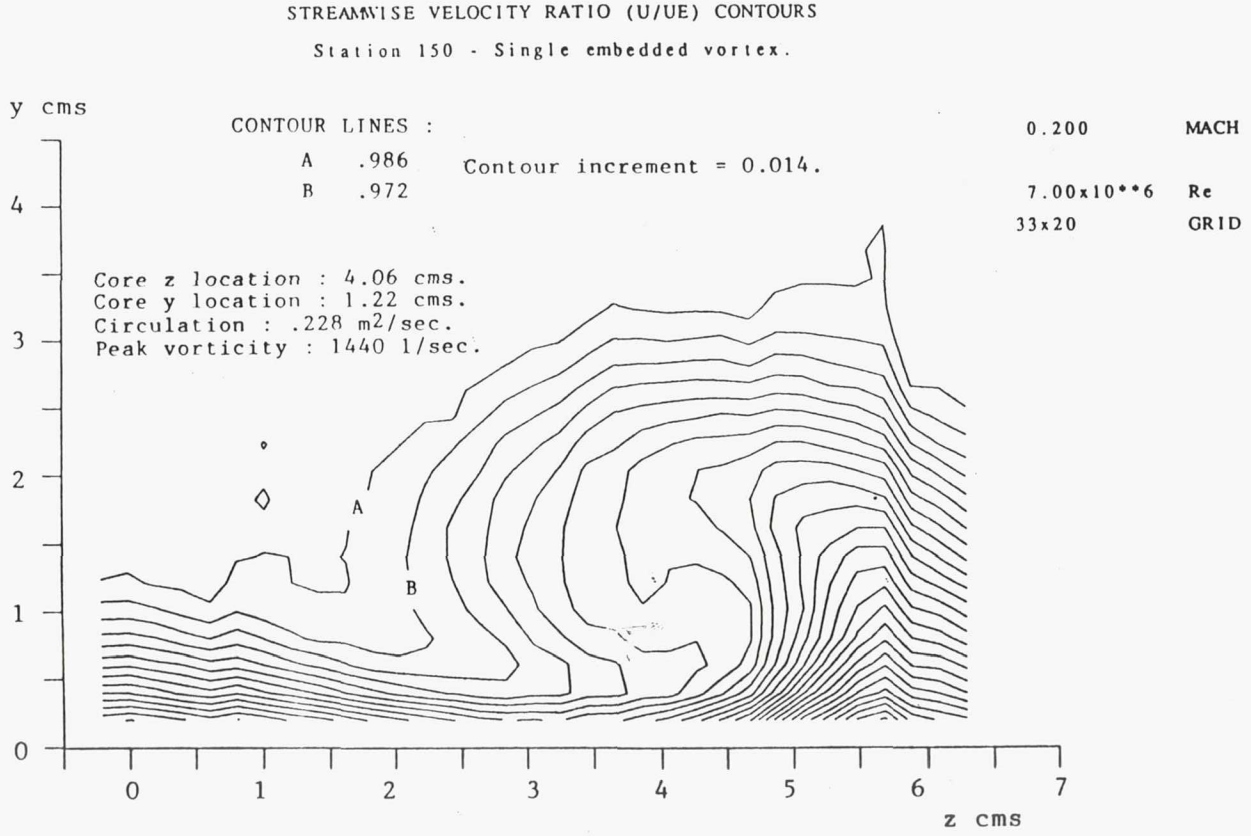

Figure 4.11c - Contours of the streamwise velocity ratio U/U_∞ of the single embedded vortex at Station 150.

4.12a

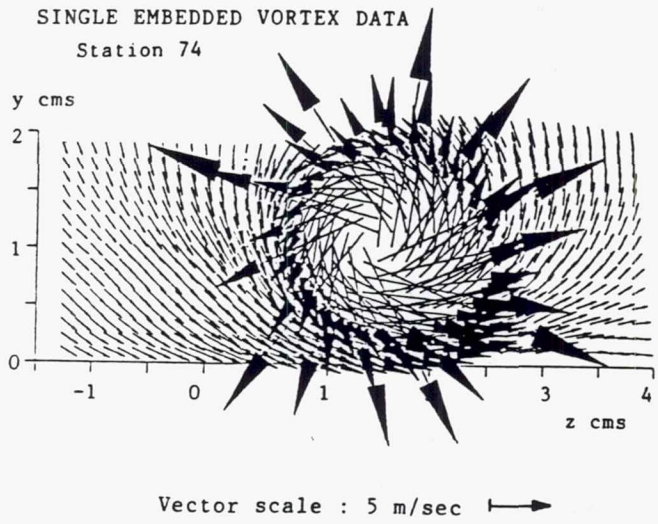

4.12b

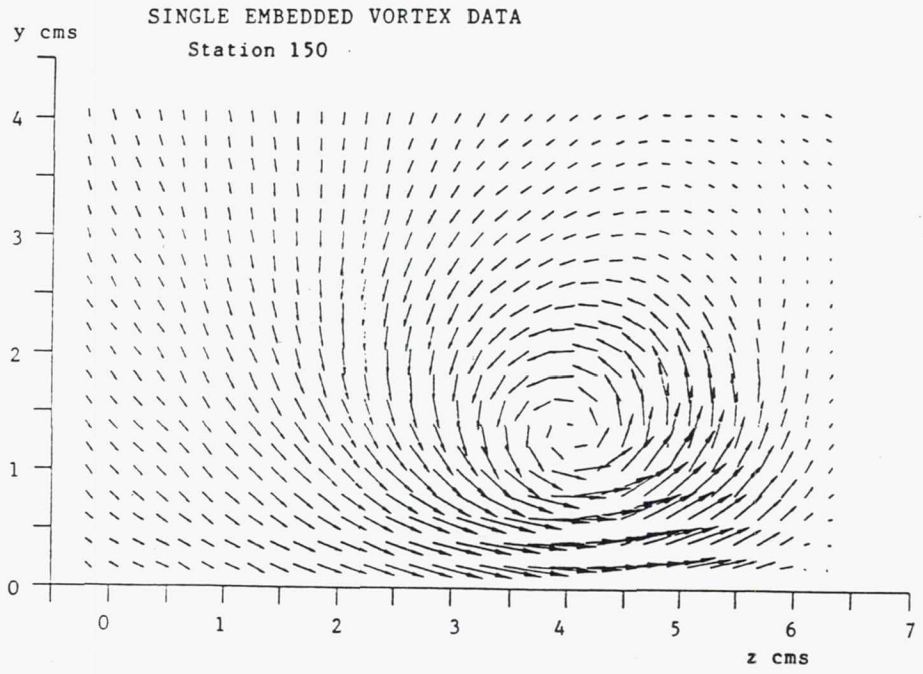

Figure 4.12a (top) - Figure 4.10a is replotted in the same vector and length scale as Figure 4.12b (bottom) to emphasize the extent to which the secondary flows have weakened between Station 74 and Station 150.

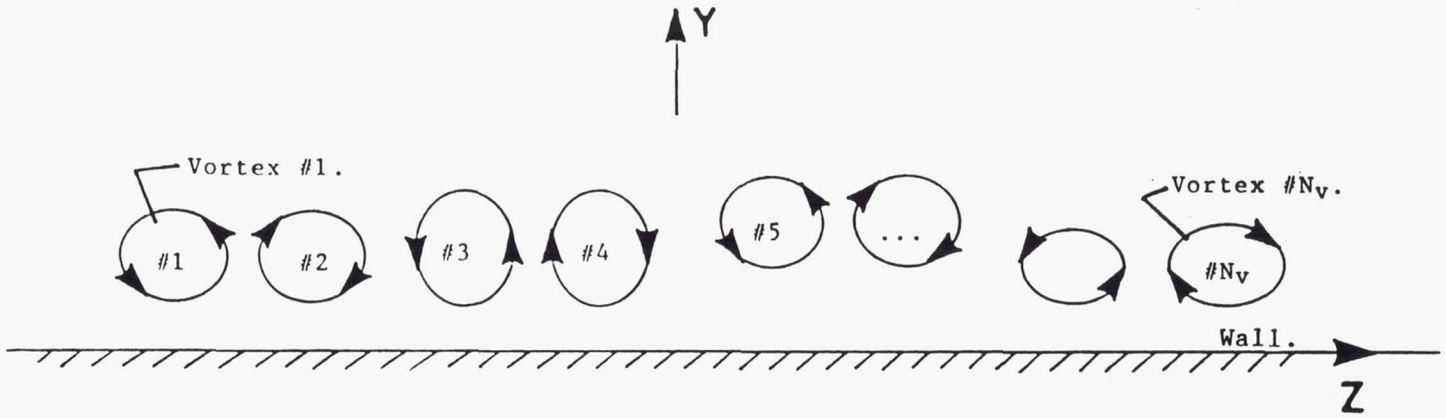

Figure 4.13 - A resulting array of N_v vortices produced by a particular setting of the vortex generators (a "test" condition).

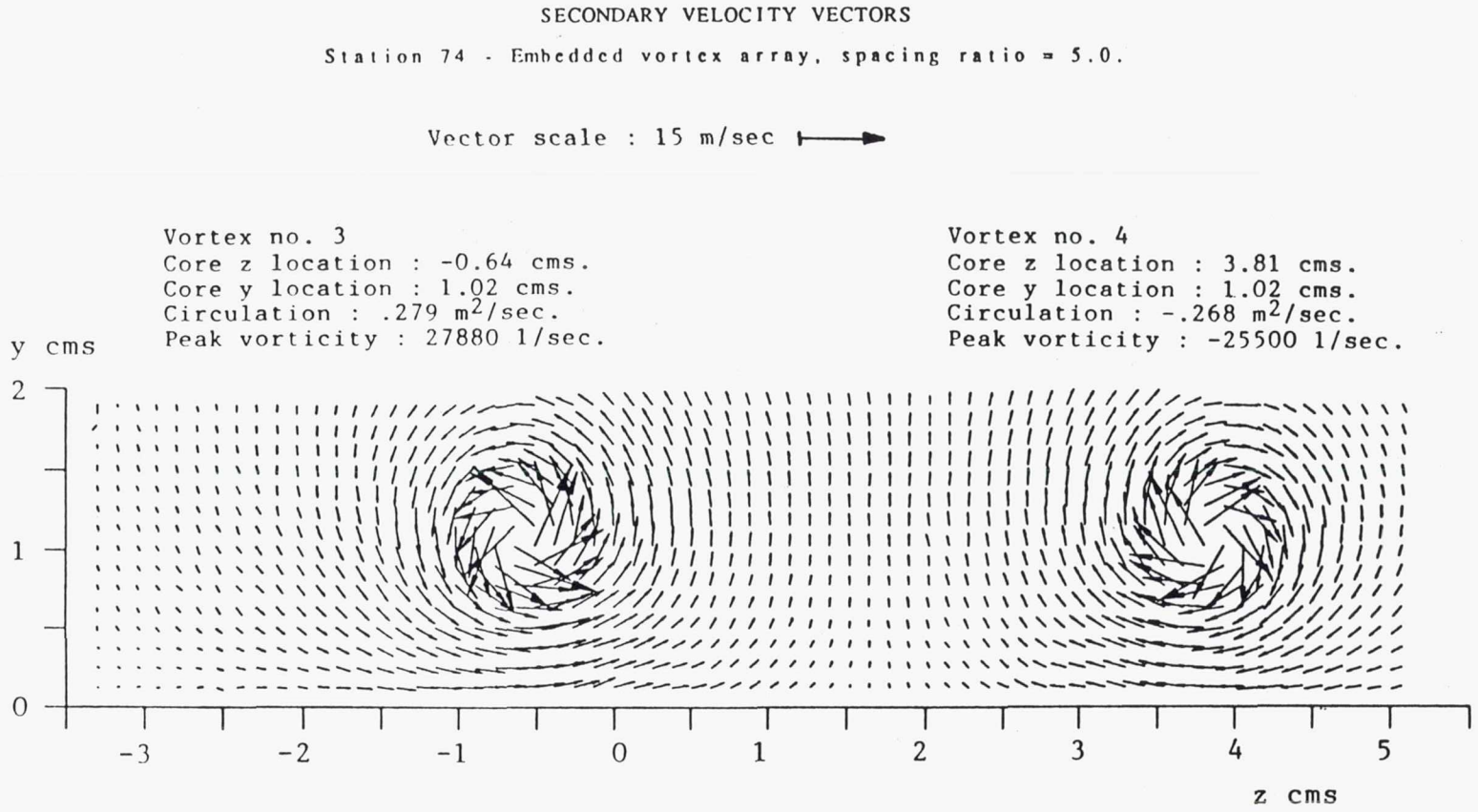

Figure 4.14a - Spacing ratio 5.0 test case, Station 74.

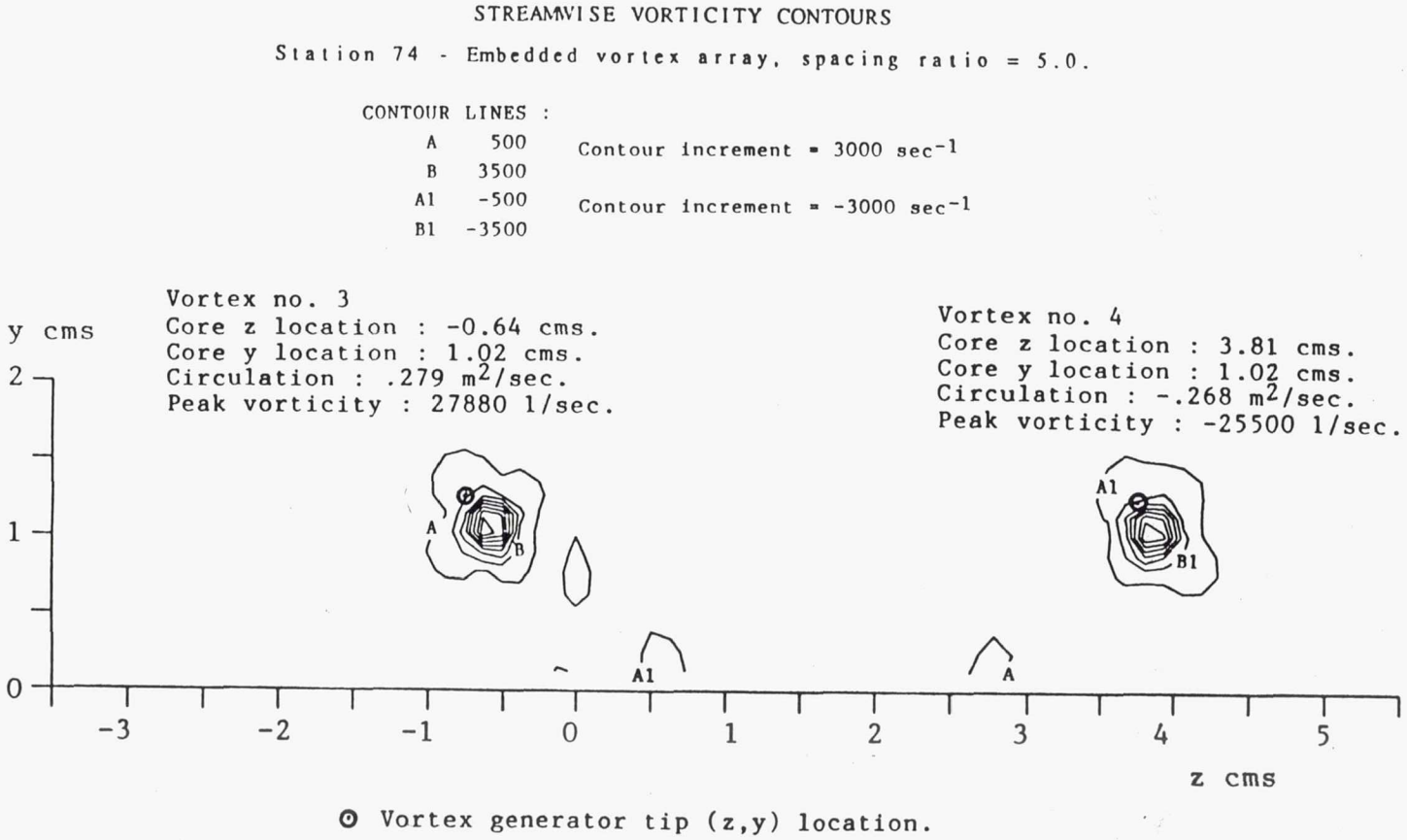

Figure 4.14b - Spacing ratio 5.0 test case, Station 74.

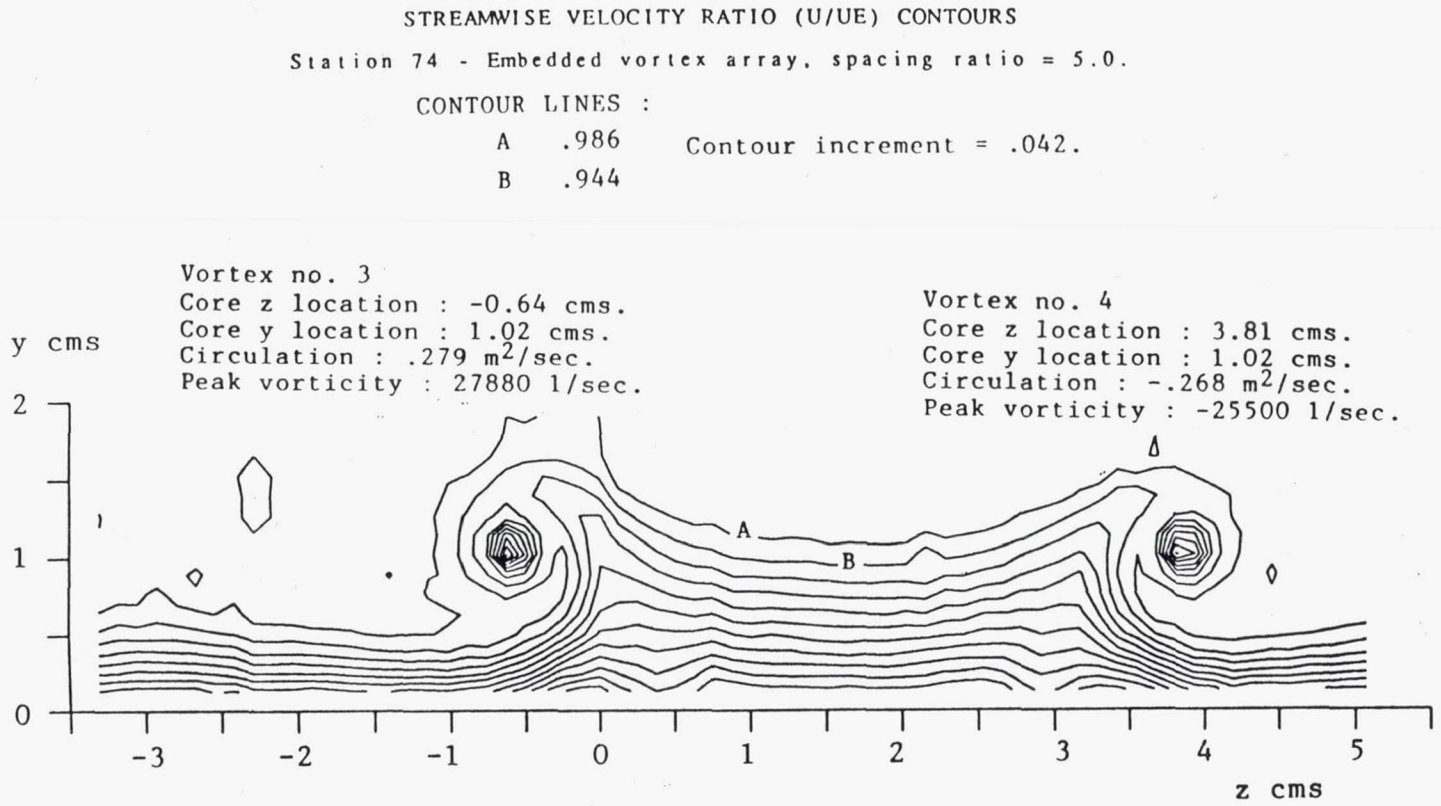

Figure 4.14c - Spacing ratio 5.0 test case, Station 74.

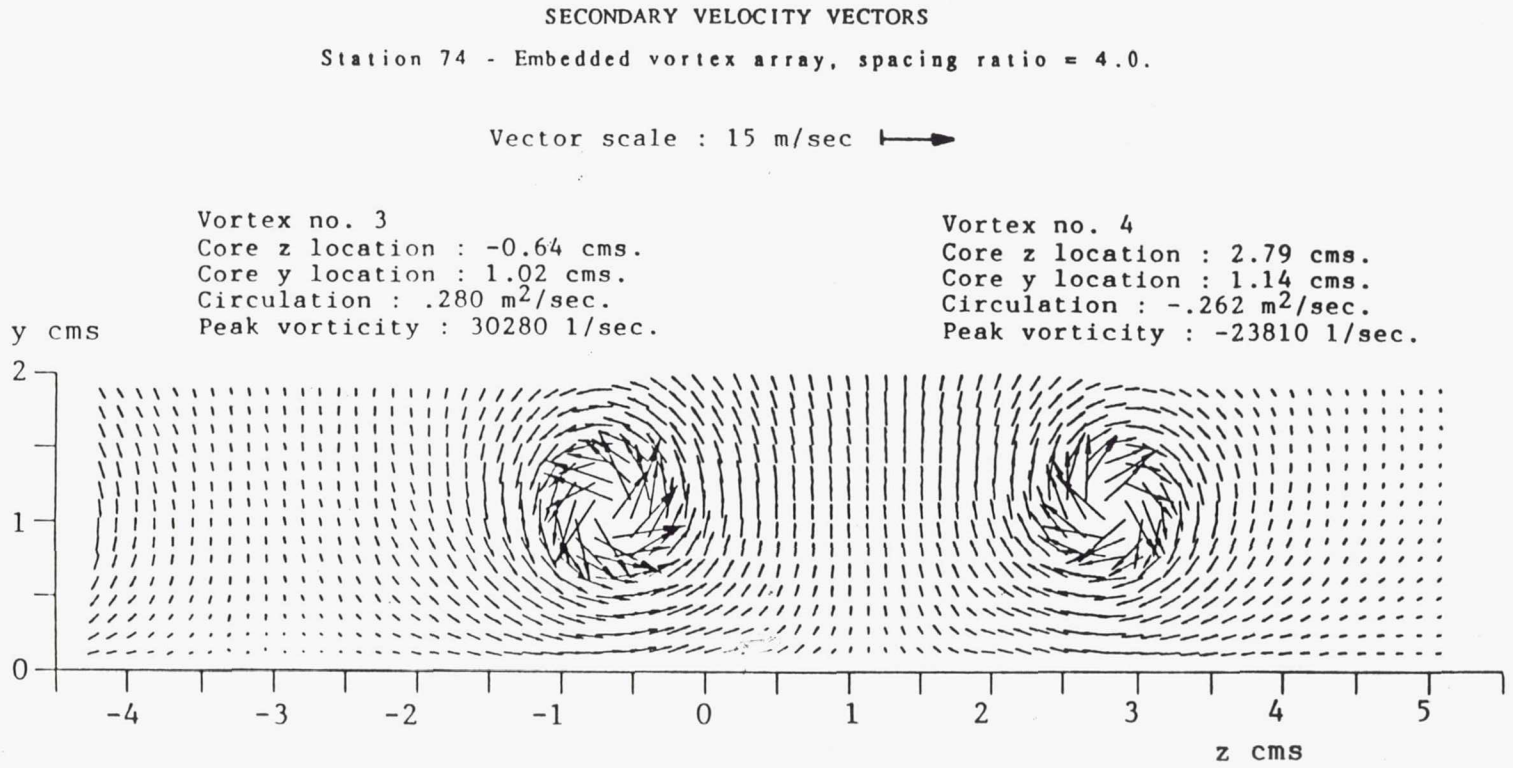

Figure 4.15a - Spacing ratio 4.0 test case, Station 74.

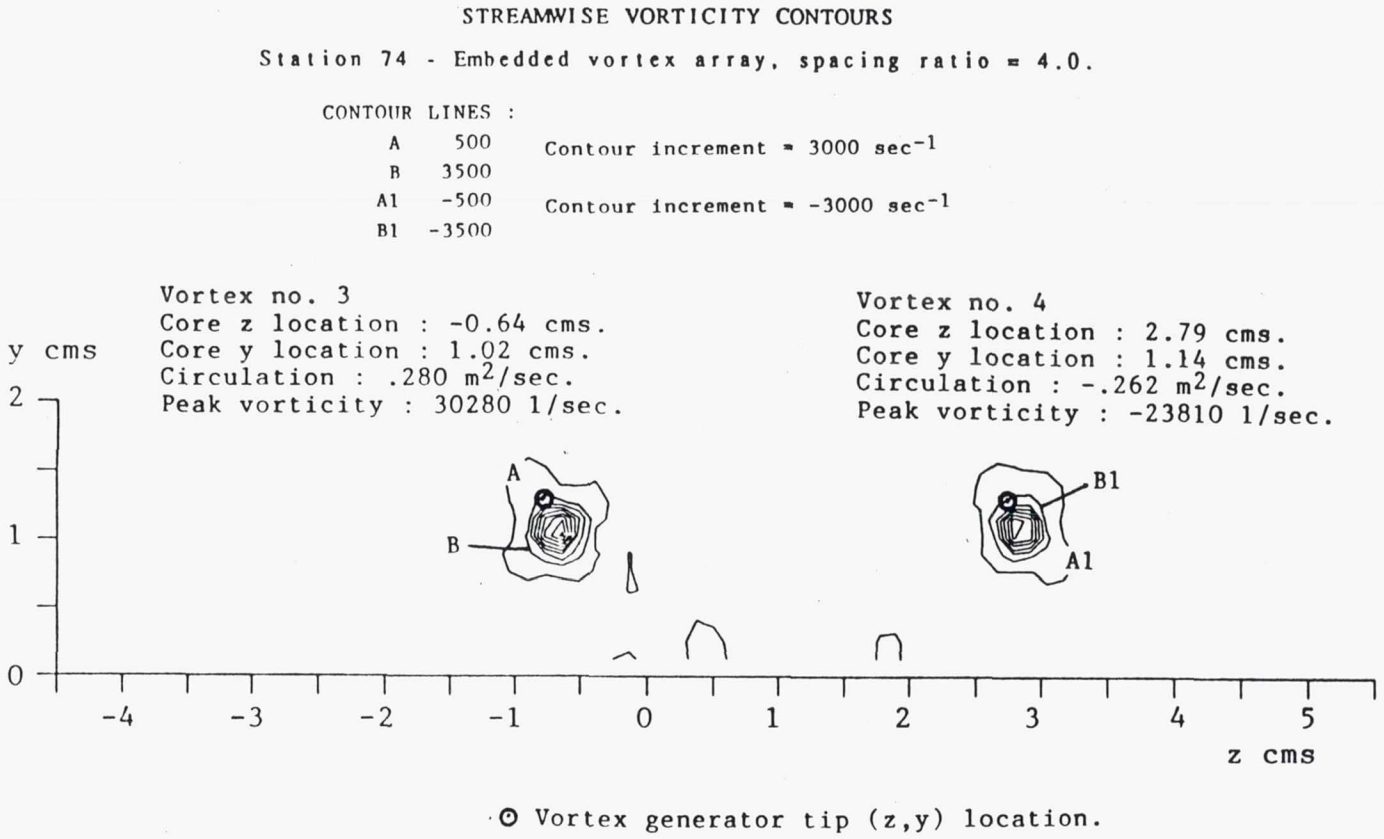

Figure 4.15b - Spacing ratio 4.0 test case, Station 74.

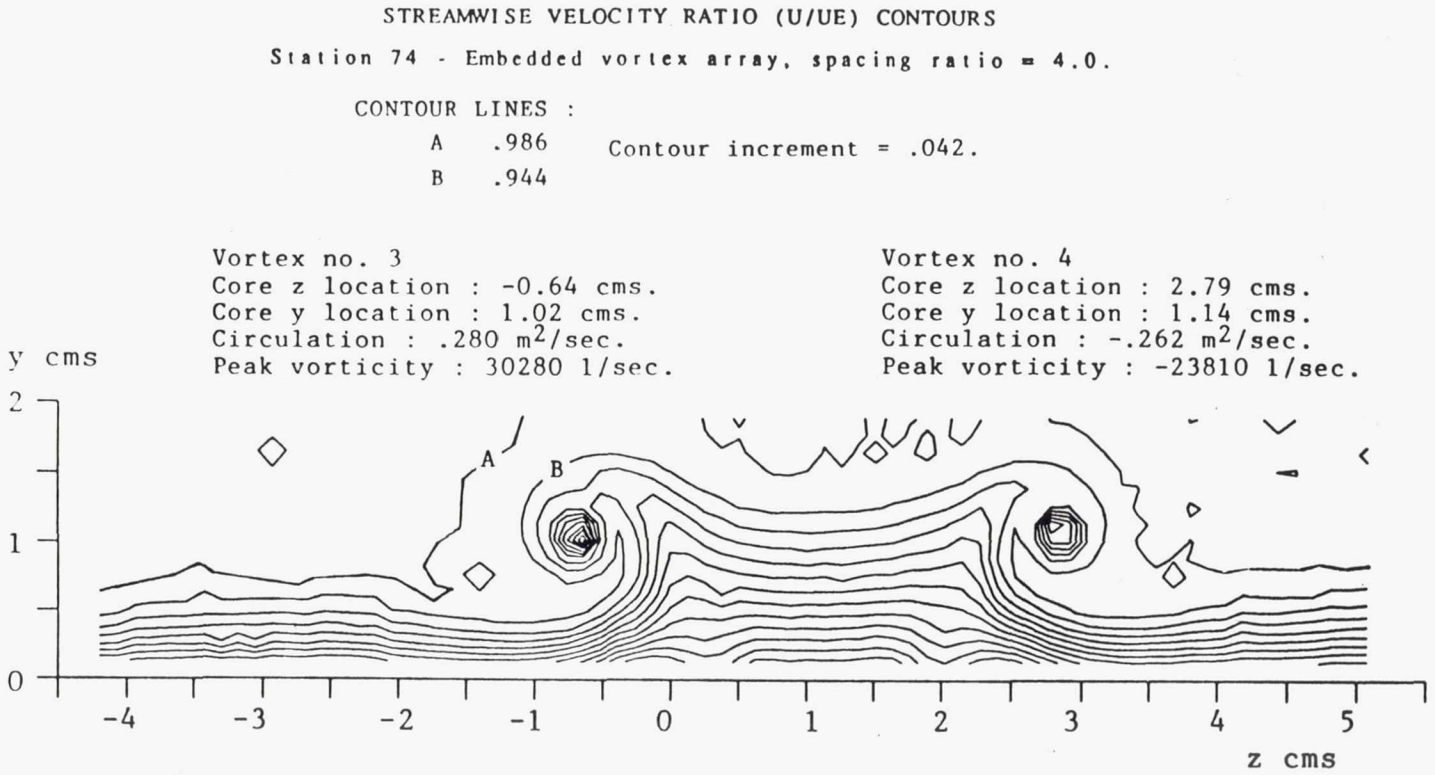

Figure 4.15c - Spacing ratio 4.0 test case, Station 74.

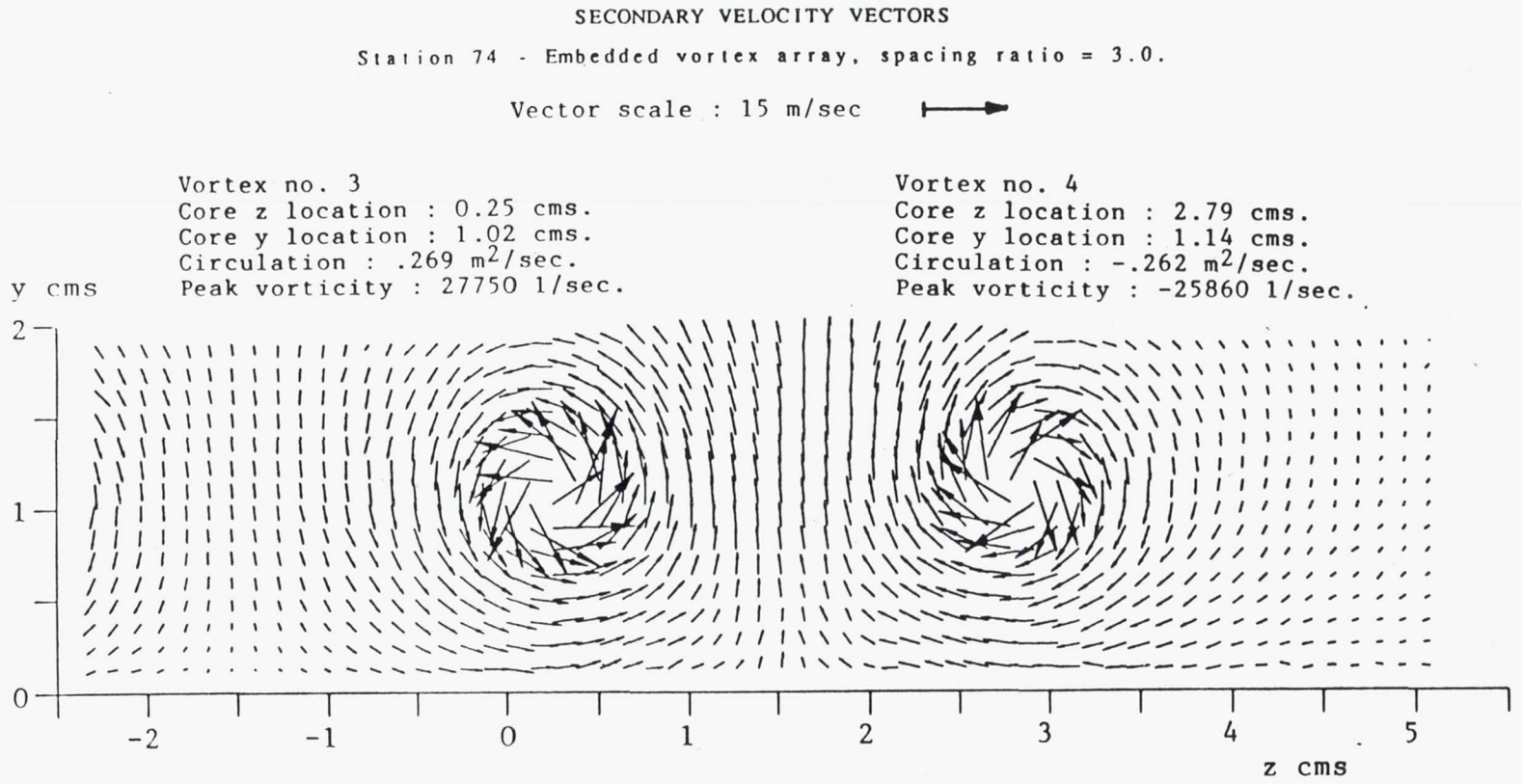

Figure 4.16a - Spacing ratio 3.0 test case, Station 74.

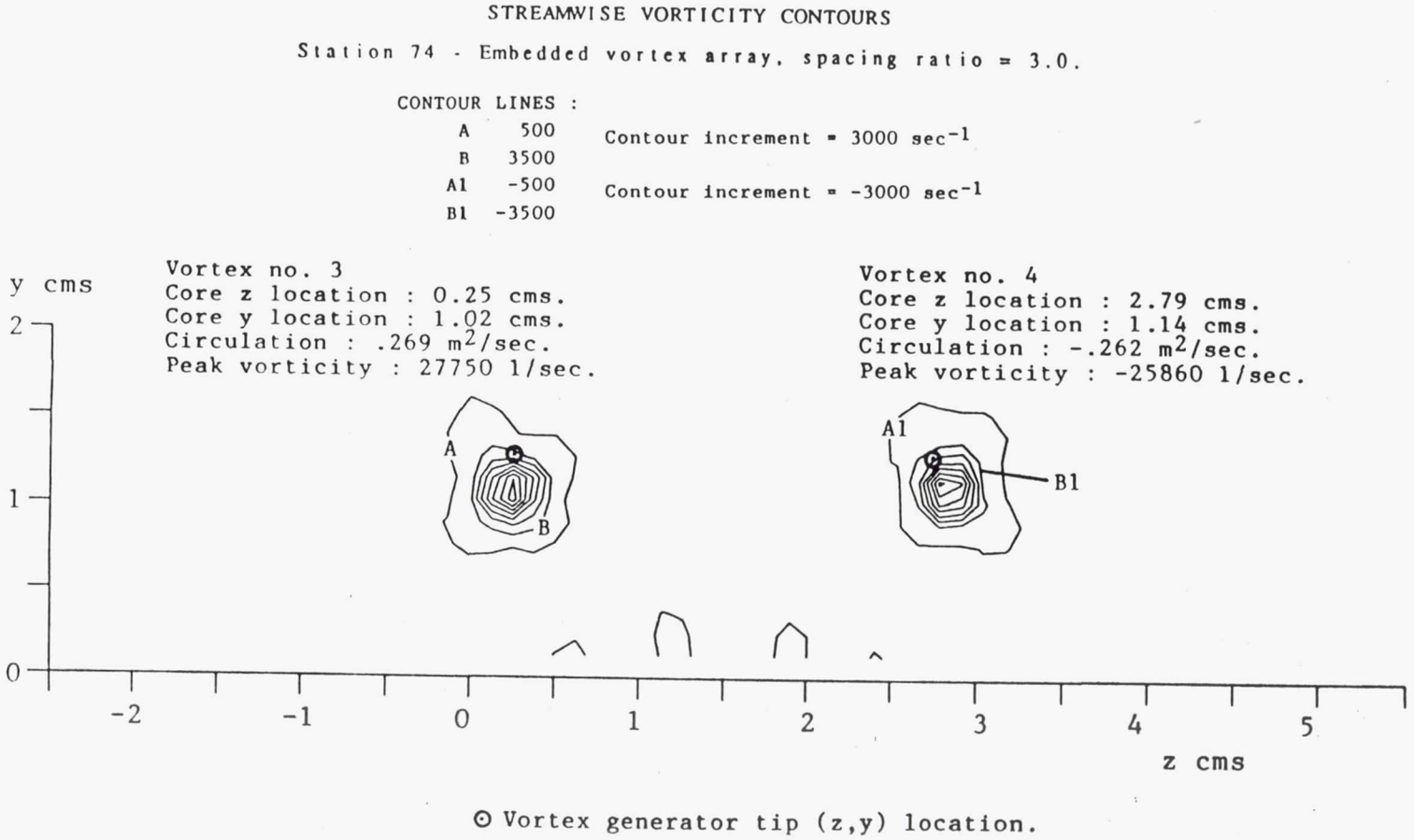

Figure 4.16b - Spacing ratio 3.0 test case, Station 74.

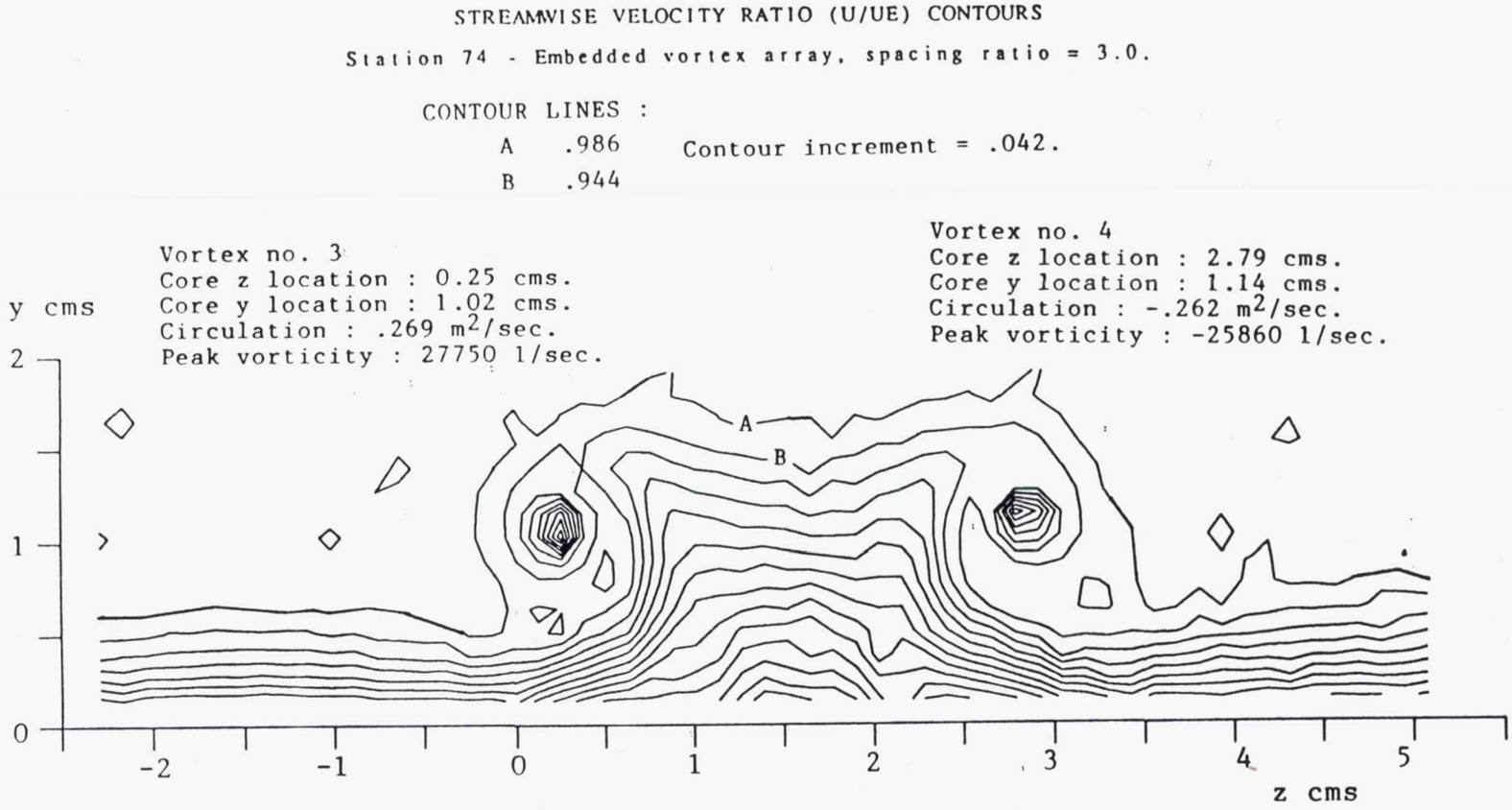

Figure 4.16c - Spacing ratio 3.0 test case, Station 74.

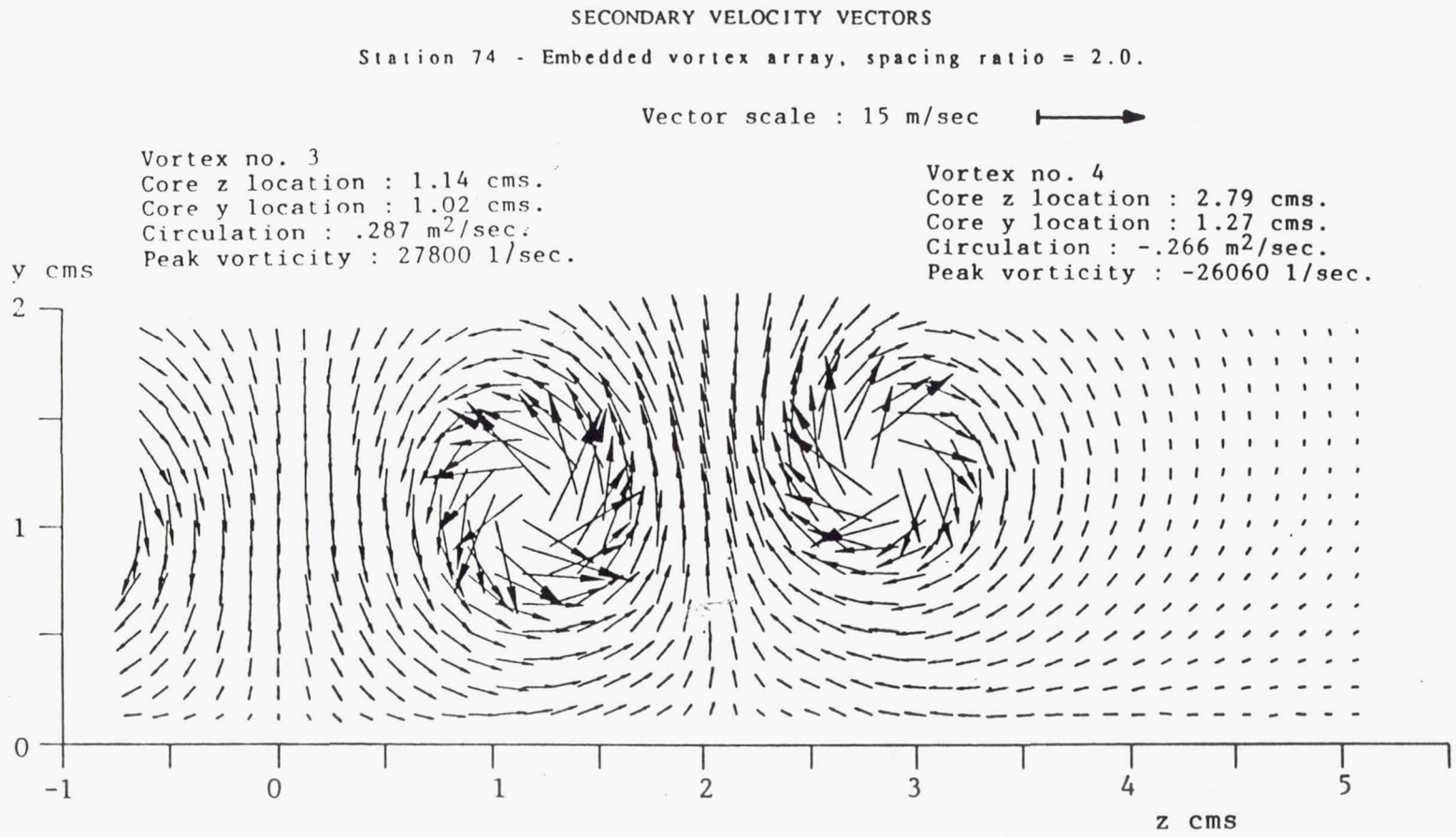

Figure 4.17a - Spacing ratio 2.0 test case, Station 74.

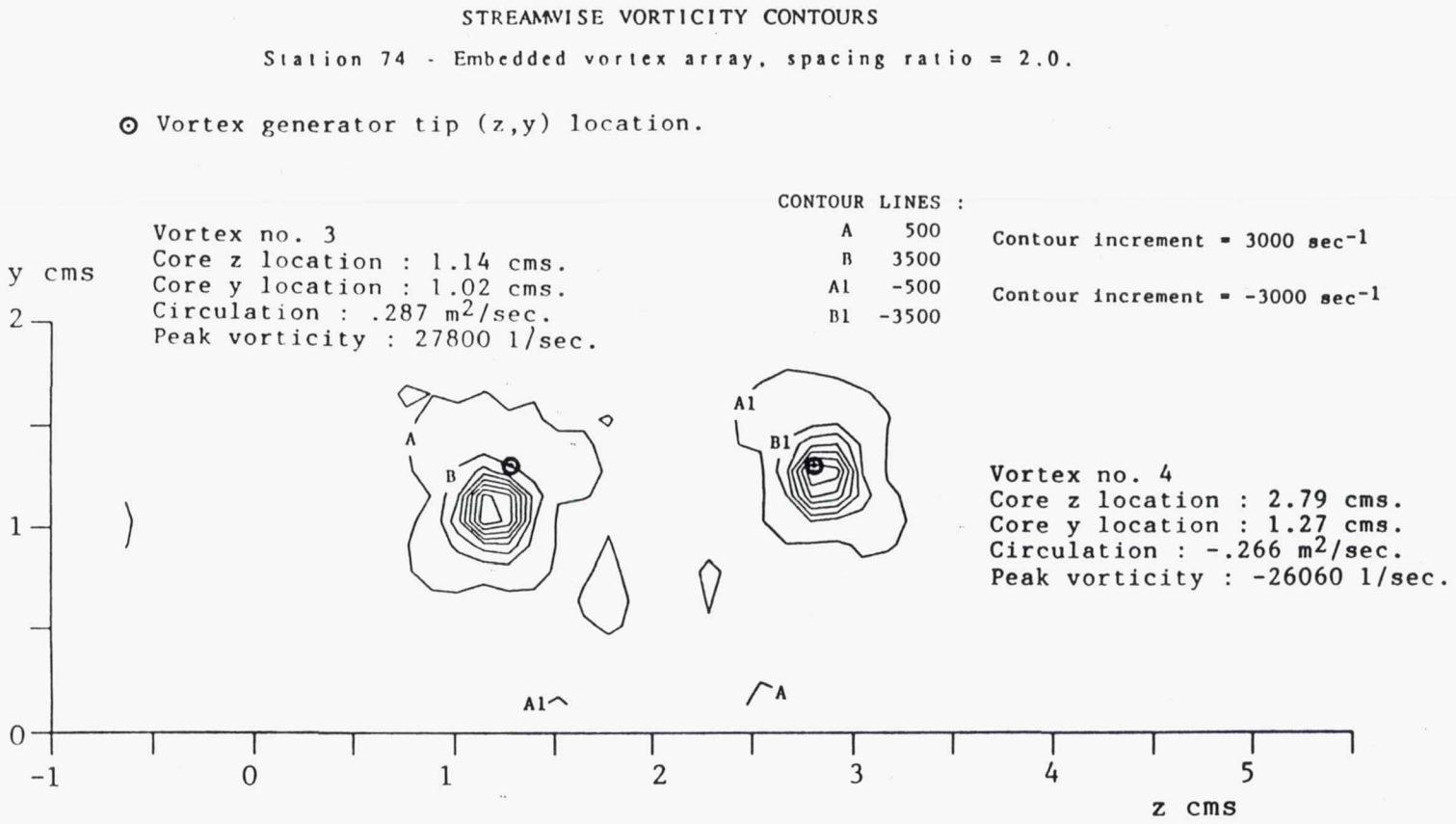

Figure 4.17b - Spacing ratio 2.0 test case, Station 74.

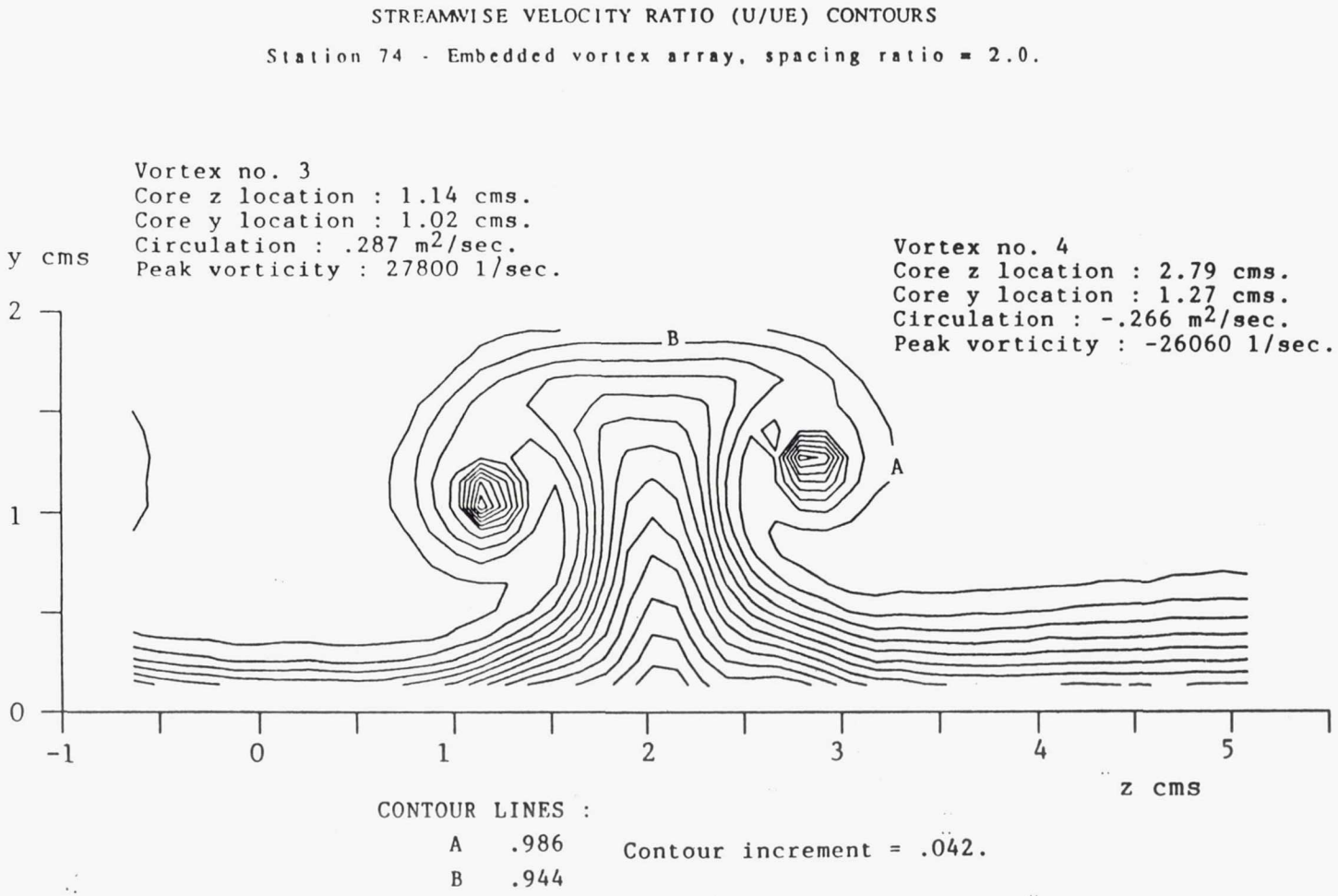

Figure 4.17c - Spacing ratio 2.0 test case, Station 74.

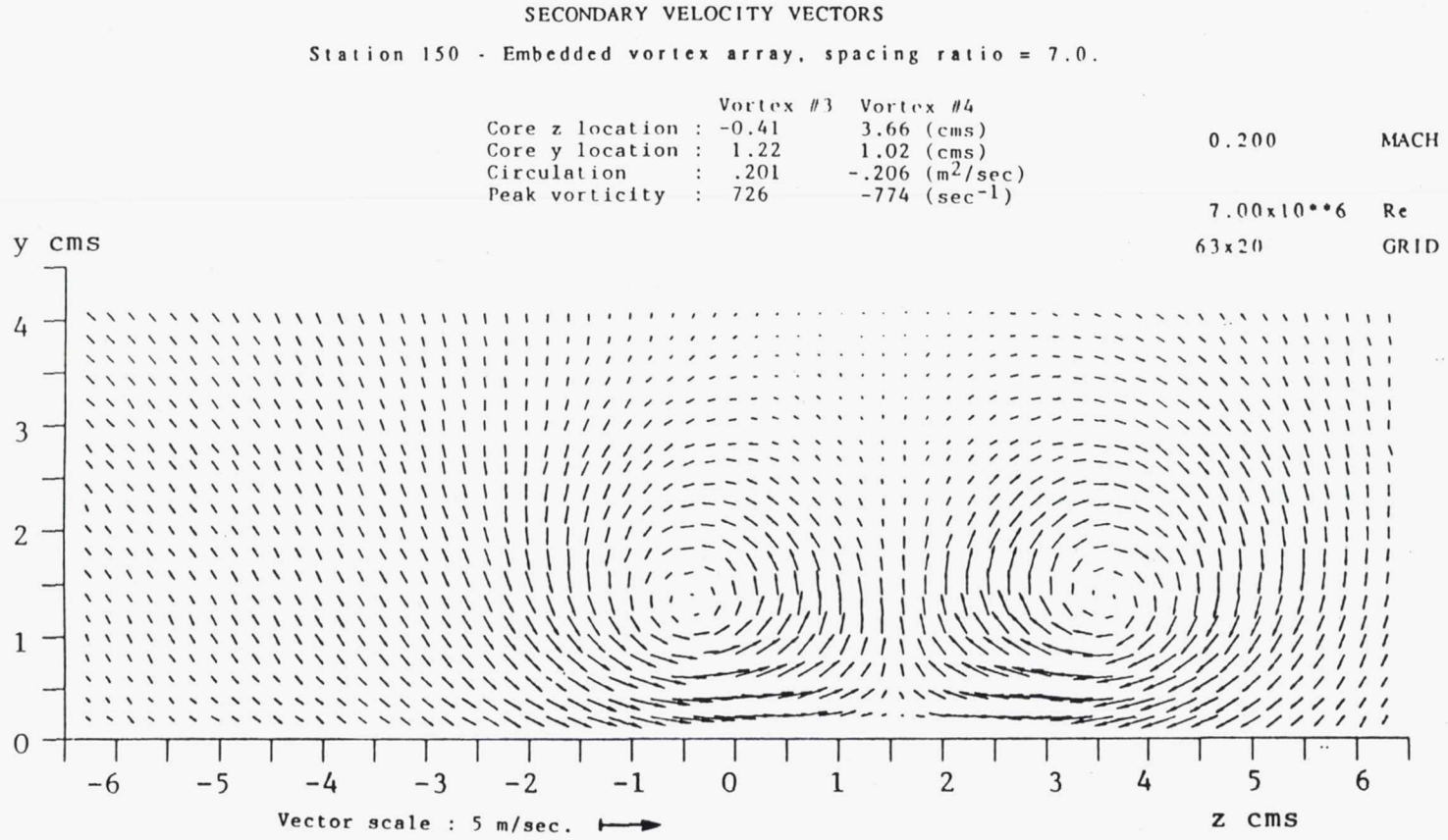

Figure 4.18a - Spacing ratio 7.0 test case, Station 150.

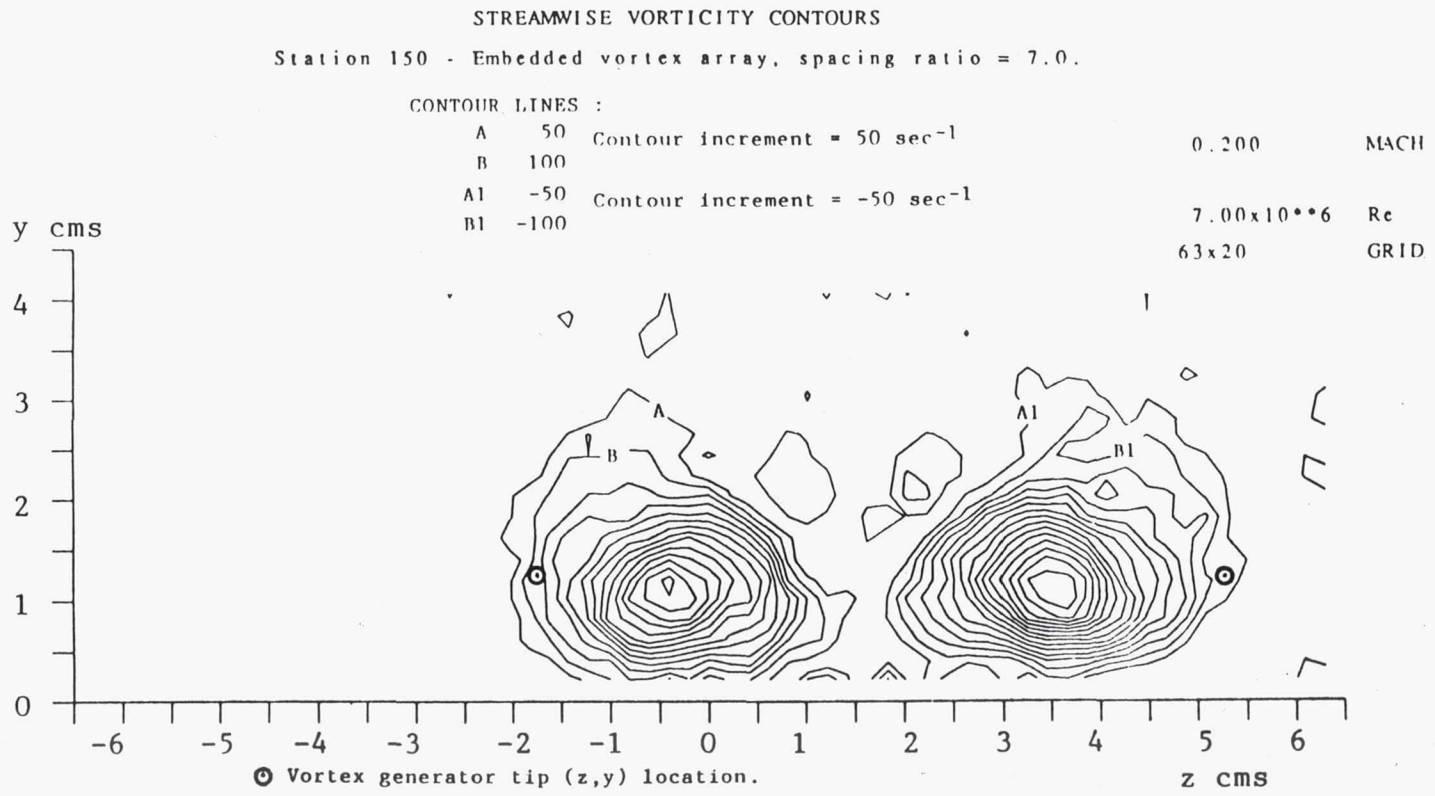

Figure 4.18b - Spacing ratio 7.0 test case, Station 150.

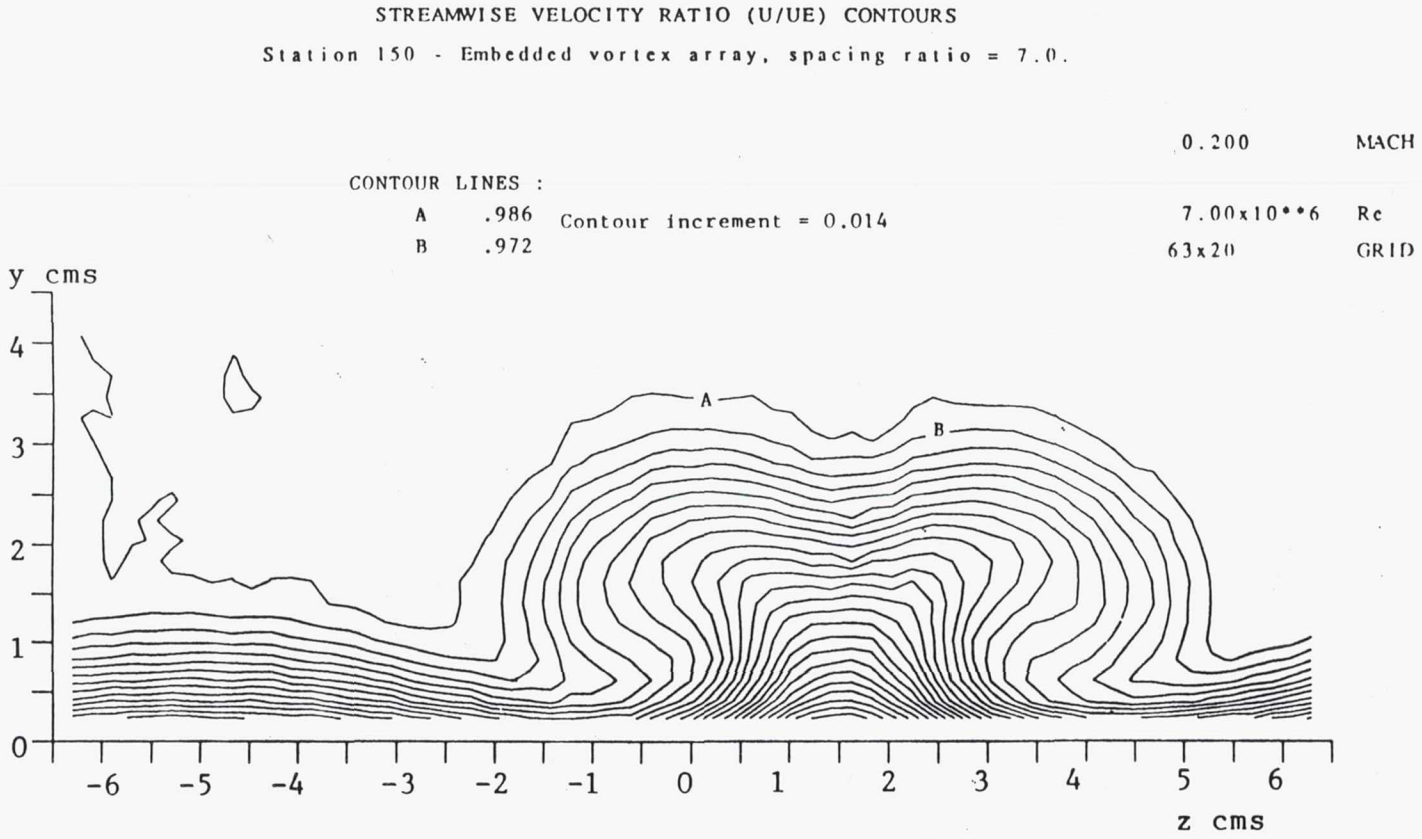

Figure 4.18c - Spacing ratio 7.0 test case, Station 150.

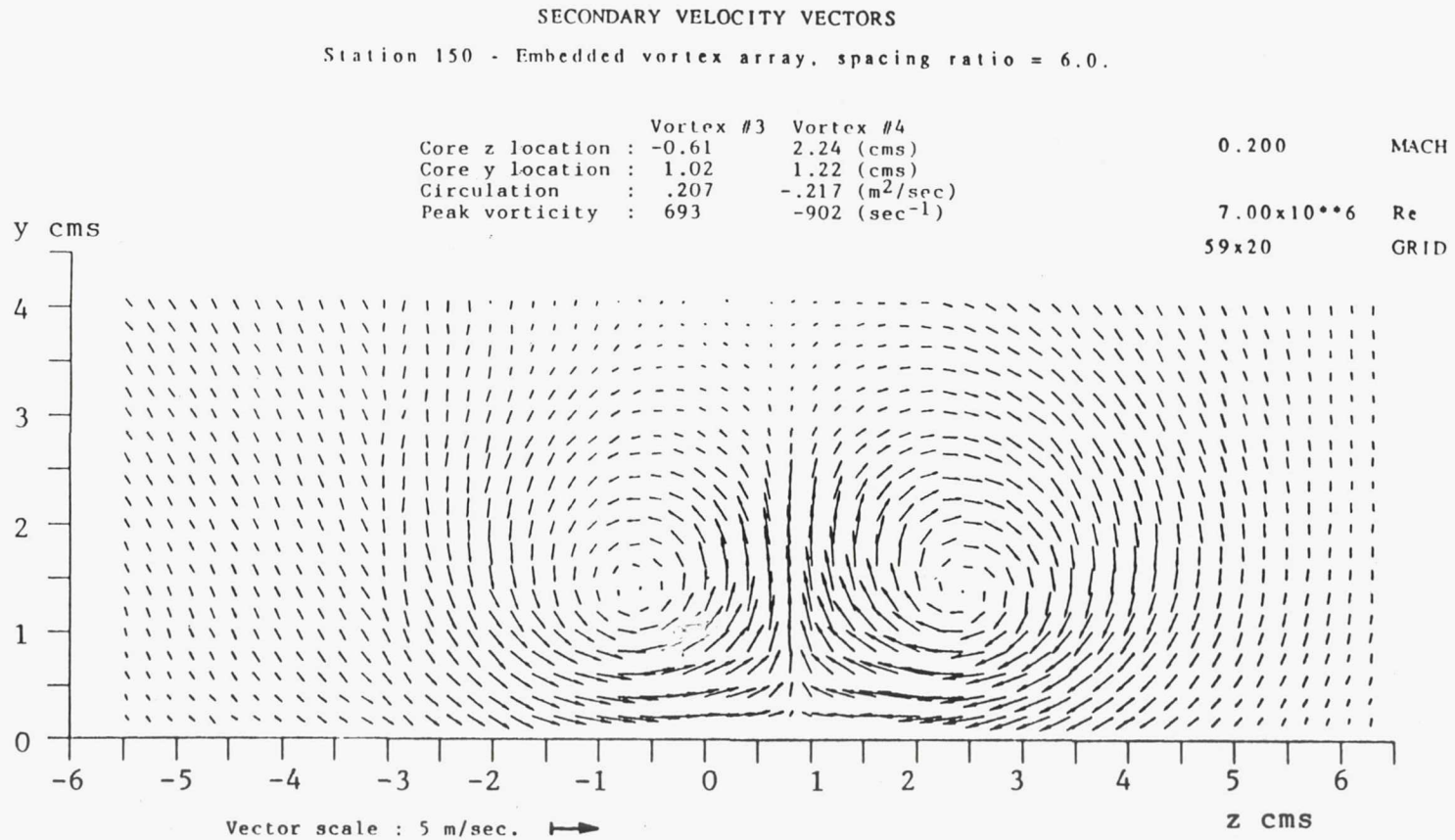

Figure 4.19a - Spacing ratio 6.0 test case, Station 150.

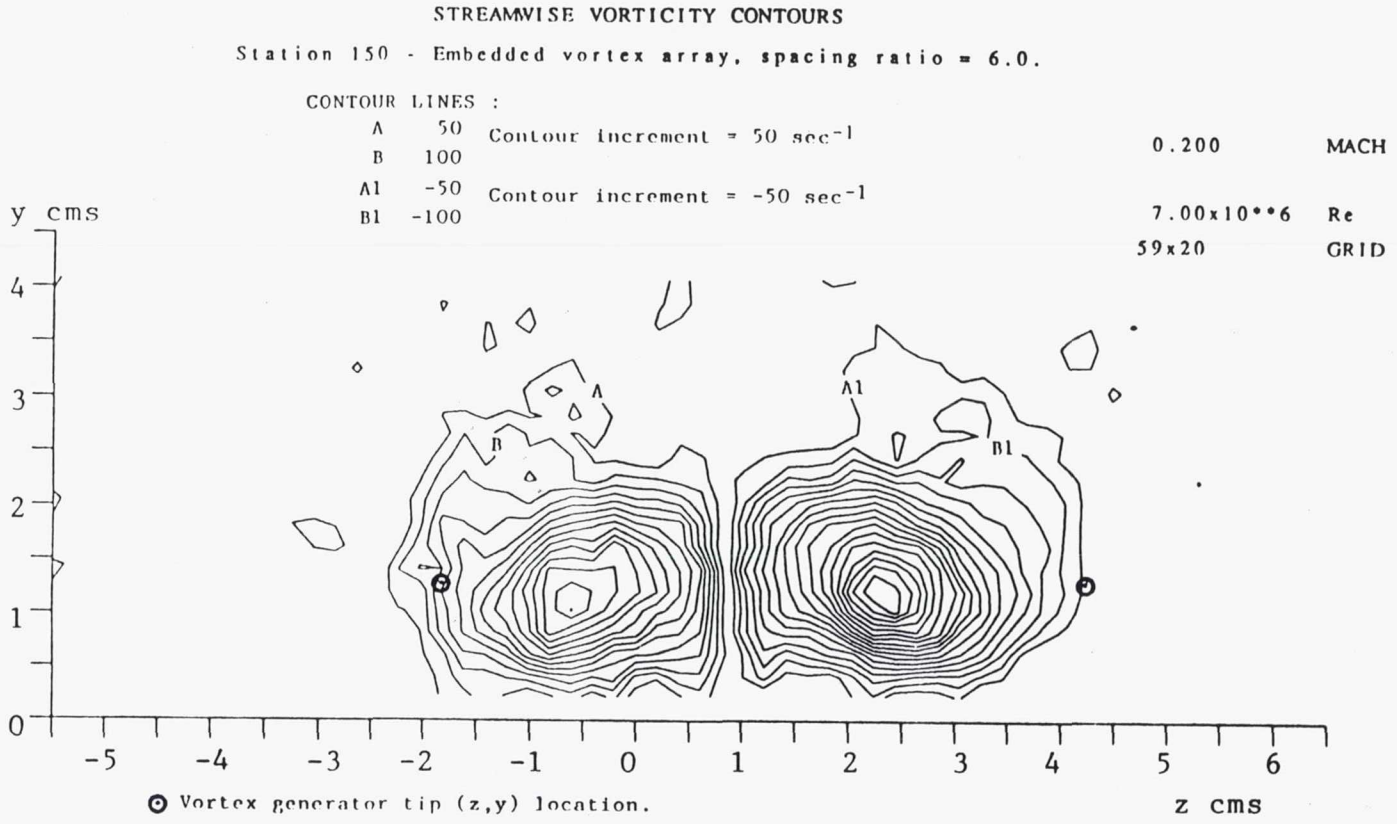

Figure 4.19b - Spacing ratio 6.0 test case, Station 150.

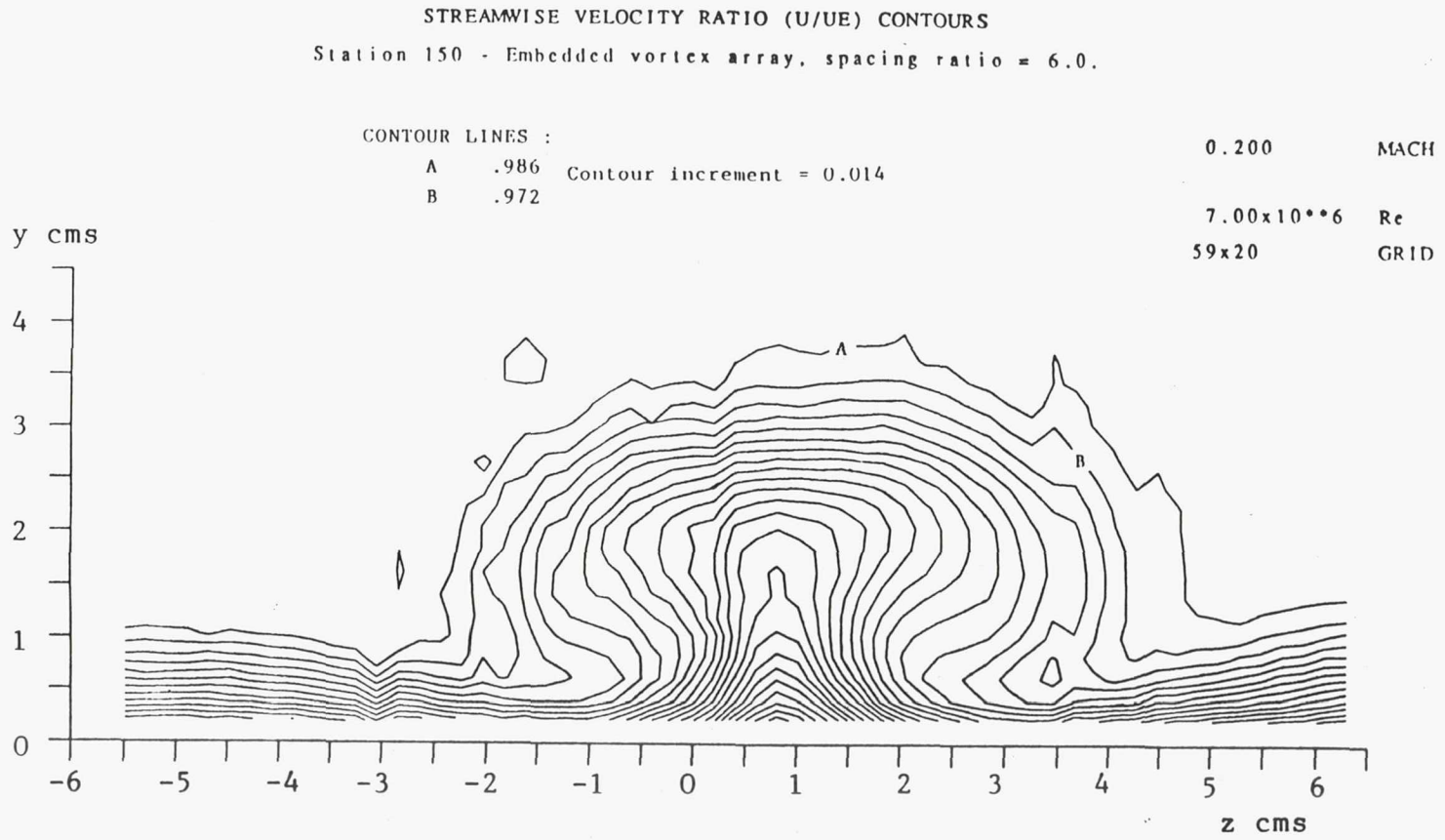

Figure 4.19c - Spacing ratio 6.0 test case, Station 150.

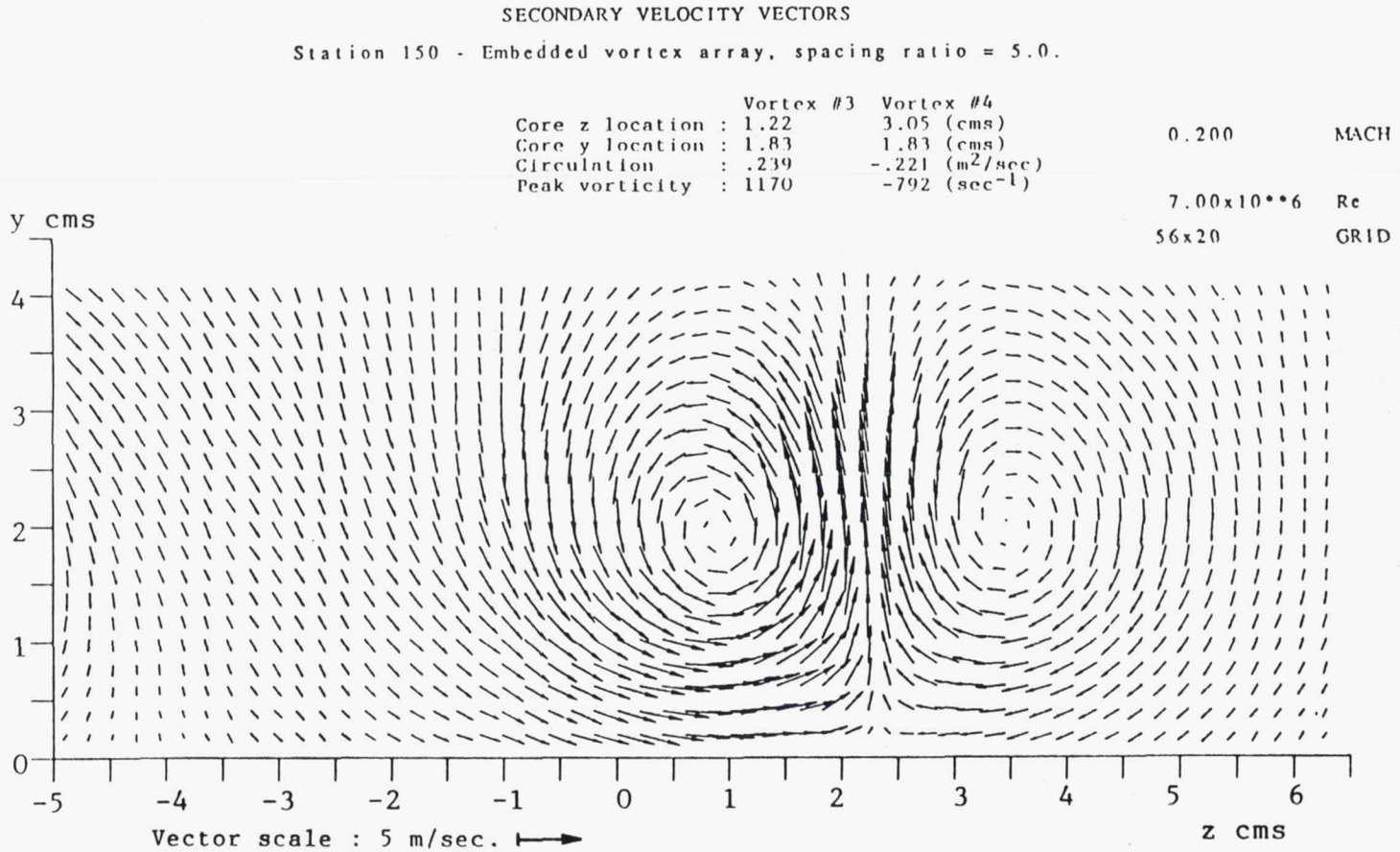

Figure 4.20a - Spacing ratio 5.0 test case, Station 150.

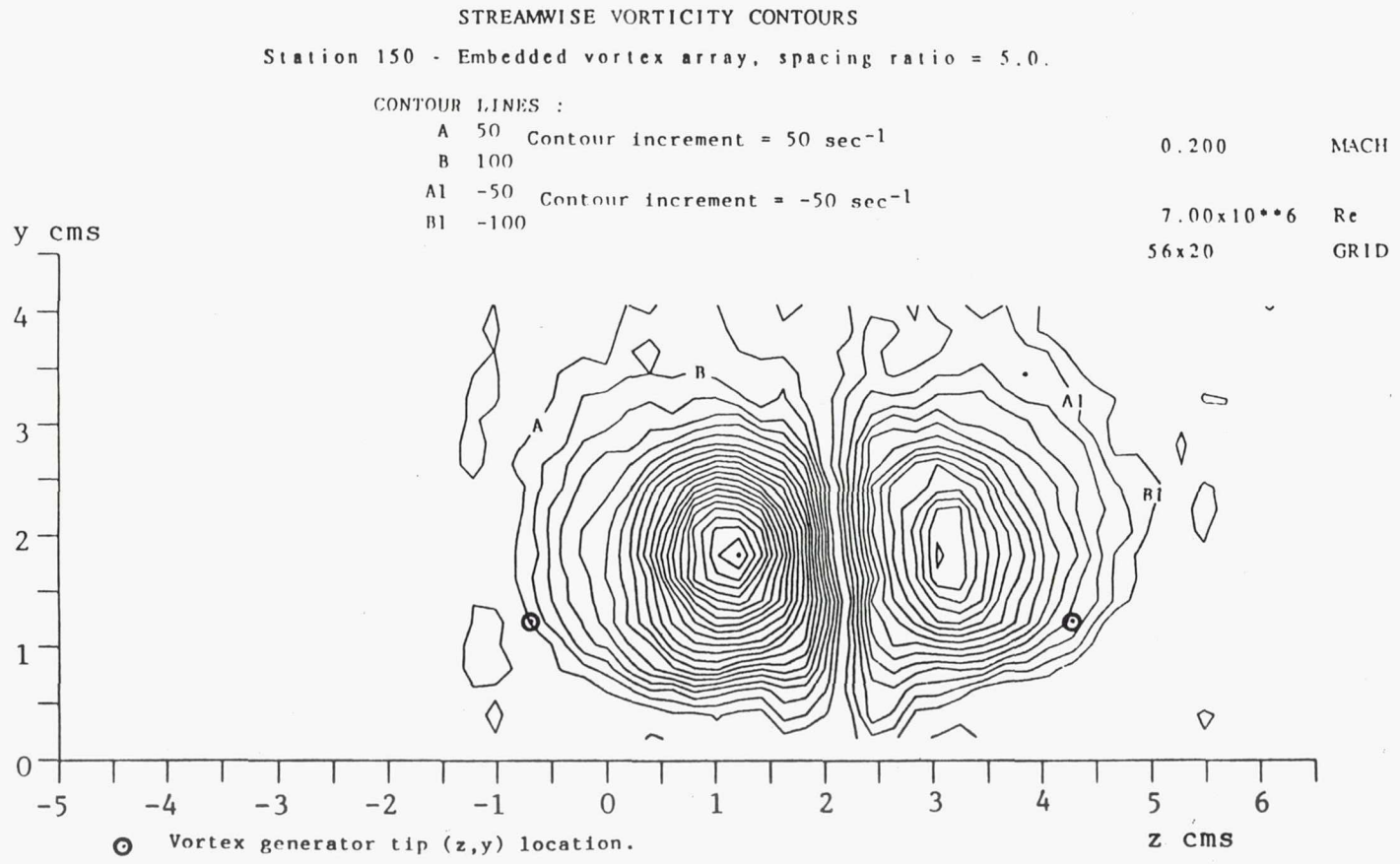

Figure 4.20b - Spacing ratio 5.0 test case, Station 150.

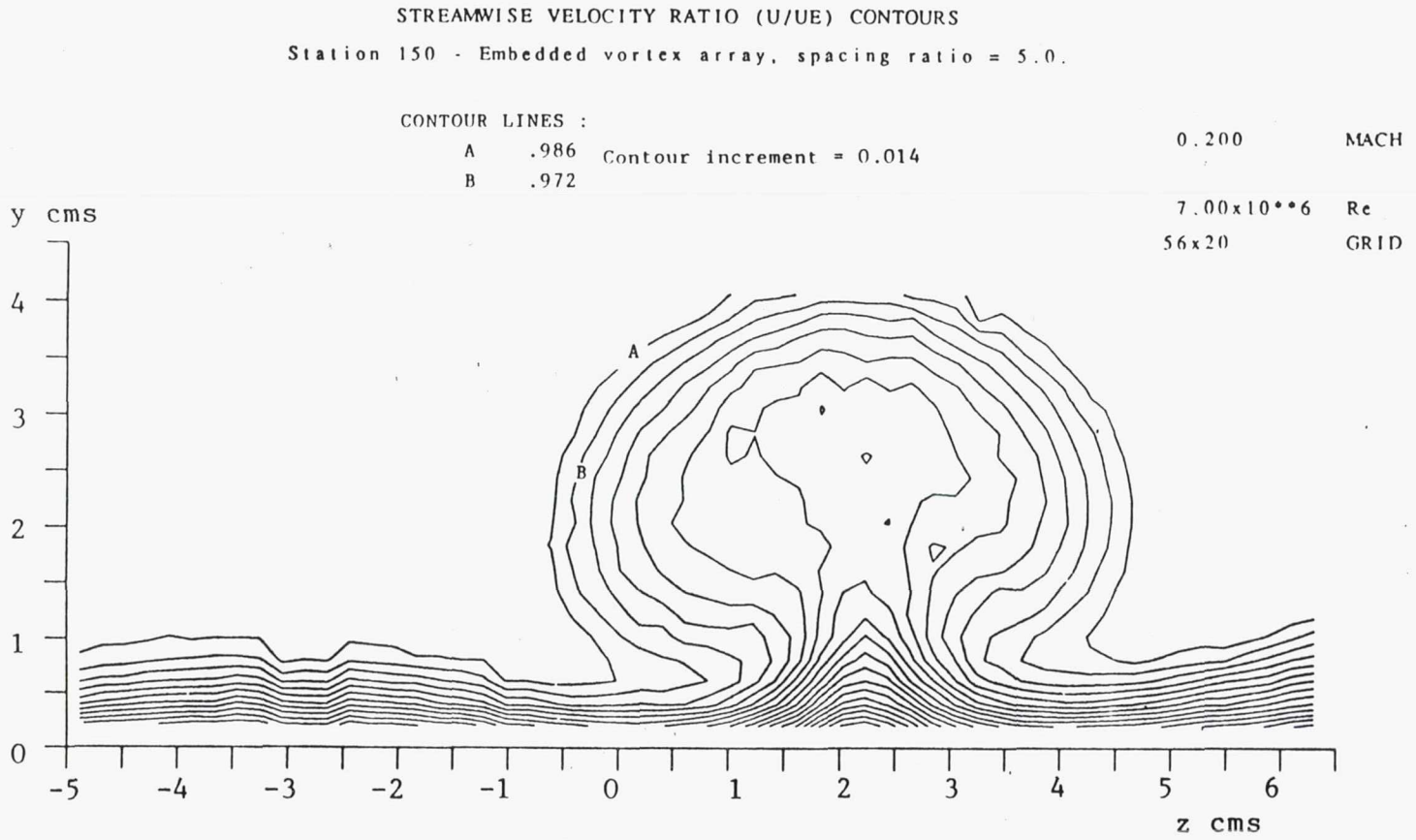

Figure 4.20c - Spacing ratio 5.0 test case, Station 150.

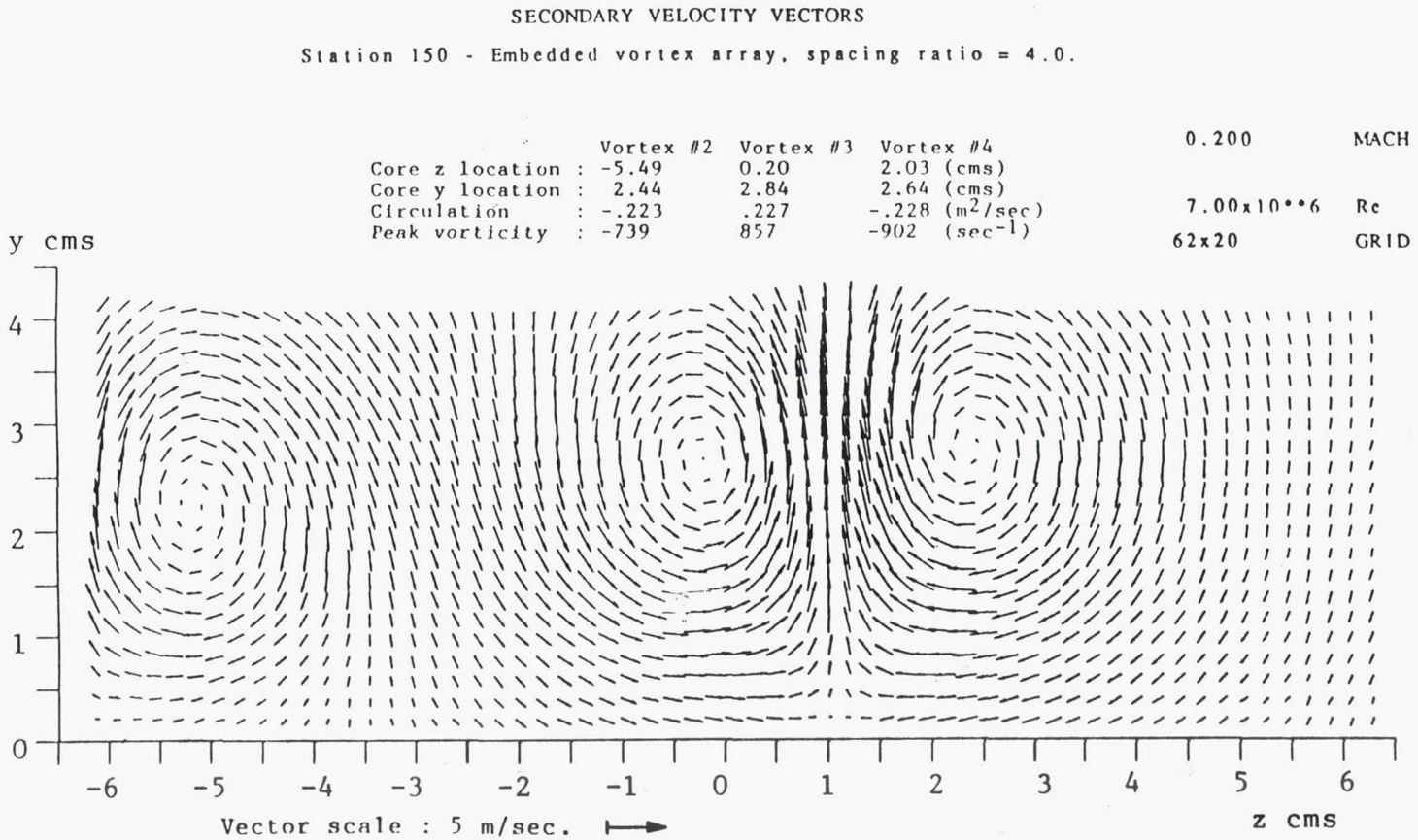

Figure 4.21a - Spacing ratio 4.0 test case, Station 150.

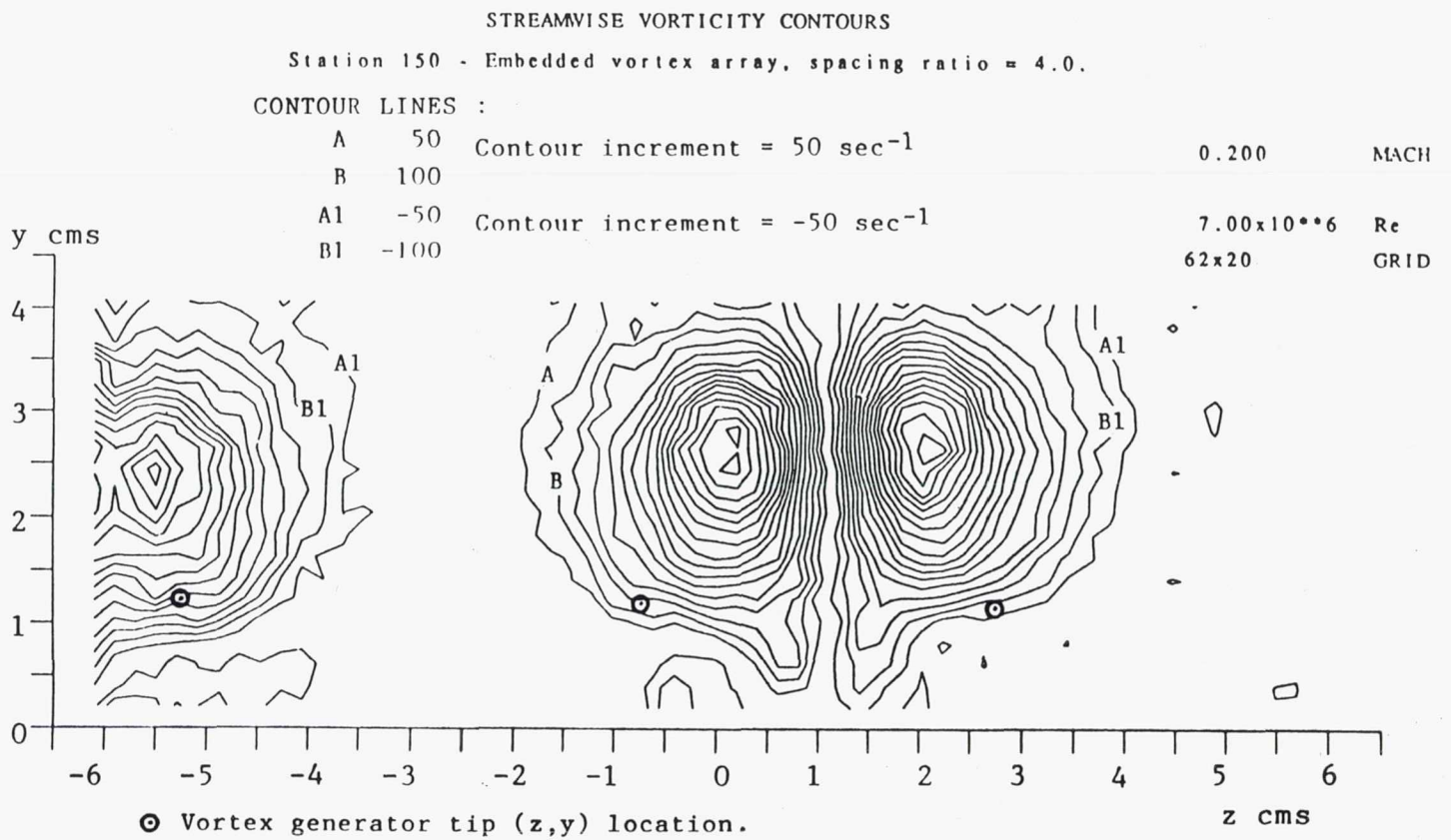

Figure 4.21b - Spacing ratio 4.0 test case, Station 150.

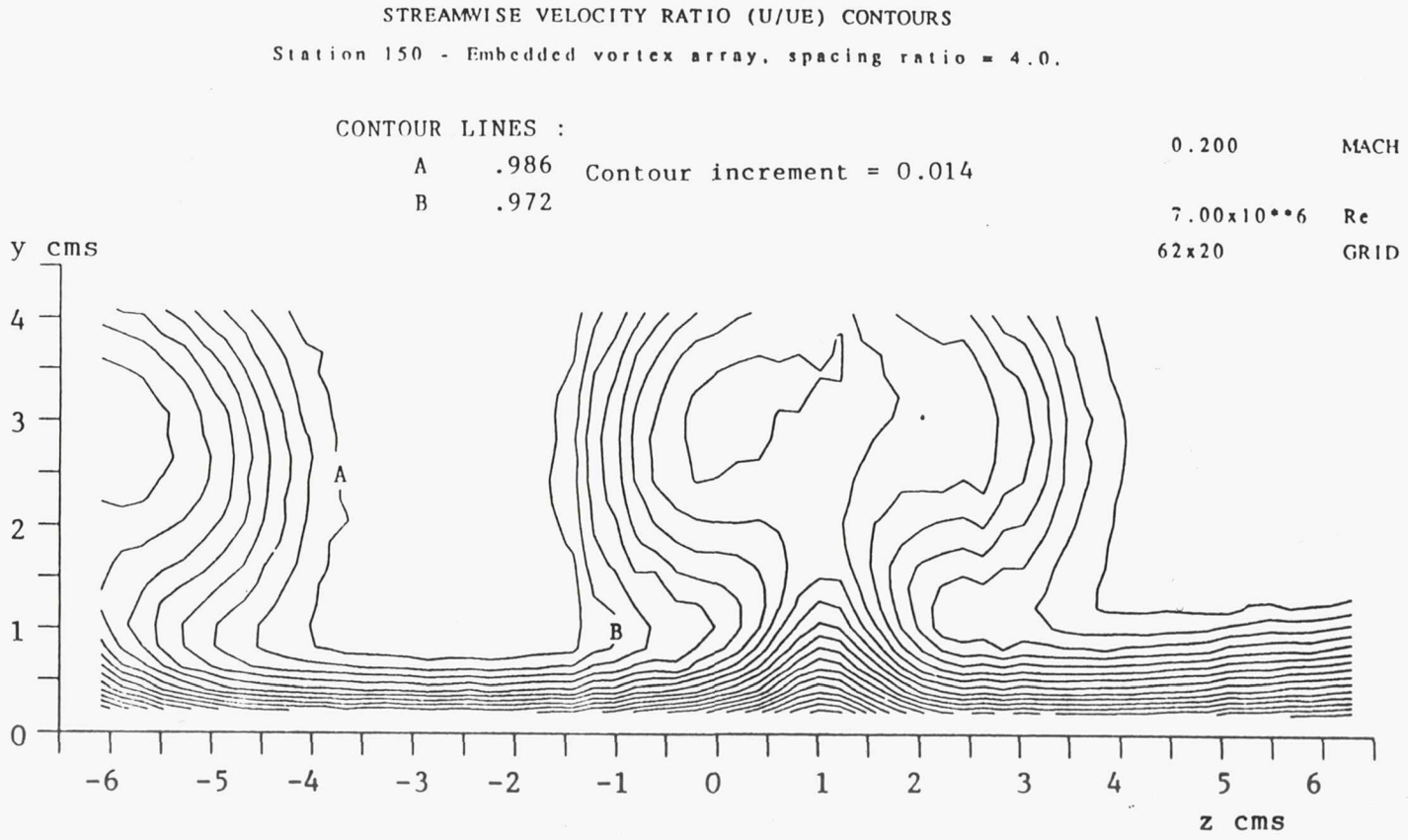

Figure 4.21c - Spacing ratio 4.0 test case, Station 150.

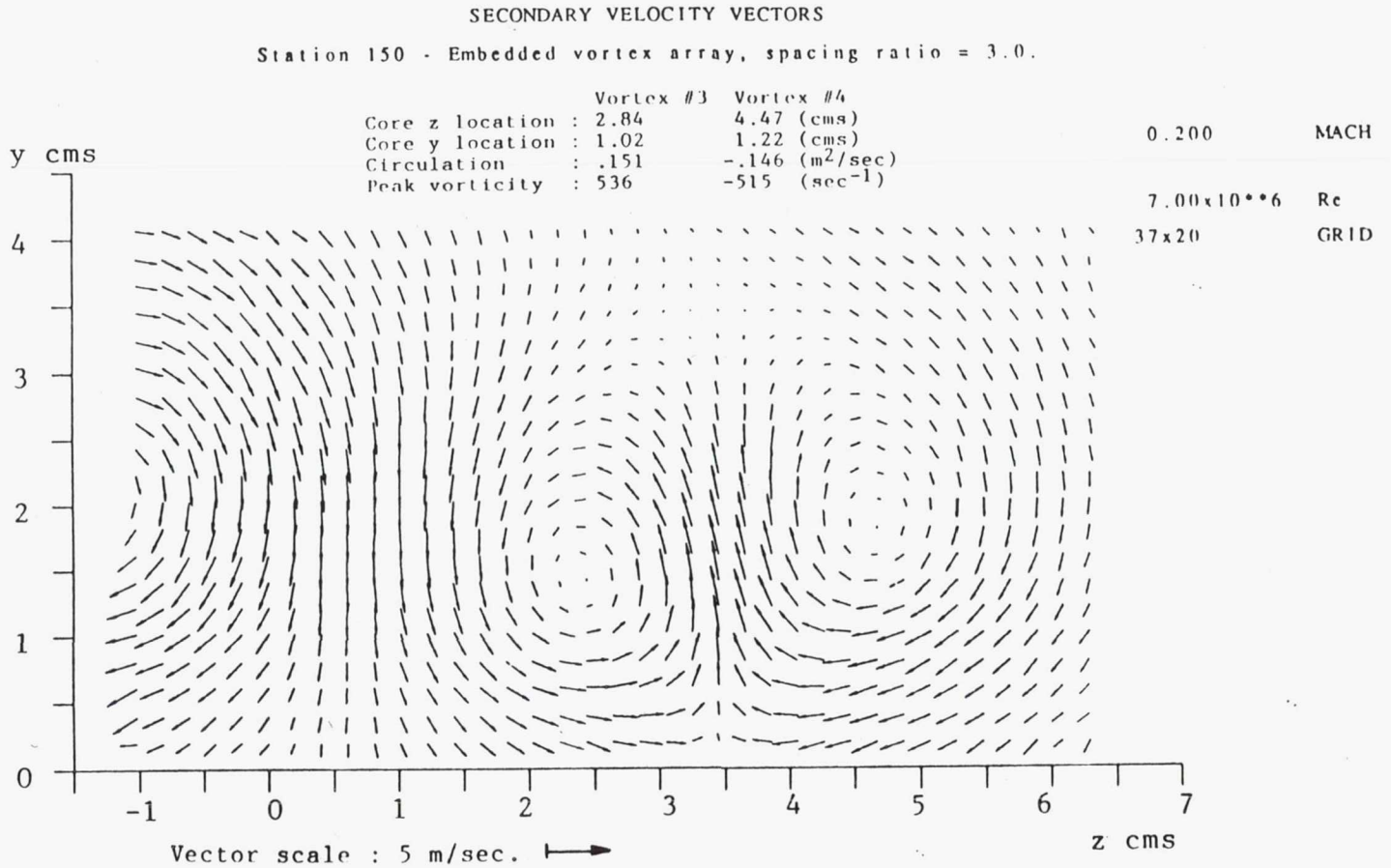

Figure 4.22a - Spacing ratio 3.0 test case, Station 150.

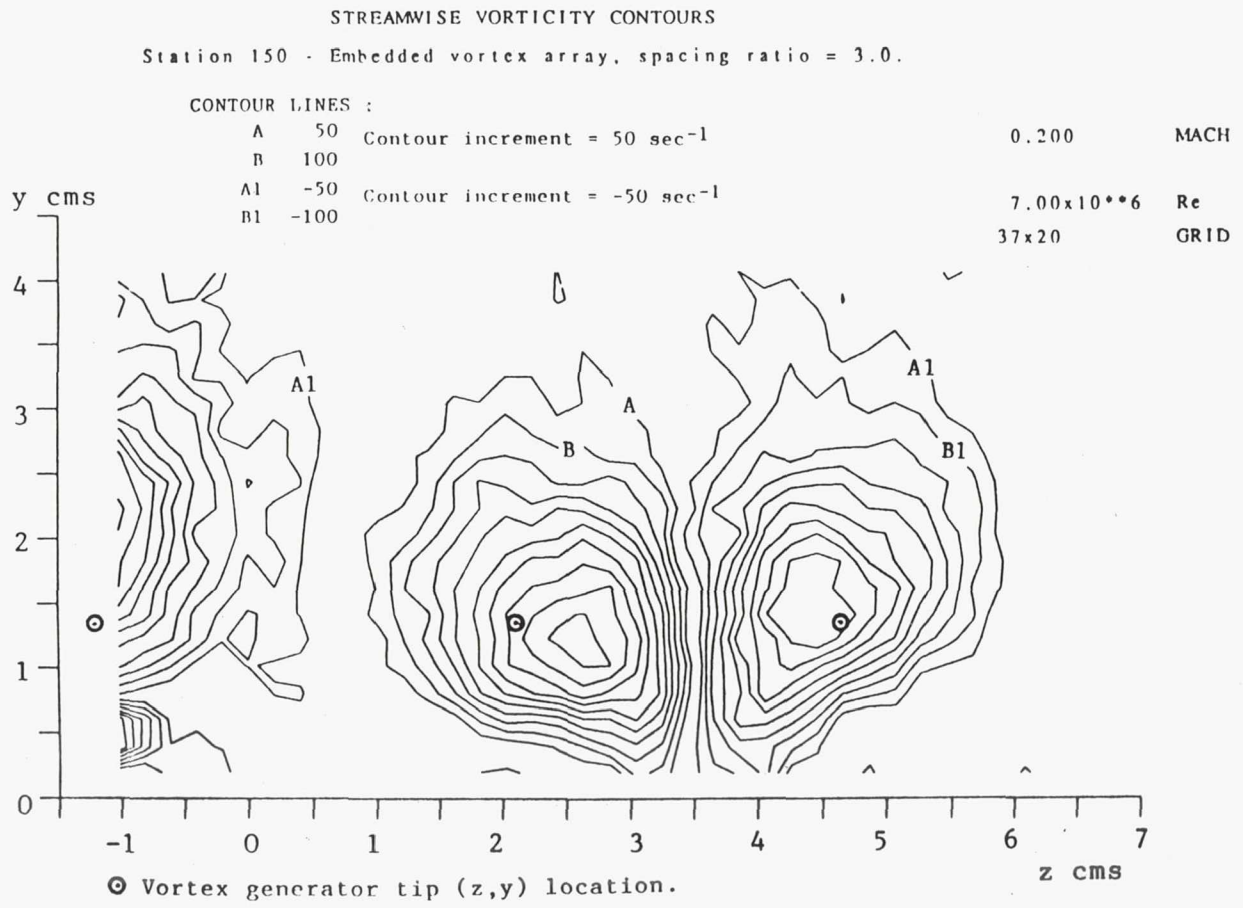

Figure 4.22b - Spacing ratio 3.0 test case, Station 150.

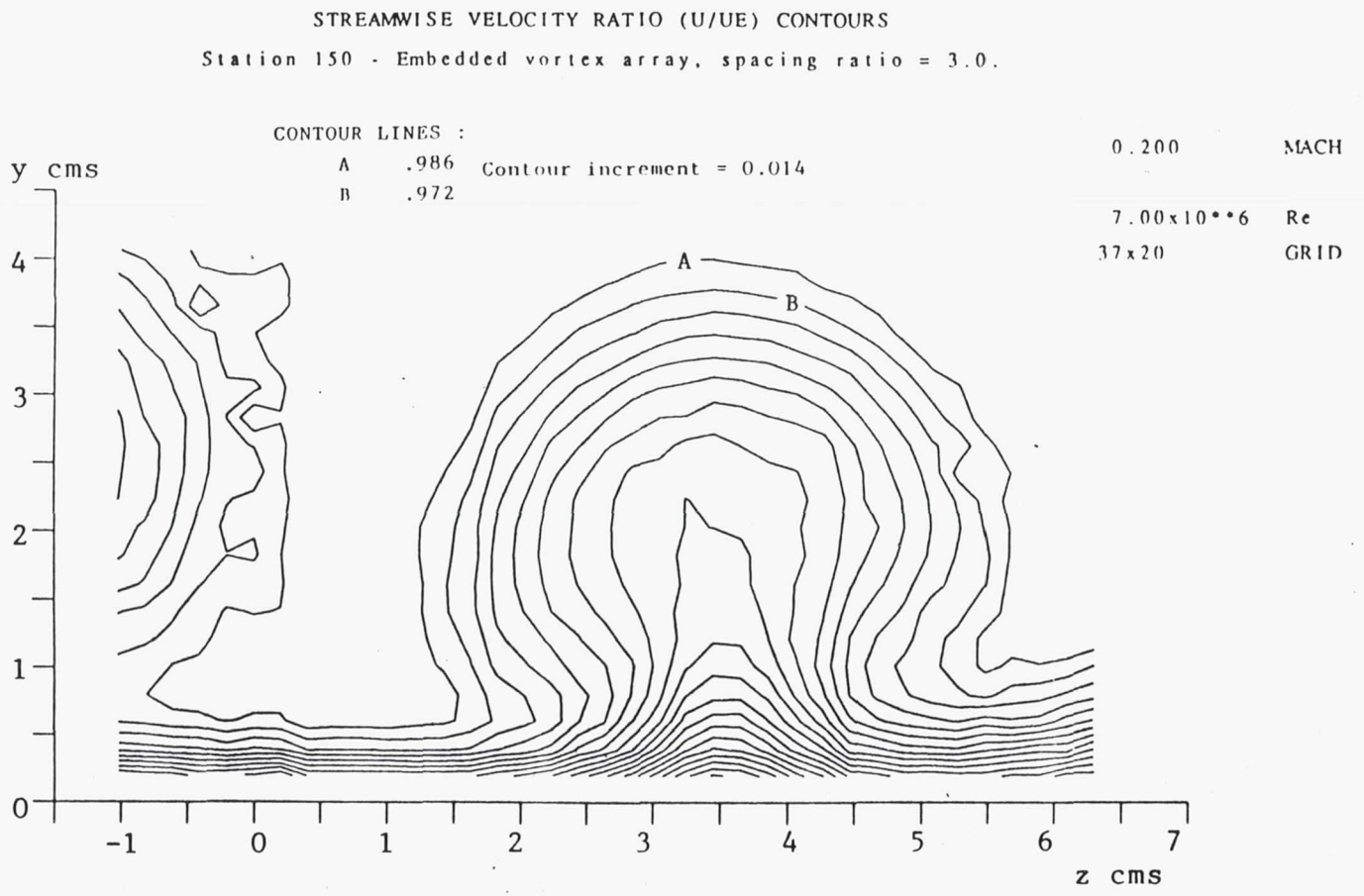

Figure 4.22c - Spacing ratio 3.0 test case, Station 150.

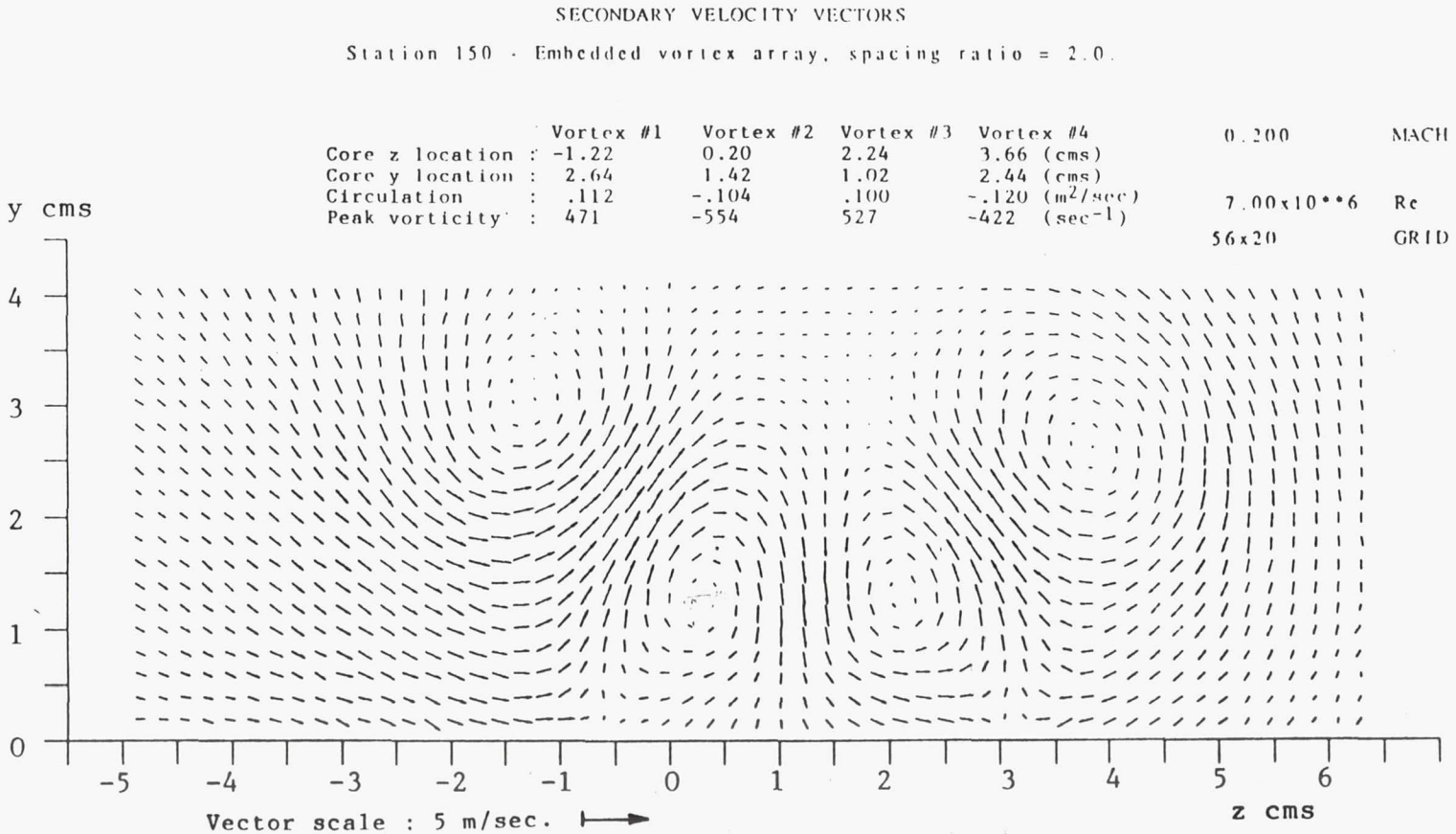

Figure 4.23a - Spacing ratio 2.0 test case, Station 150.

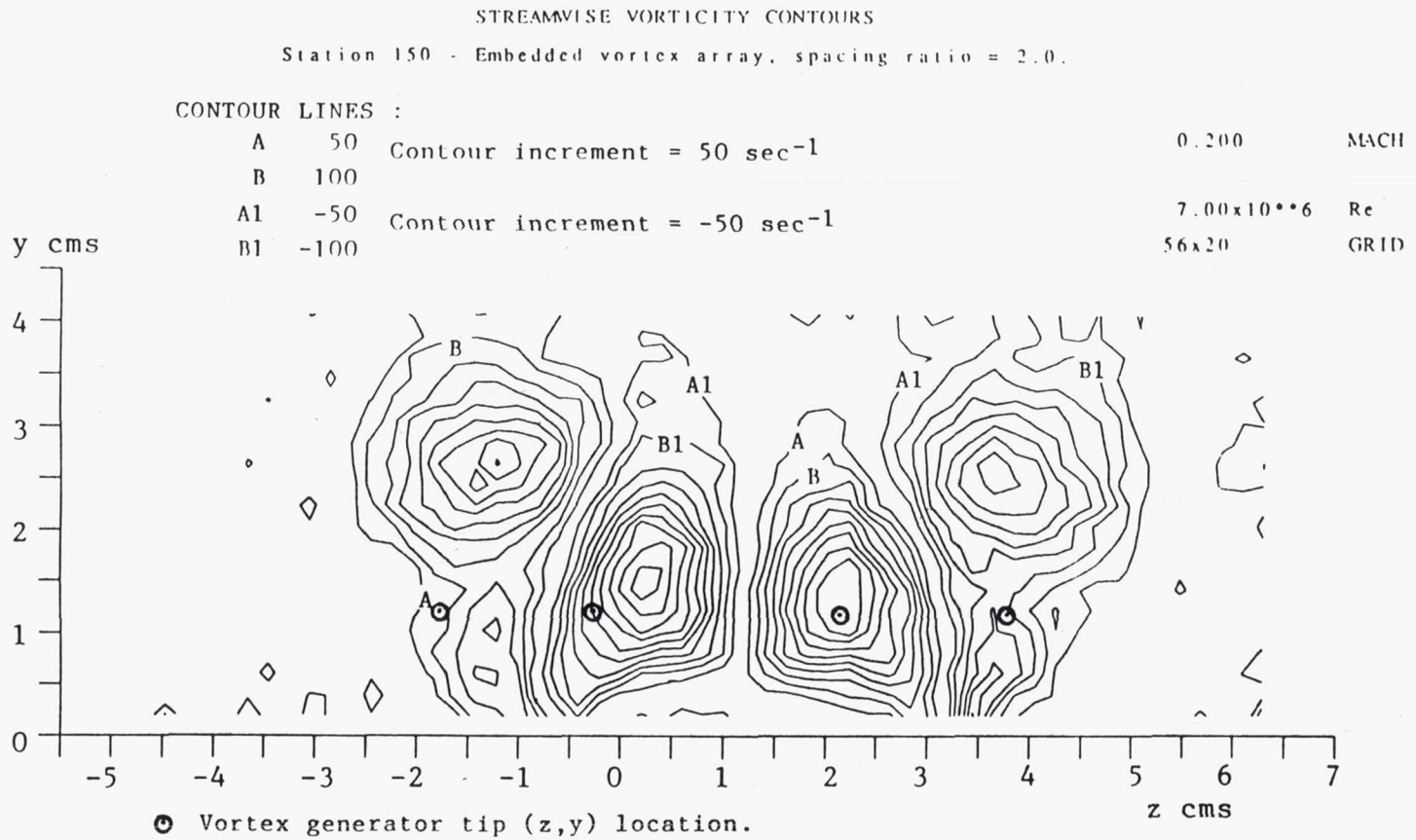

Figure 4.23b - Spacing ratio 2.0 test case, Station 150.

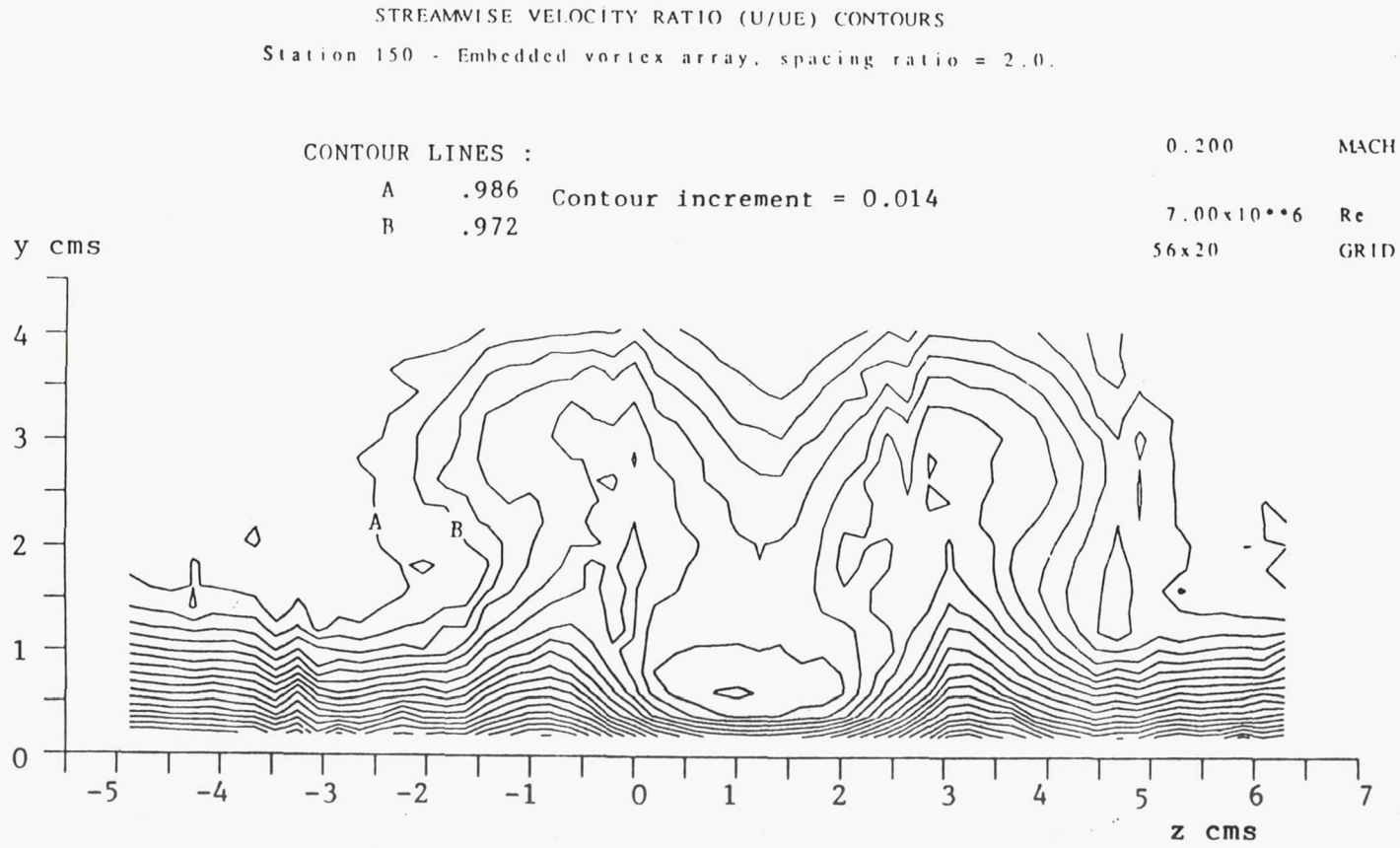

Figure 4.23c - Spacing ratio 2.0 test case, Station 150.

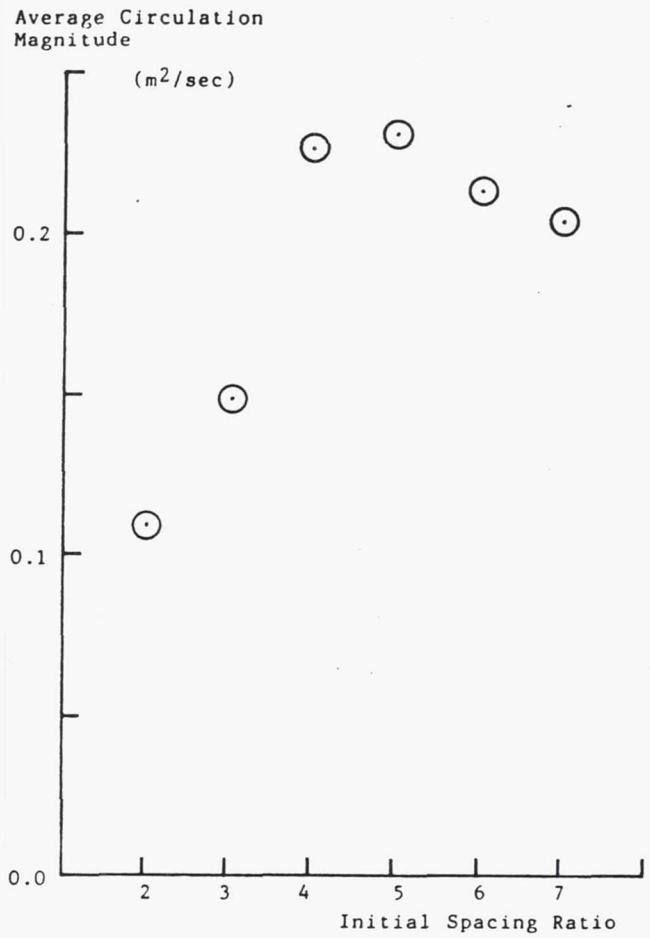

Figure 4.24 - Average circulation magnitude versus initial spacing ratio at the downstream measurement station.

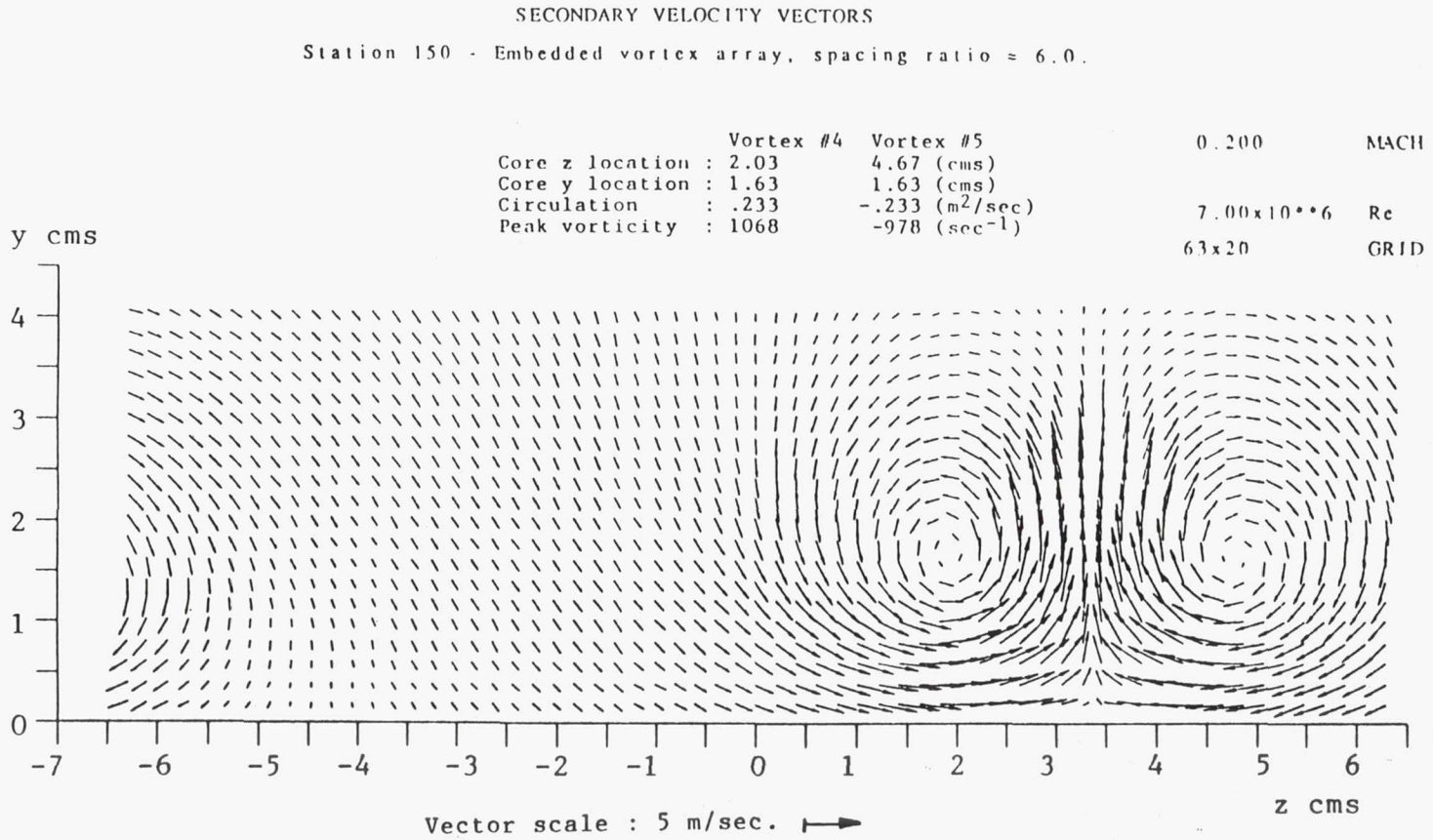

Figure 4.25a - Spacing ratio 6.0 test case, 6 blades, Station 150.

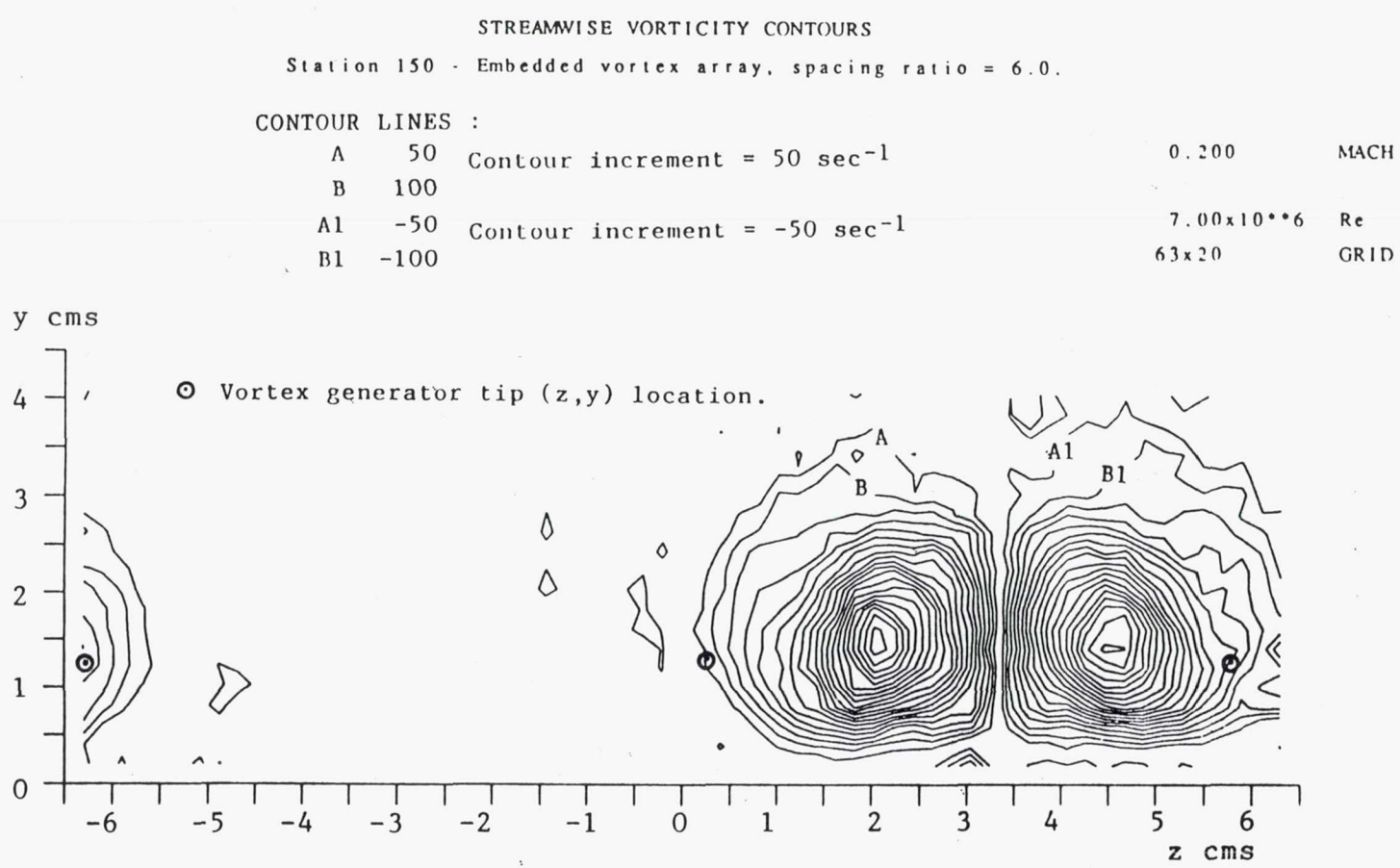

Figure 4.25b - Spacing ratio 6.0 test case, 6 blades, Station 150.

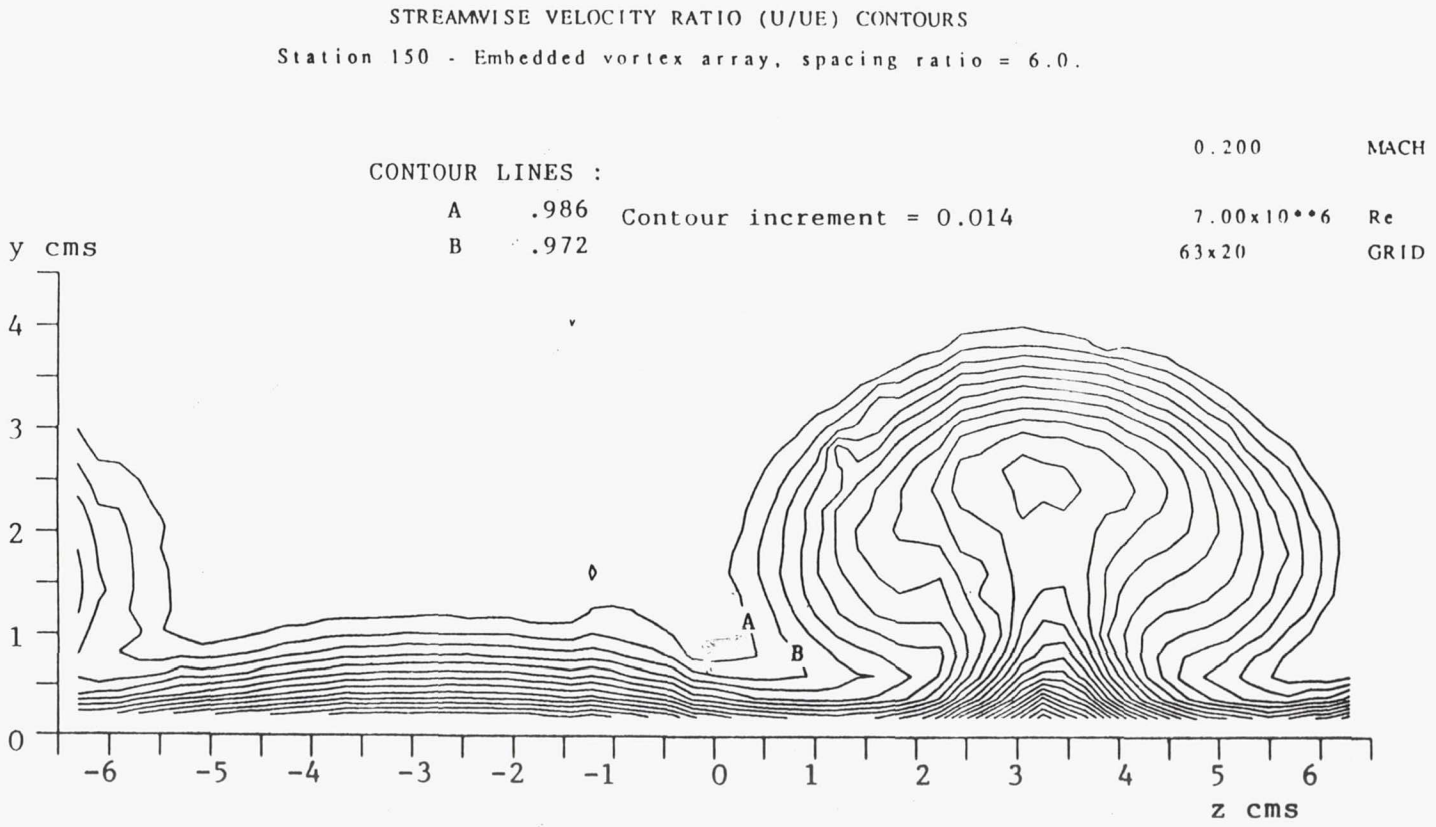

Figure 4.25c - Spacing ratio 6.0 test case, 6 blades, Station 150.

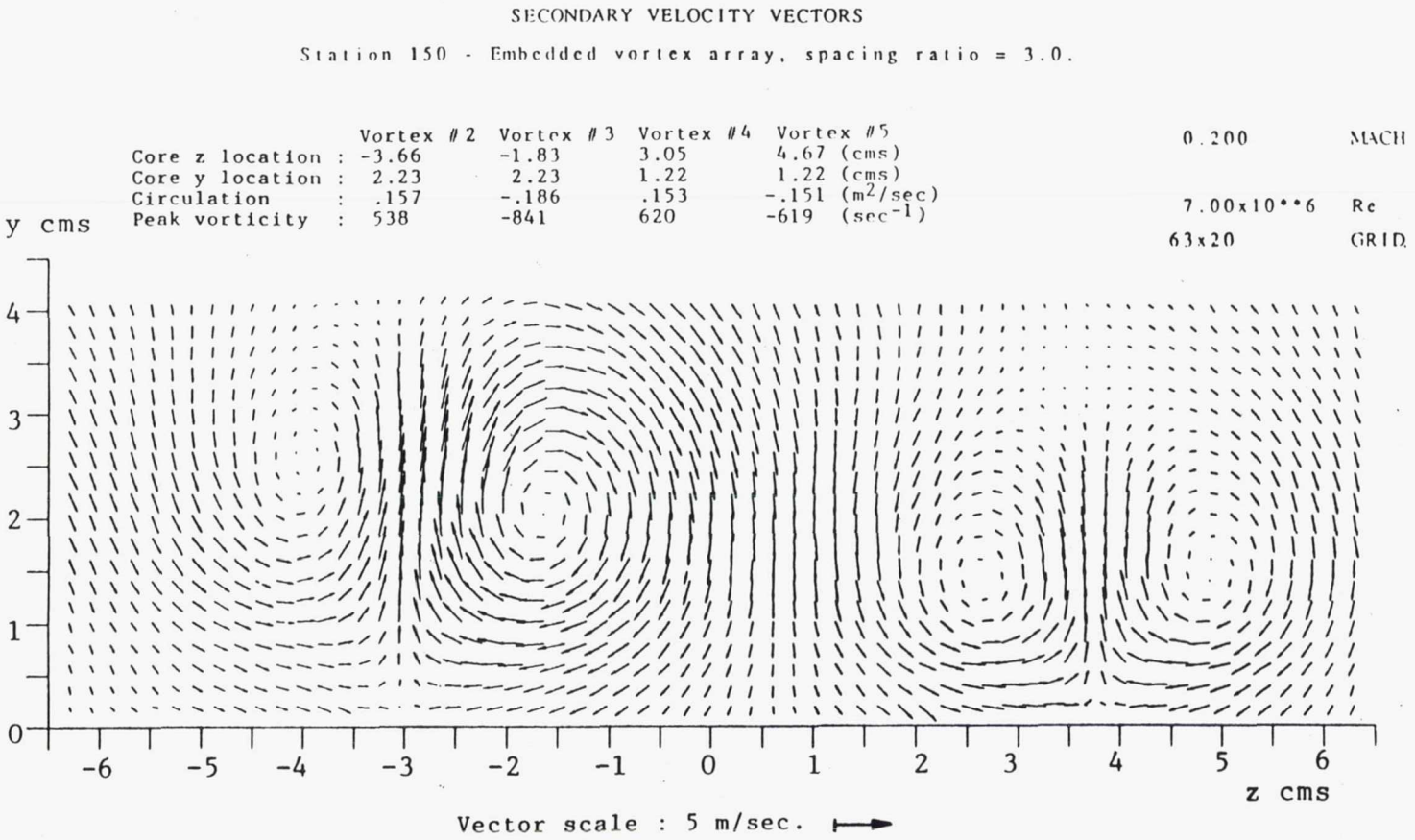

Figure 4.26a - Spacing ratio 3.0 test case, 6 blades, Station 150.

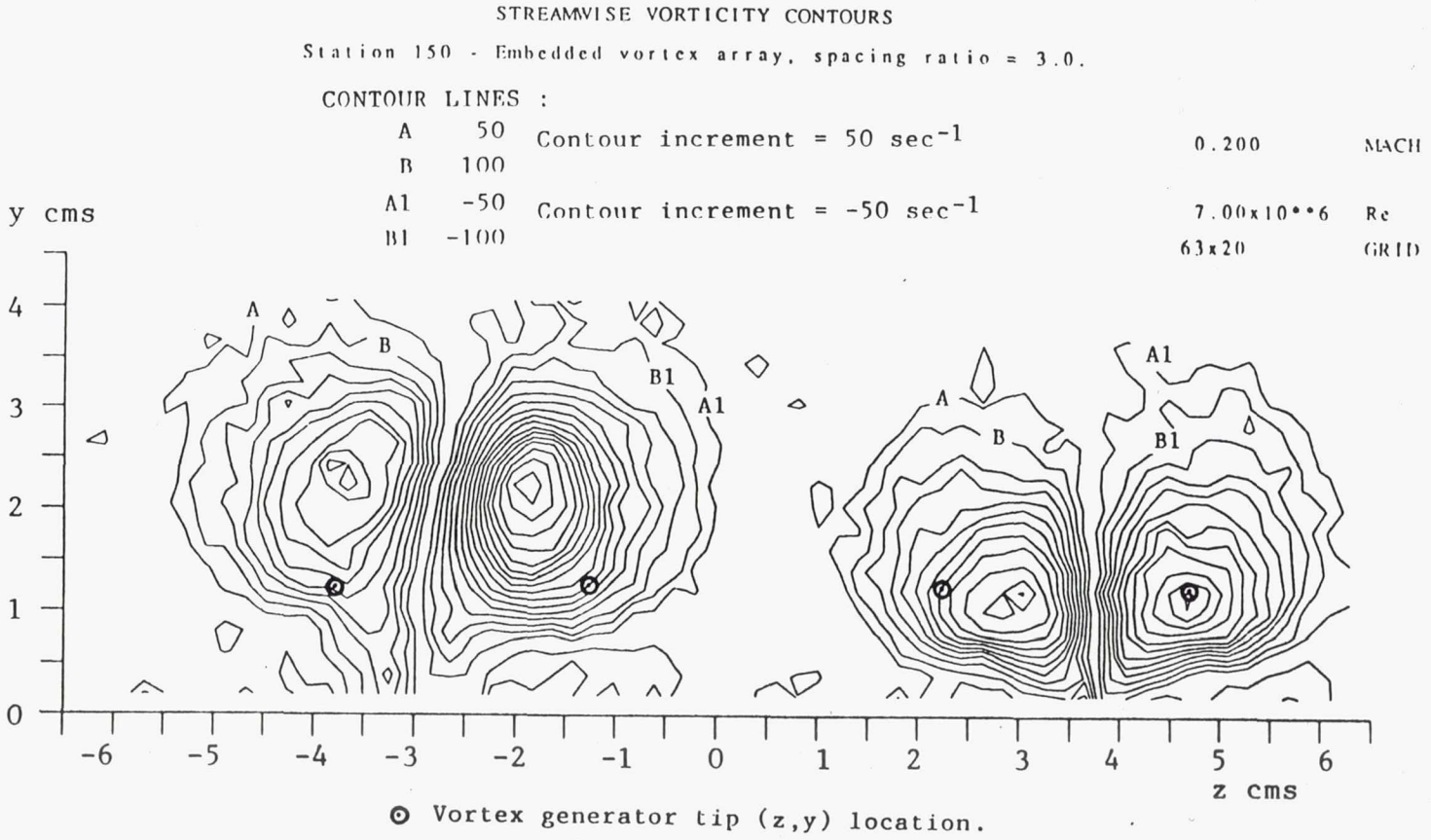

Figure 4.26b - Spacing ratio 3.0 test case, 6 blades, Station 150.

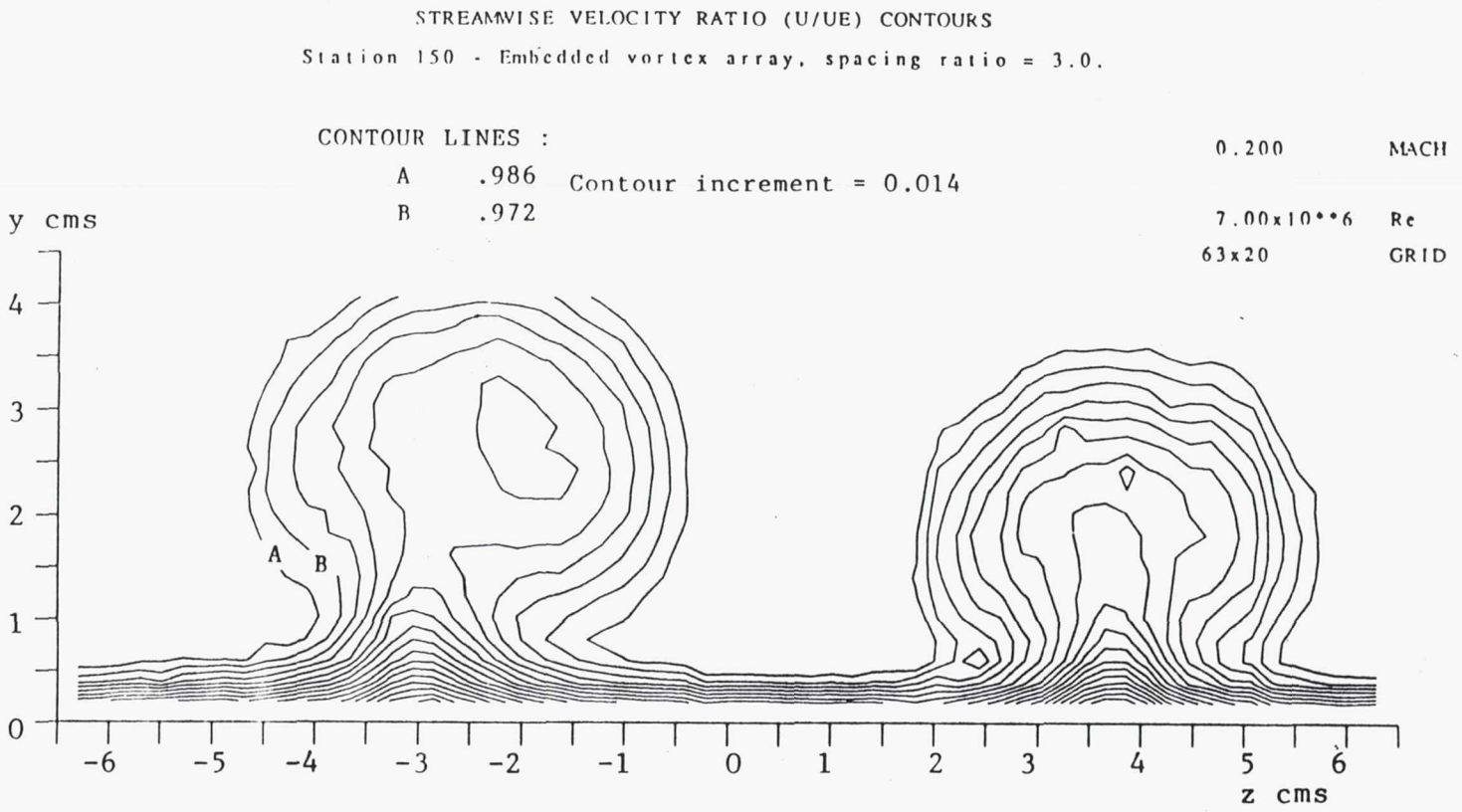

Figure 4.26c - Spacing ratio 3.0 test case, 6 blades, Station 150.

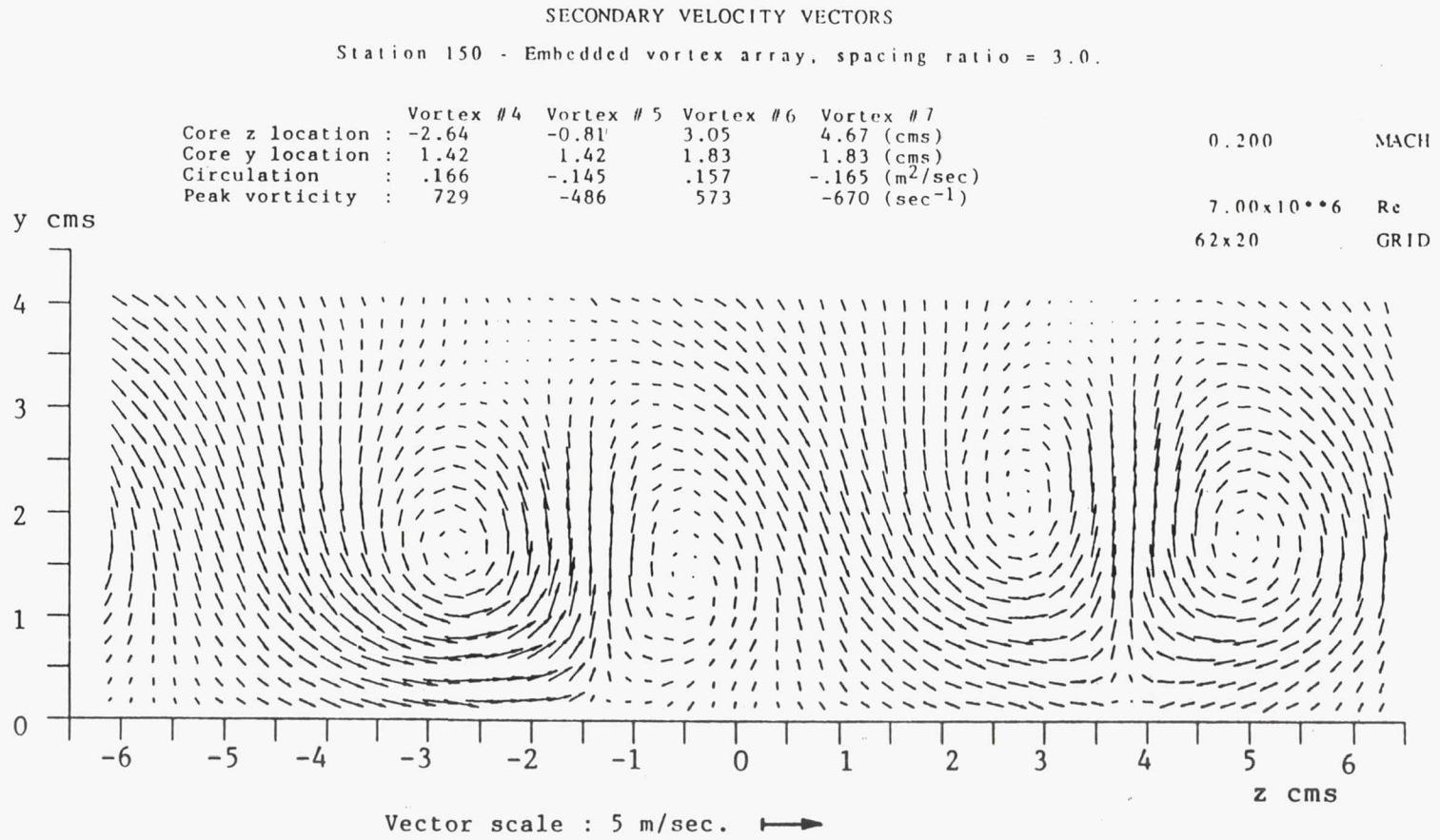

Figure 4.27a - Spacing ratio 3.0 test case, 10 blades, Station 150.

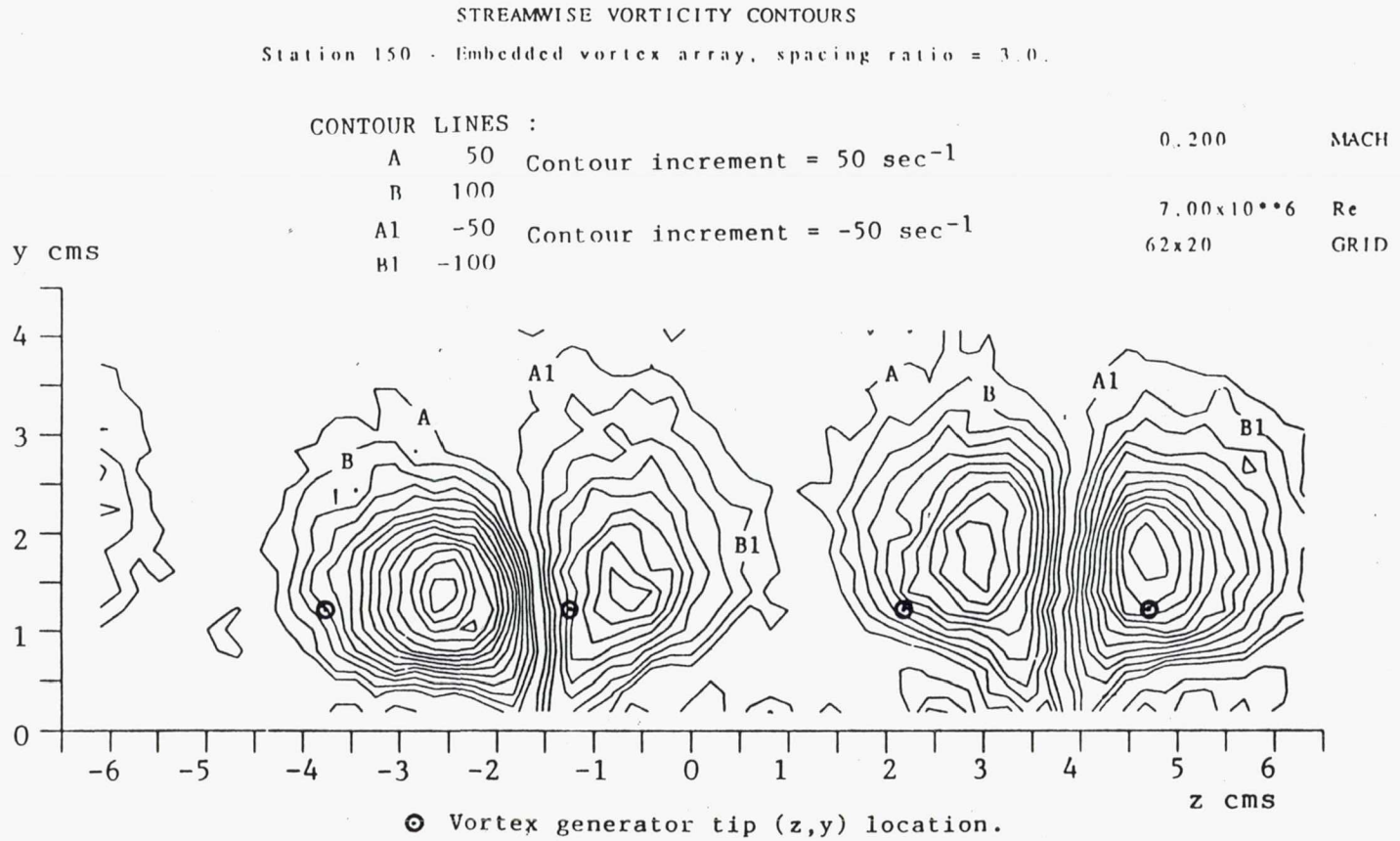

Figure 4.27b - Spacing ratio 3.0 test case, 10 blades, Station 150.

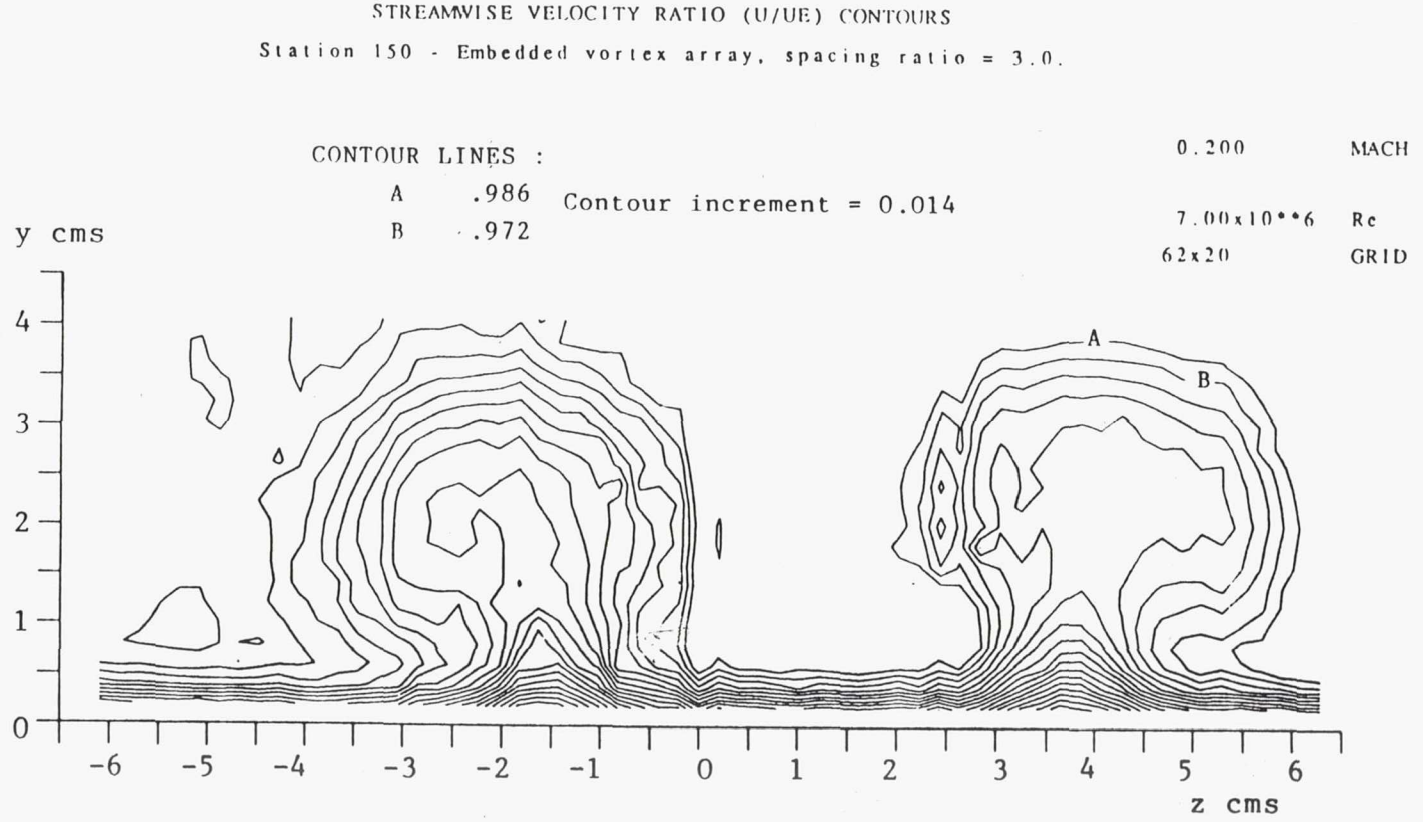

Figure 4.27c - Spacing ratio 3.0 test case, 10 blades, Station 150.

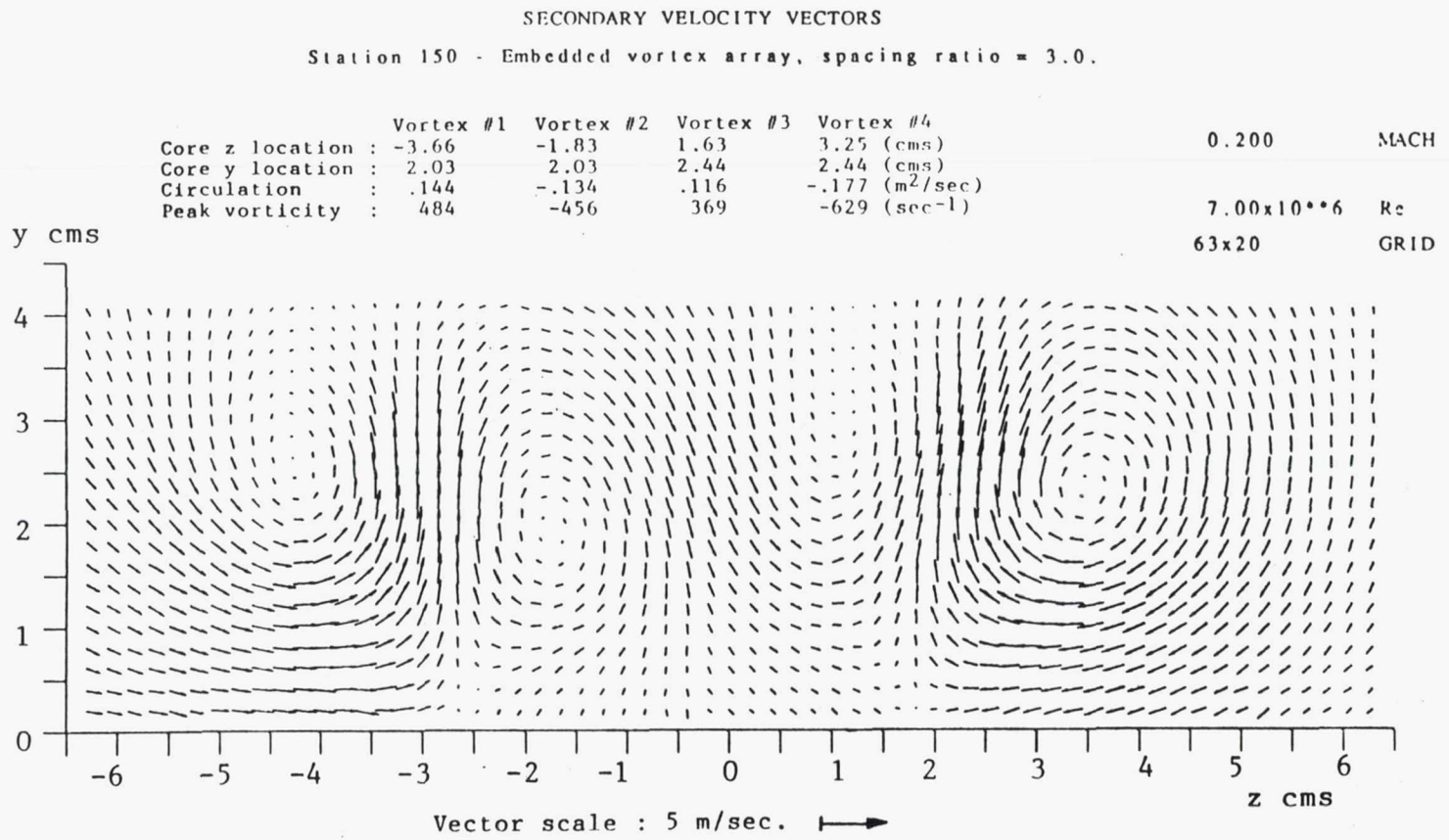

Figure 4.28a - Spacing ratio 3.0 test case, 4 small blades, Station 150.

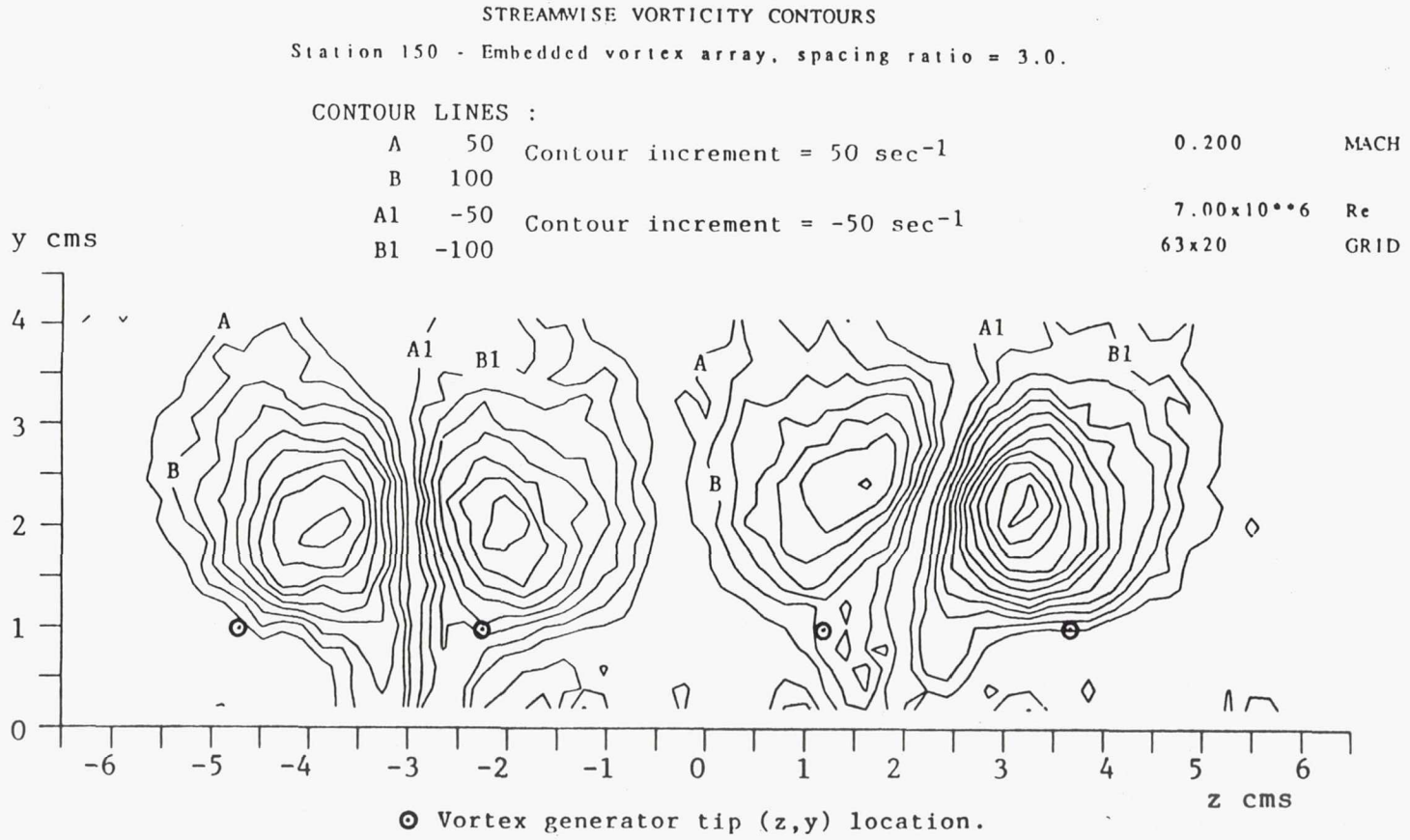

Figure 4.28b - Spacing ratio 3.0 test case, 4 small blades, Station 150.

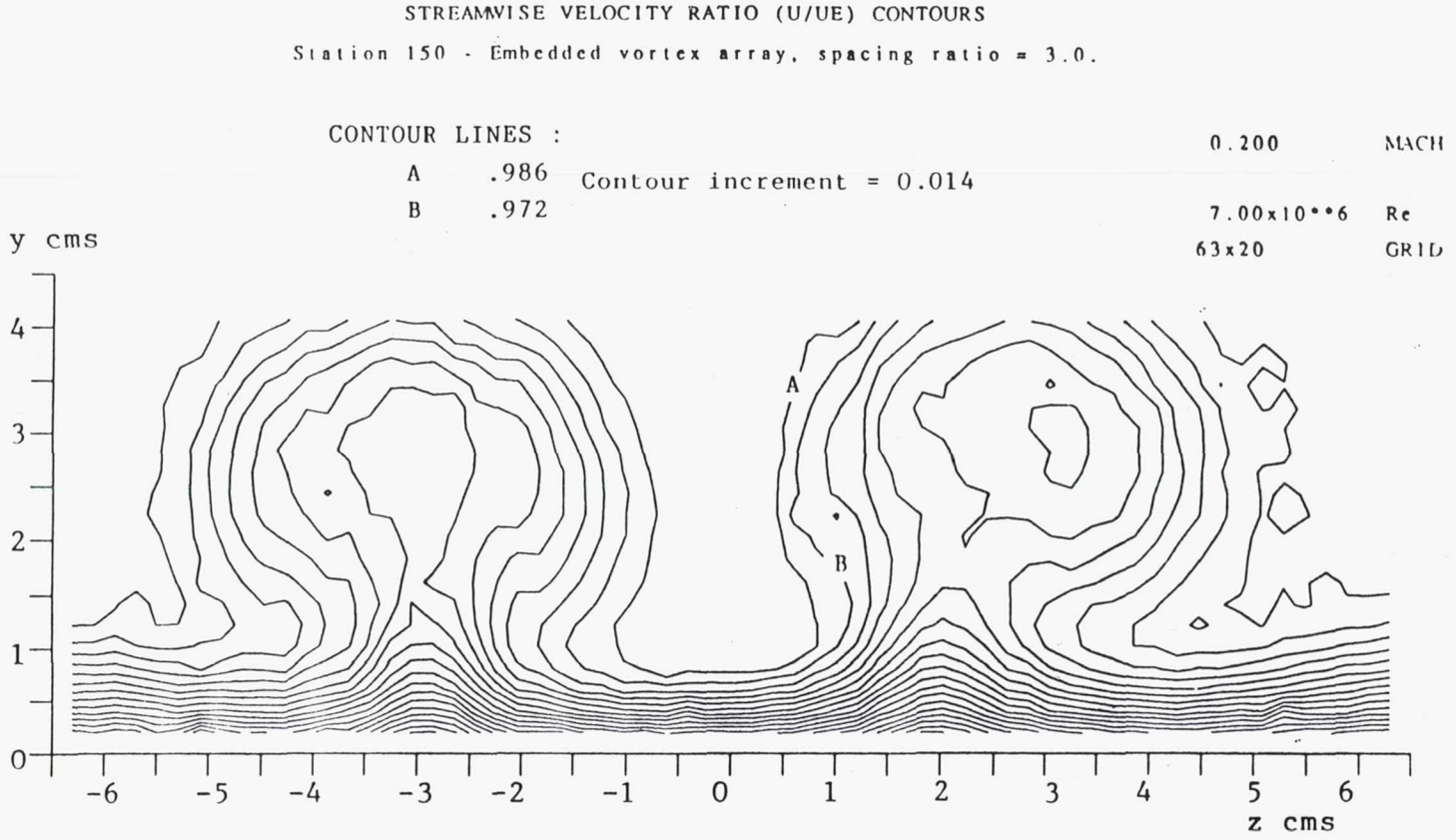

Figure 4.28c - Spacing ratio 3.0 test case, 4 small blades, Station 150.

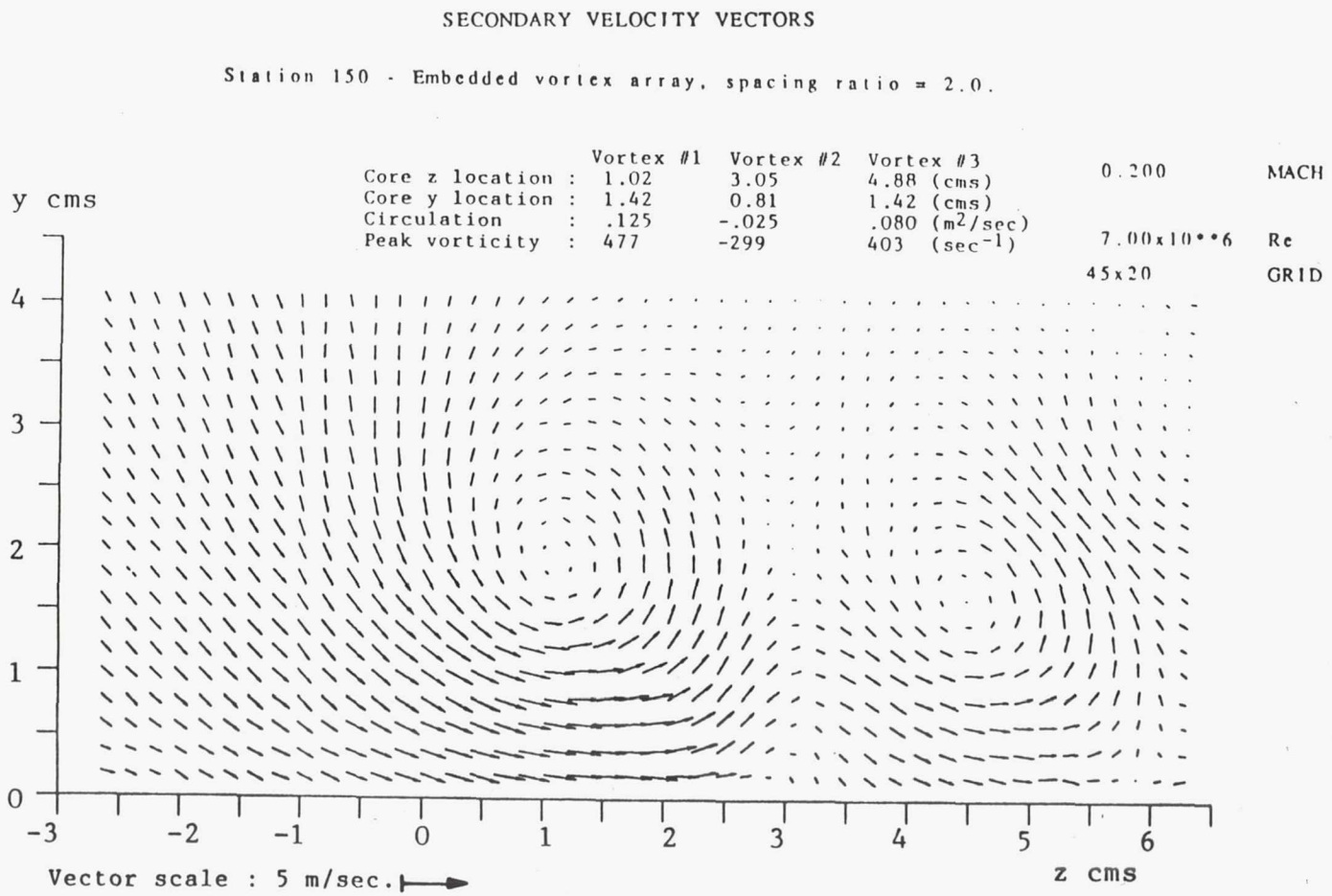

Figure 4.29a - Spacing ratio 2.0 test case, 4 small blades, Station 150.

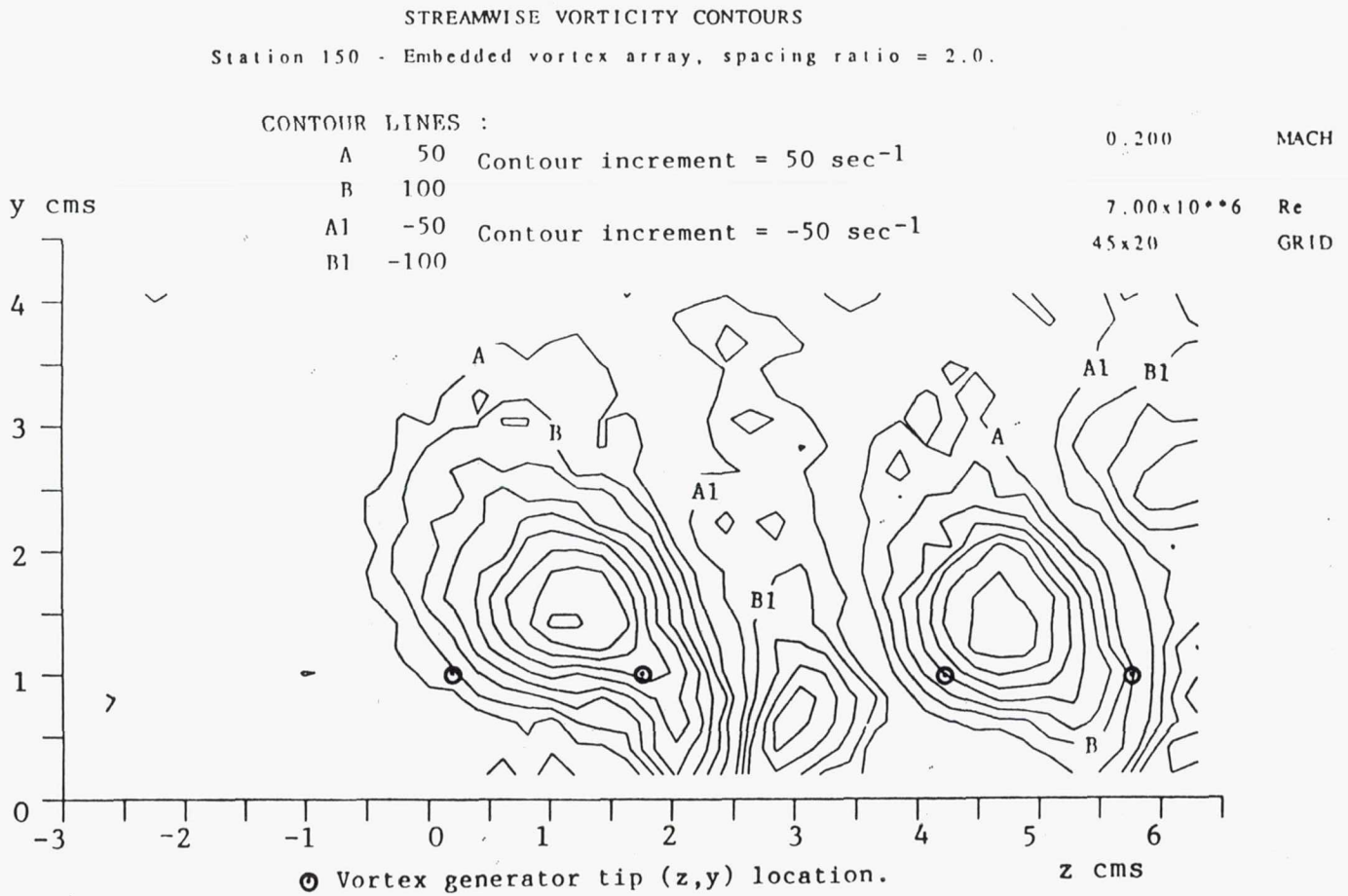

Figure 4.29b - Spacing ratio 2.0 test case, 4 small blades, Station 150.

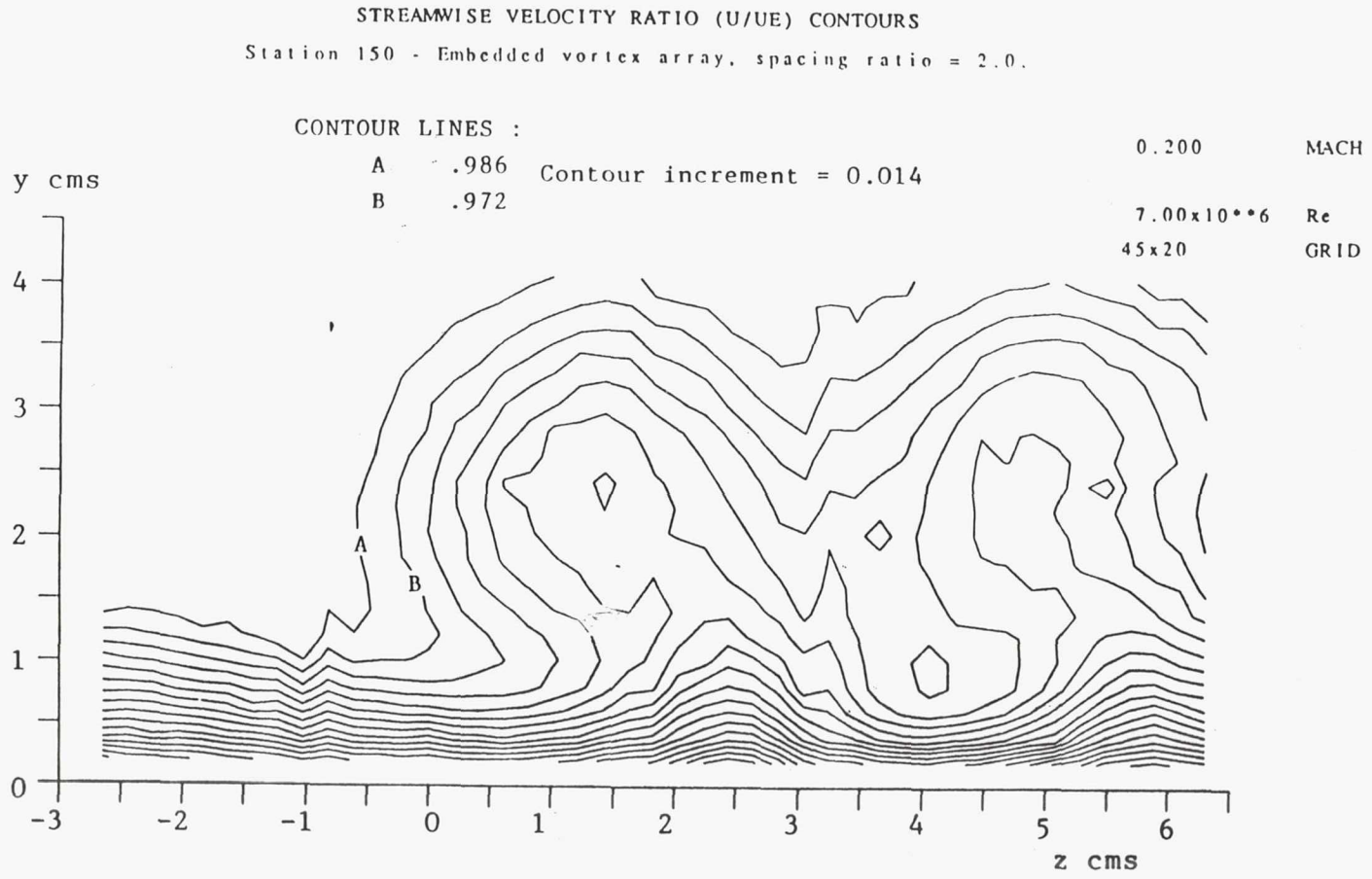

Figure 4.29c - Spacing ratio 2.0 test case, 4 small blades, Station 150.

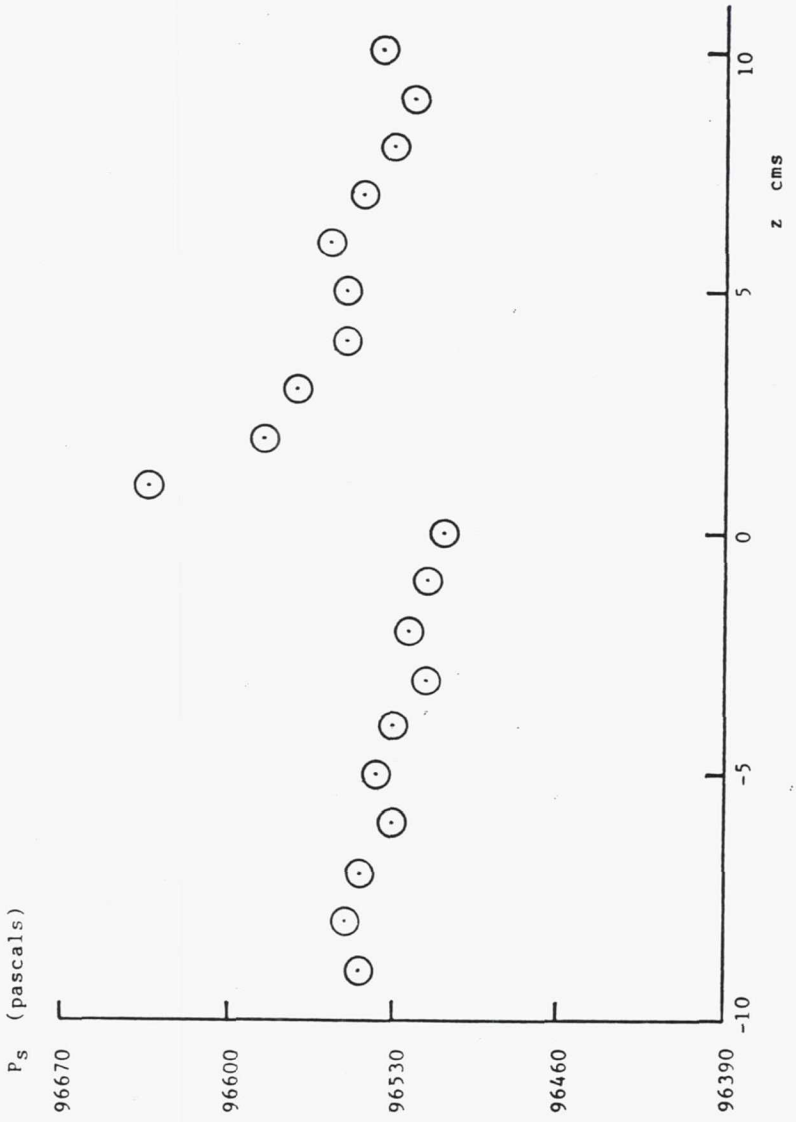

Figure 4.30 - Surface static pressure versus z at Station 66 for the case of the single embedded vortex.

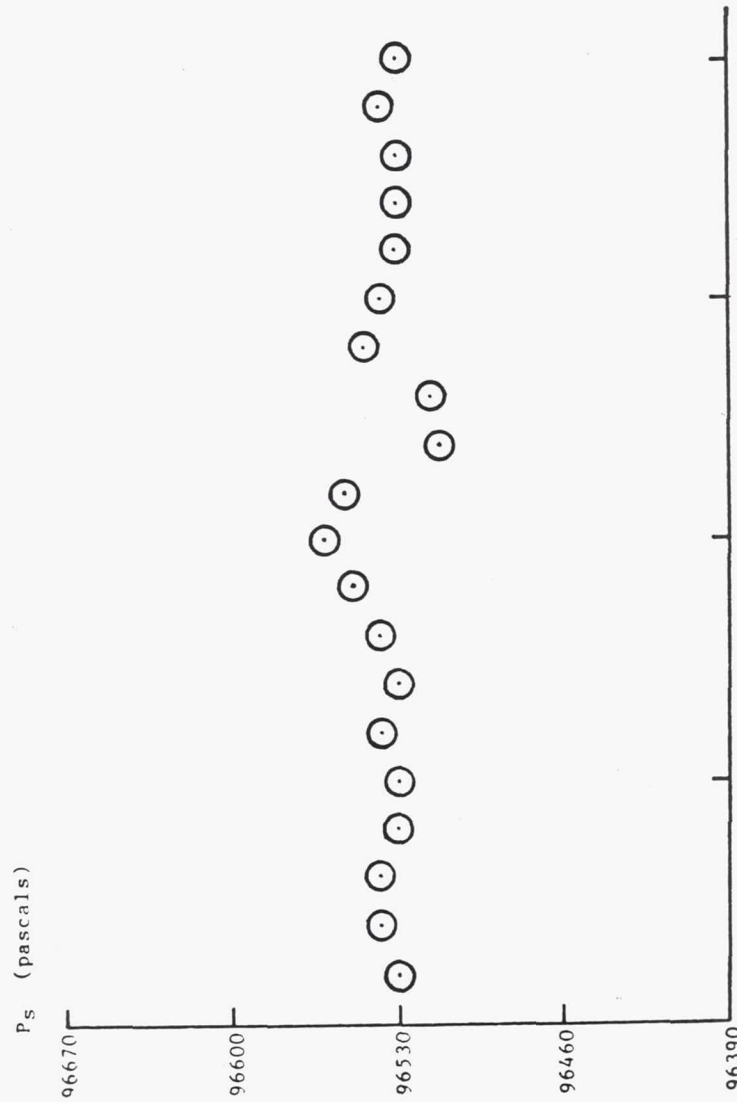

Figure 4.31 - Surface static pressure versus z at Station 81 for the case of the single embedded vortex.

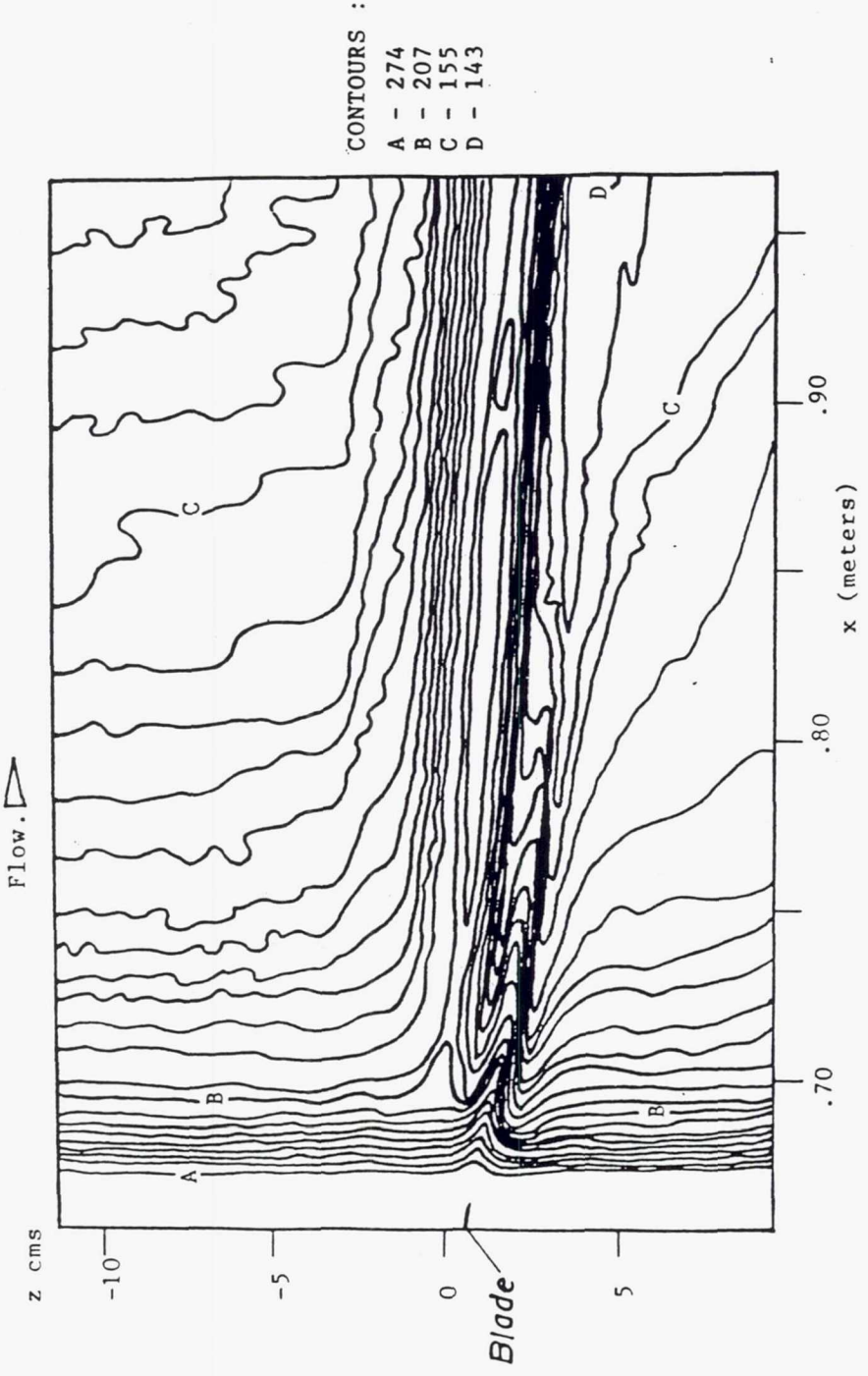

Figure 4.32 - Contours of heat transfer coefficient, h_x, on the surface of the heated splitter plate. The test case is the single embedded vortex. The units of h_x are watts/m^2 $C°$.

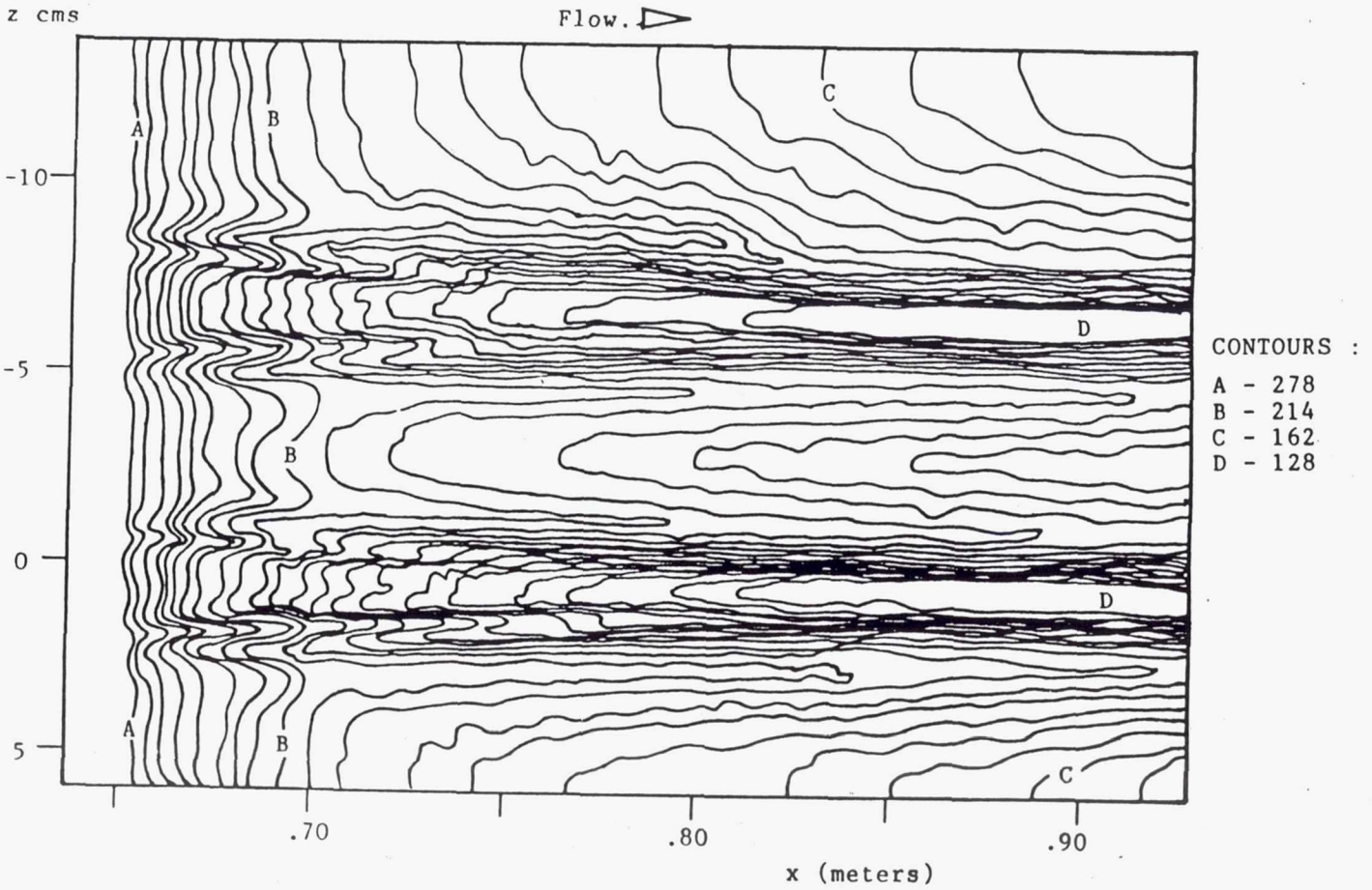

Figure 4.33 - Contours of heat transfer coefficient, h_x, on the surface of the heated splitter plate. The test case is the spacing ratio 4.0 array. The units of h_x are watts/m^2 C°.

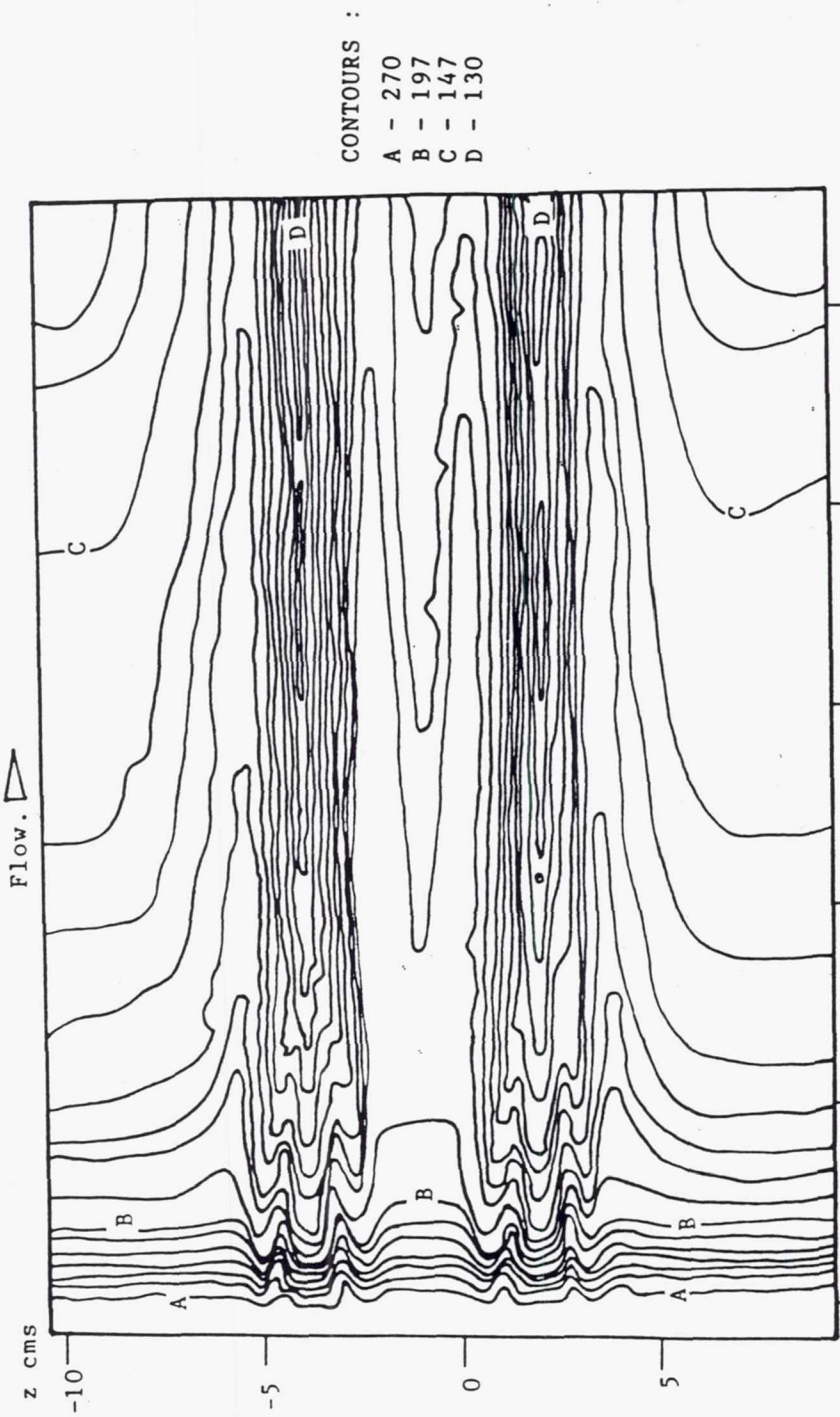

Figure 4.34 - Contours of heat transfer coefficient, h_x, on the surface of the heated splitter plate. The test case is the spacing ratio 3.0 array. The units of h_x are watts/m^2 C^o.

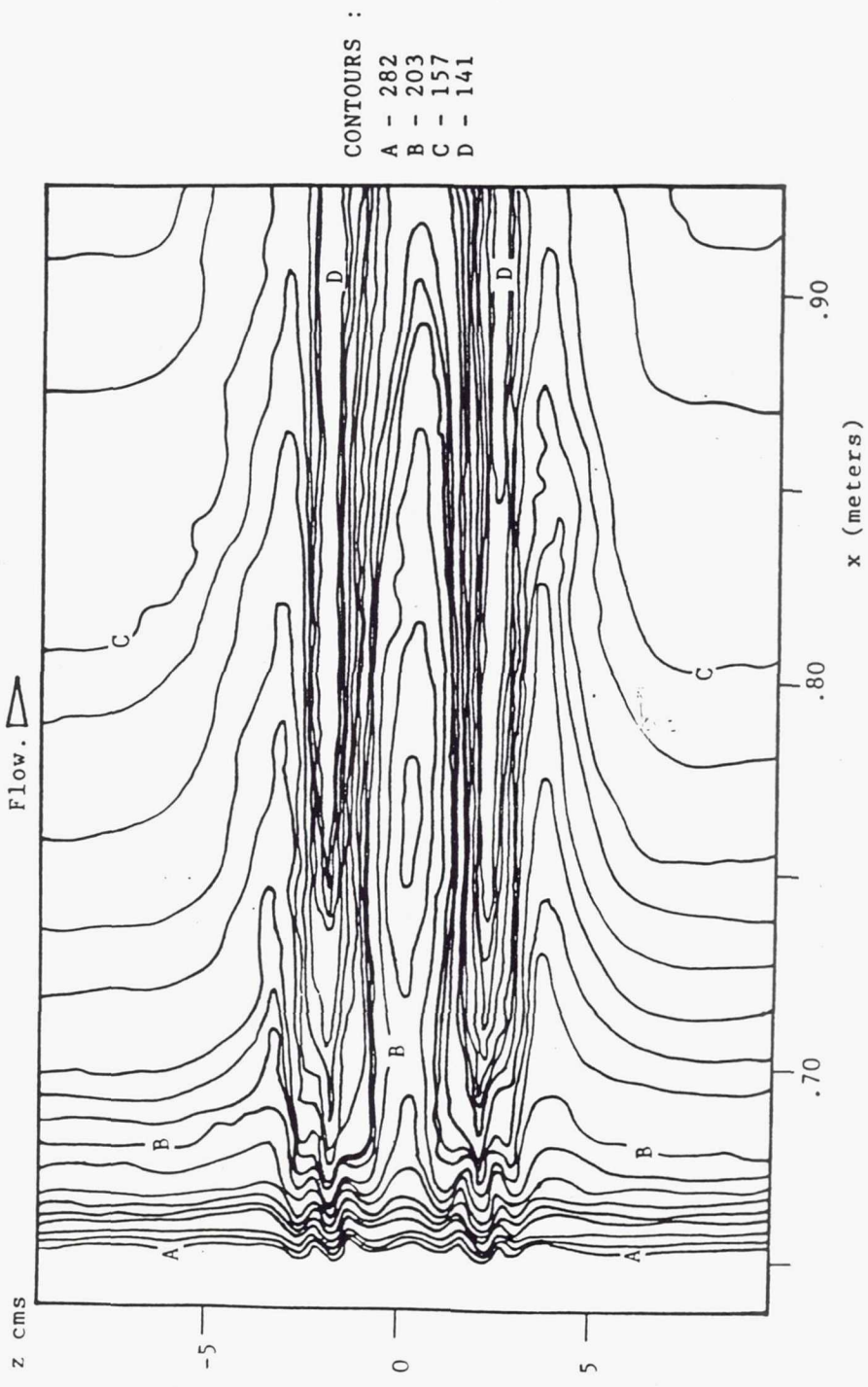

Figure 4.35 - Contours of heat transfer coefficient, h_x, on the surface of the heated splitter plate. The test case is the spacing ratio 2.0 array. The units of h_x are watts/m^2 $C°$.

Chapter 5

Modelling

The mean flow velocity and vorticity data contained in the crossplane plots of Chapter 4 reveal vortex structures that bear a remarkable similarity to the two dimensional vortex models briefly discussed in Chapter 2. Remarkable enough, in fact, to naturally invite comparison. Considering the ease with which these two dimensional models may be constructed, and the fine resolution of the data field, a comparison between the two is easily accomplished and proves instructive. Quantitative results are obtained. The question to be addressed is the following : " How close are these quantitative comparisons and to what extent may the models be used in providing a description of vortex interaction and streamwise development? "

5.1 The Oseen Model of the Viscous Vortex

The two dimensional model which finds utility here is based on the Oseen model of a viscous vortex. The following description is a brief summary of the well established derivation. The Oseen model represents the time dependent decay of a potential vortex

where the velocity at the origin ($r = 0$) is forced to zero at time $t = 0$. The model is developed mathematically through the solution of the Navier-Stokes equation (in cylindrical coordinates). The simplified momentum equation contains only the unsteady and viscous terms. By assuming that the azimuthal velocity of the decaying vortex, v_θ, is a function of r and t only, the θ- momentum equation is written :

$$\frac{\partial v_\theta}{\partial t} = \frac{-\nu}{r}\left[\frac{\partial (r v_\theta)}{r\,\partial r} + \frac{\partial^2 (r v_\theta)}{\partial r^2}\right], \tag{5.1}$$

subject to the boundary conditions :

$$\begin{aligned} v_\theta(r = 0, t) &= 0, \\ v_\theta(r \rightarrow \infty, t) &\sim \frac{\Gamma}{2\pi r} \text{ (potential velocity field)}, \\ v_\theta(r, t = 0) &= \frac{\Gamma}{2\pi r}, \end{aligned}$$

where Γ is the circulation of the potential vortex. The problem described above is analogous to Stoke's classical problem of the oscillating plate. The solution is implemented by first transforming the partial differential equation for v_θ, Eq. (5.1), into an ordinary differential equation through the use of a similarity variable η :

$$\eta = \frac{r}{\sqrt{\nu t}}.$$

The resulting ordinary differential equation :

$$f'' + \left(\frac{\eta}{2} - \frac{1}{\eta}\right) f' = 0,$$

along with the transformed boundary conditions :

$$f(\eta = 0) = 0, \quad f(\eta \rightarrow \infty) = 1,$$

is solved exactly. The angular velocity of the Oseen vortex is found to be (in terms of r and t) :

$$v_\theta = \frac{\Gamma}{2\pi r}(1 - \exp^{-r^2/(4\nu t)}). \tag{5.2}$$

Following Squire (1965) the unsteady solution is transformed to a steady one by relating the decay time to the distance between the vortex generator tip and the crossplane of interest $(x - x_0)$:

$$t = \frac{x - x_0}{u} = \frac{x^*}{u} \approx \frac{x^*}{U_\infty}. \tag{5.3}$$

The last relationship is approximate since the streamwise velocity will differ from the freestream value somewhat, due to either the core velocity deficit and/or the presence of the boundary layer. The velocity components in cartesian coordinates for an isolated Oseen vortex of strength Γ_i having a core centered on (z_i, y_i) are :

$$v_i = \frac{\Gamma_i(z - z_i)}{2\pi R_i^2}\left[1 - \exp\left\{\frac{-U_\infty R_i^2}{4\nu x^*}\right\}\right], \tag{5.4}$$

$$w_i = \frac{-\Gamma_i(y - y_i)}{2\pi R_i^2}\left[1 - \exp\left\{\frac{-U_\infty R_i^2}{4\nu x^*}\right\}\right], \tag{5.5}$$

where :

$$R_i^2 = (z - z_i)^2 + (y - y_i)^2.$$

The Oseen vortex is composed of a viscous core or "inner region" where azimuthal velocity varies linearly with r, and an inviscid outer region identical to the outer flow region of a potential vortex of strength Γ_i.

The vorticity of the Oseen vortex is determined to be :

$$\omega_x^i = \frac{1}{r}\frac{\partial}{\partial r}(rv_\theta) = \frac{U_\infty \Gamma_i}{4\pi\nu x^*} \exp\left\{\frac{-U_\infty r^2}{4\nu x^*}\right\},$$

or, in cartesian coordinates :

$$\omega_x^i = \frac{U_\infty \Gamma_i}{4\pi\nu x^*} \exp\left\{\frac{-U_\infty R_i^2}{4\nu x^*}\right\}. \tag{5.6}$$

The peak vorticity at (z_i, y_i) is thus :

$$\omega_{max}^i = \frac{U_\infty \Gamma_i}{4\pi\nu x^*}. \tag{5.7}$$

The circulation of the Oseen vortex is :

$$\int_0^\infty \omega_x^i \, 2\pi r \, dr = \Gamma_i,$$

as expected.

Since Eq. (5.1) is linear we can superimpose solutions for a representation of the wall and neighboring vortices. Figure 5.1a illustrates how a representation of a single *embedded* vortex is constructed. Eqs. (5.4) and (5.5) represent the secondary velocities v_i and w_i for the vortex above the wall. The equations for the secondary velocities of the vortex below the wall (the "image" vortex) are identical to Eqs. (5.4) and (5.5) except that the signs on the circulation (Γ_i) and normal location of the vortex (y_i) are switched. Call these velocities v_{imi} and w_{imi}. The equations representing the embedded vortex are then simply :

$$v = v_1 + v_{im1},$$

$$w = w_1 + w_{im1}. \tag{5.8}$$

Figure 5.1b illustrates the construction of an embedded array of N_v vortices. The secondary velocities of this flow field are :

$$\begin{aligned} v &= v_1 + v_{im1} + v_2 + v_{im2} + \cdots + v_{N_v} + v_{imN_v}, \\ w &= w_1 + w_{im1} + w_2 + w_{im2} + \cdots + w_{N_v} + w_{imN_v}. \end{aligned} \tag{5.9}$$

5.1.1 Comparison to Crossplane Data

The model is constructed by matching the data descriptors to the values listed in Tables 4.2 and 4.3. The peak vorticity, ω^i_{max}, does not appear explicitly in Eqs. (5.4) and (5.5). We can, however, use Eq. (5.7) and solve for the viscosity coefficient, ν, in terms of ω^i_{max}. Why the viscosity coefficient? Since the model represents embedded vortices in *turbulent* flow we could hardly expect a coefficient of viscosity typical of molecular diffusion to represent diffusion here. Thus :

$$\nu = \nu_i = \frac{U_\infty \Gamma_i}{4\pi x^* \omega^i_{max}}. \tag{5.10}$$

ν_i, the "vortex eddy viscosity", is substituted for ν in Eqs. (5.4) and (5.5). As an example, consider the single embedded vortex at Station 74. Recall that $x^* = x - x_0 = .737 - .640 = .097$ m. From the descriptors in Table 4.2 the vortex eddy viscosity is determined to be :

$$\nu_i = 5.5 \times 10^{-4} \ m^2/sec, \quad \text{(Station 74)}$$

or :

$$\nu_i/\nu_{lam} \approx 35, \quad \text{(Station 74)}$$

where ν_{lam} is the appropriate value of the kinematic viscosity of air. With ν_i represented by Eq. (5.10) the equations for the Oseen votex are written :

$$v_i = \frac{\Gamma_i(z-z_i)}{2\pi R_i^2}\left[1-\exp\left\{\frac{-\pi\omega^i_{max}}{\Gamma_i}R_i^2\right\}\right], \tag{5.11}$$

$$w_i = \frac{-\Gamma_i(y-y_i)}{2\pi R_i^2}\left[1-\exp\left\{\frac{-\pi\omega^i_{max}}{\Gamma_i}R_i^2\right\}\right], \tag{5.12}$$

$$\omega^i_x = \omega^i_{max}\exp\left\{\frac{-\pi\omega^i_{max}}{\Gamma_i}R_i^2\right\}. \tag{5.13}$$

Note how the streamwise velocity drops out when the model equations are written in terms of the vortex descriptors.

Figures 5.2a-g illustrate the comparison between the model and the data for the case of the single embedded vortex at Station 74.

Figure 5.2a illustrates the secondary velocity vector fields of both the model and data. They are strikingly similar in appearance.

Figure 5.2b illustrates the corresponding vorticity fields. The model vorticity field does not have the region of secondary vorticity found in the data. This is not surprising since the two dimensional model with inviscid boundaries has no mechanism for either the production or convection of opposite sign vorticity.

Figure 5.2c compares the w velocity profile through the vortex center (at $z_i = 1.52$ cm) for both the model and data. The model overpredicts the near wall component by about 10 percent. This, again, is probably the result of the no slip condition at the wall.

Figure 5.2d illustrates the comparison between the model and data v velocity profile through the vortex center (at $y_i = 1.03$ cm) over the spanwise length of the survey region. The velocity magnitudes are within a few percent in the regions away from the core. Near the core boundary, where $\partial v/\partial z$ is large, the v velocity profiles diverge somewhat. The divergence in the upwash region of the profile appears to be slightly greater than in the

downwash region.

Figure 5.2e illustrates the comparison between model and data w velocity profiles at $z = 0.50$ cms, located in the downwash region of the vortex. Figure 5.2f compares the w velocity profiles in the vortex upwash region at $z = 2.41$ cms. Figure 5.2f indicates that the model overpredicts the spanwise velocities in the upwash region of the vortex. This effect is not confined to the near wall region alone but extends over the y length of the survey region. The discrepancy peaks at about 30 percent near $y = 0.64$ cms.

Figure 5.2g is a contour plot of the variance between the model and data for the case of the single embedded vortex at Station 74. This variance is defined to be :

$$\frac{\left\| \vec{V}_{data} - \vec{V}_{model} \right\|}{\left\| \vec{V}_{data} \right\|}, \tag{5.14}$$

where $\vec{V}$ is the secondary velocity vector. Figure 5.2g confirms the results of the velocity profile plots – the model mimics the data to within 5 percent everywhere except in the upwash region of the vortex. Here the variance can become as large as 40 percent.

Figures 5.3a-g illustrate the corresponding comparison between the model and the data for the case of the single embedded vortex at Station 150. In general terms the comparison between model and data is not as good at the downstream station as it is at Station 74. The effects of primary and secondary vorticity convection on the core structure of the vortex seen in the crossplane data are not represented by the model. Even so, quantitative comparisons indicate that model and data still differ by only a few percent in particularly significant regions of the secondary flow field.

Figures 5.3a-b illustrate the model and data secondary velocity vector and streamwise vorticity fields, respectively. The elliptical core profile seen in the data in these two figures is not reproduced by the model. This "stiffness" of the model with respect to the structure of

the vortex core occurs for one of the same reasons that the region of opposite sign vorticity is not reproduced; namely that no mechanism exists in the two dimensional model for convection of core vorticity.

Figure 5.3c is a plot of the spanwise velocity w through the center of the vortex (at $z_i = 4.06$ cms) for both data and model. The model representation of the data here is good; the agreement is within a few percent except near the wall where the model overpredicts w by about 15 percent.

Figure 5.3d is a plot of the normal velocity v through the vortex core (at $y_i = 1.41$ cms) for both the data and model. Here the model underpredicts the v velocity in the vortex downwash by about 30 percent and overpredicts v in the upwash region by about the same amount. The data profile seems to be somewhat broader or "fatter" than the corresponding model profile. The representation of the v velocity data in and near the core is still quite good; the agreement is within a few percent.

Figures 5.3e-f illustrate w velocity profile comparisons in the downwash and upwash regions of the vortex, respectively. In the downwash region the agreement is within 15 percent where, surprisingly, the model underpredicts the w velocity in the vicinity of the wall. In the vortex upwash region the model tends to overpredict the w velocity near the wall and vortex core. The maximum discrepancy occurs near the wall and is equal to about 45 percent.

Figure 5.3g is a contour plot of the variance defined by Eq. (5.14). Although the model core lacks the elliptical profile of the data, the agreement between the two is still quite good, particularly in the region of the core and vortex downwash. As with the case at Station 74, the model and data diverge in the upwash region of the vortex. In Figure 5.3g the divergence is amplified somewhat in the upwash by the small magnitudes of the measured velocities here, since the magnitudes of these velocities appear as the denominator in Eq.

(5.14).

Oseen Model Circulation Defect for Vortices in Close Proximity

A subtle characteristic of the Oseen model poses a potential difficulty in the representation of the embedded vortex at Station 150. The model vortex illustrated in Figures 5.3a-b is constructed by matching descriptors with the corresponding data. The value of Γ_i used as input to the model equations matches the value determined from the data. However, the model vortex turns out to be weaker than the corresponding vortex revealed in the data crossplane. How can this be? The answer lies in the nature of the model and the way it is constructed.

In the same manner as the velocity field, the vorticity field of the model is pieced together by superposition. The vorticity field of the model vortex is :

$$\omega_x = \omega_x^i + \omega_{xim}^i, \tag{5.15}$$

where ω_x^i is given by Eq. (5.13), and ω_{xim}^i by Eq. (5.13) with the signs switched on Γ_i and y_i. Mathematically speaking, the "wall" in the model represents a line of top and bottom mirror image symmetry with respect to the vorticity magnitude. On the wall itself the vorticity is zero. In the case of the single embedded model vortex, the vorticity field above the wall is positive, below the wall it is negative.

As the model vortex is brought closer to its image a portion of the streamwise vorticity surrounding the core location (z_i, y_i) is cancelled by the image vorticity field. This, in turn, accounts for the discrepancy between the actual circulation of the model vortex, Γ_a, and its input value, Γ_i. Lets term the ratio $(\Gamma_i - \Gamma_a)/\Gamma_i$ the "circulation defect" of the model. The circulation defect is a function of the model vortex concentration and its normal distance

from the wall, y_i. The vortex concentration is a measure of the extent to which the vortex core has grown or diffused. A quantitative measure of concentration is the coefficient on the exponent in Eq. (5.13) :

$$B_i = \frac{\pi \omega^i_{max}}{\Gamma_i}. \tag{5.16}$$

When B_i is large the vortex is highly condensed, and the core region containing most of the primary vorticity is very small. We can now manipulate Eq. (5.15) to obtain the circulation defect :

$$\frac{\Gamma_i - \Gamma_a}{\Gamma_i} = 1 - \mathbf{erf}\left(y_i \sqrt{B_i}\right), \tag{5.17}$$

where

$$\mathbf{erf}(x) = \frac{2}{\sqrt{\pi}} \int_0^x \mathrm{e}^{-x^2}\, dx$$

is the error function. When the argument of the error function is large (i. e. when the vortex is highly condensed and/or far from the wall) the circulation of the model vortex is equal to its input value and the circulation defect is zero. When $y_i = 0$ the vortex model and its image coincide and cancel each other exactly. For this case Eq. (5.17) predicts a circulation defect of one (or "one hundred percent") as expected.

At Station 74 B_i has a value of about 325000 m^{-2}. The circulation defect here is nearly zero and no significant difference exists between the actual and input circulations of the model. This fact is easily verified by a numerical integration of the vorticity field produced by the model. An examination of Figure 5.2b would also reveal as much since the vorticity contours show a highly condensed core with plenty of space between its outer boundary and the wall.

Examination of the model vortex at Station 150 in Figure 5.3b reveals a much larger core. Here the vorticity contours seemingly merge with the wall indicating some cancellation

due to the image field. The value of B_i here is about 18000 m^{-2}. Eq. (5.17) indicates a circulation defect :

$$(\Gamma_i - \Gamma_a)/\Gamma_i = 0.031 \text{ or } 3.1\%.$$

Though the model input circulation is set equal to 0.228 m^2/sec, its true strength is about 3 percent less or 0.221 m^2/sec. This was also verified by a numerical integration of the model vorticity field.

The circulation defect occurs not only between a model vortex and its image. Any combination of counter-rotating model vortices in close proximity will have a circulation defect. For two counter-rotating vortices of roughly equal strength and concentration located sufficiently far from the wall Eq. (5.17) provides an approximation to the circulation defect :

$$\frac{\Gamma_i - \Gamma_a}{\Gamma_i} \approx 1.0 - \mathbf{erf}\left(\sqrt{B_i}\frac{r_0}{2}\right) \tag{5.18}$$

for each vortex i, where r_0 is the distance between core centers.

Although a circulation defect exists for model vortices in close proximity, a value greater than zero does not occur in this study unless the vortices have descriptors matching the data at Station 150. Even then, the discrepancy between the input circulation of the model and its actual value ranges from 0 to only about 3 percent. In most of the downstream cases modelled the discrepancy is less than 1 percent. This is verified by direct integration of the vorticity field produced by the model vortices. The circulation defect of the Oseen model does not, therefore, present a significant problem in the representation of vortex structure at either survey station.

The Elliptical Oseen Model

The streamwise vorticity contours formed from the velocity data of the single embedded vortex at Station 150 reveal a core with an elliptically distorted profile. The strong secondary flows occurring along the wall draw the initially circular distribution of core vorticity into this particular shape. The model vortex produces a vorticity profile more circular in nature. This stiffness is a characteristic of the model and is partly responsible for the circulation defect observed in the model vortices. By a few minor adjustments to the model equations the vorticity profile of the model can be given an elliptical shape which more closely resembles the data. These adjustments "unstiffen" the model profile, providing a rough representation of the distortional convective effects of the secondary flow.

An isolated elliptical Oseen vortex located at (z_i, y_i) has secondary velocities :

$$\begin{aligned} v_i &= \frac{\Gamma_i (z - z_i)}{2\pi R_{ie}^2} \left[1.0 - \exp\left\{-B_i R_{ie}^2\right\}\right], \\ w_i &= \frac{-\Gamma_i a_{ie} (y - y_i)}{2\pi R_{ie}^2} \left[1.0 - \exp\left\{-B_i R_{ie}^2\right\}\right], \end{aligned} \tag{5.19}$$

and

$$R_{ie}^2 = (z - z_i)^2 + a_{ie}(y - y_i)^2.$$

B_i is given by Eq. (5.16) and a_{ie} is termed the "ellipticity coefficient". When $a_{ie} = 1.0$ the equations of the Oseen model, Eqs. (5.11) and (5.12), are recovered. The vorticity field of the elliptical model is :

$$\omega_x^{ie} = \frac{\Gamma_i}{\pi} B_i \varphi \exp\left\{-B_i R_{ie}^2\right\} - \frac{\Gamma_i}{2\pi R_{ie}^2} \left(1.0 - \exp\left\{-B_i R_{ie}^2\right\}\right) (2\varphi - 1 - a_{ie}), \tag{5.20}$$

where :

$$\varphi = \left[(z - z_i)^2 + a_{ie}^2 (y - y_i)^2\right] / R_{ie}^2. \tag{5.21}$$

The peak vorticity of the elliptical model, ω^{ie}_{max}, is related to the peak vorticity of the Oseen model, as follows :

$$\frac{\omega^{ie}_{max}}{\omega^{i}_{max}} = \frac{1 + a_{ie}}{2}. \tag{5.22}$$

This relation is obtained by taking the limit of Eq. (5.20) as z and y go to zero.

Note that Γ_i is not the circulation of the elliptical vortex (unless $a_{ie} = 1$). The vorticity of the elliptical model goes to zero (as R_{ie} extends to infinity) much more slowly than the Oseen model. One result of this is that the flow field surrounding the elliptical vortex is only "weakly inviscid". The circulation of the elliptical vortex depends on the size of the area (vortex plus surroundings) examined. We can integrate the vorticity over the entire domain to obtain the circulation of the isolated elliptical model, Γ_{ie} :

$$\frac{\Gamma_{ie}}{\Gamma_i} = \frac{2}{\pi}\left[\frac{1}{\sqrt{a_{ie}}}\tan^{-1}(\sqrt{a_{ie}}) + \sqrt{a_{ie}}\tan^{-1}\left(\frac{1}{\sqrt{a_{ie}}}\right)\right]. \tag{5.23}$$

An examination of Figure 5.4 reveals some of the peculiarities of the isolated elliptical vortex. Figure 5.4 is a plot of the streamwise vorticity field of Eq. (5.20) with $\Gamma_i = .200$ m^2/sec, $B_i = 23000$ m^2, and $a_{ie} = 1.5$. The origin of the vortex is located at (0,0) and the figure illustrates the first quadrant in the z, y plane. Mirror image symmetry applies along both the z and y axes. To emphasize the character of the vorticity field surrounding the vortex, two different contour increments were used. The strongly positive vortex "core" has its major axis parallel to the z coordinate axis (a result of $a_{ie} > 1$). A region of weak opposite sign vorticity exists above and below the core. The line of zero vorticity runs diagonally across the figure and divides the regions of weak negative and positive vorticity. Figure 5.5a is the corresponding velocity vector plot of the isolated elliptical vortex. Figure 5.5b is the same, except that the origin has been displaced into the first quadrant to provide a more complete view of the vortex.

The wall is introduced into the elliptical model by placement of an image vortex in the same manner as discussed for the Oseen model. The descriptors of the elliptical model were then matched with the data for the single embedded vortex at Station 150 following an iterative procedure. An initial value of a_{ie} was chosen. Values of ω^i_{max} and Γ_i were adjusted until the peak vorticity and circulation of the elliptical model (determined numerically) matched the corresponding data descriptors. The model vorticity contours were then compared to the data and, if necessary, a new value of a_{ie} was put back into the model equations and the process was repeated. $a_{ie} = 1.3$ provided the best match with the data contours shown in Figure 4.11b. Figure 5.6a illustrates the secondary velocity vectors of the elliptical model. The secondary velocity field of Figure 4.11a is reproduced for comparison. Figure 5.6b illustrates the corresponding streamwise vorticity contours.

The improvements gained in profile appearance through the use of the embedded elliptical model are substantial. In quantitative terms, however, the improvements over the Oseen model (Eqs. (5.19) with $a_{ie} = 1.0$) are slight. This is demonstrated in the velocity profile plots of Figures 5.7a-d which correspond to the plots of Figures 5.3c-f.

The elliptical model of the isolated vortex, while satisfying continuity, does not represent the solution to any particular flow equation such as Eq. (5.1). The validity of superposition of equations needed to represent embedded and multiple vortices will therefore rest on shaky ground. Equations for the descriptors of the isolated elliptical vortex (i. e. Eqs. (5.22) and (5.23)) can serve only as approximations for other cases. In an array of elliptical vortices of a general composition the equations describing the peak vorticity and circulation of each vortex will be considerably more complicated than those appropriate for the isolated case. For these reasons the modelling done subsequent to this point will involve the Oseen description with $a_{ie} = 1$, unless noted otherwise.

Oseen Model Description of an Embedded Vortex Array

Figures 5.8-5.10 illustrate some examples of the Oseen model description of the embedded vortex array. The descriptors of the model vortices in each array are matched with the corresponding descriptors of the data given in Tables 4.2 and 4.3. As in the case of the single embedded vortex, the model tends to fit the data better at the upstream station. Here the vortices are newly formed and possess a highly concentrated core that is largely undistorted by the convective influences of the wall and neighboring vortices.

Figures 5.8a-b illustrate the Oseen model description of the secondary flow field produced in the crossplane at Station 74 by an embedded vortex array having an initial spacing ratio of 2.0. The crossplane data plots are included for comparison. The secondary velocity vector fields are compared in Figure 5.8a, the corresponding streamwise vorticity fields in Figure 5.8b.

Figure 5.8c is a plot of the model v velocity profile through the center of vortex no. 3 ($y = 1.16$ cms.) over the spanwise length of the survey grid. The corresponding v velocities of the data profile are plotted for comparison.

Figures 5.9a-b illustrate the Oseen model description of the secondary flow field produced in the crossplane at Station 150, again by an embedded vortex array of initial spacing ratio 2.0. Elliptically distorted core profiles can be observed in both the model vortex arrays and the data. Generally speaking, the model vortex cores are not distorted to the same extent as the vortex cores revealed in the data crossplane plots at Station 150. The two interior vortices (vortices 2 and 3) in Figure 5.9b have core vorticity profiles which seem to be more highly distorted than the profiles for either exterior vortex. This is a characteristic shared by both the model and data.

Figure 5.9c is a plot of the model v velocity profile through the center of the interior vortex pair ($y = 1.41$ cms.) over the spanwise length of the survey grid. The largest

discrepancy occurs in the downwash region of the flow generated by the two exterior vortices. Here the model v velocity magnitude is only about one third of the value indicated by the data.

Figures 5.10a-b illustrate the Oseen model description of the secondary flow field produced in the crossplane at Station 150 by a vortex array with an initial spacing ratio of 4.0. Figure 5.10c is a plot of the model v velocity profile at $y = 2.64$ cms. (roughly through the center of vortices 3 and 4) over the spanwise length of the survey grid. Here the v velocity profile contained in the data provides a close match to the model. The discrepancy peaks in the exterior downwash region (to the right of vortex no. 4) where the model underpredicts the magnitude of v by about 30 percent.

Improving Grid Estimates of the Vortex Descriptors

The Oseen model can be used to improve the grid estimate of z_i, y_i, and ω^i_{max} determined from the data in Chapter 4 and listed in Tables 4.2 and 4.3. Recall that the streamwise vorticity of the data field was determined at each grid point. The peak vorticity of each core was determined by locating the grid point having the largest magnitude of ω_x within the boundaries of that particular core. The coordinates of this grid point became (z_i, y_i). As discussed in Chapter 4, the chances that a grid point would coincide exactly with the center location of the core are slim. Thus the grid estimate of the magnitude of ω^i_{max} tends to be somewhat low. Since we have evidence that the Oseen model provides a good match to the core structure of embedded vortices, we can use this model to improve our estimates of the peak vorticity. The procedure followed is a simple one and involves interpolation of the velocity field.

Figure 5.11 diagrams the essential construction. The four vectors represent the measured secondary velocities on grid points surrounding the core central location. Since the values of

the vector components are known at these points interpolation provides a location (z_c, y_c) where the components are zero. One grid point among these four has coordinates (z_i, y_i) and is the location where $\omega_x = \omega^i_{max}$ (i. e. the previous grid estimate of the peak vorticity). We now state the vorticity magnitude peaks at (z_c, y_c) with a value of ω^i_{xc} :

$$\omega^i_{xc} = \frac{U_\infty \Gamma_i}{4\pi \nu_{ic} x^*},$$

which yields ν_{ic} in terms of ω^i_{xc} :

$$\nu_{ic} = \frac{U_\infty \Gamma_i}{4\pi \omega^i_{xc} x^*}.$$

Now using Eq. (5.6) we can write :

$$\omega^i_x = \omega^i_{max} = \omega^i_{xc} \exp\left\{ \frac{-\omega^i_{xc}\pi}{\Gamma_i} \left((z_i - z_c)^2 + (y_i - y_c)^2 \right) \right\}. \tag{5.24}$$

Note that the only unknown in this equation is the new estimate of the peak vorticity, ω^i_{xc}. This equation is solved by a numerical interpolation. The results appear in Table 5.1 along with the new estimates of $z_i, y_i,$ and ν_i. The grid estimates of these quantities (from Chapter 4) are included for comparison. Peak vorticity determined by use of the model is as much as 15 percent greater than the corresponding grid estimate from the data at Station 74. At Station 150 the vortex core structure is much more diffuse. The core has also grown in size considerably during its downstream development subsequent to Station 74. As a result the downstream values of vorticity on the offcenter grid points are much closer to the true value of the peak vorticity. Use of the model to improve the estimate of the peak vorticity results in an increase of only 1 or 2 percent over the grid values. A typical case is provided by the single embedded vortex. The grid estimates of the descriptors for this case, along with the model improvements are listed in Table 5.1.

5.2 A Model of Vortex Interaction and Development

The growth and development of an embedded vortex array of arbitrary initial spacing ratio is a three dimensional problem to which a variety of potential approaches exist for us to consider.

A brute force approach to understanding the streamwise development of an embedded vortex array might have us resolve the streamwise coordinate into a series of crossplane survey grids located between Stations 74 and 150 and separated by Δx. In a boundary layer with embedded vortices streamwise gradients are expected to be small compared to crossplane gradients and so Δx can be made to be a good deal greater than Δy and Δz. However, even if Δx were, say, ten times Δz or Δy, this would still require about 40 additional survey grids between Stations 74 and 150. The examination of 42 1000+ point crossplane survey grids for each vortex generator test condition is an ideal, but far from practical way of obtaining an understanding of the three dimensional aspects of embedded vortex array structure.

We have demonstrated the close correspondence between the two dimensional Oseen model of the viscous vortex and the secondary flow structures contained in the two widely separated data crossplanes. The approach used here to explore the developmental aspects of an embedded vortex array takes advantage of this. Recall that the model representation of the embedded vortex array is defined in terms of the vortex descriptors. There are four such descriptors for each vortex in the array : z_i, y_i, ω^i_{max}, and Γ_i. Suppose we set up the model to represent the secondary flow field typical of an embedded array at Station 74. We might choose, for example, the vortex array consisting of four vortices and having an initial spacing ratio of 4.0. The vortex descriptors for this case are found in Table 4.2. The subsequent streamwise development of our 4 element vortex array depends on the manner

in which the descriptors develop, i. e. on :

$$\partial z_i/\partial x,$$

$$\partial y_i/\partial x,$$

$$\partial \omega^i_{max}/\partial x,$$

$$\partial \Gamma_i/\partial x,$$

provided we assume that the model provides a good representation of the actual flow field at every location x during this development. Suitable physical models will be constructed to represent these descriptor gradients. The descriptor gradients will depend, in general, on the flow characteristics as well as the characteristics of the array (e. g. the initial spacing ratios, hieght ratios, and the signs and magnitudes of the descriptors themselves). With these descriptor gradients and some assumptions about the streamwise velocity field we can track the streamwise development of the embedded vortex array so that at $x + \Delta x$ the new values of the descriptors are :

$$\begin{aligned}
z_i(x+\Delta x) &\approx z_i(x) + \Delta x(\partial z_i(x)/\partial x), \\
y_i(x+\Delta x) &\approx y_i(x) + \Delta x(\partial y_i(x)/\partial x), \\
\omega^i_{max}(x+\Delta x) &\approx \omega^i_{max}(x) + \Delta x(\partial \omega^i_{max}(x)/\partial x), \\
\Gamma_i(x+\Delta x) &\approx \Gamma_i(x) + \Delta x(\partial \Gamma_i(x)/\partial x). \qquad (5.25)
\end{aligned}$$

The subsequent streamwise development of the model proceeds in this incremental manner until the downstream station is reached. Here we can check for correspondence between the model descriptors and the downstream data descriptors in Table 4.3. The models representing the descriptor gradients can be changed or adjusted until such correspondence is

achieved.

Our approach to understanding the developmental aspects of an embedded vortex array is thus an iterative one, involving the use of the Oseen model with models for the descriptor gradients. In this process the upstream data descriptors serve as input to the model, and the downstream data descriptors serve as a constraint. This combined "quasi" three dimensional model will be complete when, regardless of what Station 74 test condition is used as input, the descriptors converge to the corresponding downstream results.

5.2.1 Computational Framework of the Model

The computational model employed in this section is based on the Oseen model of the viscous vortex. The secondary velocities of the model are given by Eqs. (5.9), (5.11), and (5.12), where the number of vortices in the array to be modelled is N_v, the particular value being supplied as input to the program by the user.

The descriptors of the array are held in four matrices, each containing N_v elements. These matrices can be initialized from the data in Table 4.2, for example. The user then decides at which location x the streamwise "marching" will begin. If the initial values of the vortex descriptors are taken from a test condition listed in Table 4.2 then the streamwise marching will begin at $x = 74$ cms. The user then decides on Δx and the x location where the marching will stop. Since we are interested in comparing the downstream data descriptors to the values generated by the model we will stop our marching at $x = 150$ cms.

After initialization the program marches forward in increments of Δx. At each such streamwise location the descriptor values are modified according to Eqs. (5.25). This is done in the main body of the program. Four subroutines provide the appropriate incremental changes for the descriptors. The models constructed for each descriptor gradient are represented in these subroutines. Subroutines are also constructed to provide the velocity

and vorticity fields of the model array at the current location x. The descriptor values at each location x are stored in another matrix so it is later possible to examine the streamwise development of each vortex in the array.

When Station 150 has been reached the program uses the current values of the descriptors to generate a graphical depiction of the secondary flow field of the model vortex array using the same grid resolution as used in the data survey grid at Station 150. In this manner the resulting model vortex array may be compared directly to the data crossplane plots.

5.2.2 Developing the Descriptor Gradients

Where easily identifiable physical principles apply we attack the descriptor gradients directly. This is mostly true for gradients of z_i, y_i, and Γ_i. In the case of the peak streamwise vorticity, ω^i_{max}, we must also consult the work of others. In particular, the studies performed by the Stanford workers; Westphal, Pauley, and Eaton (1987), and Pauley and Eaton (1988), provide most of the information required.

z_i and y_i : Convection by Neighbors and Images

The streamwise gradients of z_i and y_i represent the vortex trajectories. The vortex trajectories are mostly determined by an easily identifiable factor, namely the convection by neighboring vortices and the wall. We will equate the convection due to the presence of the wall to the convection by the image vortices. Figure 5.12 illustrates an embedded array of three vortices A, C, and E. The corresponding image vortices are labelled B, D, and F. Suppose we wish to track the trajectory of vortex A. Each of the other vortices present, images included, will induce a velocity vector at z_A, y_A. The sum of these vectors will determine the trajectory of vortex A. The motion along the z axis is given by the z

component of the resultant vector :

$$w_A = w_B + w_C + w_D + w_E + w_F. \tag{5.26}$$

Motion along the y axis by the y component :

$$v_A = v_B + v_C + v_D + v_E + v_F. \tag{5.27}$$

Thus we obtain :

$$\begin{aligned} \frac{dz_A}{dt} &= w_A, \\ \frac{dy_A}{dt} &= v_A. \end{aligned}$$

If we use w_i and v_i to represent the spanwise and normal velocity components induced on the core of vortex i by all other vortices and images in the field then we have, in general :

$$\begin{aligned} \frac{dz_i}{dt} &= w_i, \\ \frac{dy_i}{dt} &= v_i, \end{aligned} \tag{5.28}$$

for the descriptor gradients of z_i and y_i.

Substitute for the time derivative following Eq. (5.3) :

$$dt = \frac{dx}{u}. \tag{5.29}$$

We could replace the streamwise velocity u in Eq. (5.29) by U_∞, its freestream value. Recall that it is the vortex core center that is being convected in Eq. (5.28). In this study the

vortex core centers are generally located on the outer edges of a highly distorted turbulent boundary layer where the streamwise velocities are not that different from the freestream value. The vortex core center does, however, have associated with it a streamwise velocity deficit, $(U_\infty - u)$, that has nothing to do with the boundary layer thickness. This is the streamwise velocity deficit analyzed by Batchelor (1964) and discussed in Chapter 2 in connection with the structure of isolated vortices. This velocity deficit has a potentially significant value, particularly if the vortex is in an early stage of development. Examining the data at the upstream station we find that a streamwise velocity deficit does occur here and peaks at the center of the vortex where $(U_\infty - u) \approx 10$ m/sec. This is 14 percent of the freestream value.

Batchelor's analysis provides a correlation for the streamwise velocity deficit at the core center of an isolated vortex :

$$(U_\infty - u) \approx \frac{\Gamma^2}{4\pi^2 \nu x} \ln\left[\frac{x U_\infty}{\nu}\right].$$

Embedded vortex structure undergoes decay at a rate greater than that observed for isolated vortices. The velocity deficit in the core of embedded vortex i is written :

$$(U_\infty - u) = \frac{\Gamma_i^2}{4\pi^2 \nu_i (x + x_t)} \ln\left[\frac{(x + x_t) U_\infty}{\nu_i}\right], \tag{5.30}$$

where both Γ_i and ν_i are functions of x. The velocity deficit at the upstream station is matched to the data result by adjusting the length constant x_t. It is found that x_t is about 6 meters. With this value of x_t Eq. (5.30) predicts a streamwise velocity deficit of about 1-2 m/sec at the downstream station, a value in agreement with the data taken there.

The streamwise gradients of z_i and y_i are thus :

$$\begin{aligned} \frac{dz_i}{dx} &= \frac{w_i}{u}, \\ \frac{dy_i}{dx} &= \frac{v_i}{u}, \end{aligned} \tag{5.31}$$

where u follows from Eq. (5.30) :

$$u = U_\infty - \frac{x^* \omega^i_{max} \Gamma_i}{\pi U_\infty (x + x_t)} \ln \left[\frac{(x + x_t) x^* 4\pi \omega^i_{max}}{\Gamma_i} \right], \tag{5.32}$$

where Eq. (5.10) has been used to replace ν_i.

Γ_i : Wall Friction Effects

Wall shear stress is a vector quantity in a boundary layer with strong crossflows. Secondary flows having a strong spanwise velocity component occur under the core of an embedded vortex. These flows give rise to a corresponding spanwise component of the wall shear stress. In turn, this stress results in a torque opposing the rotation of the vortex. The streamwise gradient of vortex circulation is first developed on the premise that any such gradient occurs as a result of the spanwise component of the wall shear stress.

Figure 5.13a is another diagram of three embedded vortices in some stage of development at some crossplane location x. An elemental torque opposing the rotation of vortex i is generated by the secondary flow at location z, a distance r from the center of vortex i. The magnitude of this elemental torque is dM_i :

$$dM_i = \tau_i \, y_i \, dz \, dx, \tag{5.33}$$

where τ_i is the local value of the spanwise component of the wall shear stress. Integrate this

result over z to obtain the moment M_i opposing the rotation of vortex i :

$$M_i = \frac{dH_i}{dt} = y_i\, dx \int_{z_{L1}}^{z_{L2}} \tau_i\, dz, \tag{5.34}$$

where H_i is the angular momentum of vortex i of elemental thickness dx. The limits of integration on Eq. (5.34) are a subject that needs some discussion. In the case of a single embedded vortex it is obvious that $z_{L2} \rightarrow \infty, z_{L1} \rightarrow -\infty$. In the case of a counter-rotating vortex array of the kind examined in this study the appropriate limits of integration are found at the stagnation points in the spanwise component of velocity at the wall. Each embedded vortex in the array sets up a zone of wall velocity, $w(z, y = 0)$, having an orientation (sign) opposite of the zones set up by the neighboring vortices on either side. Figure 5.13b depicts the functional form of $w(z, y = 0)$ versus z for the secondary velocity field created by the three embedded vortices of Figure 5.13a. Stagnation points z_{L1} and z_{L2} bound the w wall velocity zone created by vortex i. Eq. (5.34) written for the exterior vortex $i + 1$ in Figure 5.13a is, for example,

$$\frac{dH_{i+1}}{dt} = y_{i+1}\, dx \int_{z_{L2}}^{\infty} \tau_{i+1}\, dz.$$

To complete this portion of the analysis a further assumption is required : *The change in angular momentum of the model vortex is proportional to the change in its circulation.* To motivate this assumption consider the angular momentum of the isolated Oseen vortex of radius r_0 and elemental thickness dx :

$$H_i = \Gamma_i\, \rho\, dx \left[\frac{r_0^2}{2} - \frac{1}{2B_i}(1 - \exp\{-B_i r_0^2\})\right] \approx \Gamma_i\, \rho\, dx \left[\frac{r_0^2}{2}\right], \tag{5.35}$$

where B_i is given by Eq. (5.16) and $r_0 >$ (core radius of vortex). The term in the square

brackets is essentially geometric, having units of area. A similar expression can be written for vortex i within an Oseen model of an embedded vortex array, although in this case a neat closed form solution similar to Eq. (5.35) does not exist.

Now write the angular momentum of vortex i as :

$$H_i = C_{wf}\,\rho\,dx\,\Gamma_i,$$

where C_{wf} is the constant of proportionality with units of m^2. Thus :

$$d\Gamma_i = \frac{1}{C_{wf}\rho\,dx} dH_i.$$

Substituting into Eq. (5.34) and using Eq. (5.29) to represent the time increment dt we obtain the streamwise circulation gradient :

$$\frac{d\Gamma_i}{dx} = \frac{y_i}{C_{wf}\rho u}\int_{z_{L1}}^{z_{L2}} \tau_i\,dz. \tag{5.36}$$

τ_i, the spanwise component of the wall shear stress, is a function of both wall coordinates, i. e. $\tau_i = \tau_i(x,z)$. An approximate expression for this function is developed from the assumption that τ_i is proportional to the spanwise component of the secondary velocity at the wall. This correlation is suggested by the work of Pauley and Eaton (1988) :

$$\tau_i = C_\tau \tau_{2Dx} w(z, y=0), \tag{5.37}$$

where $w(z, y=0)$ is the spanwise velocity of the model at the wall, τ_{2Dx} is the wall shear stress of the corresponding two dimensional boundary layer at x, and C_τ is a scaling constant.

Applying Eq. (5.37) to the results of the Stanford study yields :

$$C_\tau \sim .046 \text{ sec/m.} \tag{5.38}$$

A relationship for τ_{2Dx} appropriate for the turbulent boundary layer of the present study comes from White (1974) :

$$\tau_{2Dx} = \frac{\rho_\infty U_\infty^2}{2} C_f = \frac{\rho_\infty U_\infty^2}{2} \left(.455 \left[\ln \left\{ \frac{.06 U_\infty x}{\nu} \right\} \right]^{-2} \right),$$

or :

$$\tau_{2Dx} \approx 1330 \left(\ln \left(285000 x \right) \right)^{-2}. \tag{5.39}$$

Substitute Eq. (5.37) into (5.36) :

$$\frac{d\Gamma_i}{dx} = \frac{y_i C_\tau \tau_{2Dx}}{C_{wf} \rho u} \int_{z_{L1}}^{z_{L2}} w(z, y = 0)\, dz. \tag{5.40}$$

As noted earlier, values of the secondary velocities and vorticity of the model array can be determined at any location (z, y) in the crossplane at x. This is done by the velocity and vorticity subroutines. Thus $w(z, y = 0)$ is calculated wherever needed in the crossplane at x. The subroutine for $d\Gamma_i$ first searches the line $(z, y = 0)$ for the points where w is zero (stagnation points). These points represent the z location of the limits of integration in Eq. (5.40). They are stored in a matrix with $(N_v - 1)$ elements. The integral in Eq. (5.40) is then carried out numerically for each vortex in the array. Questions regarding the panel number (or numerical resolution of the integral) and the length of z-axis required for the outer limits of integration in the case of the single embedded vortex or exterior array vortices are answered by convergence tests with specific examples from the data. In these

tests a guess at the value of C_{wf} in Eq. (5.40) is used. Obtaining a meaningful value of C_{wf} is done through an iterative procedure. In particular, the descriptor data of the single embedded vortex provides for a test case where wall friction effects alone are the most likely explanation of circulation decay. The value of C_{wf} is adjusted until the model converges to the data descriptor results of the single embedded vortex at Station 150. Before performing this test, however, a suitable representation of the streamwise gradient of ω^i_{max} is needed.

ω^i_{max} : Decay of Peak Vorticity

Eq. (5.10) indicates the relationship between the vortex eddy viscosity and ω^i_{max}. Since the vortex eddy viscosity depends in a general way on the nature of the core turbulence the streamwise development of ω^i_{max} cannot readily be tied to some aspect of the mean secondary flow field in the crossplane.

Since the values of the peak vorticity are known at the boundaries of the streamwise domain we might ask if there is a more fundamental approach which could establish the functional form of the decay between these boundaries. The *rate* at which the decay takes place could then be used as an adjustable model parameter whose range of probable values would depend on the resulting model behavior. The simplest meaningful assumption about the decay of ω^i_{max} is that it is proportional to ω^i_{max}, producing some exponential decay form. We can improve on this by considering the decay of peak vorticity observed by the Stanford workers.

Figure 5.14 illustrates the streamwise decay of ω^i_{max} observed by Westphal, Pauley, and Eaton (1987) of a single embedded vortex. The case A1 represents the decay of an initially weak vortex in an early stage of development. The case A2 represents the decay of an initially weak vortex in a later stage of development and the case A3 an initially stonger vortex in a later stage of decay. In all three cases we see the decay behavior is decidedly nonlinear, but

becoming less so as the decay proceeds downstream. Figure 5.15 illustrates the streamwise decay of ω^i_{max} observed by Pauley and Eaton (1988). Case no. 1 represents the decay of a vortex paired with another vortex in a counter-rotating downflow configuration with an initial spacing ratio of 3.0. Case no. 2 also represents the decay of a vortex in a counter-rotating pair of $S/\delta = 3.0$, but here the two vortices constitute an upflow pair. The rate of decay of ω^i_{max} with respect to x is greater for the upflow pair. This is attributed to the spreading of the vorticity field of each vortex by its neighbor. Vorticity spreading is enhanced when the neighboring vortex maintains close proximity during streamwise development, as it does in the case of an initially close upflow vortex pair. Case no. 3 is the decay of a vortex in a counter-rotating array of initial spacing ratio 7.0. We again note the character of the decay; initially $d\omega^i_{max}/dx$ is large and then tails off as the decay proceeds downstream.

Figure 5.16 illustrates the functional representation of ω^i_{max} employed here. ω^i_{max} is fixed on the upstream and downstream boundaries to the values found in the data. ω^i_{Lmax} represents the upstream value of ω^i_{max} The data indicates about a 12 percent variance in the upstream values of ω^i_{max}, with no correlation to array initial spacings. ω^i_{Rmax} represents the downstream value of ω^i_{max}. Here the data indicates a 45 percent variance with the smaller initial spacing ratios producing the lower values of ω^i_{Rmax}. Note, however, that ω^i_{Rmax} is only about 2-4 percent of ω^i_{Lmax} over the range of initial spacing ratios examined. Figure 5.16 specifically diagrams the case of the single embedded vortex. The model representation of ω^i_{max} over x is given by :

$$\begin{aligned} \omega^i_{max}(x,\xi) &= \left[\omega^i_{Lmax} - \frac{\Delta\omega}{\Delta x}(x - x_L)\right] \\ &\quad - \frac{2\Delta\omega}{\pi}\sum_{n=1}^{\infty}\frac{1}{n}\exp(-n^2\xi)\sin\left(n\pi\frac{x - x_L}{\Delta x}\right), \end{aligned} \tag{5.41}$$

where :

$$\Delta\omega = \omega^i_{Lmax} - \omega^i_{Rmax}, \text{ and}$$

$$\Delta x = x_R - x_L = .76 \text{ m.}$$

The streamwise decay of ω^i_{max} is written formally as :

$$\frac{d\omega^i_{max}}{dx} = \frac{-\Delta\omega}{\Delta x}\left[1 + 2\sum_{n=1}^{\infty}\exp(-n^2\xi)\cos\left(n\pi\frac{x - x_L}{\Delta x}\right)\right]. \tag{5.42}$$

Eq. (5.41) represents the unsteady one dimensional diffusion of heat through a substance having thermodynamic properties independant of temperature. Initially the "temperature" of the entire domain is ω^i_{Rmax}, and at "time" $\xi = 0$ the left boundary "temperature" jumps to ω^i_{Lmax}. As ξ proceeds to infinity a linear profile connecting upstream and downstream values of ω^i_{max} is obtained. We might be tempted to justify Eq. (5.41) on physical grounds, comparing the steady state streamwise diffusion of vorticity to the unsteady diffusion of heat through a transformation such as that given by Eq. (5.3). To do so, however, would require much more information about the properties of the diffusive medium, i. e. the turbulent structure of the vortex core. Eq. (5.41) is meant to be a curve fit only. The parameter ξ is our required "rate of decay" adjustment parameter. In Figure 5.16 the decay behavior of the peak vorticity, as determined from Eq. (5.41), is examined for four values of ξ. The summation in Eq. (5.41) is carried out to 15 terms, giving numerical convergence beyond the fourth decimal place for ω^i_{max} in units of 1/sec. For $\xi = 0.1$ the peak vorticity decays in a rapid fashion, much like the decay behavior of the upflow pair of embedded vortices, or the initially strong single vortex, as observed by the Stanford workers. For values of $\xi = 0.5$, 1.0, or 1.5 the decay is more gradual and similar to the decay behavior of the

embedded downflow pair of vortices diagrammed in Figure 5.15 or the initially weak single embedded vortex diagrammed in Figure 5.14. As ξ extends to infinity the linear profile is obtained.

Numerical integration limits and resolution on both the x and z axes are set to obtain convergence to four decimal places in the results. Since we don't know what value of the decay constant ξ is appropriate for the case of the single embedded vortex we will test a few ξ values representing the wide range of possible decay behavior as diagrammed in Figure 5.16. For each value of ξ chosen, a value of the wall friction constant C_{wf} is determined in such a way that the descriptors z_i, y_i, and Γ_i match the data as closely as possible. Table 5.2 lists these results. The match of model descriptors to data descriptors is very good, implying that the descriptor gradients of z_i, y_i, and Γ_i have been correctly modelled. $C_{wf} = 1.4 \times 10^{-4}$ m^2 *independant of* ξ. On the assumption that wall friction effects are responsible for the decay of circulation, the independance of C_{wf} and ξ is not surprising. That this is so, is explained as follows.

ξ represents the decay of peak vorticity which is, in effect, the rate at which the viscous core grows. Circulation decay is governed by the strength of the secondary flow at the wall which, for the most part, lies outside of the core region. In this region of potential flow, the strength of the secondary velocities depends much more strongly on Γ_i than it does on ω^i_{max}. Using Eqs. (5.8), (5.11), and (5.12) we could write for the case of the single embedded vortex :

$$\begin{aligned} v_{i,wall} &\sim \frac{\Gamma_i(z - z_i)}{2\pi R_i^2} - \frac{\Gamma_i(z - z_i)}{2\pi R_i^2} = 0, \\ w_{i,wall} &\sim \frac{\Gamma_i y_i}{2\pi R_i^2} + \frac{\Gamma_i y_i}{2\pi R_i^2} = \frac{\Gamma_i y_i}{\pi R_i^2}. \end{aligned}$$

Thus, regardless of the rate at which the core grows (i. e. the development of ω^i_{max}), the

secondary velocity behavior at the wall remains roughly the same, providing consistency in the rate at which circulation decays in the model.

Using the value of C_{wf} determined for the case of the single embedded vortex we now apply the model to the other four element array test cases examined. For spacing ratios of 2.0 through 5.0 the data provides the input to the model at Station 74. Array symmetry, as outlined in Chapter 4, is assumed. For spacing ratios of 6.0 and 7.0 initial values of Γ_i are an average of those obtained with the other spacing ratios at Station 74, and (z_i, y_i) are estimated from the actual positions at which the vortex generators were mounted. Table 5.2 compares the resulting downstream model descriptors to the data descriptors at Station 150. The same four values of ξ examined in the case of the single embedded vortex are considered again for each of the 6 array spacing ratios. To produce the descriptor results given in Table 5.2, a value of $\xi = 1.5$ was used. The model matches the data well for spacing ratios 7.0, 6.0, 5.0, and 4.0. Again, this is true regardless of the value of ξ chosen. The model descriptors do not match the data descriptors for spacing ratios of 3.0 and 2.0. Changing the value of ξ does not improve the model's performance at these spacing ratios. The culprit seems to be the behavior of Γ_i. Since Γ_i does not decay to the same extent as that observed in the data in these tighter arrays, the model vortex trajectories suffer an "enhanced motion" resulting in a degree of travel in the secondary plane that is not seen in the data. For a spacing ratio of 2.0, the final value of Γ_i is about twice the value it should be.

Figures 5.17a-g compare the downstream secondary velocity and vorticity fields of both the model and data. The two interior vortices of Figure 5.17g, the spacing ratio 2.0 case, are in such close proximity that they have nearly cancelled each other out. This circulation defect exhibited by the model results from collision trajectories that bring the vortex cores into closer proximity than that exhibited in the data. To solve this problem of "enhanced

motion" we must first determine what mechanism, besides wall friction, is responsible for the additional loss of circulation at spacing ratios less than 4.0.

Γ_i : Circulation Decay by Proximity Effects

The close connection between vortex angular momentum and circulation requires us to treat carefully any "mysterious" changes in these quantities. Angular momentum is a conserved quantity and so its disappearance from some region of the flow must be countered with an equivalent "appearance" in another such region. In this regard, however, there is no mystery to the behavior of the spacing ratio 2.0 and 3.0 cases. It must be kept in mind that all vortex arrays tested were *counter-rotating* and since angular momentum is a vector quantity with magnitude and sign we see that the overall balance of angular momentum in the array is kept, at least within the uncertainty brought about through differing wall friction losses. These observations follow from the values of circulation calculated for individual vortices in the arrays, as given in Table 4.3.

The question about the particular loss mechanism remains, though. How is it that an individual vortex is weakened to the extent exhibited in the spacing ratio 2.0 and 3.0 cases? Is it possible that some portion of the vortex core has been removed from the measurement domain? The contour plots of Chapter 4 would seem to rule this possibility out. Thinking of circulation as an integrated vorticity we might wonder if the vortex path has been turned in such a manner that the vorticity in the crossplane has been reduced. The vortex traces obtained from the heat transfer test indicate that there is some curvature to these paths, but certainly not enough to explain the observed losses. The recovery of the streamwise velocity deficit in the core provides a stretching mechanism for the vorticity present there. Different array configurations provide differing rates at which this deficit is recovered. The result, however, relates only to the concentration of core vorticity and not its integrated

sum. A loss in angular momentum results from an applied torque, and correspondingly, this seems to be the answer to a circulation loss as well. The applied torque may originate from turbulent stress gradients generated by the collision of opposing vortex cores.

The model indicates that wall frictional effects can account for circulation losses when the initial spacing of the vortex generators is large enough. If opposing torques applied by turbulent stress gradients are responsible for circulation losses, this mechanism must somehow be activated when the vortices are in close proximity, i. e. in tighter initial arrays. This would seem to indicate that the turbulent stress levels of significance were confined to the core regions of the embedded vortices. This idea is consistent with the picture of an isolated vortex presented by Owen (1970), Uberoi (1978), and others. The isolated vortex core is the only location where turbulent stresses may be maintained. The turbulent stress field is confined to the core in a region with an irregular, circularly shaped boundary across which the turbulent stresses vanish and an area of potential outer flow exists. The velocity deficit in the core of the vortex sustains the turbulence levels found there. The turbulent stress field of the embedded vortex core is surrounded by the turbulent field of the boundary layer. In this case it is a matter of turbulence intensity, with the level of turbulent kinetic energy in the core far exceeding that occurring in the surrounding boundary layer. These are the observations of Pauley and Eaton (1988).

Although the details of the turbulent stress behavior remain unknown, this proximity factor suggests an alternate approach consistent with our mean flow modelling. Thinking of circulation as an integrated vorticity and noting that it possesses both sign and magnitude we can draw an analogy to a similar problem in heat transfer analysis. Figure 5.18 diagrams the construction. Two thin conducting tubes are buried in a diffusive medium a distance D from one another. The temperature of the medium is T_m. An imaginary line halfway between each tube divides the medium into the "source" domain and the "sink" domain.

At time $t = 0$ a hot liquid fills the source tube and brings its surface temperature to $T_{source} > T_m$ while a cold liquid fills the sink tube and correspondingly drops its surface temperature to $T_{sink} < T_m$ such that $T_{source} - T_m = T_m - T_{sink} = \Delta T$. While the heat transferred from the source domain into the sink domain depends on the diffusive properties of the medium (i. e. the conductivity k) it is also a function of the temperature gradient at $D/2$. In particular, until a temperature gradient exists at $D/2$ no heat is transferred from one domain to the other. Once a temperature gradient exists heat transfer between the domains, in general, becomes proportional to it. Suppose now the outer surface of both tubes represents the core boundaries of a pair of counter-rotating vortices. The "source" core is of strength Γ_i and the "sink" core of strength $-\Gamma_i$. Outside the core boundaries the flow field is potential and so the streamwise vorticity is zero. Inside the source core the vorticity varies from zero at the boundary to ω^i_{max} at the center. Inside the sink core the vorticity varies from zero to $-\omega^i_{max}$ in the same fashion. As the two vortices develop downstream their outer boundaries expand into the surrounding medium at a rate determined by the diffusive properties of the medium. As long as the radius of each core remains less than $D/2$ the integrated vorticity of each core retains magnitude Γ_i, and the vorticity gradient at $D/2$ is zero. When both core boundaries coincide with the location $D/2$ the vorticity gradient between vortex cores becomes nonzero and vorticity diffuses from the source core to the sink core at a rate proportional to the gradient at $D/2$. The structure of the vorticity field of each core is the same, differing only in sign. Thus the transfer process is essentially a cancellation process in which the positive vorticity crossing the source core boundary at $D/2$ cancels an equivalent amount of negative vorticity in the sink core. The integrated vorticity over each core area is now somewhat less than Γ_i in magnitude. This qualitative description of the circulation loss mechanism forms the basis of the routine employed here. A line connects the cores of a counter-rotating pair of vortices, vortex i and vortex $i+1$, in

Figure 5.19a. Label this coordinate axis R. The circulation decay of vortex i is then :

$$\frac{d\Gamma_i}{dx} = \left.\frac{d\Gamma_i}{dx}\right|_{wf} + \left.\frac{d\Gamma_i}{dx}\right|_{prox}, \tag{5.43}$$

where $(d\Gamma_i/dx)_{wf}$ is the circulation decay due to wall friction and :

$$\left.\frac{d\Gamma_i}{dx}\right|_{prox} \propto \left|\frac{d\omega_x}{dR}\right|_{R=R_{0i}}. \tag{5.44}$$

The location at which the derivative $d\omega_x/dR$ is evaluated is taken to be the location on the line R where the vorticity changes sign, $R = R_{0i}$. In the model, R_{0i} is representative of the boundary between the "domains" of the vortices. Since the "loss" by one vortex is the "gain" by its opposite signed neighbor we can write :

$$\frac{d\Gamma_{i+1}}{dx} = \left.\frac{d\Gamma_{i+1}}{dx}\right|_{wf} - \left.\frac{d\Gamma_i}{dx}\right|_{prox}. \tag{5.45}$$

The model is constructed to evaluate the vorticity field and vorticity gradients at any location (z, y) in the crossplane at x, thus enabling the evaluation of Eqs. (5.43) through (5.45). The only additional requirement is the constant of proportionality in Eq. (5.44), C_{prox} :

$$\left.\frac{d\Gamma_i}{dx}\right|_{prox} = C_{prox}\frac{\Gamma_i}{|\Gamma_i|}\left|\frac{d\omega}{dR}\right|_{R=R_{0i}}. \tag{5.46}$$

The ratio of circulation to its absolute value is meant to ensure that the proximity loss term has the correct sign – the magnitude of the vortex circulation must decrease with x. For the sign convention followed here (clockwise rotation negative) C_{prox} is a negative constant. Consider the array of counter-rotating vortices in Figure 5.19b. The circulation decay of

vortex no. 1 (an exterior vortex) is given by :

$$\frac{d\Gamma_1}{dx} = \left.\frac{d\Gamma_1}{dx}\right|_{wf} + C_{prox}\frac{\Gamma_1}{|\Gamma_1|}\left|\frac{d\omega}{dR}\right|_{R=R_{01}} . \tag{5.47}$$

Circulation decay of vortex no. 2 (an interior vortex) is :

$$\frac{d\Gamma_2}{dx} = \left.\frac{d\Gamma_2}{dx}\right|_{wf} - C_{prox}\frac{\Gamma_1}{|\Gamma_1|}\left|\frac{d\omega}{dR}\right|_{R=R_{01}} + C_{prox}\frac{\Gamma_2}{|\Gamma_2|}\left|\frac{d\omega}{dR}\right|_{R=R_{02}} , \tag{5.48}$$

since vortex no. 2 has two opposite sign neighbors to which a loss of vorticity is possible. An equation analogous to Eq. (5.48) is written for the other interior vortices in the array and an equation analogous to Eq. (5.47) for the other exterior vortex. The program subroutine handling circulation decay first evaluates the wall friction loss for each vortex in the array. The subroutine then connects, in turn, each counter-rotating pair of neighboring vortices with a line through the respective vortex centers. The subroutine evaluates the location along this line where the vorticity changes sign and here the derivative $d\omega/dR$ is evaluated. C_{prox} is determined from trial and error using the test cases with initial spacing ratios of 2.0 and 3.0. Model behavior for a variety of decay rates ξ is also examined.

Table 5.3 lists resulting model descriptors for the range of C_{prox} values producing reasonable behavior. The test case used is the initial spacing ratio 2.0 array. A decay constant of $\xi = 0.5$ was chosen. The model descriptors are closest to the data descriptors for $C_{prox} = -1.4 \times 10^{-6}$ m^2 although Γ_i is a bit large for vortices 1 and 4, and the model overestimates y_i for vortices 2 and 3. The model estimates of y_i for vortices 2 and 3 become progressively worse as C_{prox} is dropped (in magnitude) below 1.4×10^{-6} m^2.

Keeping the value of C_{prox} fixed at -1.4×10^{-6} m^2, we now play with the decay constant ξ. The results are given in Table 5.4. Dropping the decay constant to 0.2 in the spacing ratio 2.0 test case dramatically improves the behavior of the model. Table 5.4 provides the

values of ξ (with C_{prox} fixed) for which the resulting model descriptors most closely match the data descriptors. The spacing ratio 4.0 test case is typical of the larger spacings. When ξ is below about 1.2 (taken from Table 5.4) the model underestimates the vortex circulations at the downstream station. When $\xi \approx 1.2$ the model and data most closely coincide, and for $\xi > 1.2$ the model descriptors change very little. Table 5.4 clearly indicates a trend in ξ with respect to spacing ratio : ξ increases with increased spacing. The observed behavior of the decay constant with respect to spacing ratio condition is a very encouraging result. It verifies what we expect intuitively and agrees with the observations made by the Stanford workers : *Vortices in close proximity decay faster.*

5.3 Applications of the Model

5.3.1 Predicted Streamwise Development

With the model now closely matching the downstream data descriptors over the range of spacing ratios covered in the experimental portion of the test we can examine the predicted vortex array streamwise development. This is done through the "UPDATE" matrices generated by the model program. The UPDATE matrix lists the descriptors of each vortex at regular intervals of x between the x locations corresponding to the upstream and downstream data stations. Table 5.5 is a sample UPDATE matrix generated by the model program for the case of the single embedded vortex. The decay constant chosen in the generation of Table 5.5 is $\xi = 1.5$.

The results obtained in the UPDATE arrays may be plotted out. The following plots are generated from initial conditions corresponding to those covered in the experimental portion of the study (single embedded vortex and four blade arrays). Figure 5.20a plots the predicted trajectory of the single embedded vortex in the $x-z$ plane (viewed from above the

flow surface). The path drawn out from $x = 64$ cm to $x = 94$ cm may be compared to the contour lines of heat transfer coefficient in Figure 4.32. The projection of the trajectory of the vortex in the $z-y$ plane is also shown in Figure 5.20a. Corresponding vortex trajectories for the spacing ratios of 4.0 and 2.0 are given in Figures 5.20b and 5.20c. Again, these may be compared to the tracks revealed in the heat transfer visualization study, Figures 4.33 and 4.35 respectively.

Figure 5.21a is a plot of the predicted circulation decay of the single embedded vortex. The decay curve drawn is independant of the decay constant ξ. Here it is chosen to be $\xi = 1.5$. Figure 5.21b is a plot of the circulation decay of vortex no. 3 in the spacing ratio 4.0 array. The decay constant chosen is $\xi = 1.2$, the minimum value for which the downstream descriptors most closely match the data. Figure 5.21c is the corresponding plot for vortex no. 3 in the spacing ratio 2.0 array with $\xi = 0.15$.

5.3.2 Model Secondary Velocity and Vorticity Fields at Station 150

The model program generates downstream plots of secondary velocity vectors and streamwise vorticity contours which may be compared to the data results. The descriptors of the vortices appearing in these plots are found in Table 5.4. For spacing ratios between 4.0 and 7.0 of the $N_v = 4$ test conditions the model velocity and vorticity plots are nearly indistinguishable from those given in Figures 5.17b-5.17e. Figure 5.17a is also an accurate depiction of the model structure of the single embedded vortex at Station 150. Figures 5.22a-b illustrate the model structure of the 4 vortex array of spacing ratio 3.0 and 2.0 respectively. With the problem of enhanced strength and motion solved by the application of proximity losses, these model plots are now much closer in appearance to the corresponding data plots; Figures 4.22a-b for the spacing ratio 3.0 test case and Figures 4.23a-b for the spacing ratio 2.0 test case.

The model can be used to predict the mean flow structure and development of an embedded array of counter-rotating vortices created by a general arrangement of vortex generators. Suppose an eight blade array of equally spaced vortex generators produces counter-rotating vortices initially equal in strength. What flow structure results as the spacing ratio is decreased from 7.0 to 2.0? Figures 5.23a-f depict some portion of the resulting model arrays at the downstream station. The spacing ratio 3.0 array may be compared to the data results in Figures 4.27a-b. The eight blade array of spacing ratio 2.0 produces an interesting result seen in Figure 5.23f. Here the vortices have packed themselves together and all eight are visible in the viewing domain. The close proximity of these vortices during development results in large losses in individual vortex strengths. This "washing out" effect is evident in the velocity plot where small secondary flow vectors make individual vortex structure difficult to discern. The secondary flow structure is easier to see when the velocity field is replotted in a different vector length scale, as it is in Figure 5.23g. The vortices depicted in Figure 5.23g undergo a great deal of shape distortion. In particular, the second vortex from the end on either side of the array is in a peculiar state of distortion. Table 5.6 lists the descriptor values predicted at the downstream station for these eight blade arrays.

5.3.3 Comparison to Stanford Mean Flow Results

To test the general applicability of the flow model a comparison to independant test results is desirable. An extensive examination of the structure and development of embedded vortex pairs was carried out by the Stanford workers Pauley and Eaton (1988). Fine resolution of secondary flow structure in the crossplane at several downstream locations was carried out for a downflow pair of counter-rotating vortices of initial spacing ratio 3.0, and an upflow pair, also of initial spacing ratio 3.0. The freestream velocity of the Stanford study was 16.0 m/sec, and the boundary layer thickness at the vortex generator mounting

station was approximately 1.3 cms. The hieght ratio of the vortex generators was about 1.5. An attempt at mimicking the Stanford mean flow results was carried out by first changing the parameters in the model subroutines to reflect the Stanford flow conditions. The fitting constants C_{wf} and C_{prox} were not changed. Using the upstream data descriptors given in the Stanford study as input to the model program the downstream flow structure and development of the embedded vortex pairs was generated by the model program. The downstream data descriptors of the Stanford study and the descriptor results of the model program are compared in Table 5.7. The model reproduces the descriptor quantities to within 10 percent of the observed values. This quantitative level of performance inspires confidence in the general applicability of the model. Circulation decay versus x is plotted in Figure 5.24 for the downflow pair of vortices. Circulation decay for the upflow pair is compared in Figure 5.25.

Figure 5.26a, taken from the Stanford study, diagrams the measured secondary velocity vector field of the embedded downflow pair. Figure 5.26b diagrams the corresponding model results. Figures 5.27a-b are a similar comparison between the data and model descriptions of the embedded upflow pair.

5.4 Summary Remarks

We began by comparing the structure of the two dimensional Oseen model of the viscous vortex to the measured crossplane structure of an embedded vortex. Proper placement of image vortices was necessary to model the influence of the wall. We found that good qualitative and quantitative comparisons between model and data were obtained when the vortex descriptors were matched between the two. The problem of the model circulation defect was examined for cases of close vortex to vortex and vortex to image proximity. No

significant loss of model circulation was found when the model was used to imitate the flow field of the single embedded vortex as measured at both the upstream and downstream locations. The two dimensional Oseen model best reproduced the measured vortex structure at the upstream station. Extensive core vorticity convection, resulting in shape distortions of the initially circular core and evident in the data at the downstream station, were not reproduced by the Oseen model. These elliptical distortions could be reproduced by adjusting the equations of the Oseen model. The resulting complexity, however, made this approach impractical for all but the case of the single embedded vortex.

A three dimensional model of vortex interaction and development is constructed on the premise that the Oseen model provides a sufficient representation of the secondary flow field of the embedded vortex. The mean flow field of the embedded vortex array is characterized in terms of the vortex descriptors and its development in terms of the rates of change (with respect to x) of these descriptors. Models of physical processes are implemented to describe the descriptor gradients. Vortex convection is induced by both neighbors and images. Circulation losses are attributed to opposing torques generated by wall friction and turbulent stress gradients. In the latter case, significant torque is generated only when the vortices are found to be in close proximity. Although the decay of peak vorticity is modelled by a curve fit, correct model behavior is obtained only when the rate of peak vorticity decay is correlated to the initial spacing of the vortex generators. This result is consistent with observations made in the Stanford studies. By proper fitting of the circulation loss constants, C_{wf} and C_{prox}, the three dimensional model convincingly reproduces the mean flow data results discussed in Chapter 4. The general applicability of the model is verified by reproduction of the Stanford mean flow results recorded for pairs of counter-rotating vortices.

Spacing	Vortex #	Model Estimate of Peak Vorticity** (sec^{-1})	Model Estimate of (z_i, y_i)** (cms)		$\frac{\nu_i}{\nu_{lam}}$
Station 74					
(single)	1	30712 (29640)	1.49,1.04	(1.52,1.02)	34.5
2.0	3	32007 (27800)	1.19,1.10	(1.14,1.02)	33.8
	4	-28548 (-26060)	2.84,1.26	(2.79,1.27)	35.1
3.0	3	30855 (27750)	0.25,1.08	(0.25,1.02)	32.9
	4	-28728 (-25860)	2.84,1.13	(2.79,1.14)	34.4
4.0	3	33615 (30280)	-0.66,1.07	(-0.64,1.02)	31.4
	4	-27288 (-23810)	2.84,1.09	(2.79,1.14)	36.2
5.0	3	32161 (27880)	-0.58,1.08	(-0.64,1.02)	32.7
	4	-29324 (-25500)	3.85,1.07	(3.81,1.02)	34.5
Station 150					
(single)	1	1461 (1440)	4.03,1.14	(4.06,1.22)	68.4

**Previous grid estimates of vortex descriptors are in brackets ().

Table 5.1 - The refined estimates of the vortex descriptors based on the Oseen model.

Spacing	Vortex # N_v		Circulation (m^2/sec)	(z_i, y_i) (cms)	
(single)	1	1	0.230 (0.228)	3.94,1.04	(4.06,1.22)
2.0	4	3	0.264 (0.100)	0.67,2.26	(2.24,1.02)
		4	-0.242 (-0.120)	2.03,3.08	(3.66,2.44)
3.0	4	3	0.245 (0.151)	0.37,2.20	(2.84,1.02)
		4	-0.233 (-0.146)	2.10,2.55	(4.47,1.22)
4.0	4	3	0.241 (0.227)	-0.06,2.30	(0.20,2.84)
		4	-0.232 (-0.228)	1.93,2.46	(2.03,2.64)
5.0	4	3	0.228 (0.239)	0.75,1.83	(1.22,1.83)
		4	-0.222 (-0.221)	2.86,1.90	(3.05,1.83)
6.0	4	3	0.216 (0.207)	-0.26,1.44	(-0.61,1.02)
		4	-0.212 (-0.217)	2.19,1.46	(2.24,1.22)
7.0	4	3	0.213 (0.201)	-0.29,1.20	(-0.41,1.22)
		4	-0.210 (-0.206)	3.35,1.27	(3.66,1.02)

Notes :

1.) The decay constant, ξ , was set equal to 1.5.

2.) Vortex data descriptors at Station 150 are in brackets ().

Table 5.2 - The downstream results of the three dimensional model with circulation decay modelled by wall friction effects.

Spacing	Vortex # N_v		Circulation (m^2/sec)	(z_i, y_i) (cms)
C_{prox} = -2.00 E-06 m^2, ξ = 0.5.				
2.0	4	1	0.138 (0.112)	-1.45,2.26 (-1.22,2.64)
		2	-0.078 (-0.104)	-0.07,1.66 (0.20,1.42)
		3	0.081 (0.100)	1.68,1.70 (2.24,1.02)
		4	-0.125 (-0.120)	3.02,2.24 (3.66,2.44)
C_{prox} = -1.40 E-06 m^2, ξ = 0.5.				
2.0	4	1	0.157 (0.112)	-1.42,2.73 (-1.22,2.64)
		2	-0.110 (-0.104)	0.08,1.68 (0.20,1.42)
		3	0.119 (0.100)	1.74,1.72 (2.24,1.02)
		4	-0.151 (-0.120)	3.11,2.75 (3.66,2.44)
C_{prox} = -1.00 E-06 m^2, ξ = 0.5.				
2.0	4	1	0.197 (0.112)	-1.57,2.96 (-1.22,2.64)
		2	-0.139 (-0.104)	-0.24,2.02 (0.20,1.42)
		3	0.148 (0.100)	1.23,2.03 (2.24,1.02)
		4	-0.187 (-0.120)	2.53,2.94 (3.66,2.44)

Notes :

1.) Spacing ratio 2.0 test case considered, data descriptors at Station 150 appear in brackets ().

Table 5.3 - The downstream results of the three dimensional model with circulation decay modelled by wall friction effects and proximity losses. The decay rate parameter ξ is fixed at 0.5. C_{prox} is adjusted to obtain the closest possible agreement to the data descriptors.

Spacing	N_v	Vortex #	ξ	Circulation (m^2/sec)	z_i, y_i (cms)
2.0	4	1	0.15	0.115 (0.112)	-1.33,2.42 (-1.22,2.64)
		2	"	-0.102 (-0.104)	0.07,1.53 (0.20,1.42)
		3	"	0.104 (0.100)	2.09,1.48 (2.24,1.02)
		4	"	-0.126 (-0.120)	3.47,2.42 (3.66,2.44)
3.0	4	3	0.35	0.157 (0.151)	2.23,1.43 (2.84,1.02)
		4	"	-0.153 (-0.146)	3.82,1.65 (4.47,1.22)
4.0	4	3	1.20	0.229 (0.227)	-0.01,2.25 (0.20,2.84)
		4	"	-0.226 (-0.228)	1.91,2.42 (2.03,2.64)
5.0	4	3	1.40	0.225 (0.239)	0.78,1.82 (1.22,1.83)
		4	"	-0.220 (-0.221)	2.89,1.87 (3.05,1.83)
6.0	4	3	1.50	0.216 (0.207)	-0.26,1.44 (-0.61,1.02)
		4	"	-0.212 (-0.217)	2.19,1.46 (2.24,1.22)
7.0	4	3	1.50	0.213 (0.201)	-0.29,1.20 (-0.41,1.22)
		4	"	-0.210 (-0.206)	3.35,1.27 (3.66,1.02)

Notes :

1.) C_{prox} = -1.40 E-06 m^2.

2.) Vortex data descriptors are enclosed in brackets ().

3.) Refer to Figure 5.22b for an illustration of the resulting model structure of the initial spacing ratio 2.0 array at Station 150; and Figure 5.22a for the spacing ratio 3.0 array.

Table 5.4 - The downstream results of the three dimensional model with circulation decay modelled by wall friction effects and proximity losses. Here the proximity loss constant, C_{prox}, is fixed and ξ is adjusted to obtain the closest possible agreement to the downstream data descriptors.

X (ms)	z_i (ms)	y_i (ms)	Circulation (m^2/sec)	Peak Vorticity (sec^{-1})
.7366	.0152	.0102	.2810	29640.0
.7874	.0170	.0102	.2759	26914.1
.8382	.0188	.0102	.2710	24216.8
.8636	.0198	.0102	.2686	22890.5
.9144	.0216	.0102	.2639	20304.0
.9398	.0226	.0102	.2617	19051.8
.9906	.0244	.0102	.2573	16646.5
1.016	.0253	.0102	.2551	15499.1
1.067	.0271	.0102	.2509	13325.7
1.092	.0280	.0102	.2498	12302.8
1.118	.0289	.0102	.2468	11323.5
1.168	.0305	.0102	.2429	9496.5
1.194	.0314	.0102	.2410	8648.0
1.245	.0330	.0102	.2372	7075.1
1.270	.0337	.0102	.2354	6347.2
1.321	.0352	.0102	.2318	4996.4
1.346	.0360	.0102	.2301	4367.6
1.397	.0374	.0102	.2266	3186.5
1.422	.0381	.0102	.2250	2626.6
1.473	.0394	.0102	.2217	1547.9
1.499	.0400	.0102	.2202	1440.0

Table 5.5 - The downstream development of the vortex descriptors for the case of the single embedded vortex as predicted by the model.

Spacing	Vortex #	X (cms)	Circulation (Data) (m^2/sec)	Circulation (Model) (m^2/sec)	Peak Vorticity (Data) (sec^{-1})
Downflow pair.					
3.0	2	66	.2416	.2416(input)	2032
		97	.1904	.1988	1363
		142	.1414	.1506	691
		188	.1216	.1253	243
Upflow pair.					
3.0	2	66	-.2272	-.2272(input)	-2112
		97	-.1760	-.1832	-1000

Notes :

1.) z_i, y_i are not listed. The motion of the core centers can be observed in Figures 5.26-5.27.

Table 5.7 - A comparison of the downstream vortex descriptors observed in the Stanford study of Pauley and Eaton (1988) to those obtained by the model. The test cases are the upflow and downflow counter-rotating pairs illustrated in Figures 5.26 and 5.27.

Spacing	Vortex #	INPUT DESCRIPTORS (z_i, y_i) (cms)	PREDICTED STATION 150 DESCRIPTORS (z_i, y_i) (cms)	Circulation (m^2/sec)	Peak Vorticity (sec^{-1})
7.0	7	12.26,1.02	13.88,1.23	0.211	900.0
	8	18.74,1.02	17.06,1.25	-0.207	-900.0
6.0	7	10.26,1.02	11.65,1.41	0.214	900.0
	8	15.74,1.02	14.27,1.44	-0.210	-900.0
5.0	7	10.09,1.02	11.15,1.75	0.219	900.0
	8	14.54,1.02	13.37,1.79	-0.214	-900.0
4.0	7	8.50,1.02	9.18,2.25	0.226	900.0
	8	12.00,1.02	11.14,2.32	-0.218	-900.0
3.0	7	6.04,1.02	6.26,1.76	0.158	500.0
	8	8.55,1.02	7.96,1.91	-0.156	-500.0
2.0	7	5.01,1.02	4.80,1.44	0.102	500.0
	8	6.67,1.02	6.26,2.22	-0.134	-500.0

Notes :

1.) Input circulation = $\pm$ 0.270 m^2/sec, input peak vorticity = $\pm$ 27000 sec^{-1}. The decay constant, ξ, was chosen in accordance with the correlation to initial spacing ratio given in Table 5.4.

Table 5.6 - The upstream and downstream descriptors of the $N_v = 8$ arrays as predicted by the model.

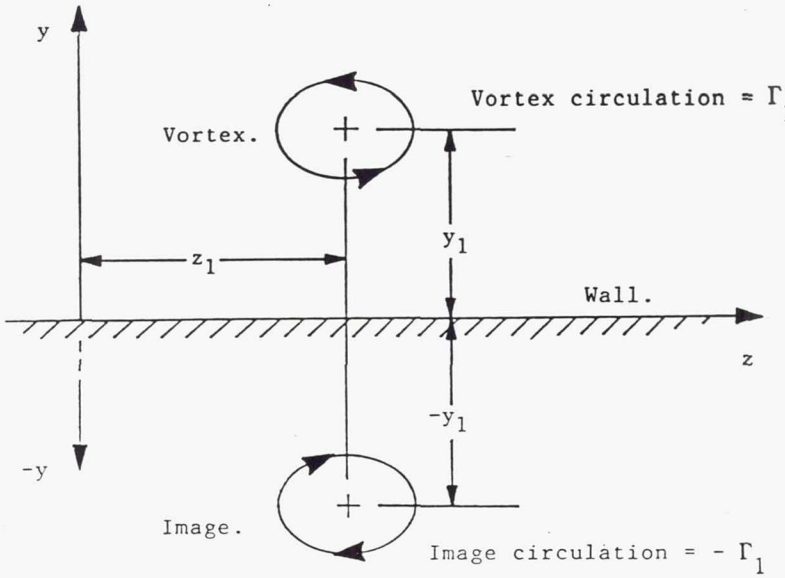

5.1a

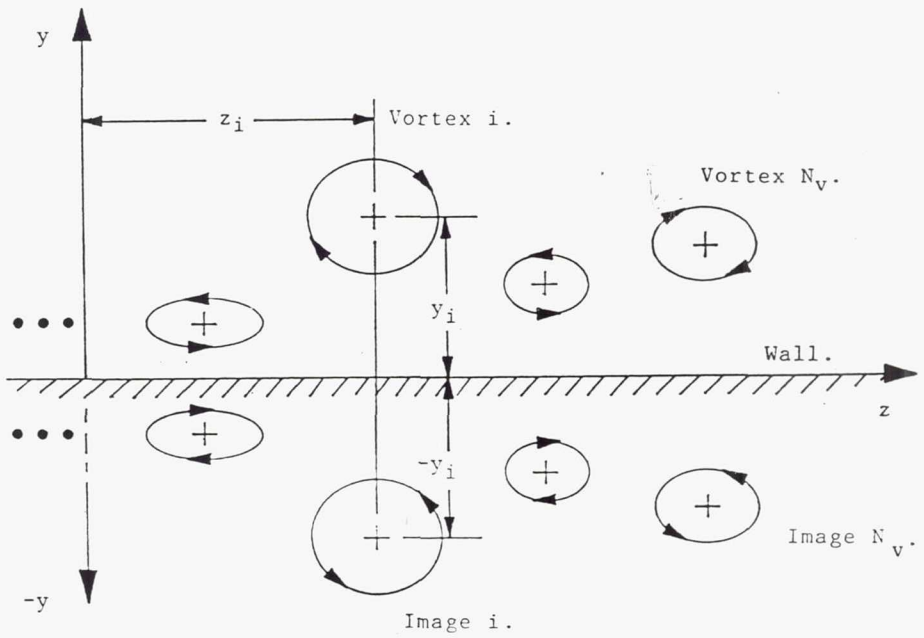

5.1b

Figure 5.1a (top) - A diagram illustrating the construction of an Oseen model representation of a single embedded vortex.

Figure 5.1b (bottom) - A diagram illustrating the construction of an embedded array of N_v vortices

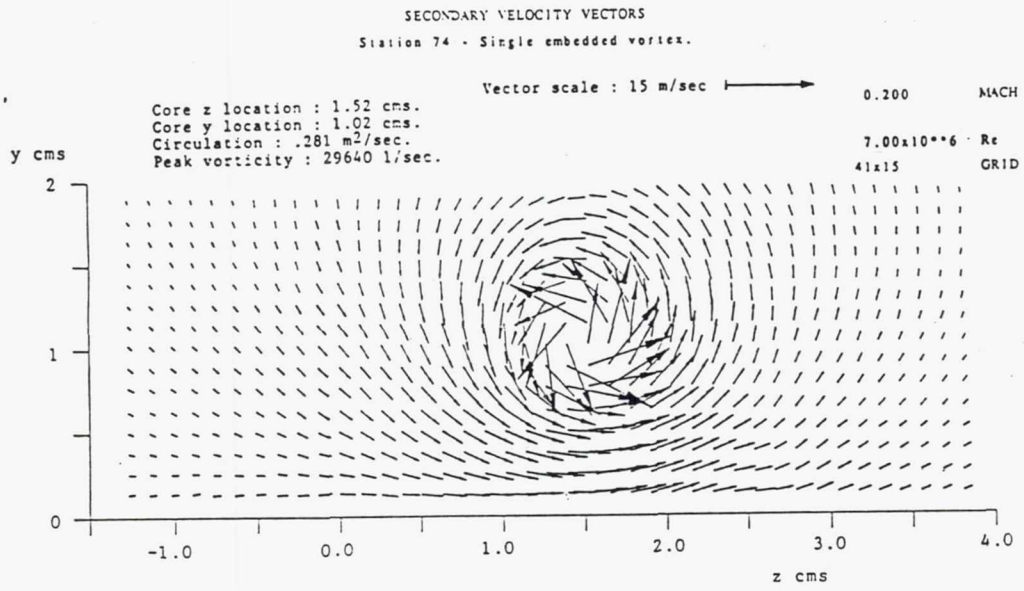

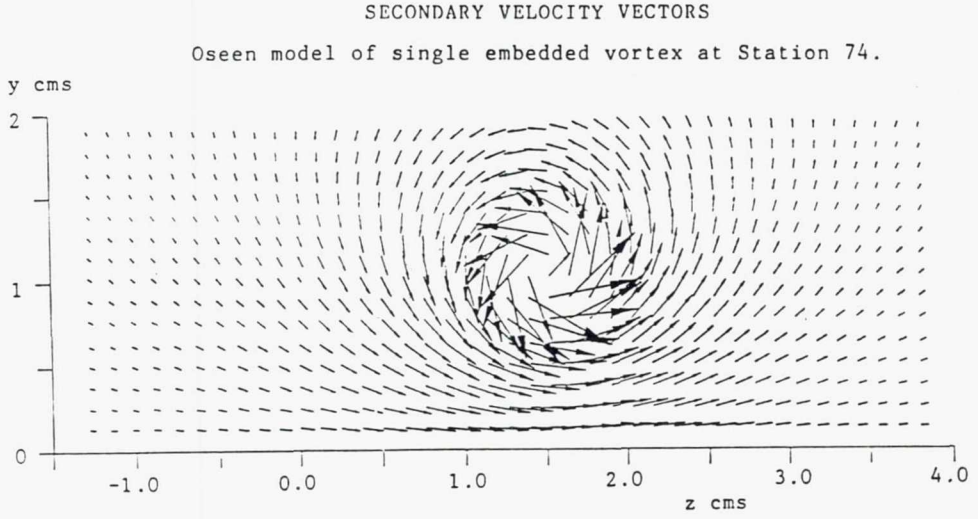

Figure 5.2a - A comparison of the secondary velocity field of the single embedded vortex (top) and model (bottom) at Station 74.

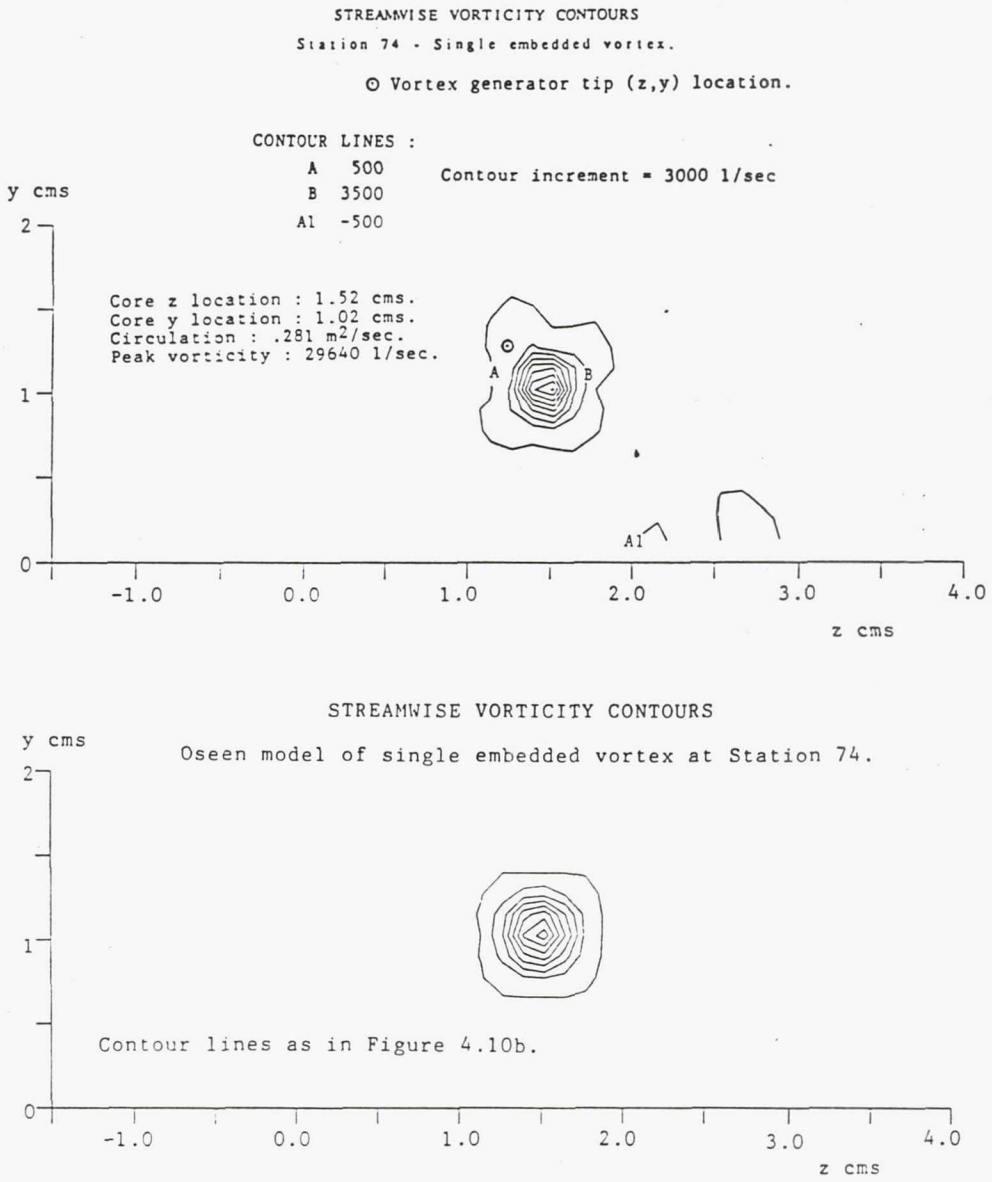

Figure 5.2b - A comparison of the streamwise vorticity field of the single embedded vortex (top) and model (bottom) at Station 74.

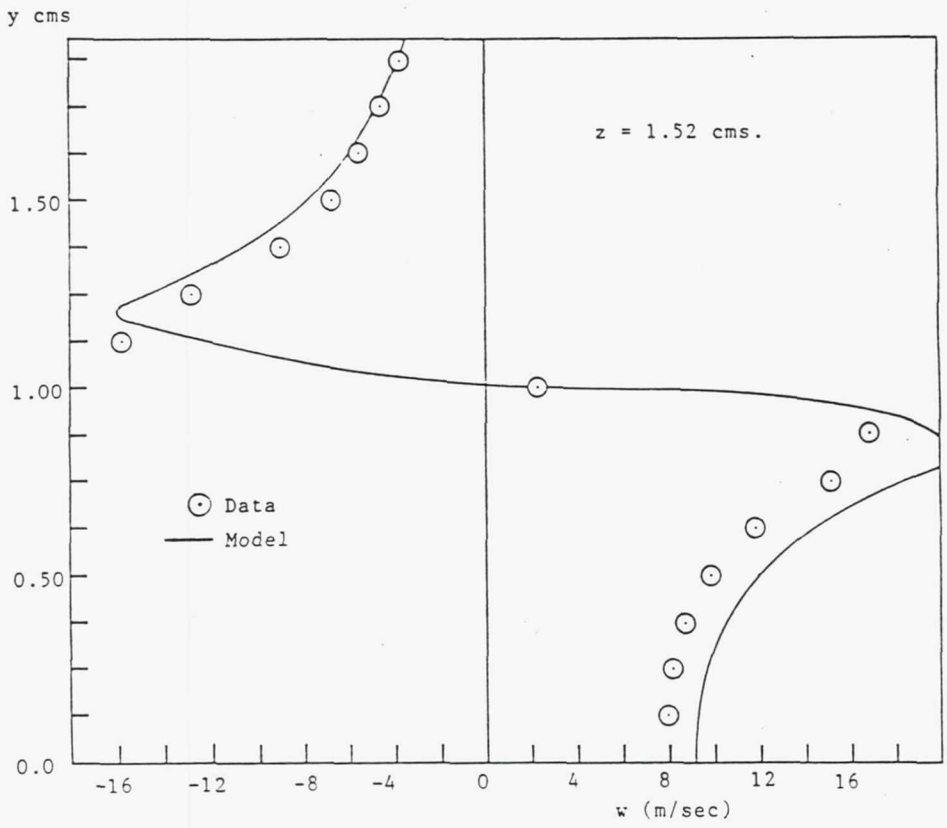

Figure 5.2c - A comparison of the w velocity profiles through the vortex center. Single embedded vortex at Station 74.

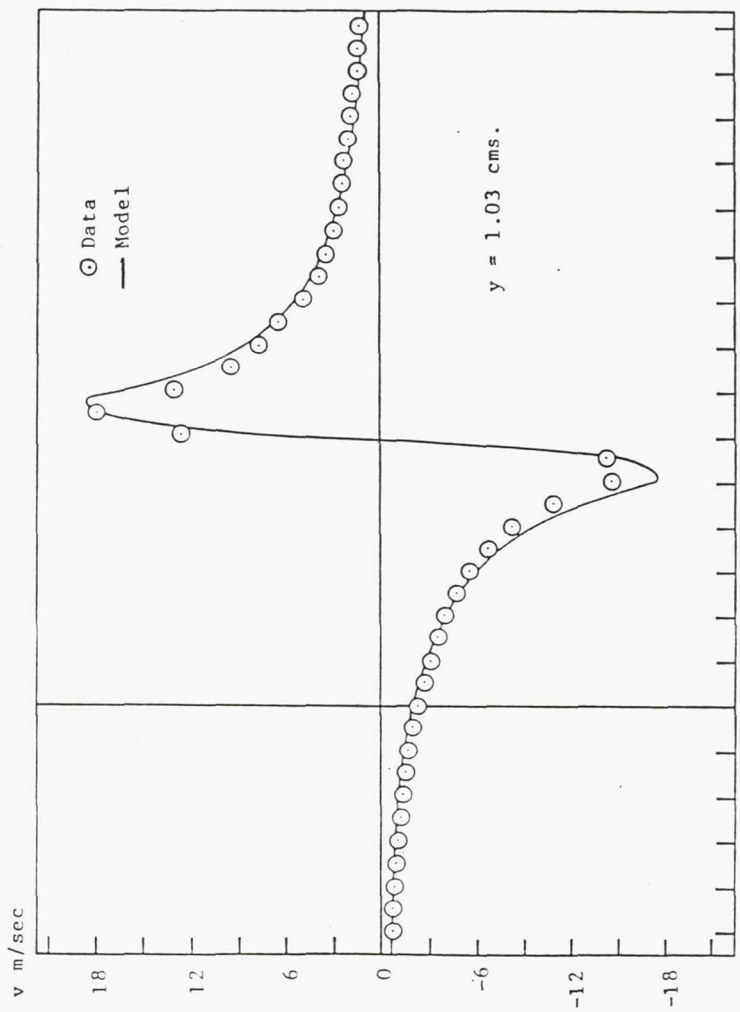

Figure 5.2d - A comparison of the v velocity profiles through the vortex center. Single embedded vortex at Station 74.

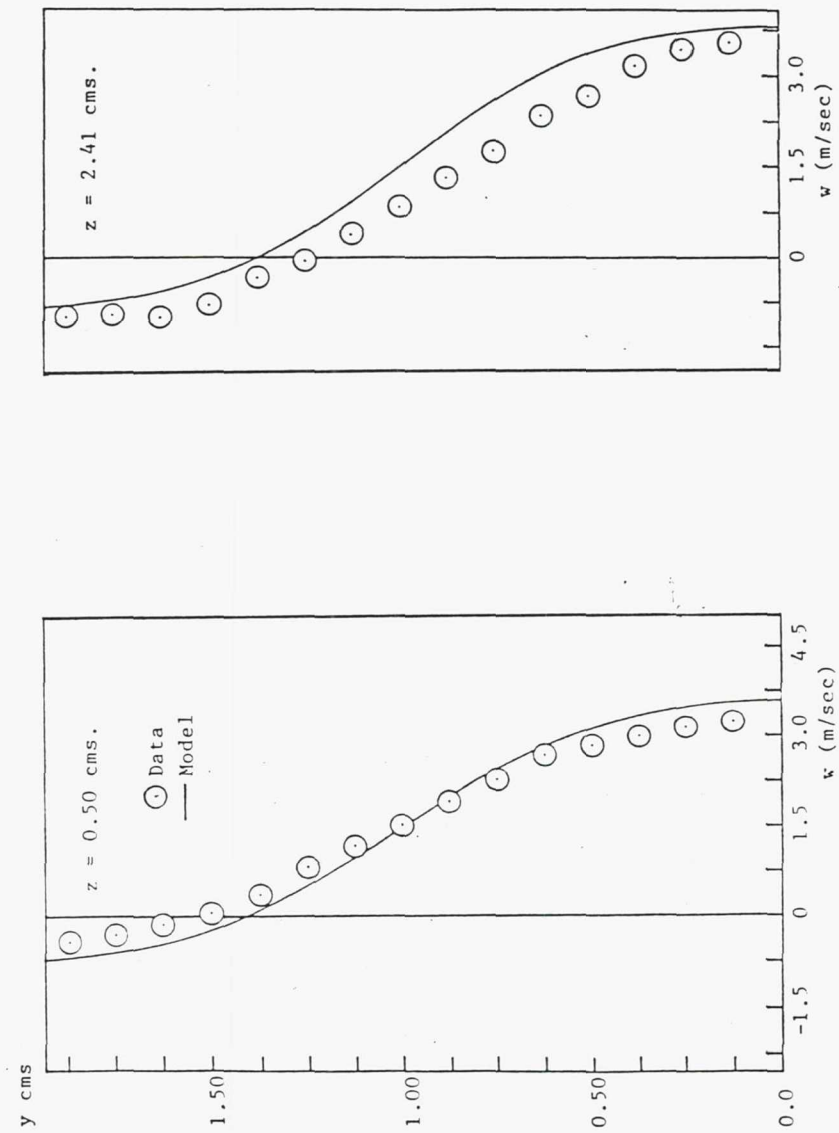

Figures 5.2c-f - A comparison of the w velocity profiles in the vortex downwash region (Figure 5.2e at the left) and in the vortex upwash region (Figure 5.2f at the right). Single embedded vortex at Station 74.

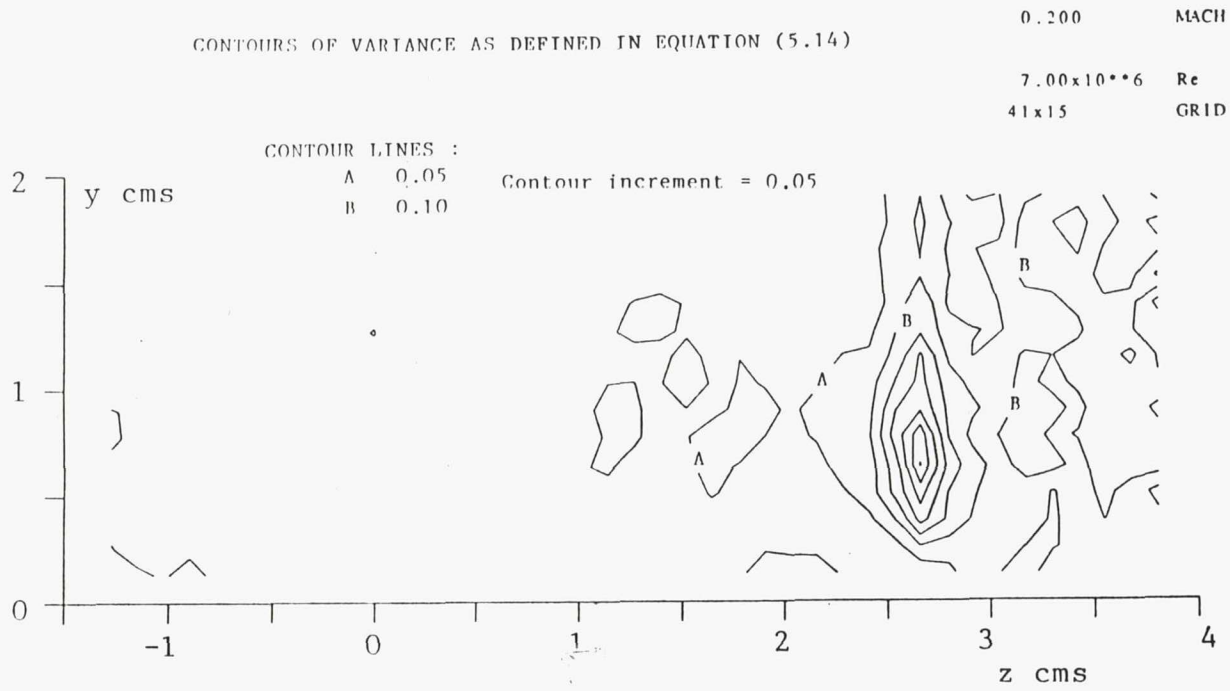

Figure 5.2g - Contours of the variation between model and data for the case of the single embedded vortex at Station 74. The variation peaks in the vortex upwash region.

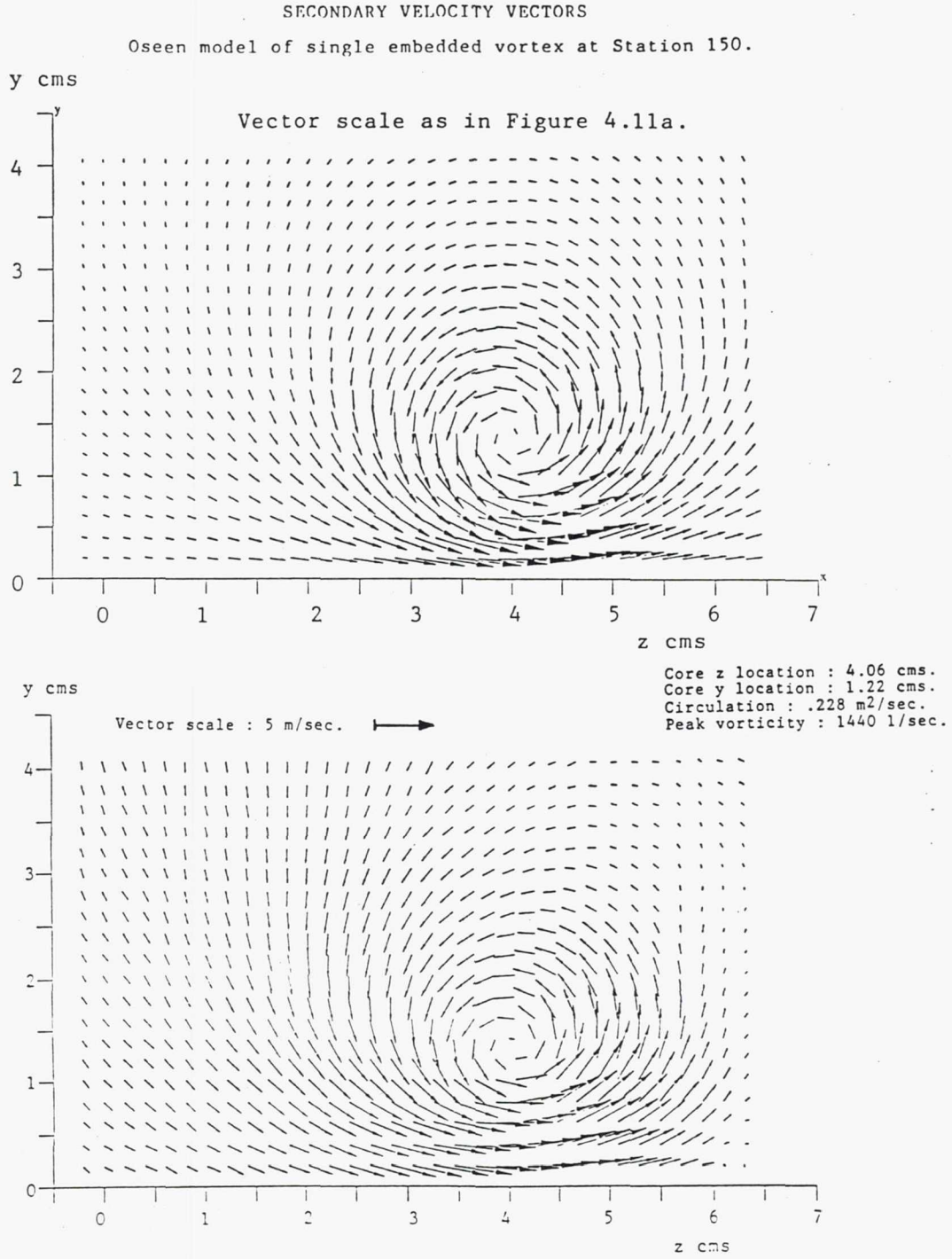

Figure 5.3a - Secondary velocity field of the Oseen model of the single embedded vortex at Station 150 (top). Figure 4.11a is included for comparison (bottom).

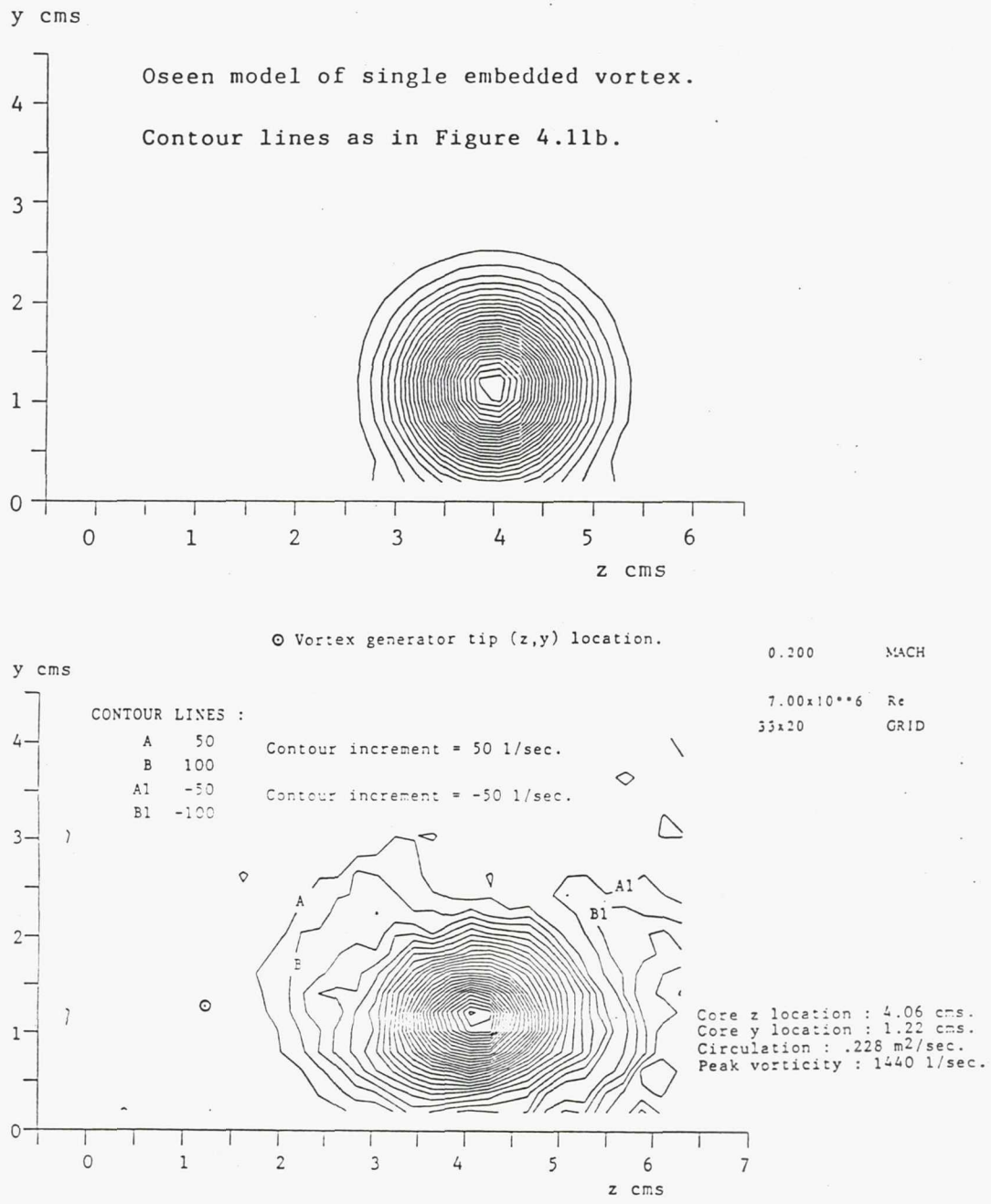

Figure 5.3b - Streamwise vorticity contours of the Oseen model of the single embedded vortex at Station 150 (top). Figure 4.11b is included for comparison.

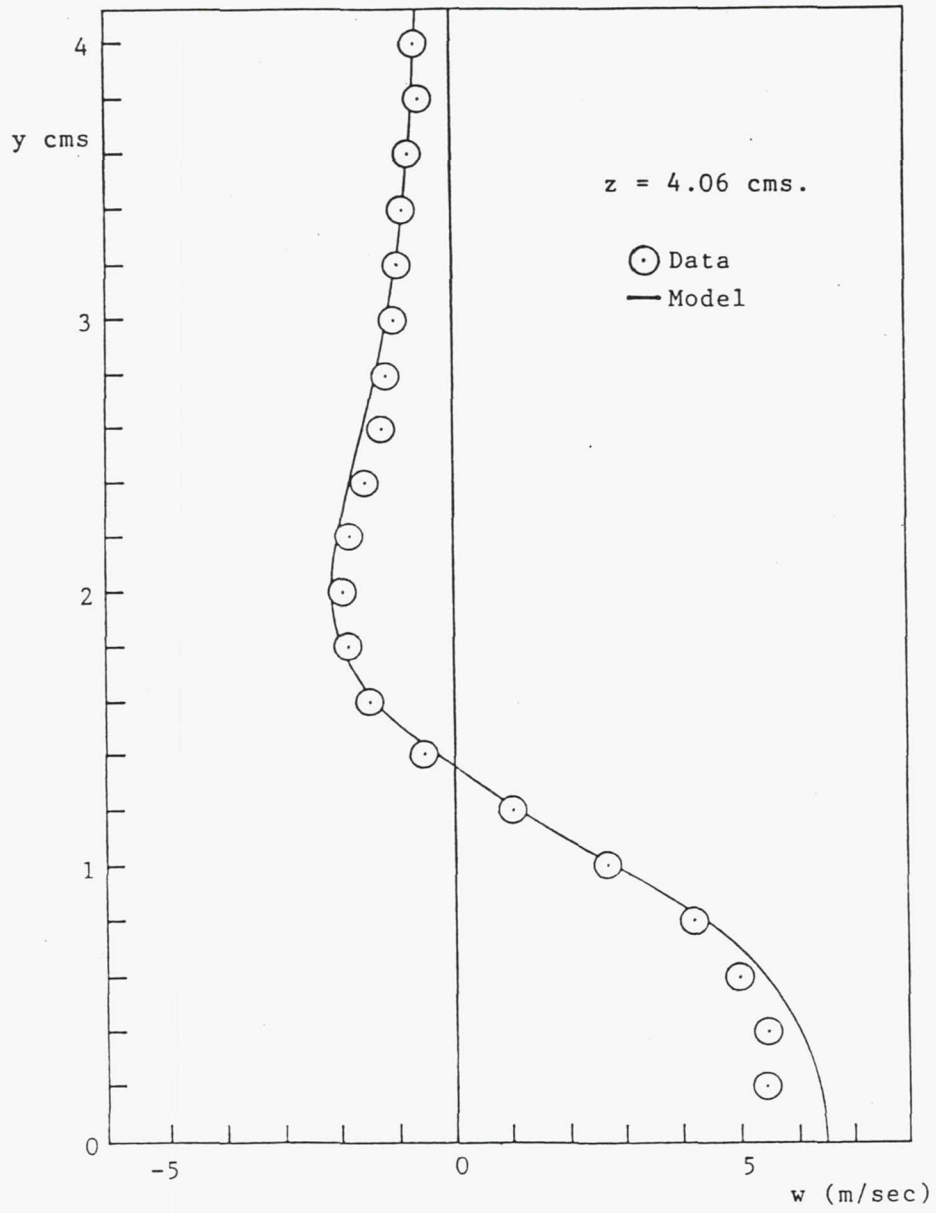

Figure 5.3c - Comparison of model and data w velocity profiles through the center of the single embedded vortex at Station 150.

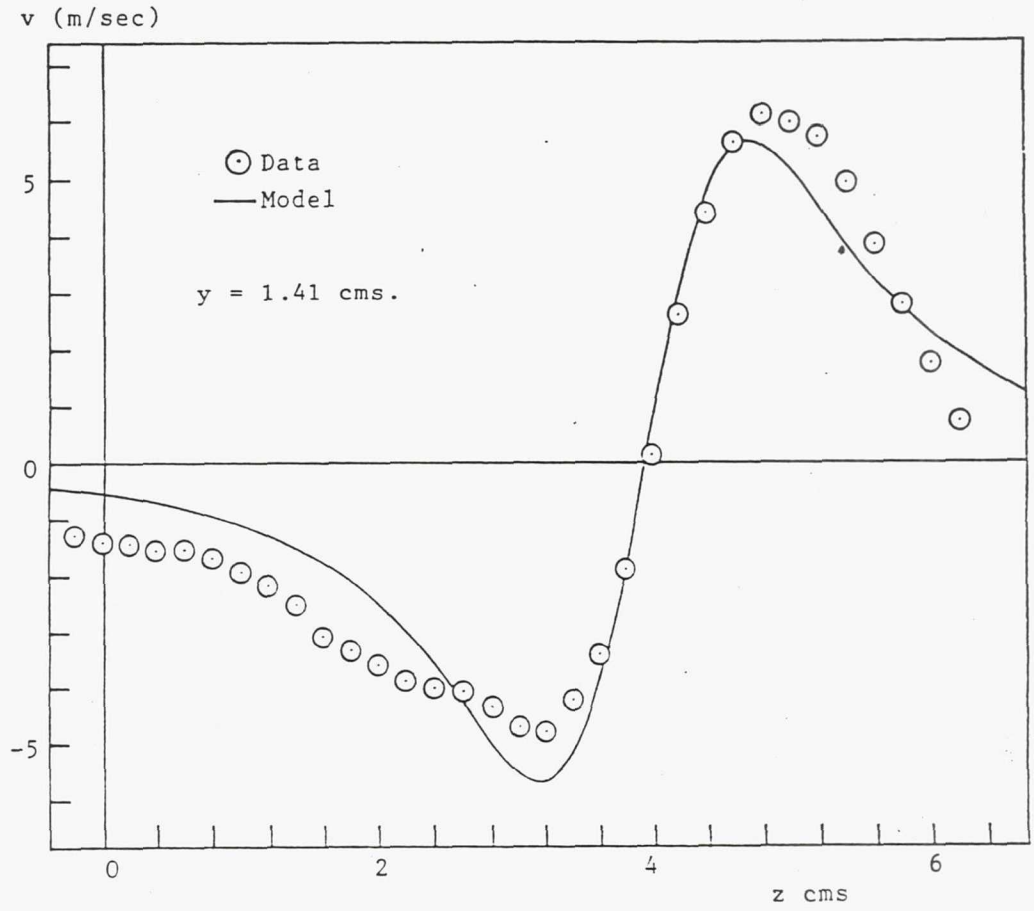

Figure 5.3d - Comparison of model and data v velocity profiles through the center of the single embedded vortex at Station 150.

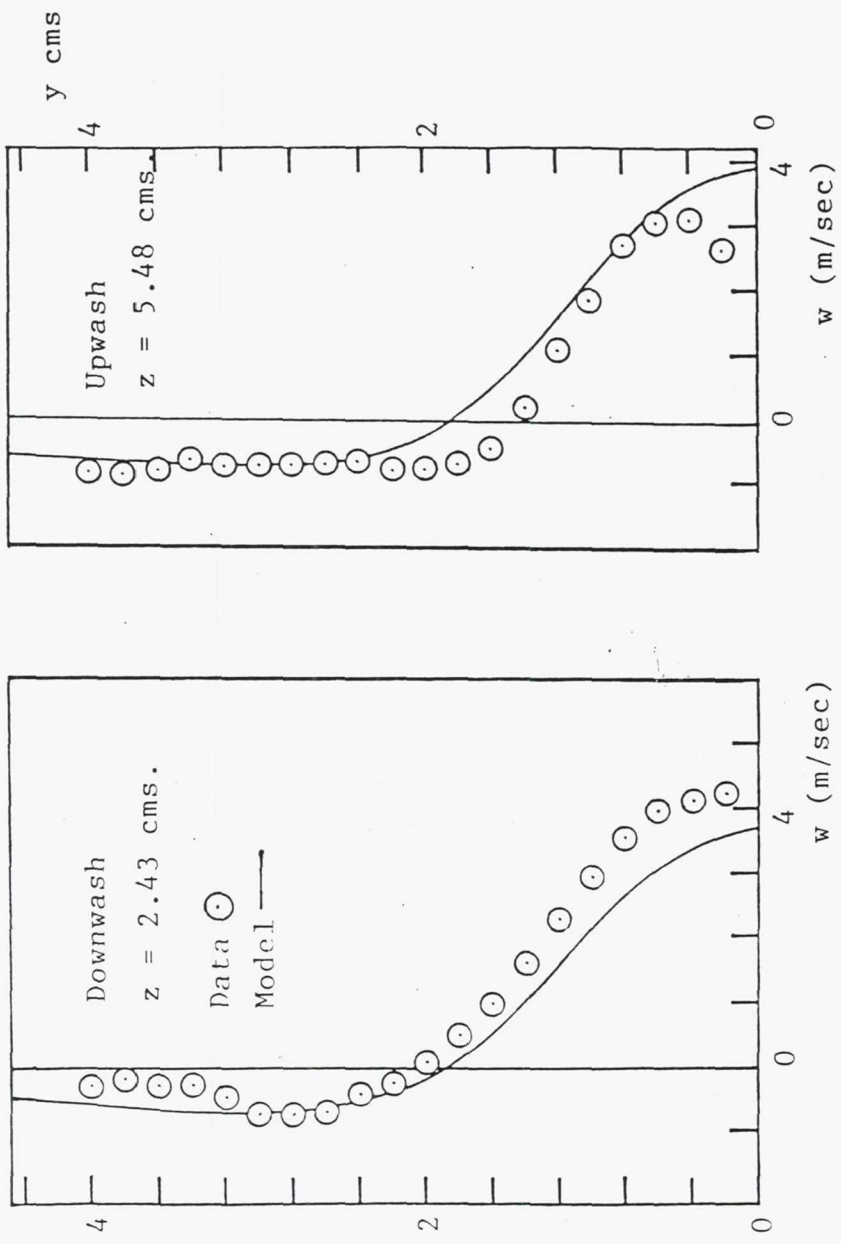

Figure 5.3e (left) - Comparison of model and data w velocity profiles in the downwash region of the single embedded vortex at Station 150.

Figure 5.3f (right) - Comparison of model and data w velocity profiles in the upwash region of the single embedded vortex at Station 150.

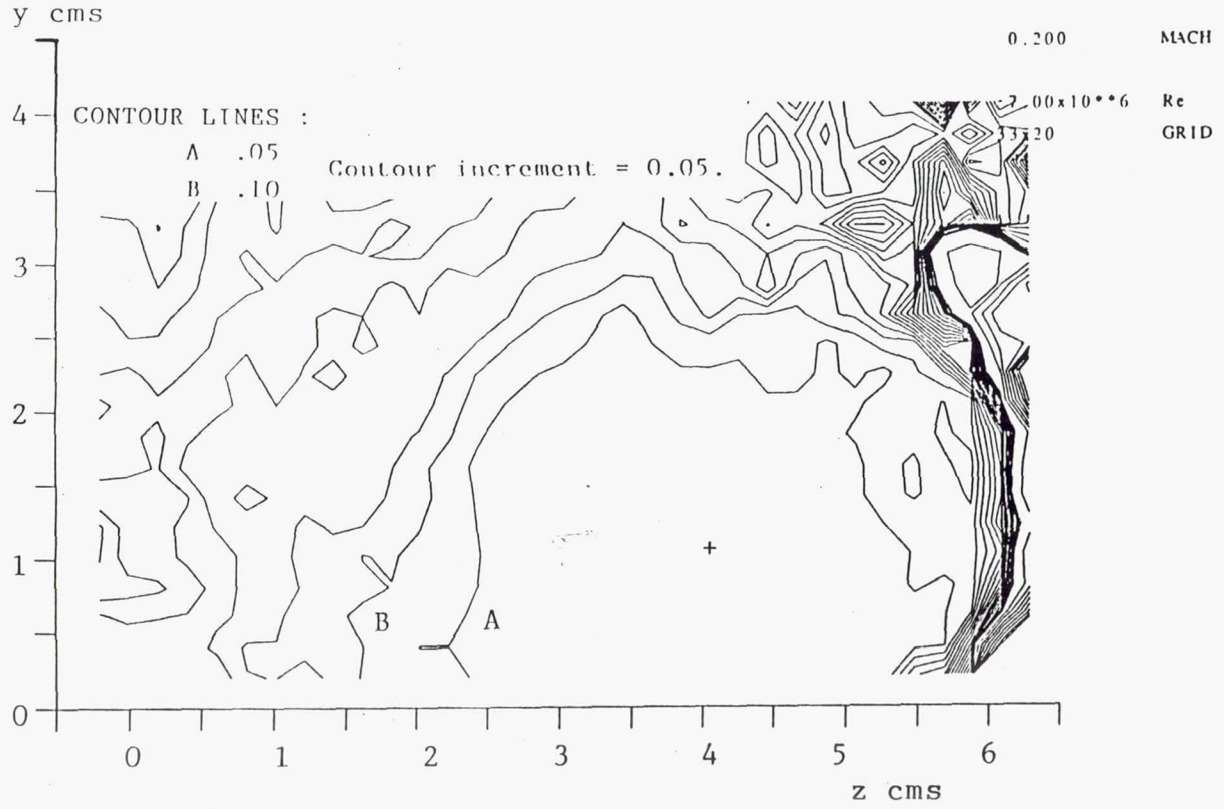

Figure 5.3g - Contours of variance between model and data of single embedded vortex at Station 150, as defined in Eq. (5.14).

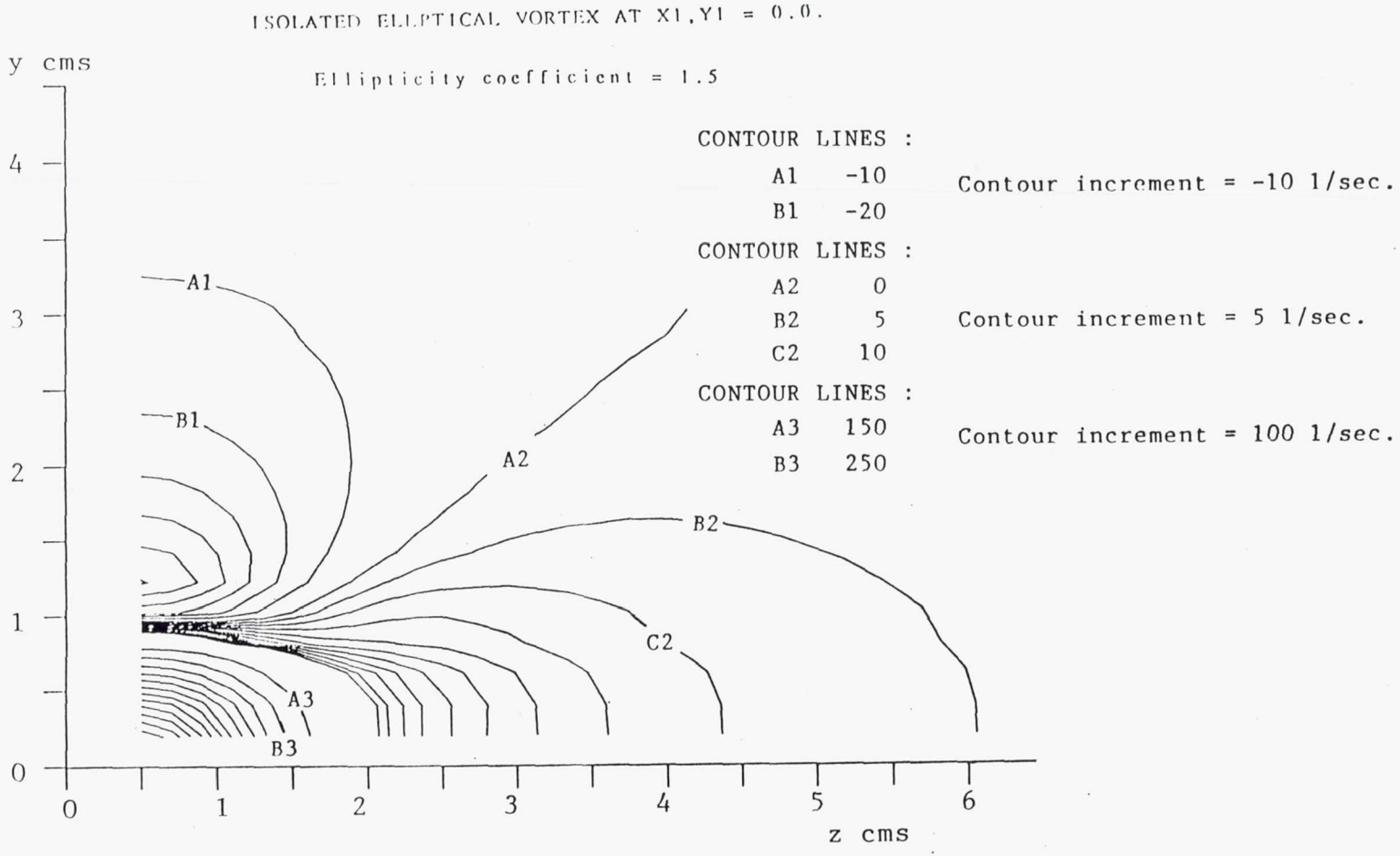

Figure 5.4 - The streamwise vorticity field of the isolated elliptical model.

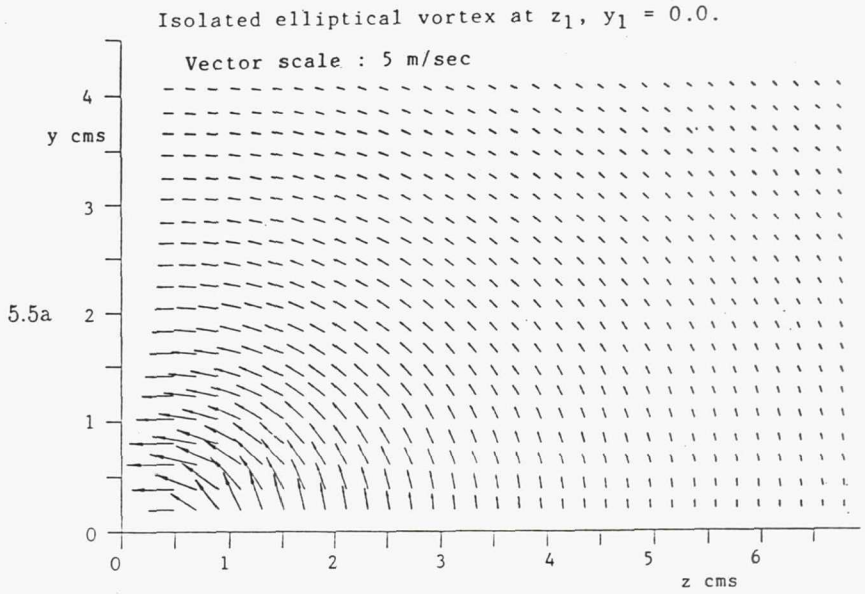

5.5a

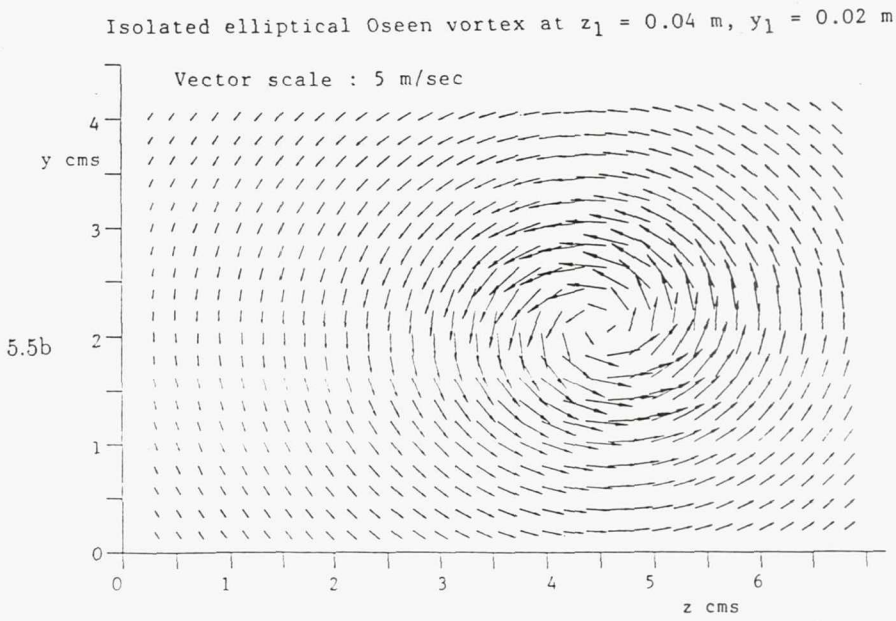

5.5b

Figure 5.5a (top) - The velocity vector plot corresponding to Figure 5.4.

Figure 5.5b (bottom) - The velocity vector plot of the elliptical vortex in Figure 5.4, now displaced into the first quadrant.

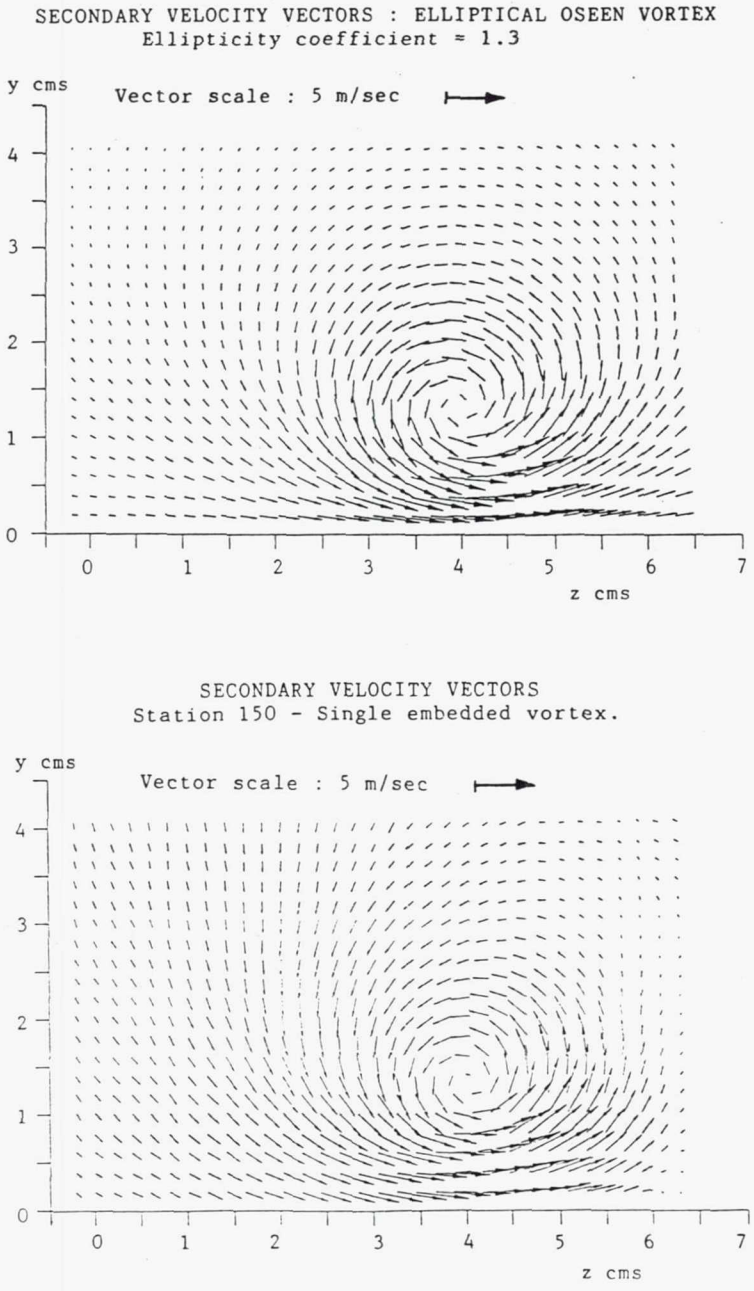

Figure 5.6a - A comparison of the secondary velocity fields of the elliptical model (top) and the data (Figure 4.11a at the bottom).

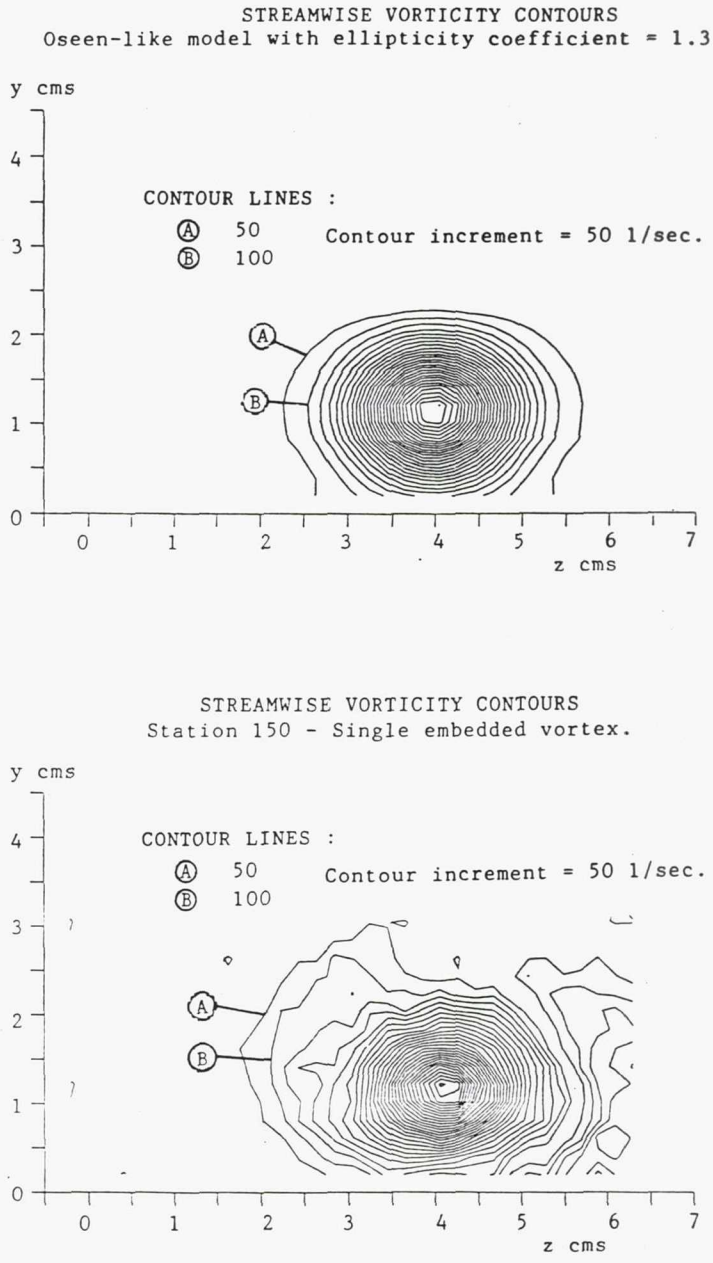

Figure 5.6b - A comparison of the streamwise vorticity fields of the elliptical vortex model (top) and the data (Figure 4.11b at the bottom).

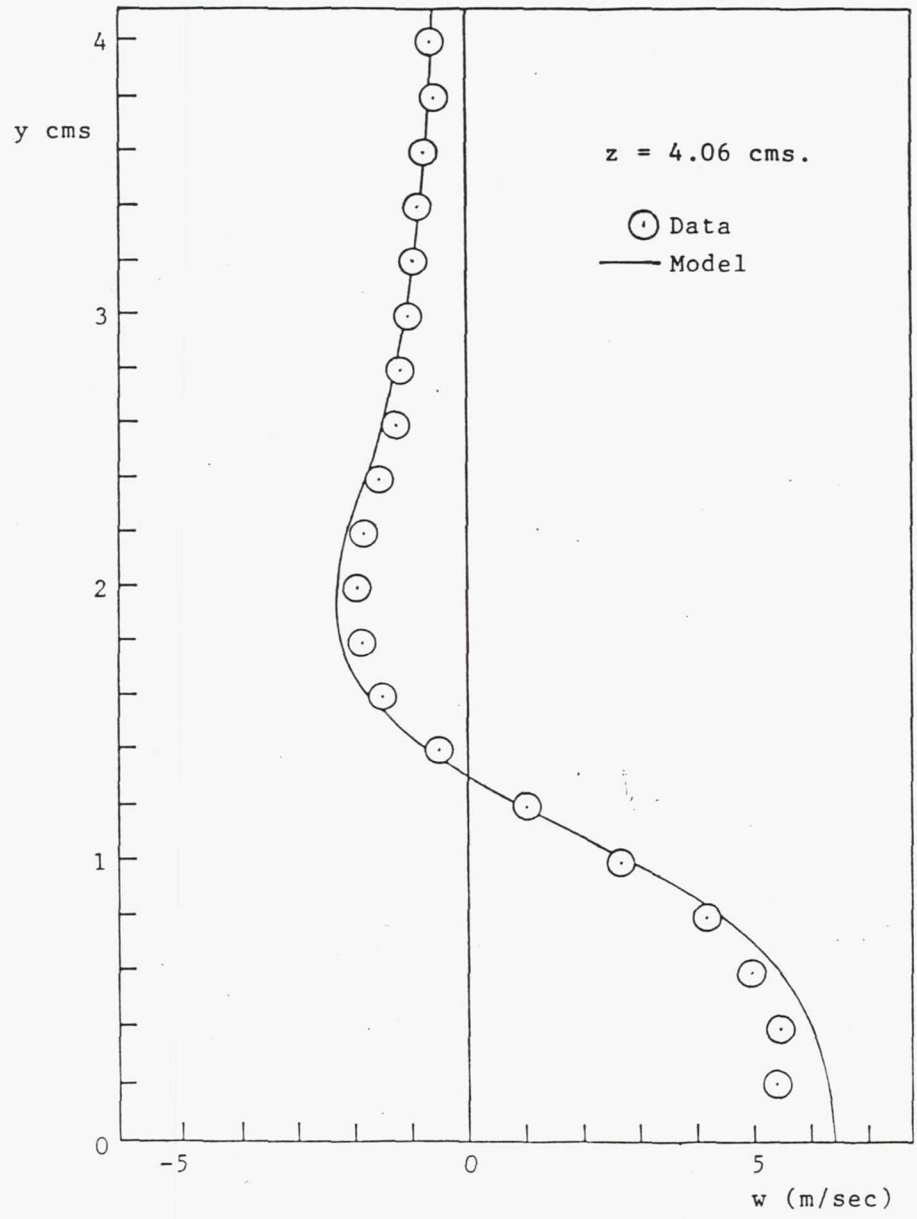

Figure 5.7a - Comparison of elliptical model and data w velocity profiles through the center of the single embedded vortex at Station 150.

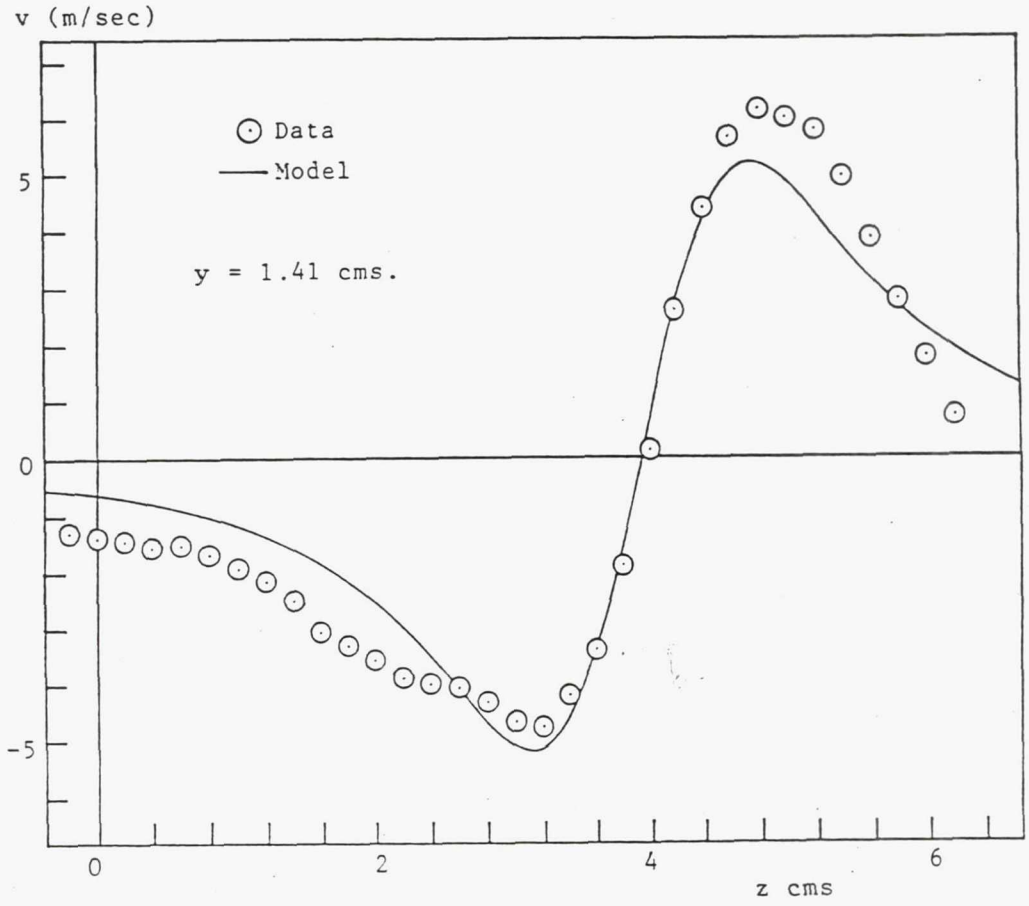

Figure 5.7b - Comparison of elliptical model and data v velocity profiles through the center of the single embedded vortex at Station 150.

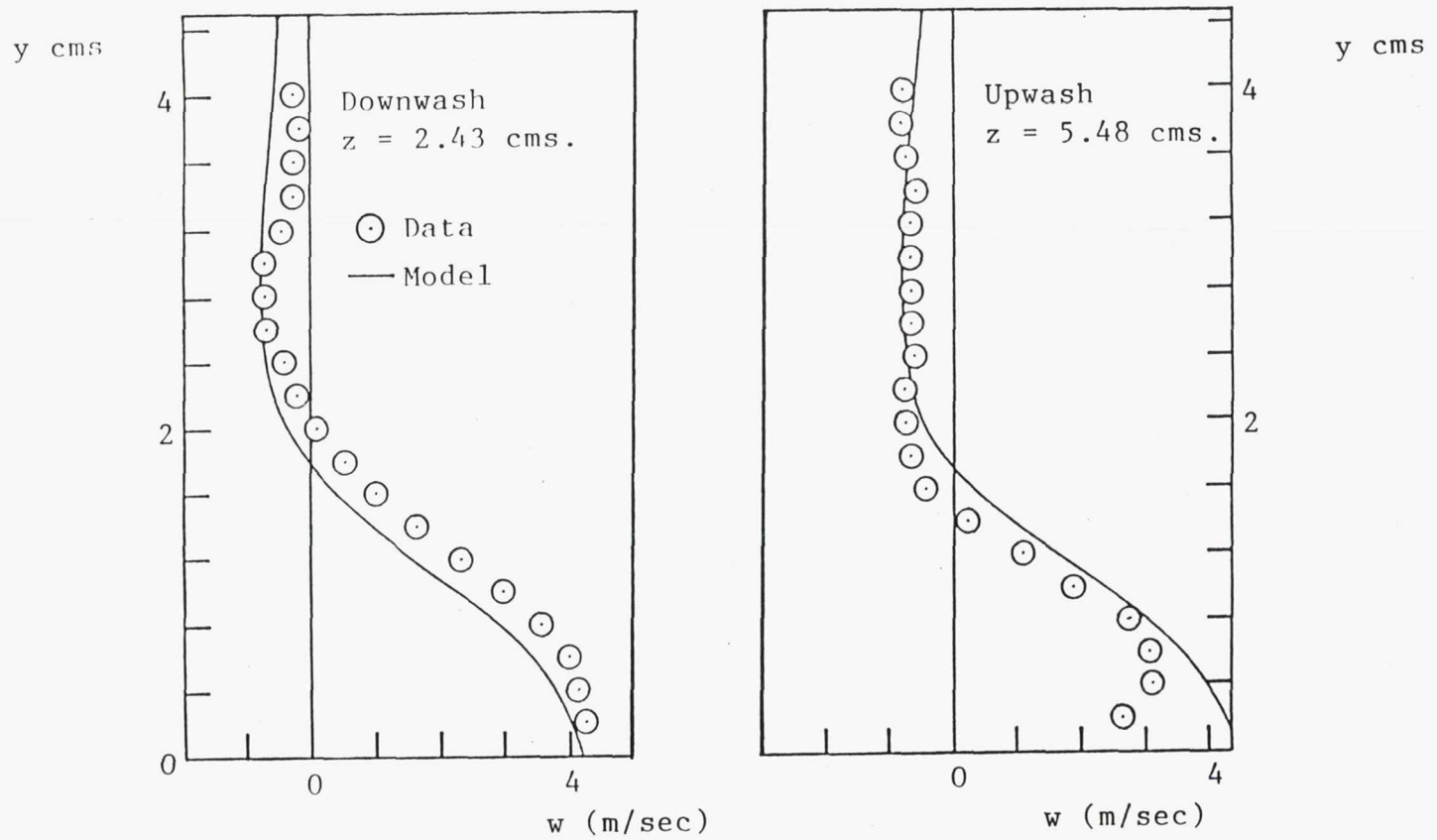

Figure 5.7c (left) - Comparison of the elliptical model and data w velocity profiles in the downwash region of the single embedded vortex at Station 74.

Figure 5.7d (right) - Comparison of elliptical model and data w velocity profiles in the upwash region of the single embedded vortex at Station 150.

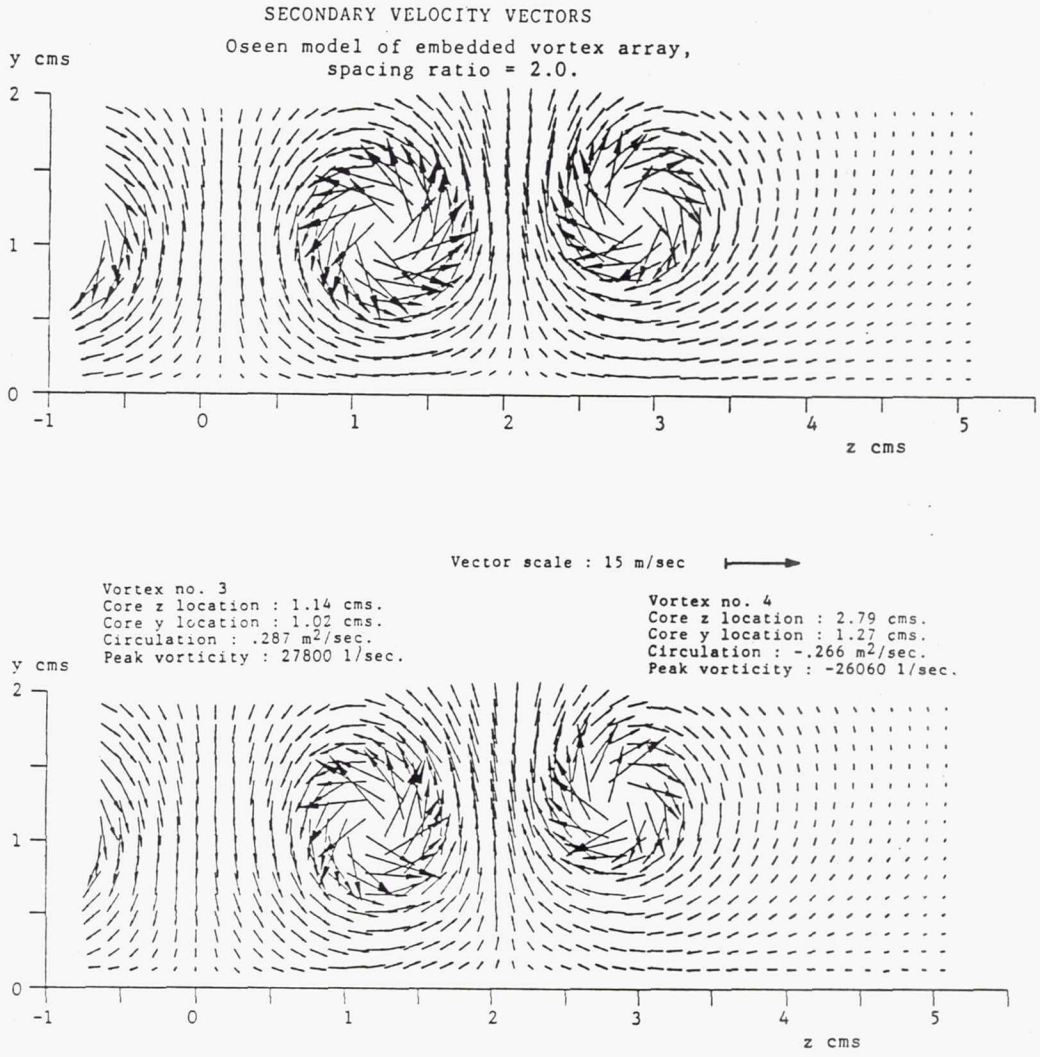

Figure 5.8a - A comparison of the secondary velocity fields of the Oseen model (top) of the initial spacing ratio 2.0 array at Station 74, and the data (bottom).

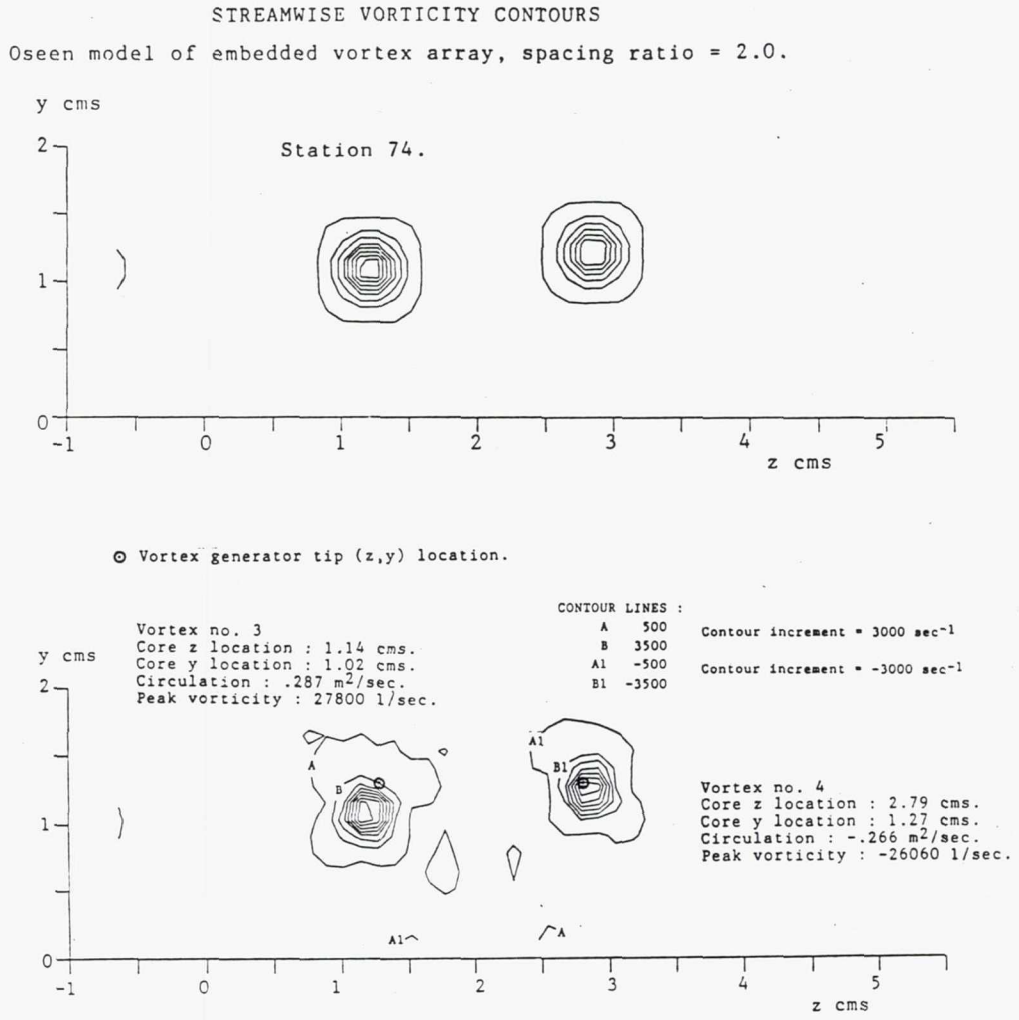

Figure 5.8b - A comparison of the streamwise vorticity fields of the Oseen model (top) of the initial spacing ratio 2.0 array at Station 74, and the data (bottom).

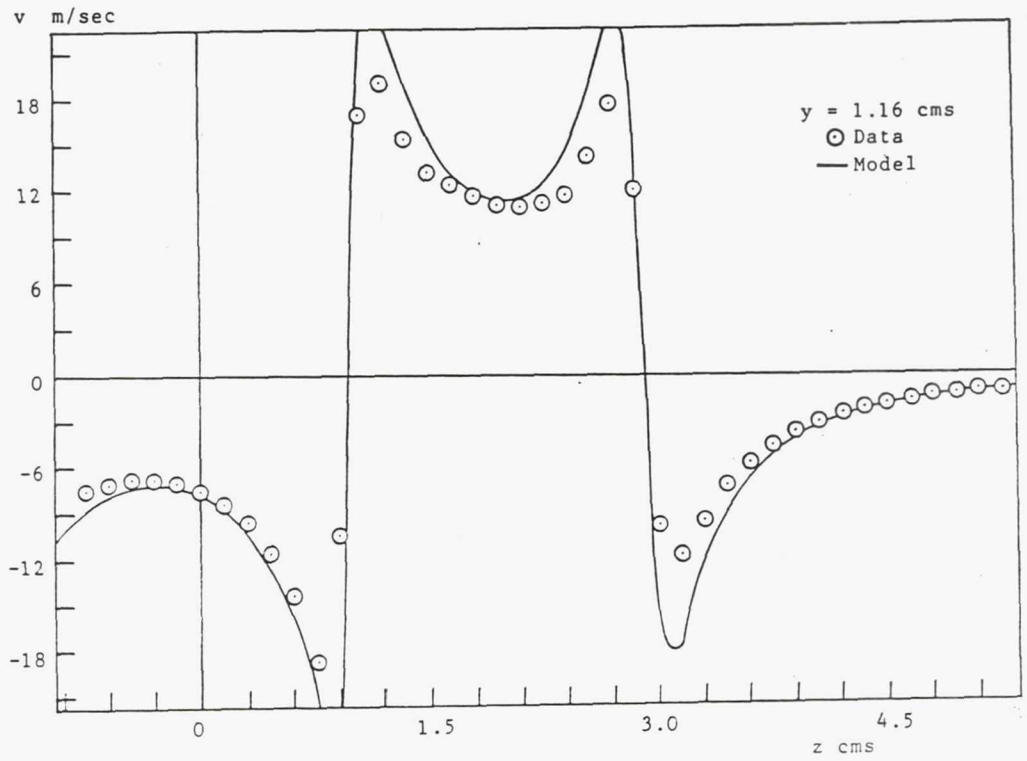

Figure 5.8c - A comparison between the model and data v velocity profiles through the approximate centers of vortices 3 and 4 of the spacing ratio 2.0 array at Station 74.

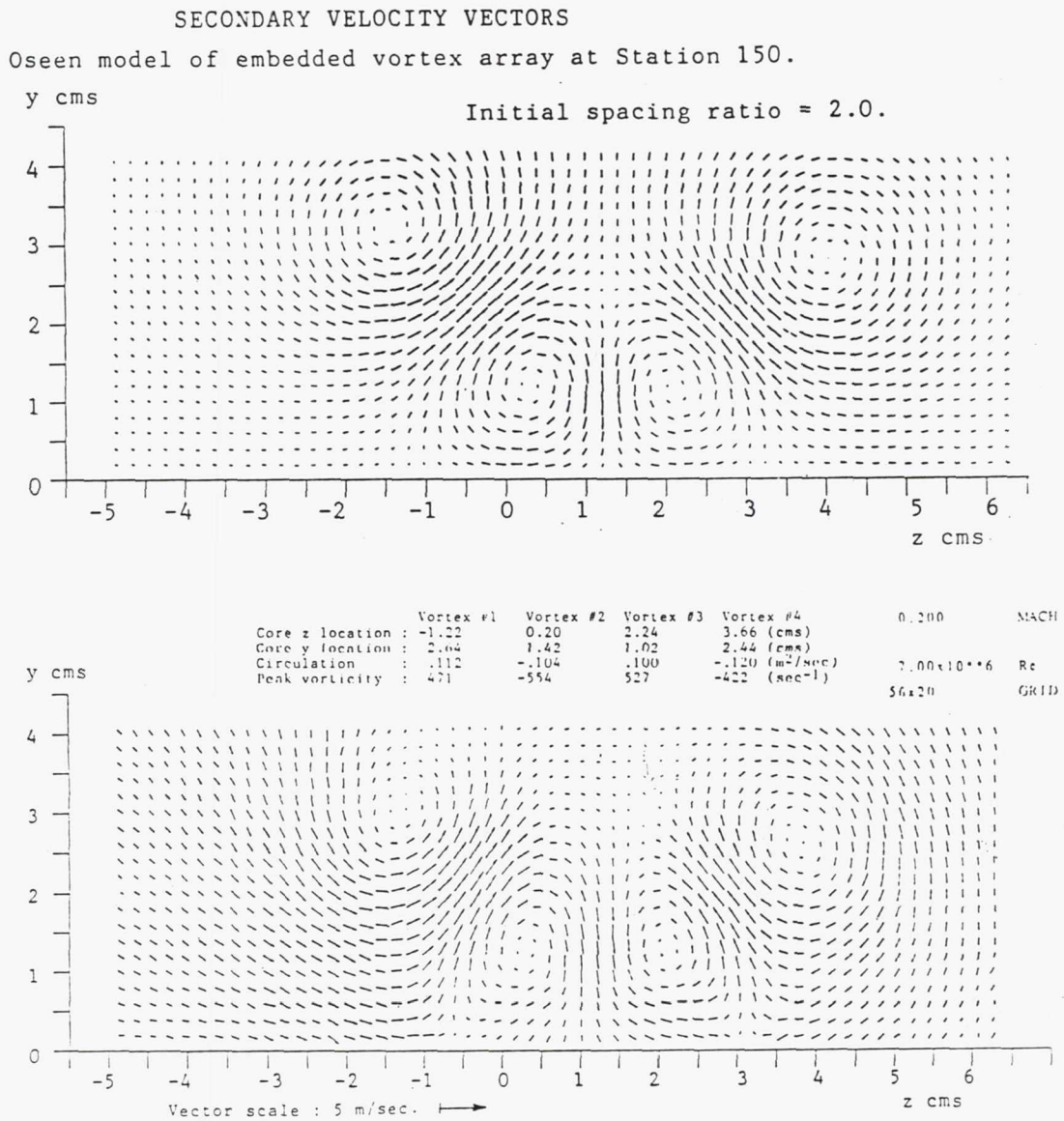

Figure 5.9a - A comparison of the secondary velocity fields of the Oseen model (top) and data (bottom). The test case is the spacing ratio 2.0 array at Station 150.

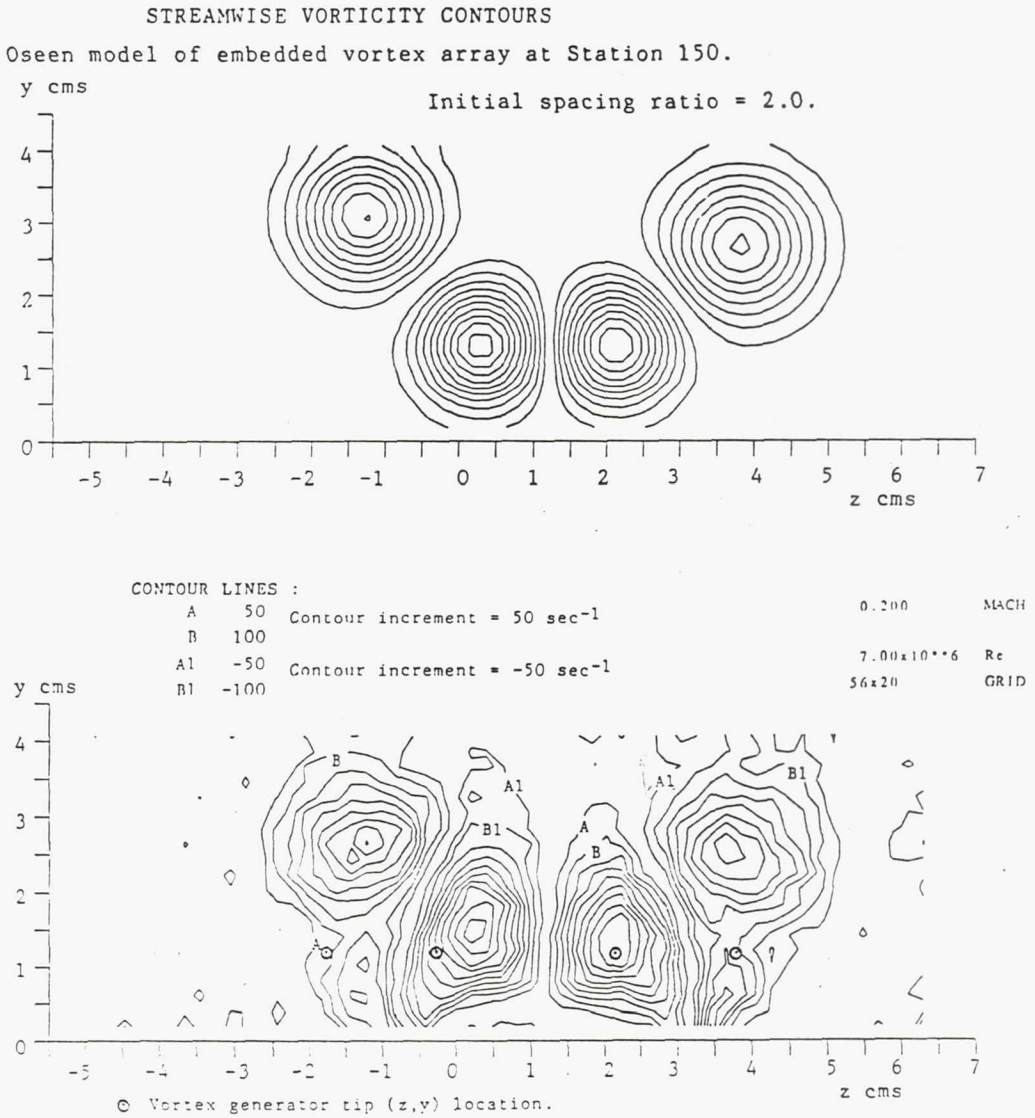

Figure 5.9b - A comparison of the streamwise vorticity fields of the Oseen model (top) and data (bottom). The test case is the spacing ratio 2.0 array at Station 150.

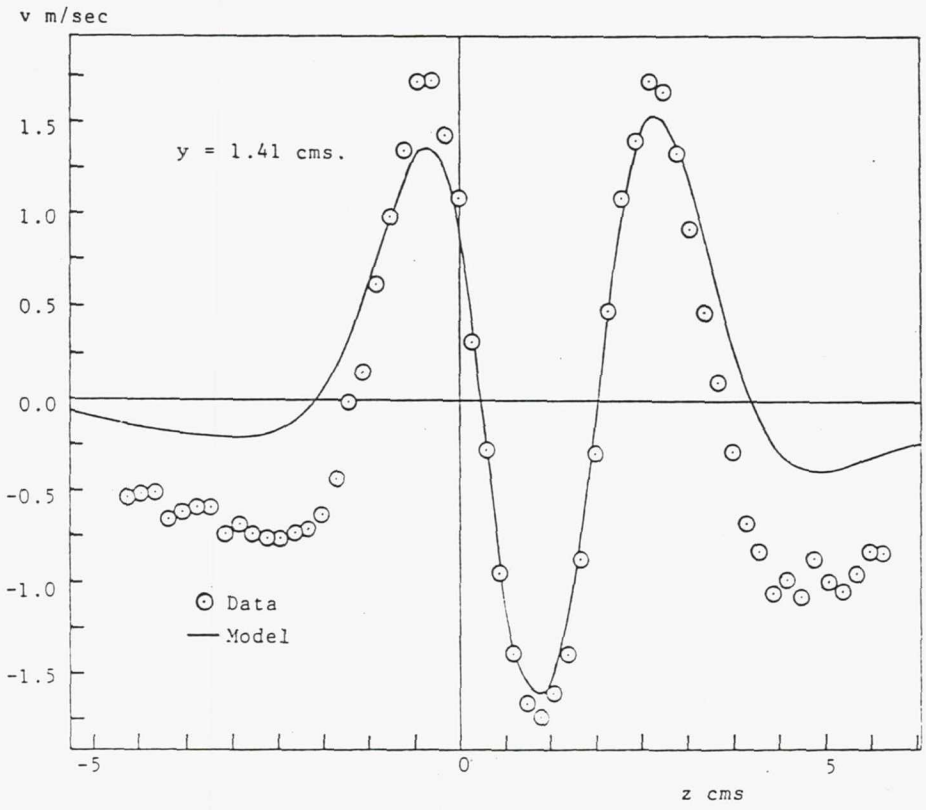

Figure 5.9c - A comparison between the model and data v velocity profiles through the center of vortices 2 and 3 of the spacing ratio 2.0 array at Station 150.

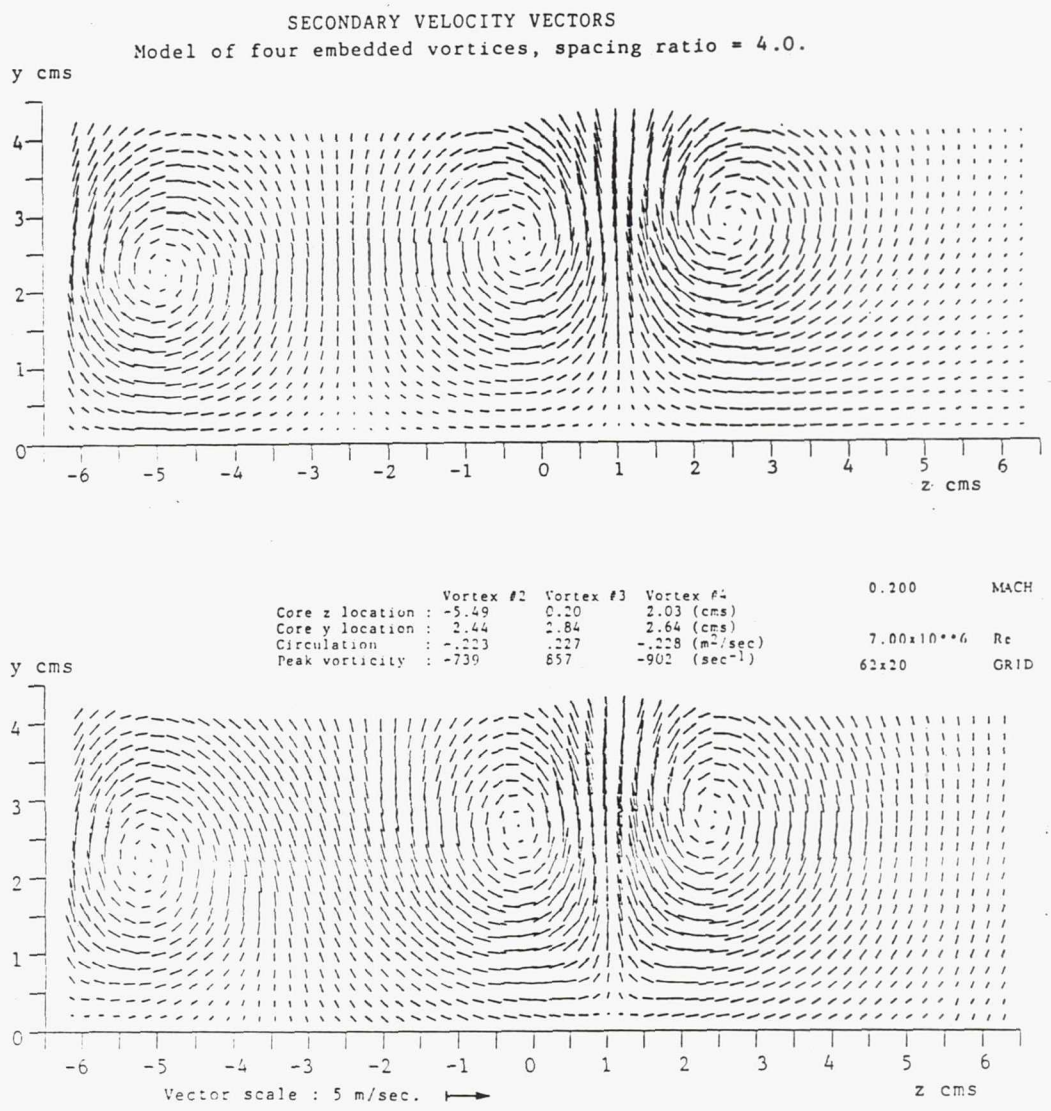

Figure 5.10a - A comparison of the secondary velocity fields of the Oseen model (top) and data (bottom). The test case is the spacing ratio 4.0 array at Station 150.

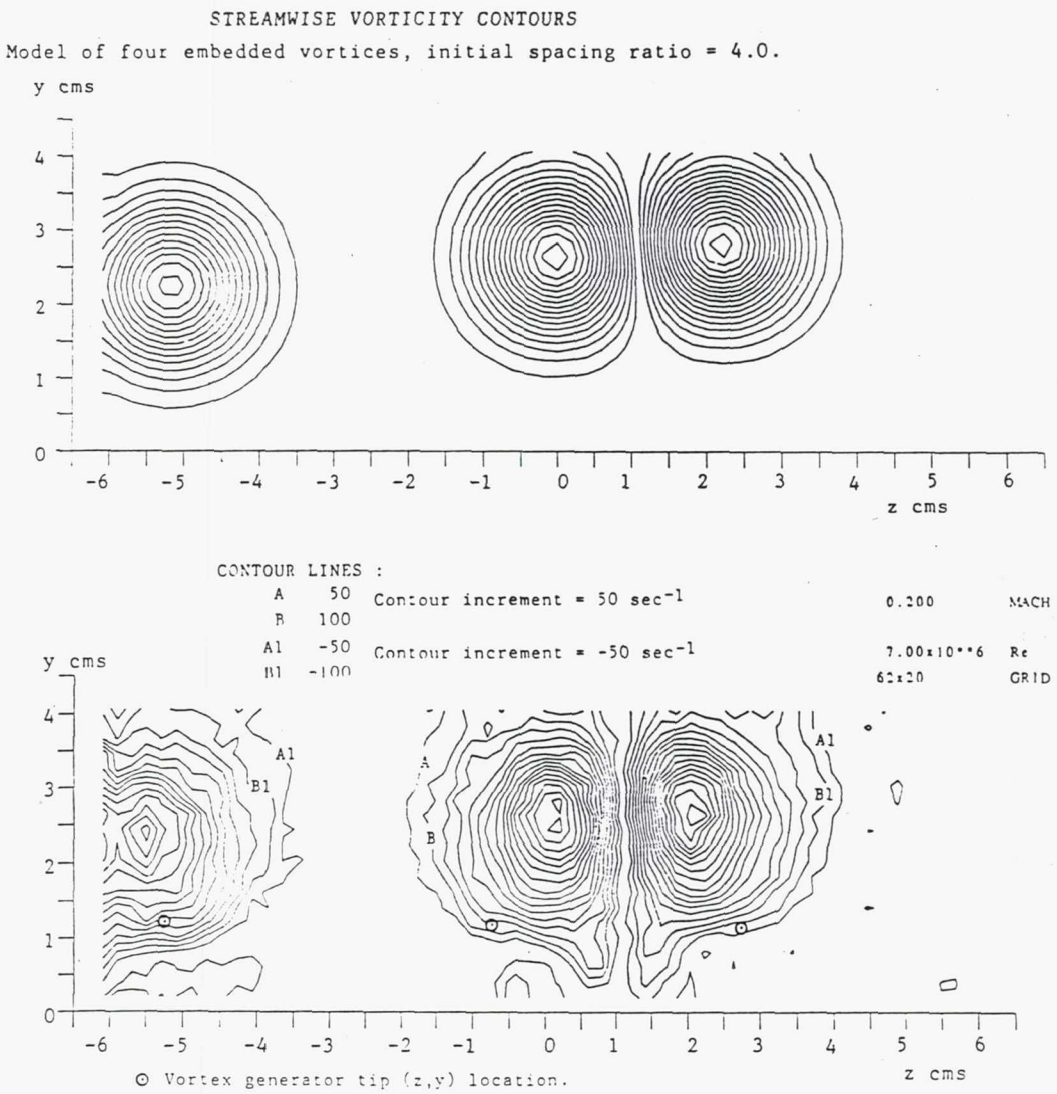

Figure 5.10b - A comparison of the streamwise vorticity contours of the Oseen model (top) and data (bottom). The test case is the spacing ratio 4.0 array at Station 150.

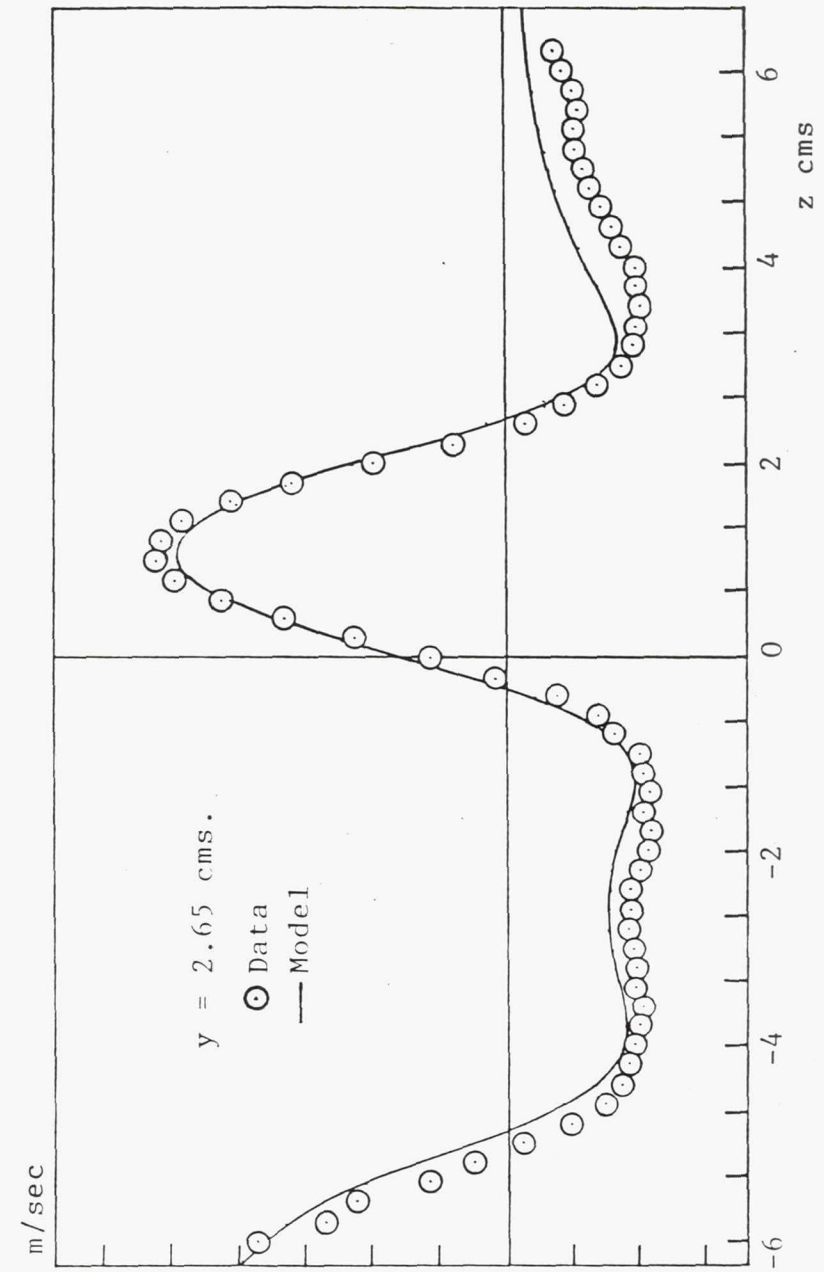

Figure 5.10c - A comparison between the model and data v velocity profiles through the approximate centers of vortices 3 and 4 of the spacing ratio 4.0 array at Station 150.

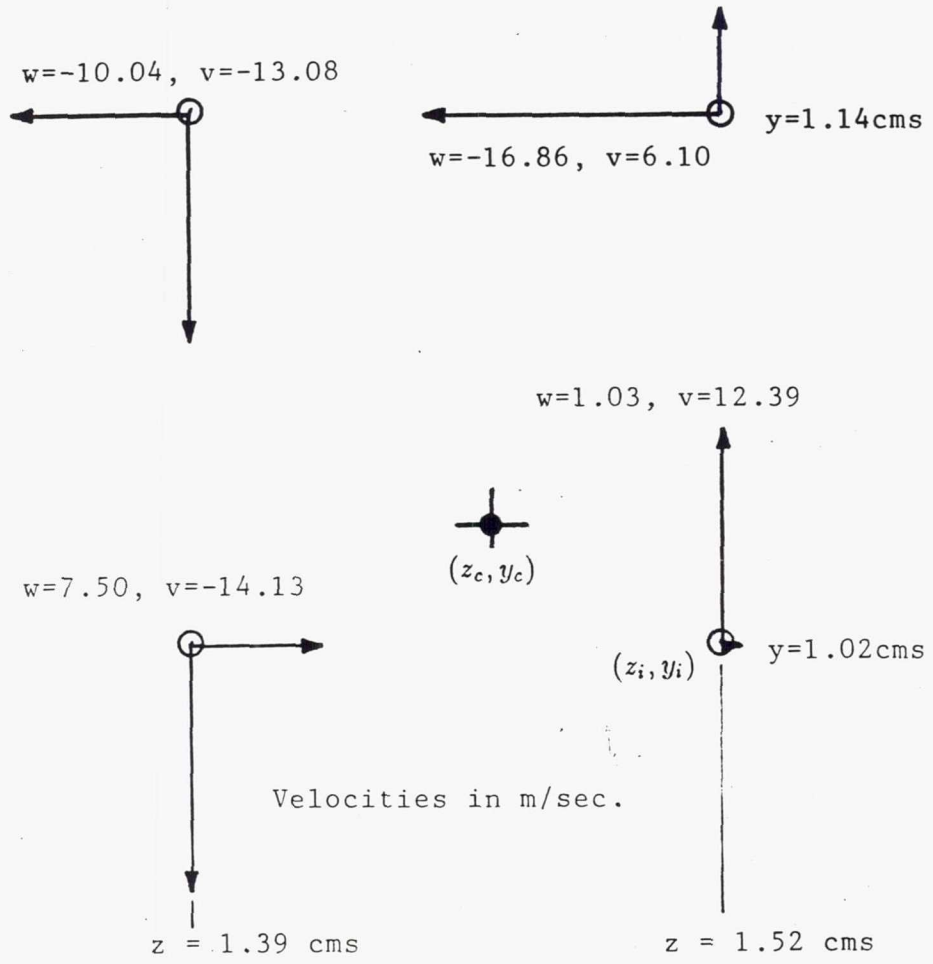

Figure 5.11 - The four grid points surrounding the core center for the case of the single embedded vortex at Station 74. The velocity vector components were measured by the five hole probe. Interpolation of this velocity data provides an estimate of the core location (z_c, y_c). The grid estimate of peak vorticity is ω^i_{max} located at (z_i, y_i). Iterative solution of Eq. (5.24) provides a refined estimate of the peak vorticity.

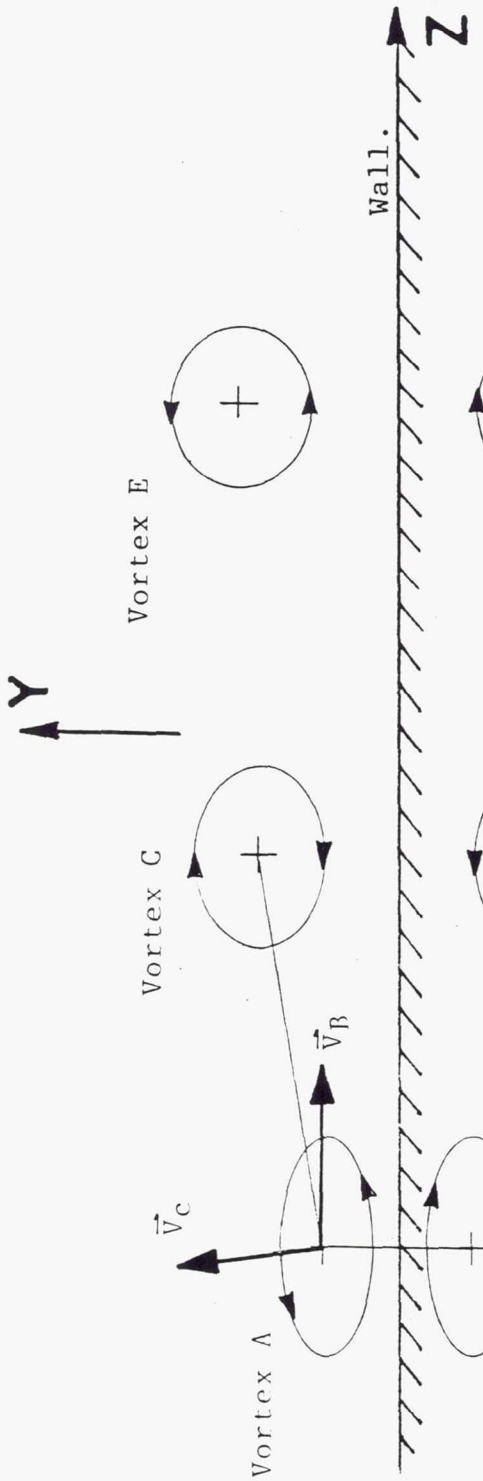

Figure 5.12 - A demonstration of vortex convection in the crossplane. Neighboring vortex C induces a convective velocity, $\vec{V}_C$, on the core of vortex A. Image B induces $\vec{V}_B$ on the core of vortex A as well. Likewise, every vortex and image in the field induces a convective velocity on the core of vortex A. The sum of these vectors determines the trajectory of vortex A in the crossplane.

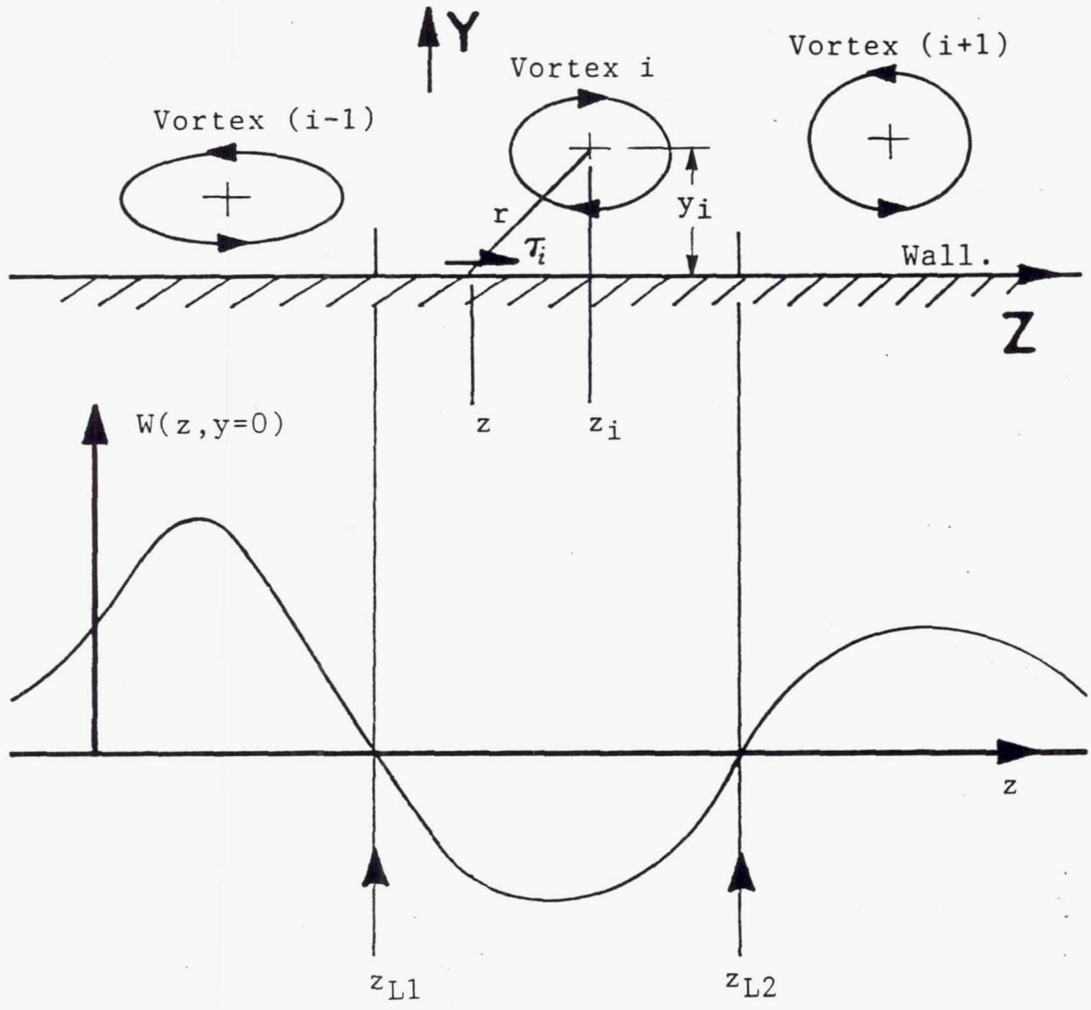

Figure 5.13a (top) - The secondary flow field generated by vortex i gives rise to a local spanwise component of wall shear stress, $\tau_i(z)$, which opposes the rotation of vortex i.

Figure 5.13b (bottom) - Each embedded vortex in the counter- rotating array sets up a zone of wall velocity, $w(z, y = 0)$, differing in sign from the zones created by neighboring vortices on either side. The stagnation points in $w(z, y = 0)$ are labelled z_{L1} and z_{L2}.

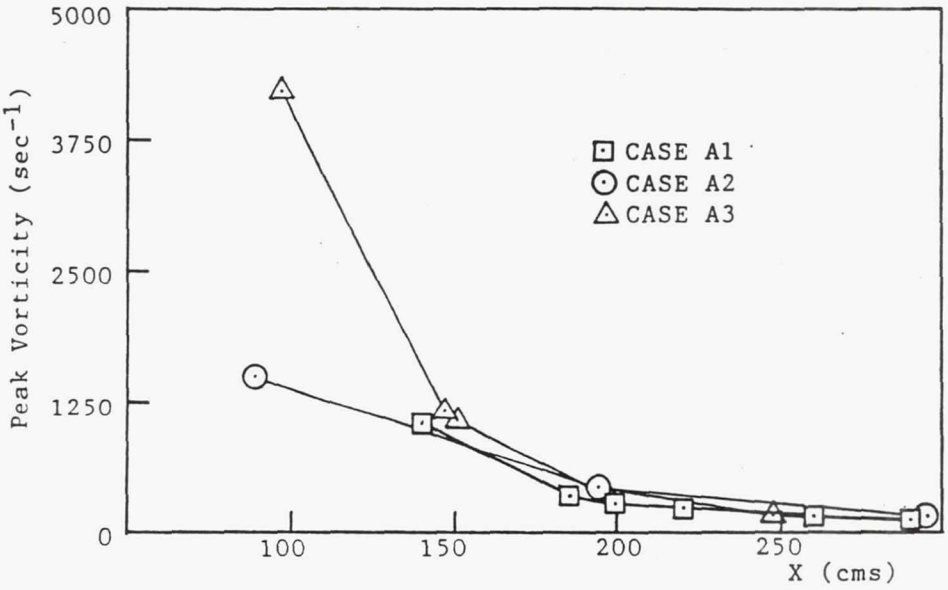

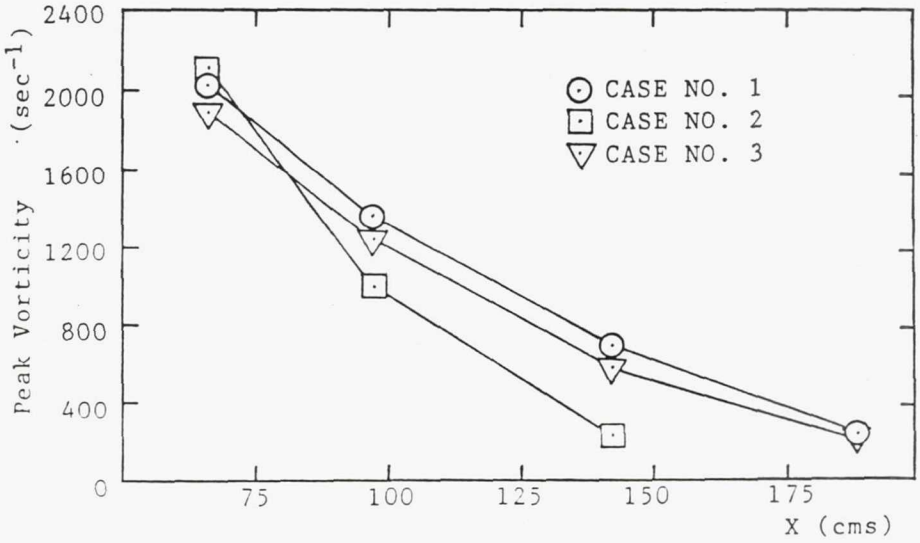

Figure 5.14 (top) - The decay of peak vorticity with streamwise distance x observed for single embedded vortices. From Westphal, Pauley, and Eaton (1987).

Figure 5.15 (bottom) - The decay of peak vorticity with streamwise distance x observed for counter-rotating vortex pairs. From Pauley and Eaton (1988).

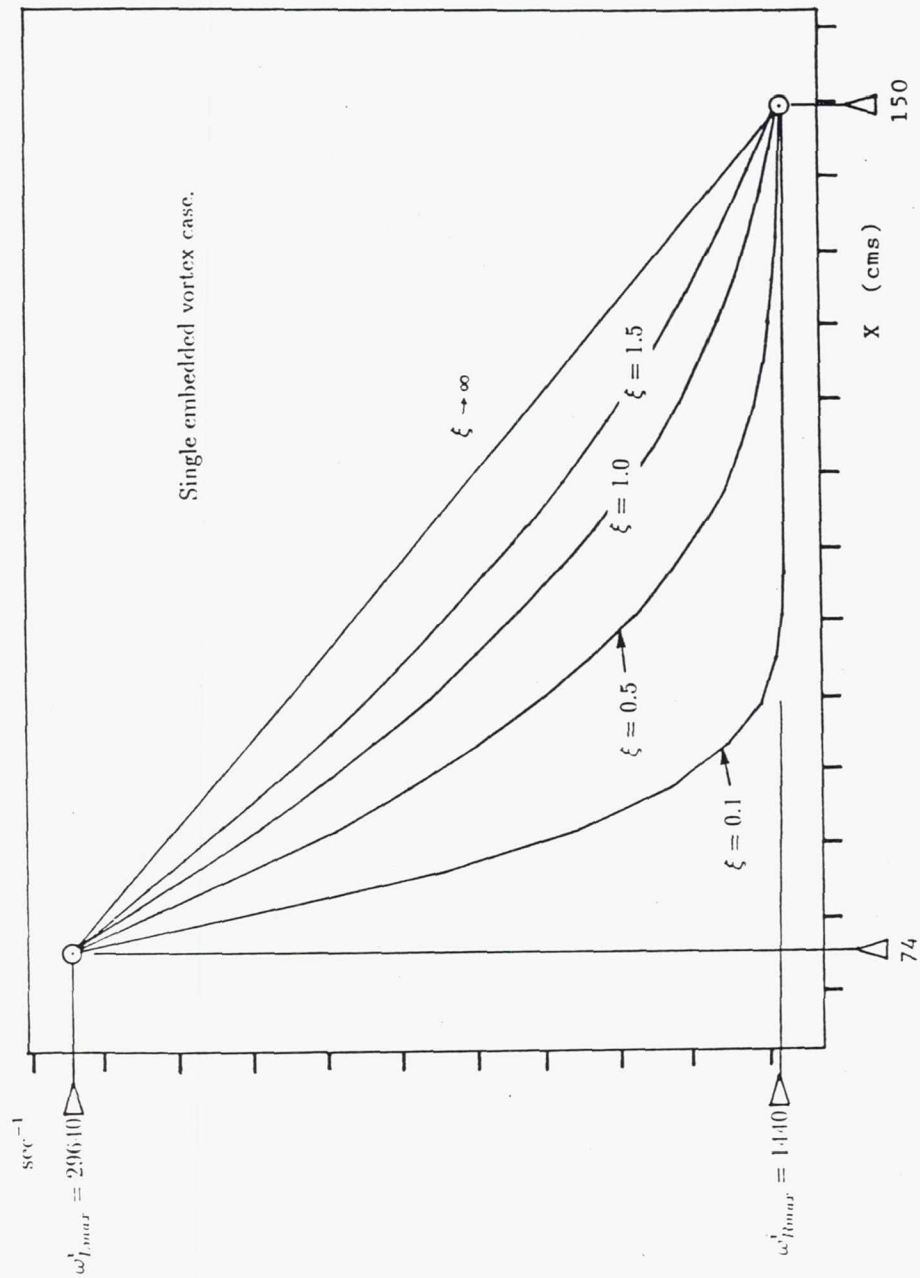

Figure 5.16 - The representation of peak vorticity decay employed in the model (Eq. (5.41)).

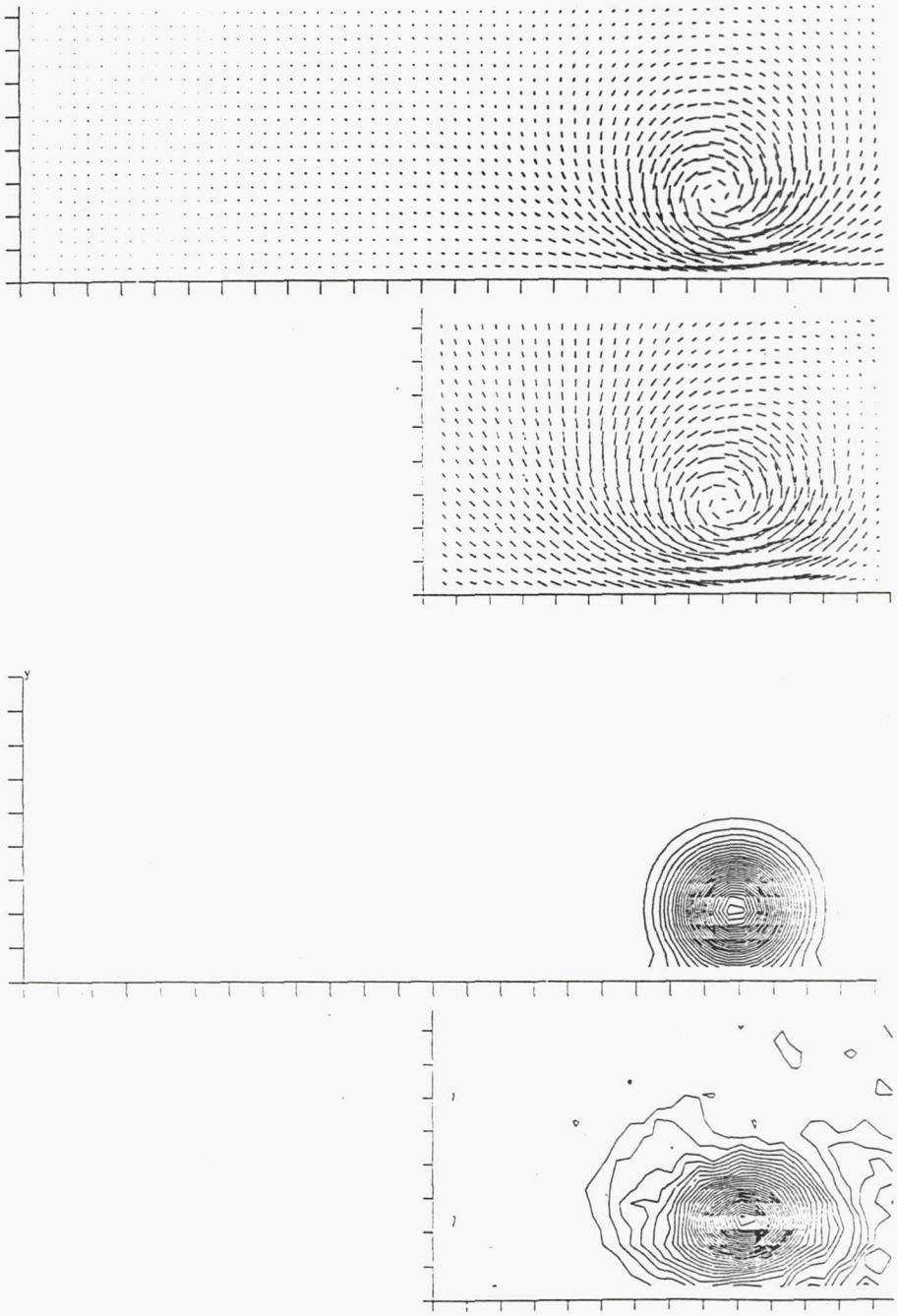

Figure 5.17a - A comparison of the downstream results of the three dimensional model (upper plots) to the data. Circulation decay is by wall friction effects. The test condition is the single embedded vortex.

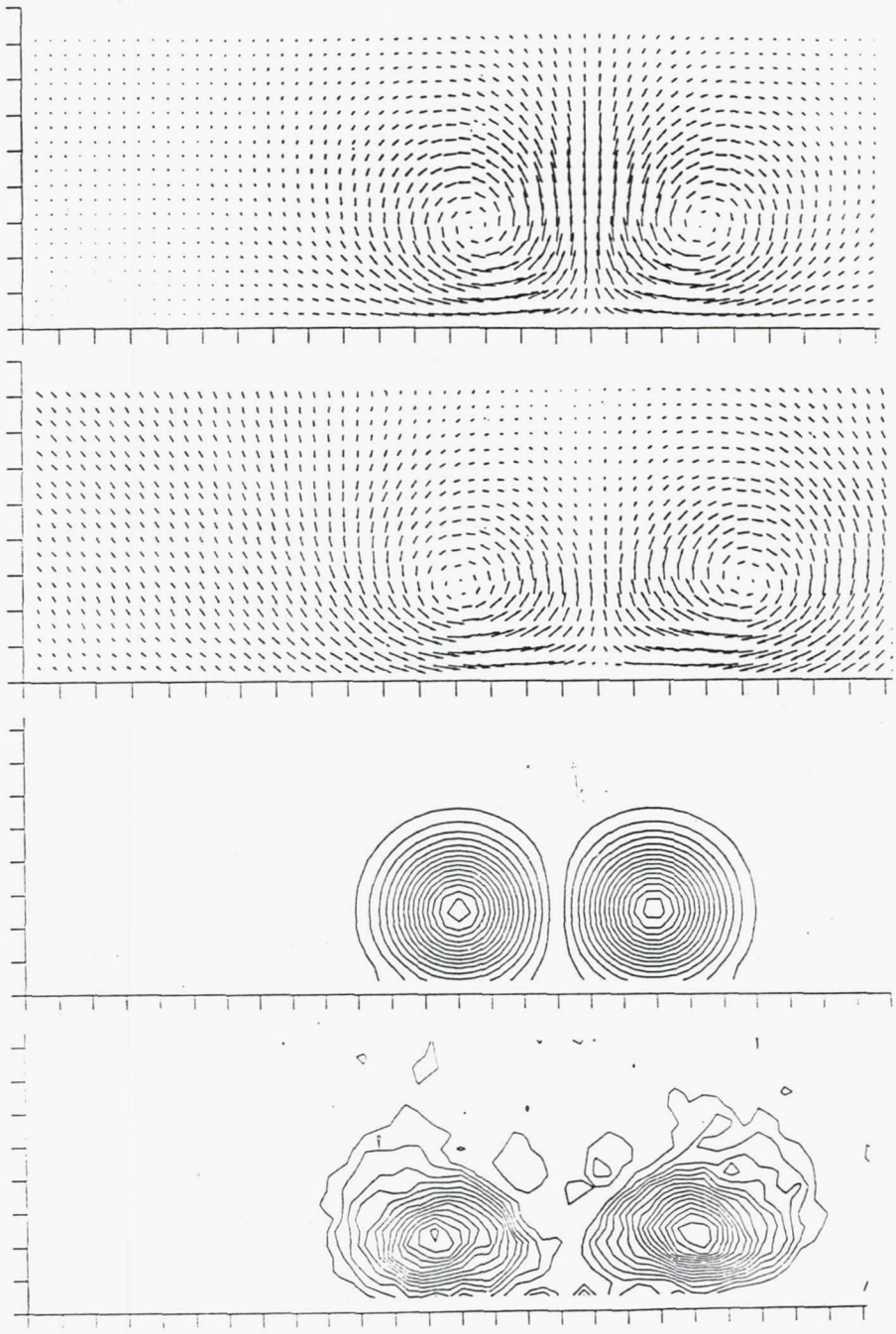

Figure 5.17b - A comparison of the downstream results of the three dimensional model (upper plots) to the data. Circulation decay is by wall friction effects. The test condition is the spacing ratio 7.0 array.

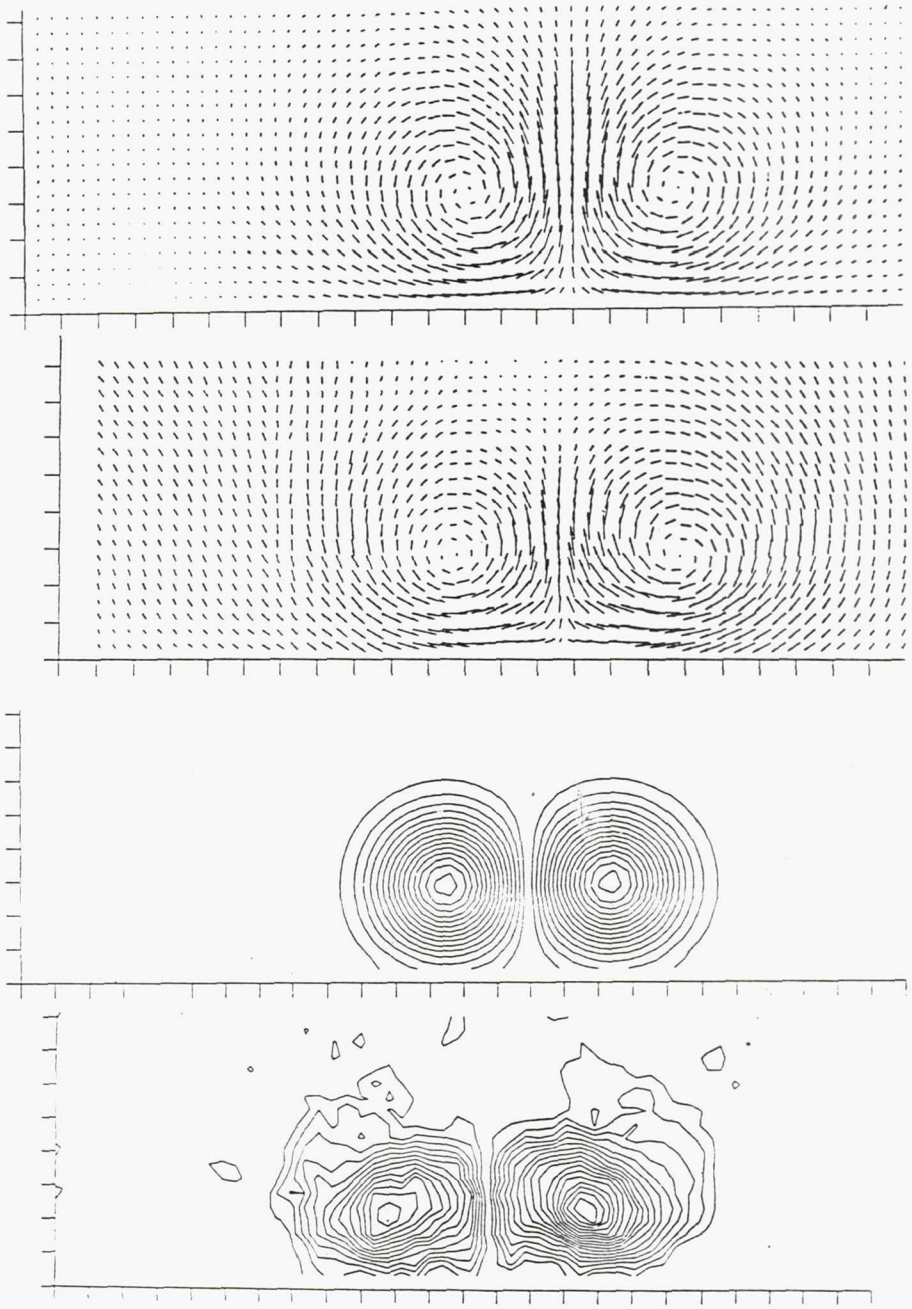

Figure 5.17c - A comparison of the downstream results of the three dimensional model (upper plots) to the data. Circulation decay is by wall friction effects. The test condition is the spacing ratio 6.0 array.

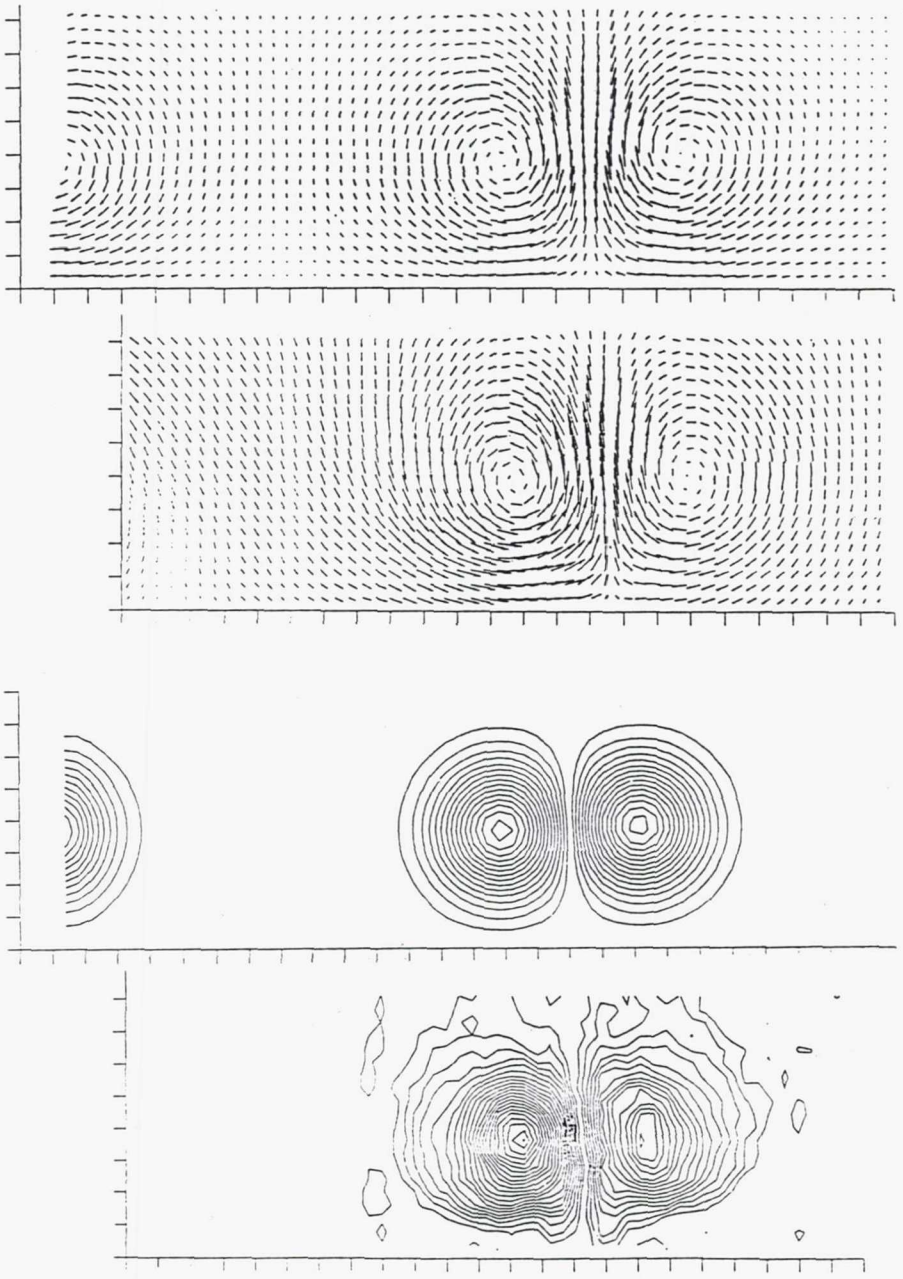

Figure 5.17d - A comparison of the downstream results of the three dimensional model (upper plots) to the data. Circulation decay is by wall friction effects. The test condition is the spacing ratio 5.0 array.

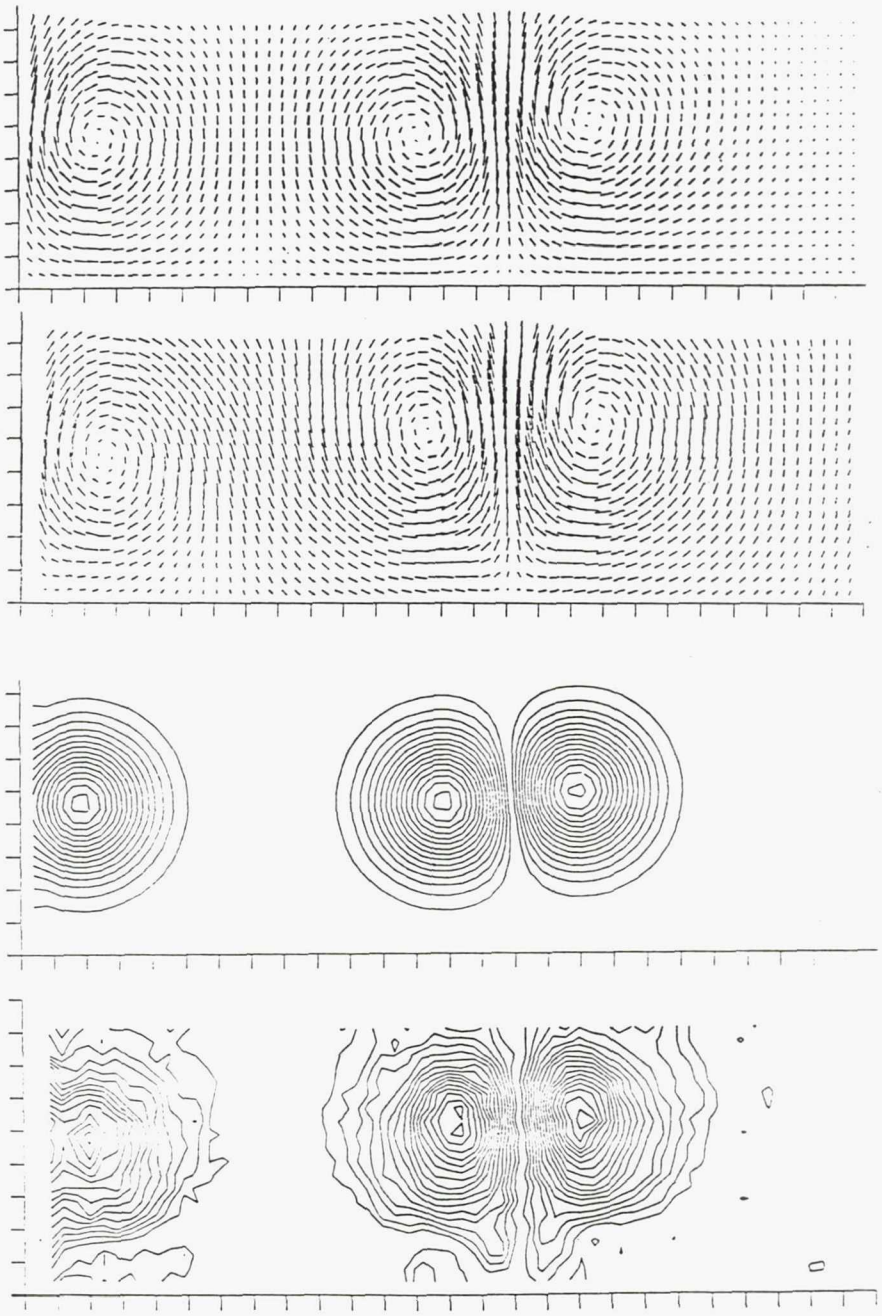

Figure 5.17e - A comparison of the downstream results of the three dimensional model (upper plots) to the data. Circulation decay is by wall friction effects. The test condition is the spacing ratio 4.0 array.

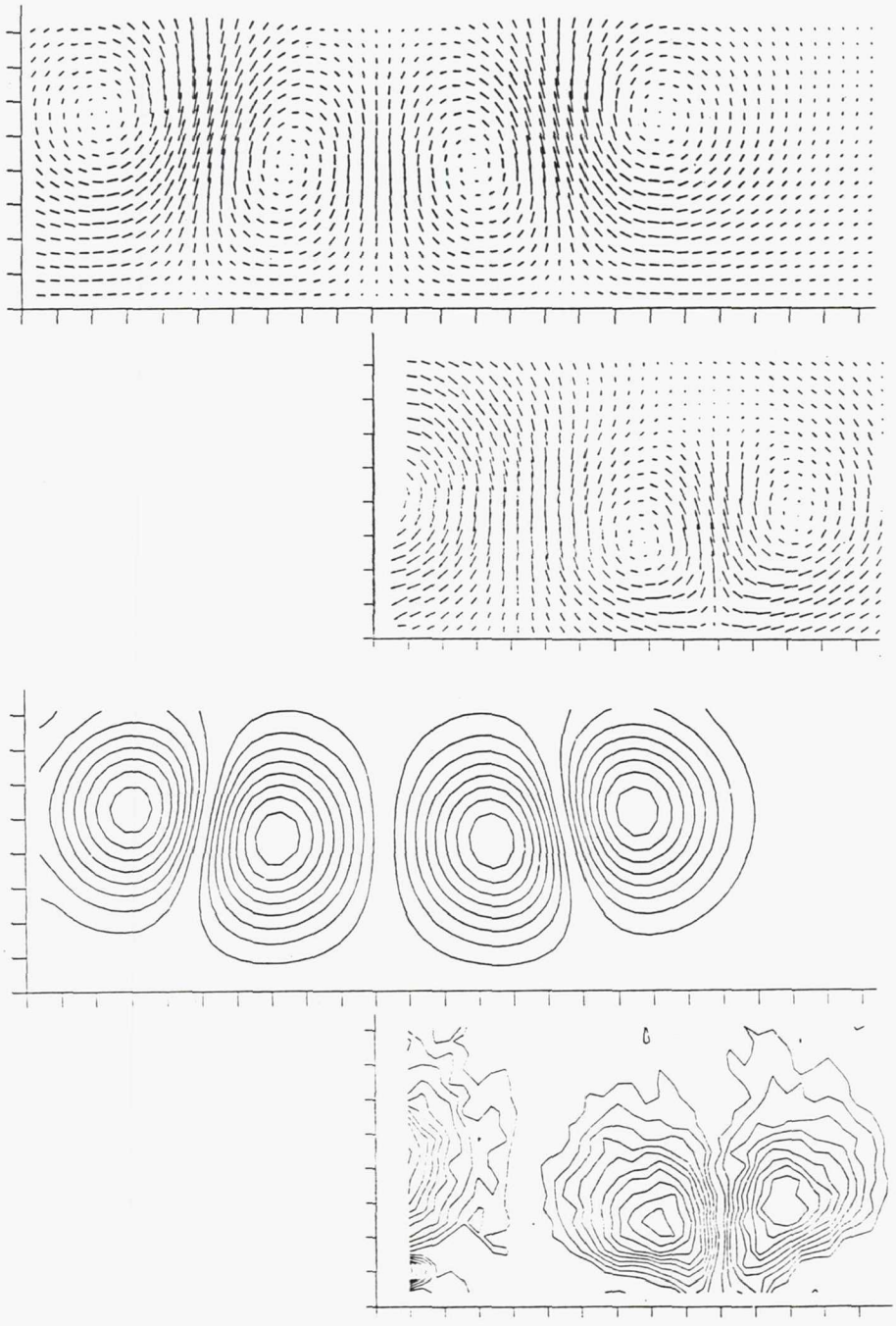

Figure 5.17f - A comparison of the downstream results of the three dimensional model (upper plots) to the data. Circulation decay is by wall friction effects. The test condition is the spacing ratio 3.0 array.

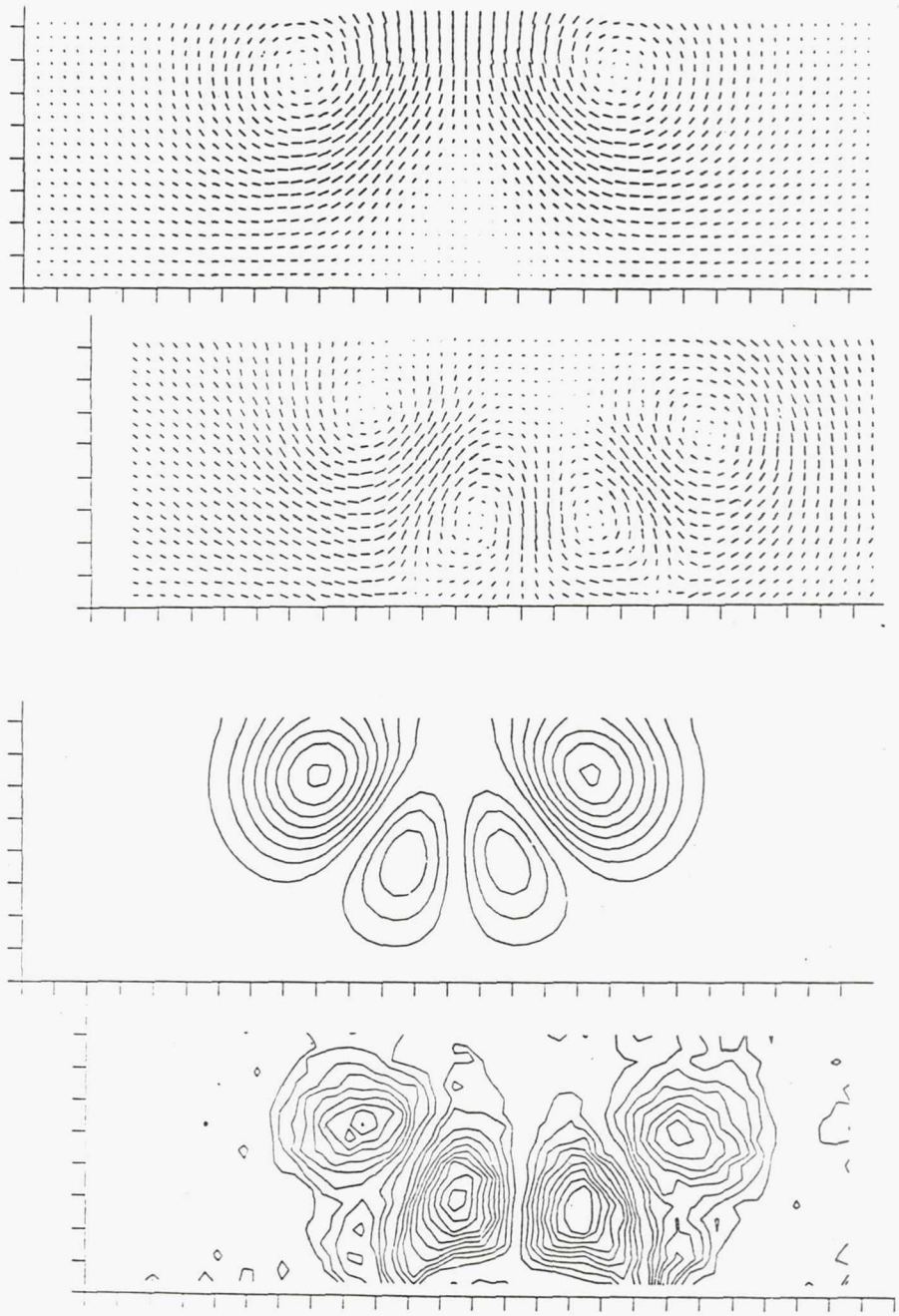

Figure 5.17g - A comparison of the downstream results of the three dimensional model (upper plots) to the data. Circulation decay is by wall friction effects. The test condition is the spacing ratio 2.0 array.

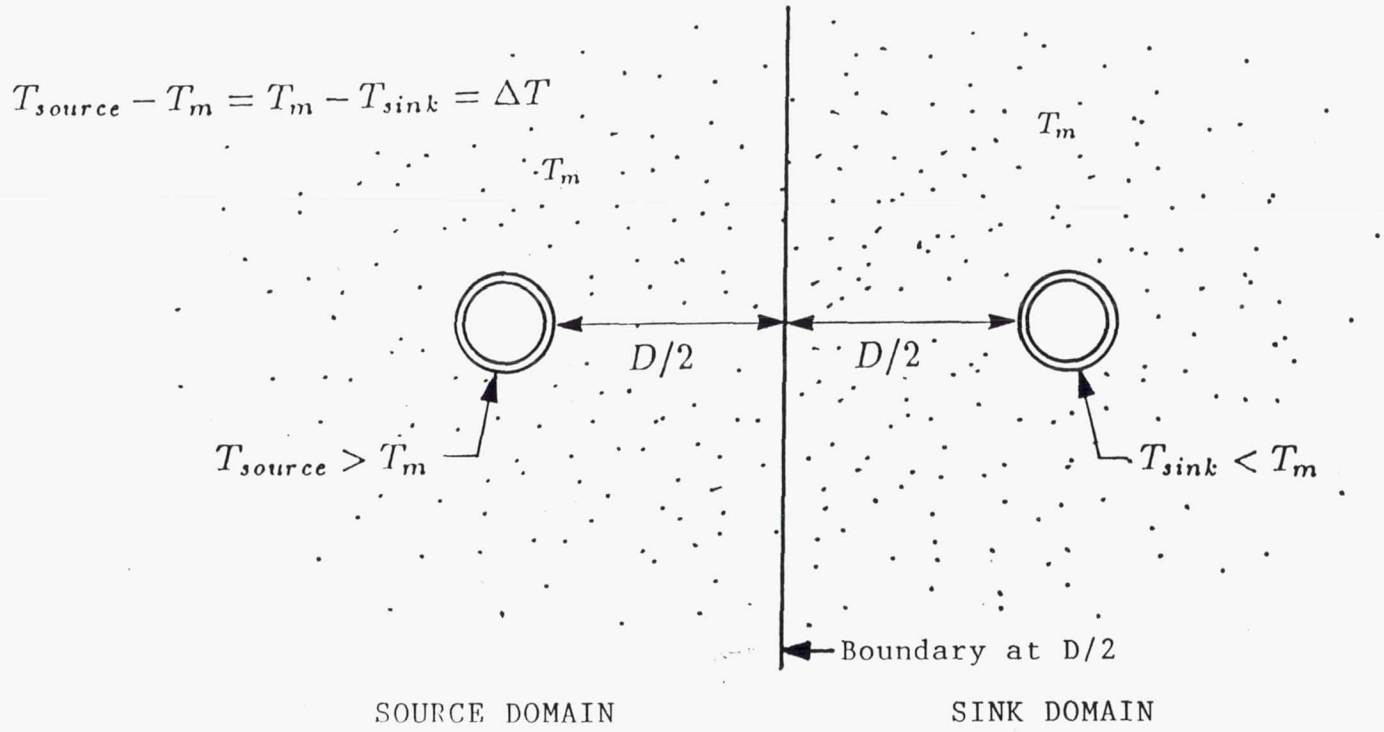

Figure 5.18 - Construction of a heat transfer analogy to proximity circulation losses. At time $t = 0$ a hot liquid fills the source tube and a cold liquid fills the sink tube. The heat transfer between domains is proportional to the temperature gradient at $D/2$.

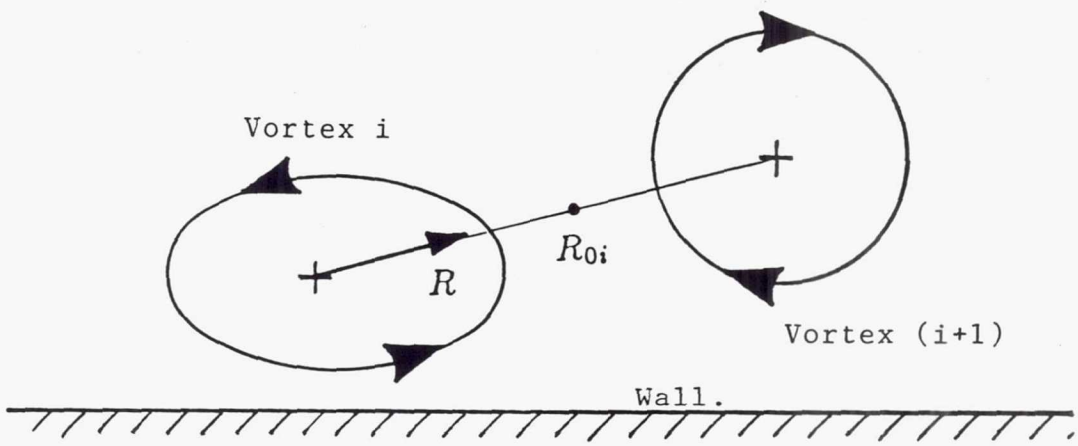

5.19a

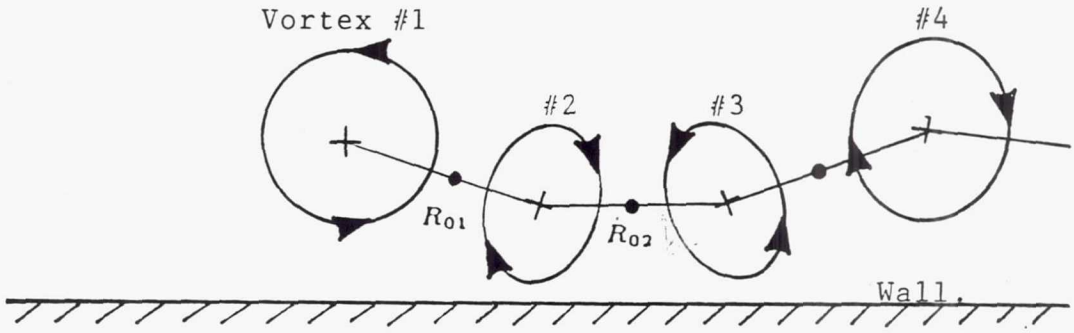

5.19b

Figure 5.19(a-b) - Demonstration of the construction required for evaluating proximity circulation losses. In Figure 5.19a (top) R represents the coordinate axis along the line connecting adjacent cores. R_{0i} is the location on R where the vorticity changes sign in the model. In Figure 5.19b (bottom) the interior vortices suffer proximity losses to both adjacent neighbors.

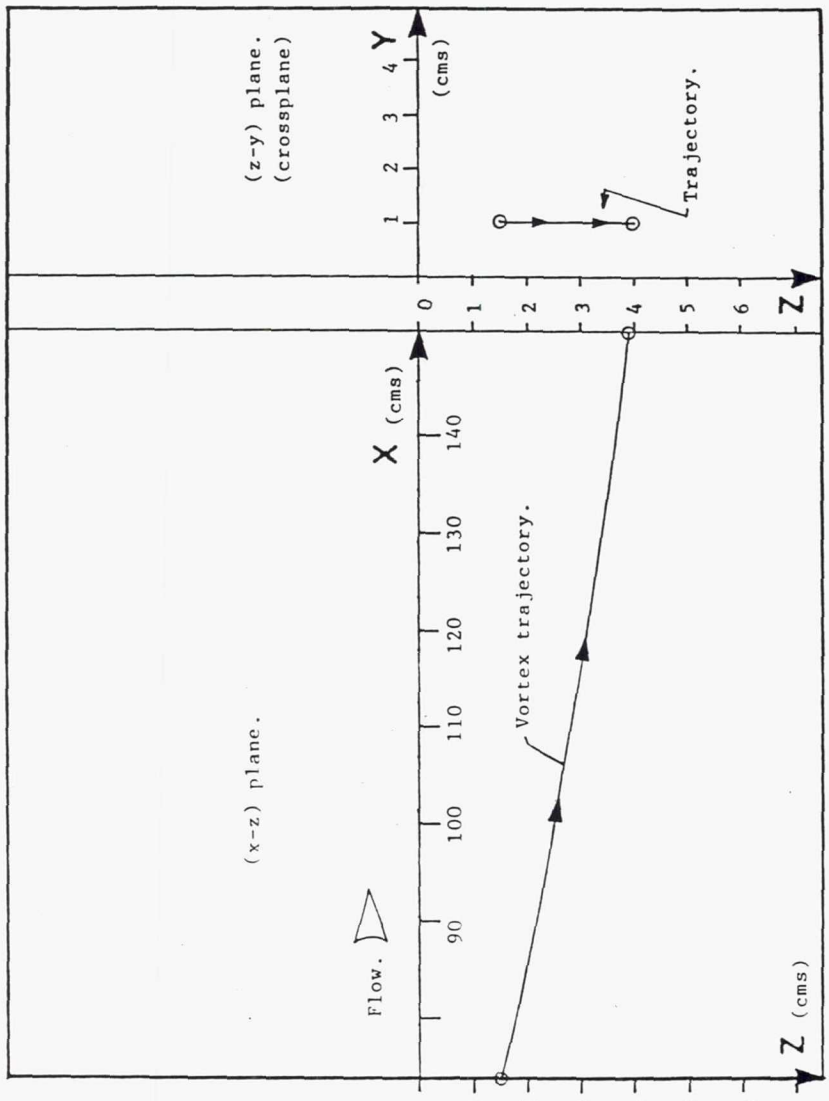

Figure 5.20a - Predicted trajectory of the single embedded vortex in the (x, z) and (z, y) planes.

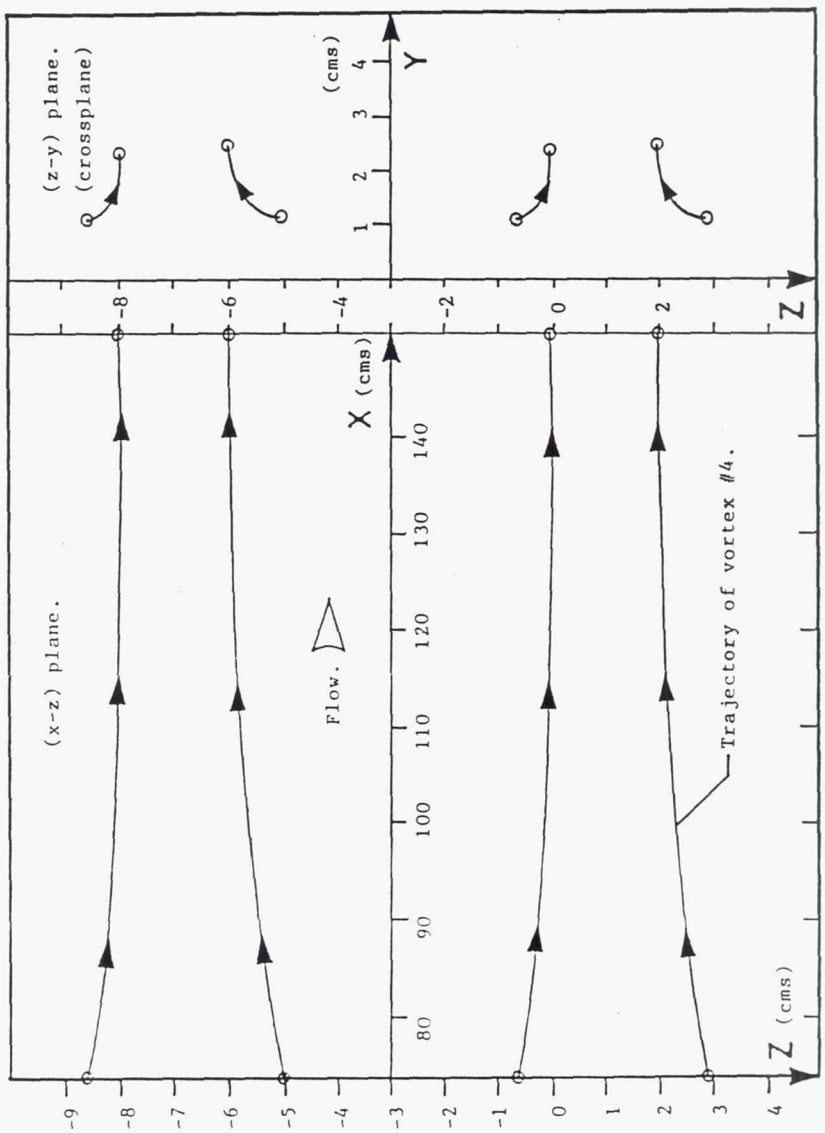

Figure 5.20b - Predicted trajectories of the vortices in the spacing ratio 4.0 array.

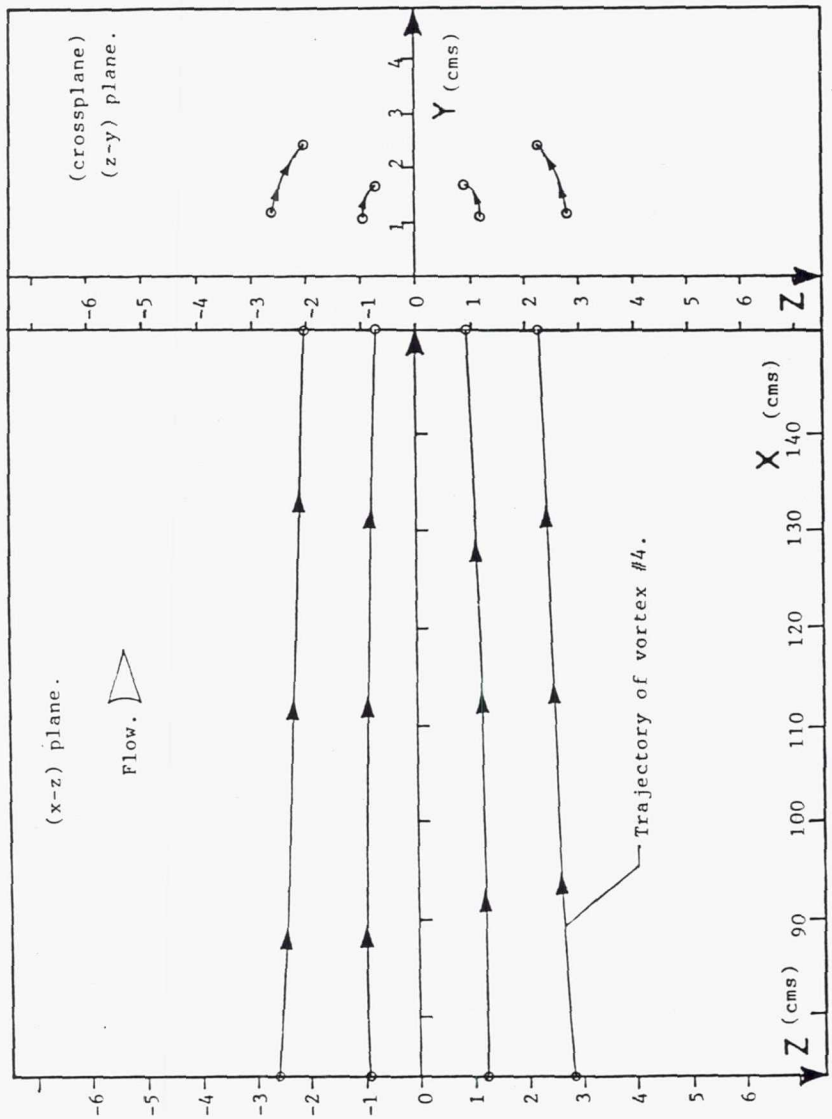

Figure 5.20c - Predicted trajectories of the vortices in the spacing ratio 2.0 array.

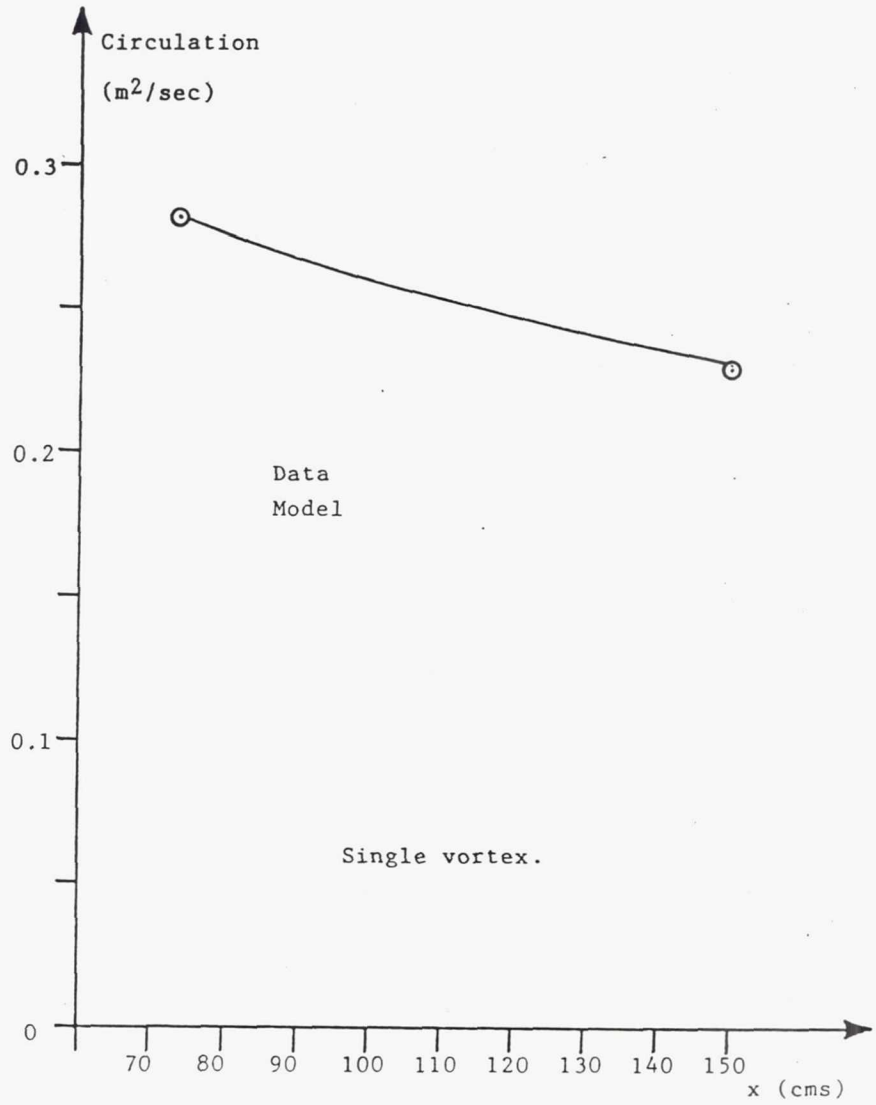

Figure 5.21a - Predicted circualtion decay with x for the case of the single embedded vortex.

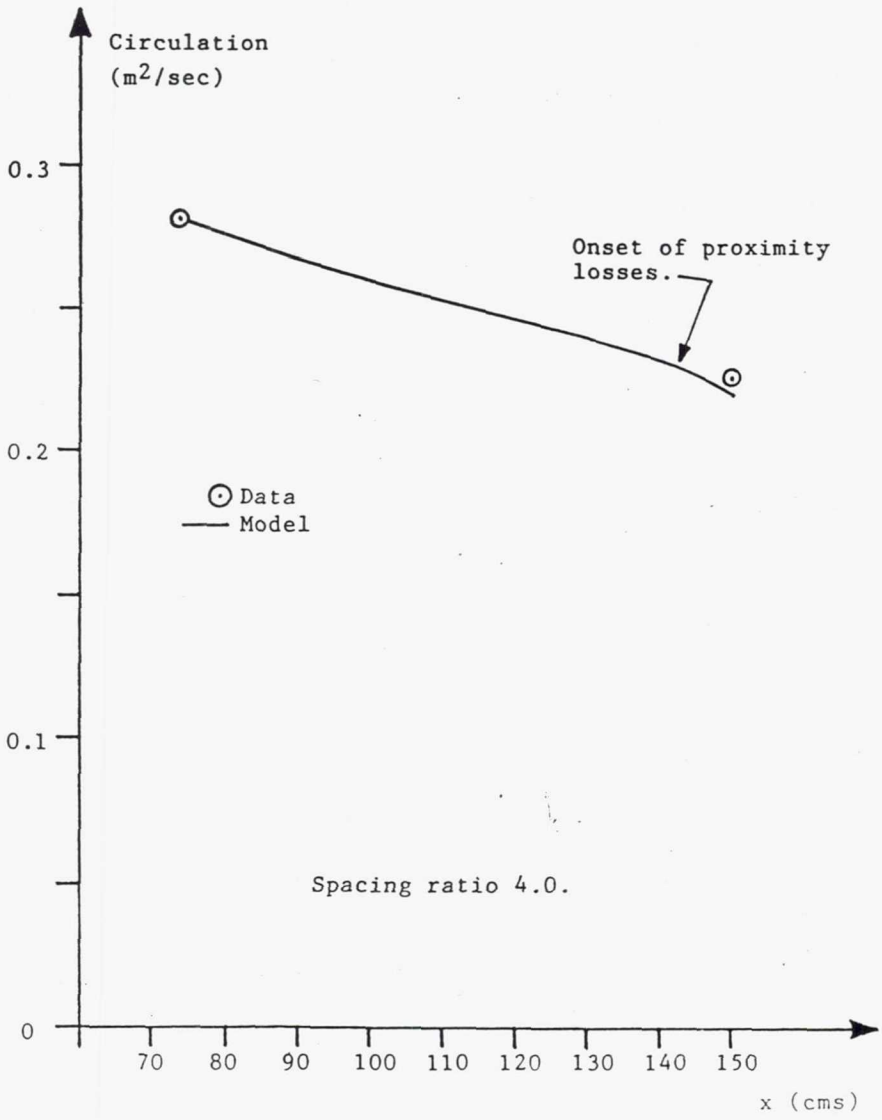

Figure 5.21b - Predicted circulation decay with x for vortex no. 3 in the spacing ratio 4.0 test case.

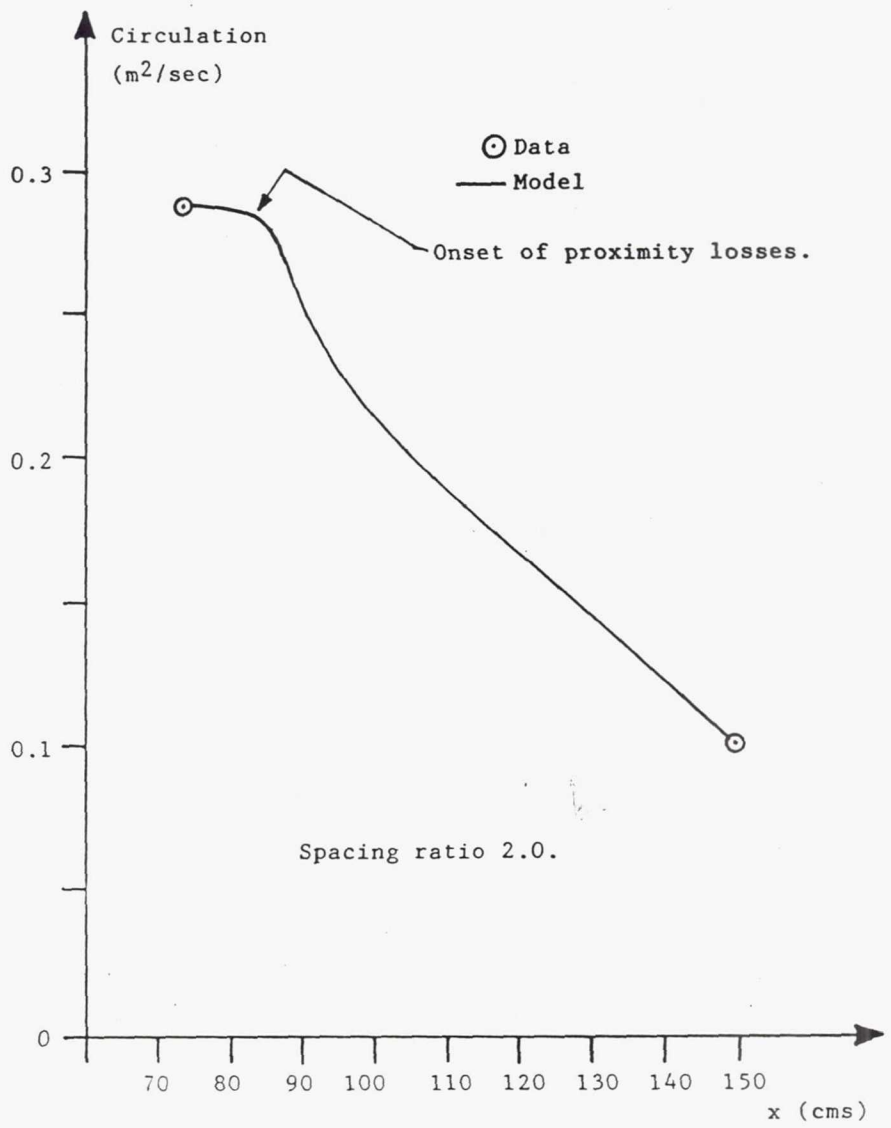

Figure 5.21c - Predicted circulation decay with x for vortex no. 3 in the spacing ratio 2.0 test case.

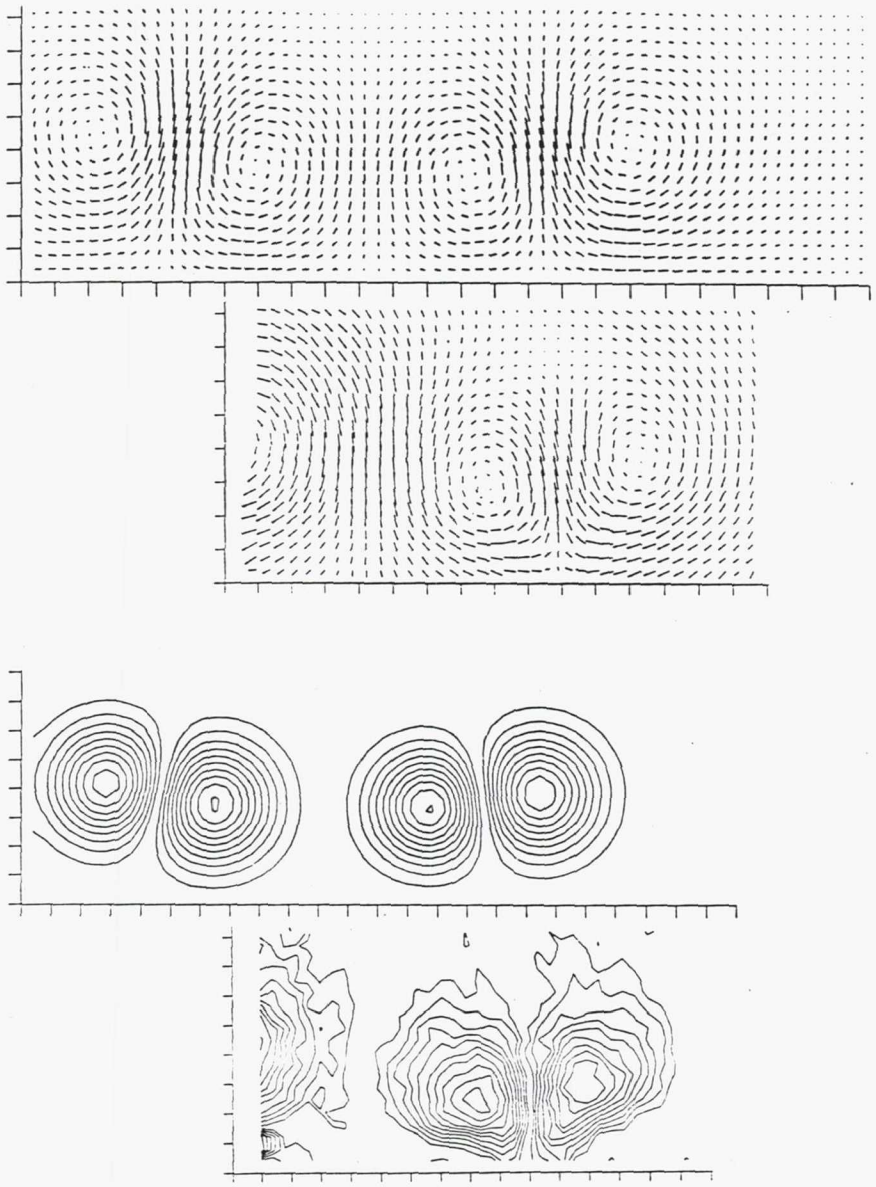

Figure 5.22a - A comparison of the downstream results of the three dimensional model (upper plots) to the data. Circulation decay is now by wall friction effects and proximity losses. The test condition is the initial spacing ratio 3.0 case.

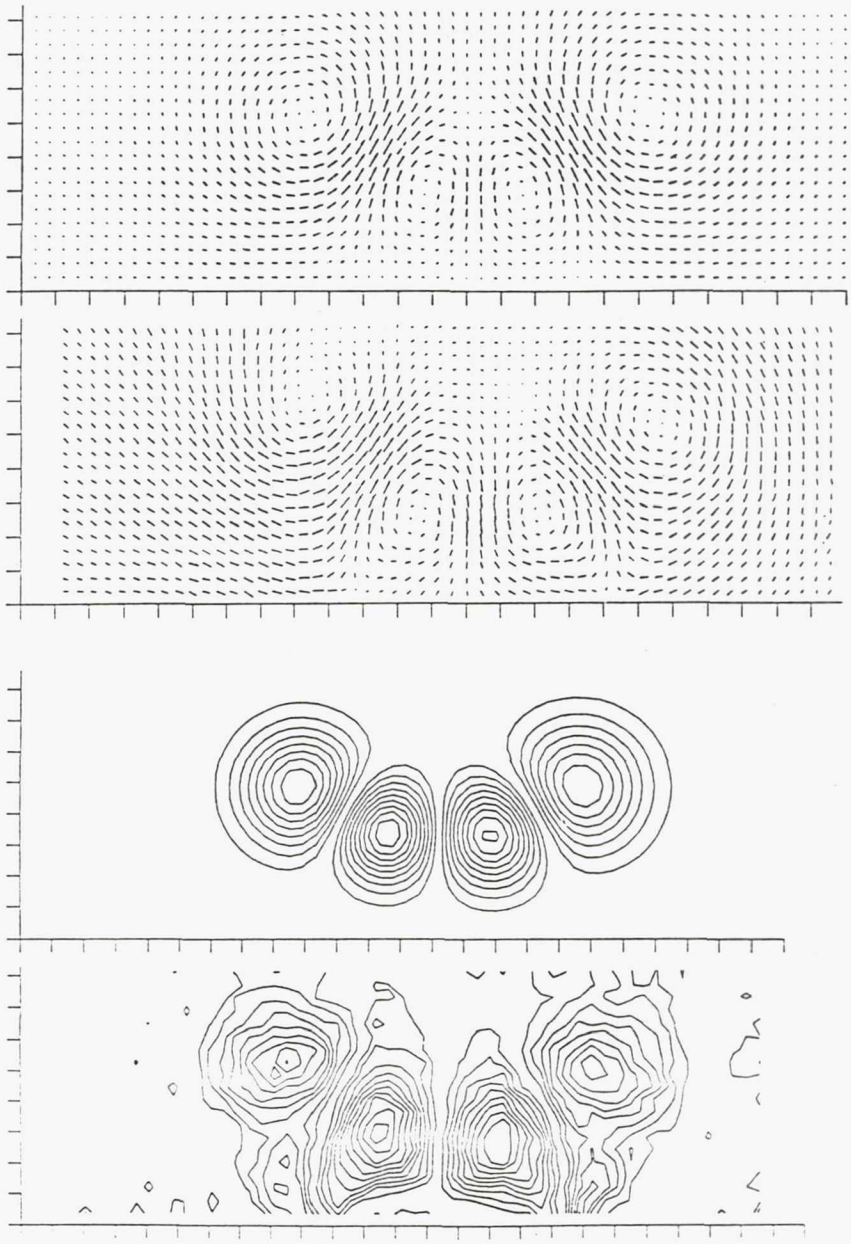

Figure 5.22b - A comparison of the downstream results of the three dimensional model (upper plots) to the data. Circulation decay is now by wall friction and proximity losses. The test condition is the initial spacing ratio 2.0 case.

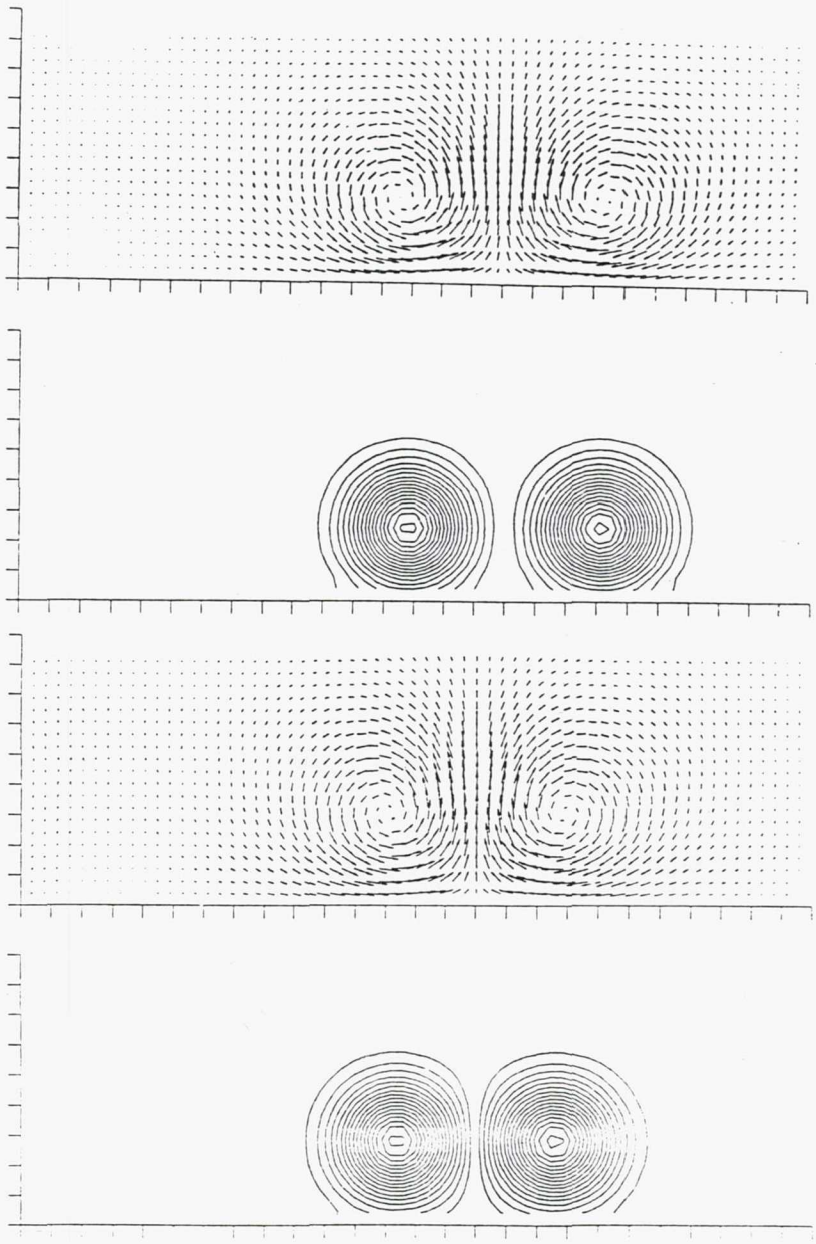

Figures 5.23(a-b) - The predicted downstream velocity and vorticity structure of an eight element array of embedded vortices. Figure 5.23a (top two plots) shows a portion of the spacing ratio 7.0 array. Figure 5.23b (bottom two plots) shows a portion of the spacing ratio 6.0 array.

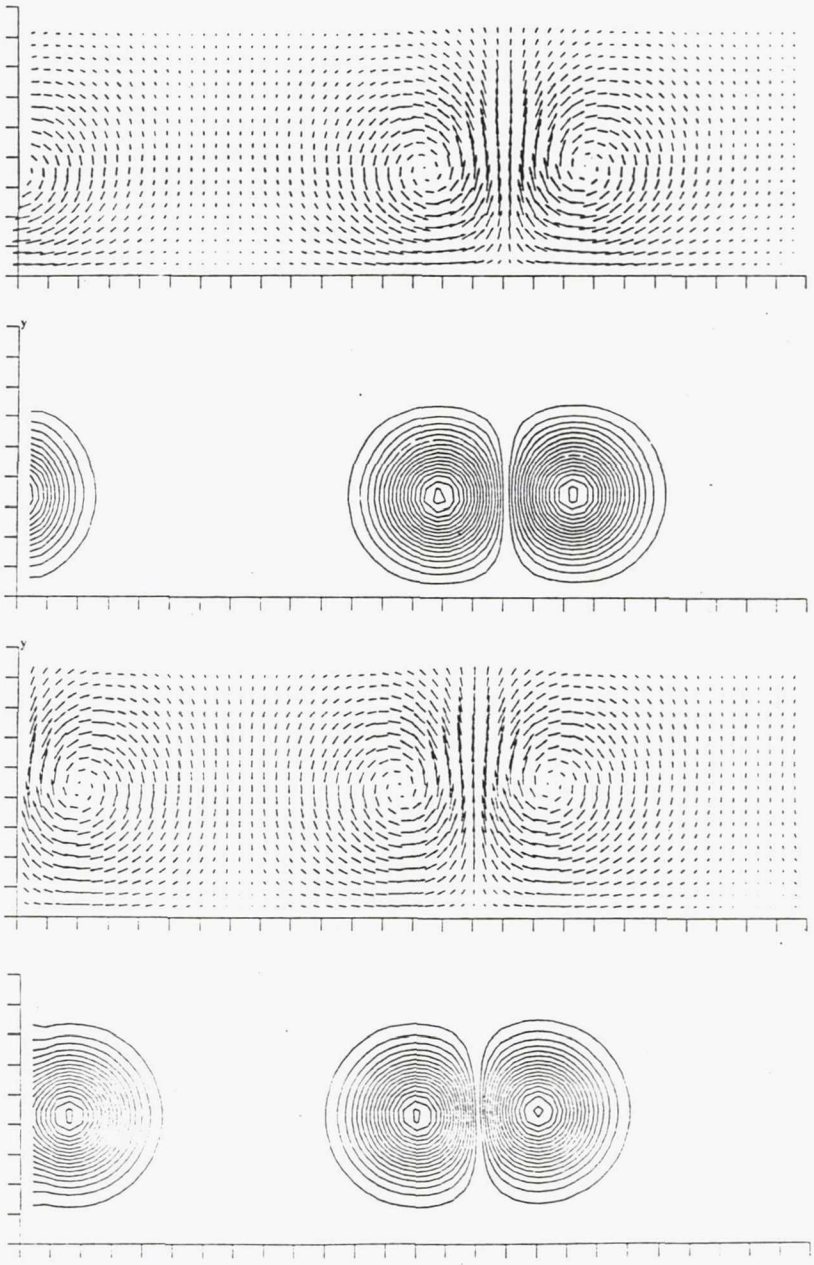

Figures 5.23(c-d) - The predicted downstream velocity and vorticity structure of an eight element array of embedded vortices. Figure 5.23c (top two plots) shows a portion of the spacing ratio 5.0 array. Figure 5.23d (bottom two plots) shows a portion of the spacing ratio 4.0 array.

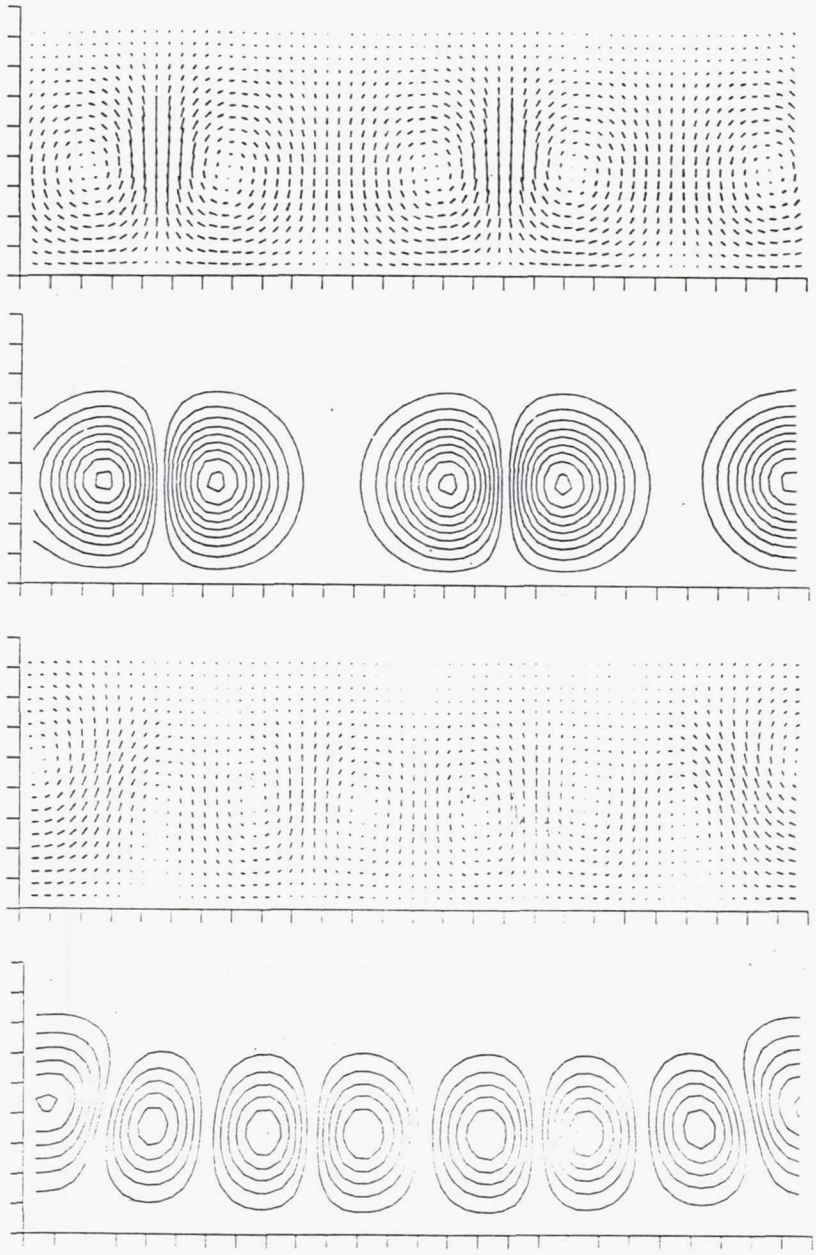

Figures 5.23(e-f) - The predicted downstream velocity and vorticity structure of an eight element array of embedded vortices. Figure 5.23e (top two plots) shows a portion of the spacing ratio 3.0 array. Figure 5.23f (bottom two plots) shows a portion of the spacing ratio 2.0 array.

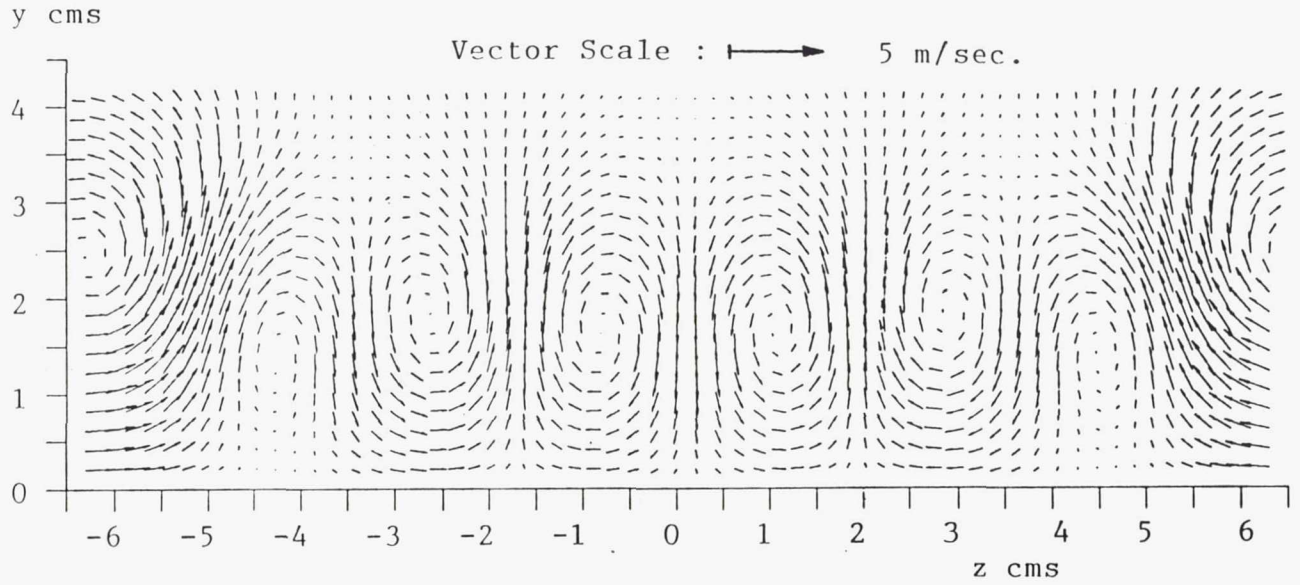

Figure 5.23g - The velocity plot in Figure 5.23f redrawn with a larger vector scale.

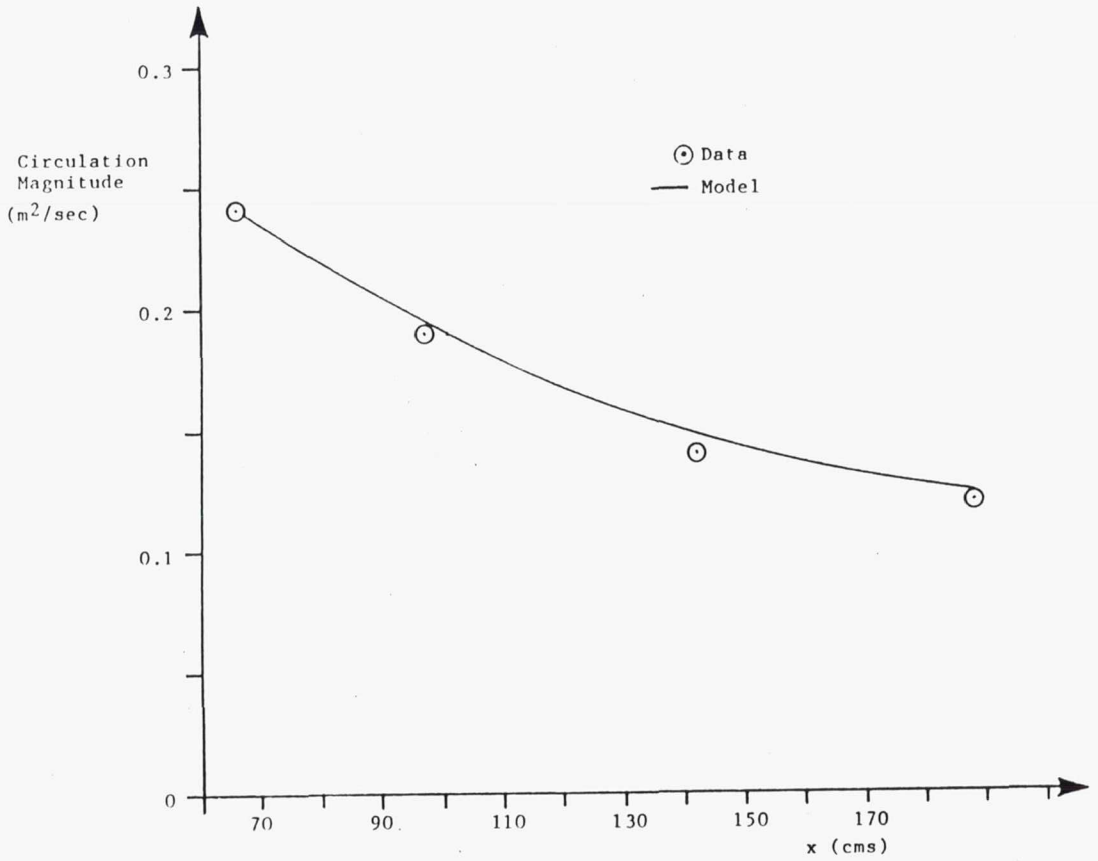

Figure 5.24 - A comparison of the streamwise circulation decay for the downflow pair of vortices studied by Pauley and Eaton (1988) to the decay results predicted by the model.

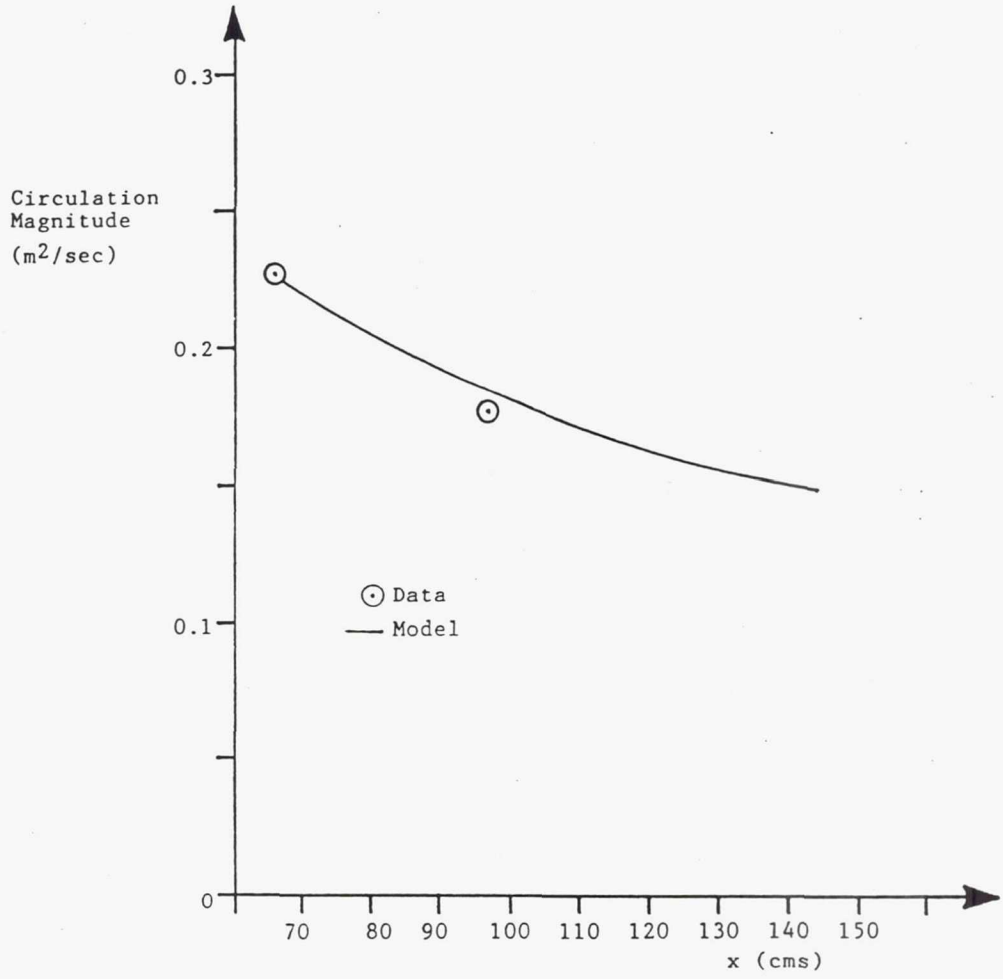

Figure 5.25 - A comparison of the streamwise circulation decay for the upflow pair of vortices studied by Pauley and Eaton (1988) to the decay results predicted by the model.

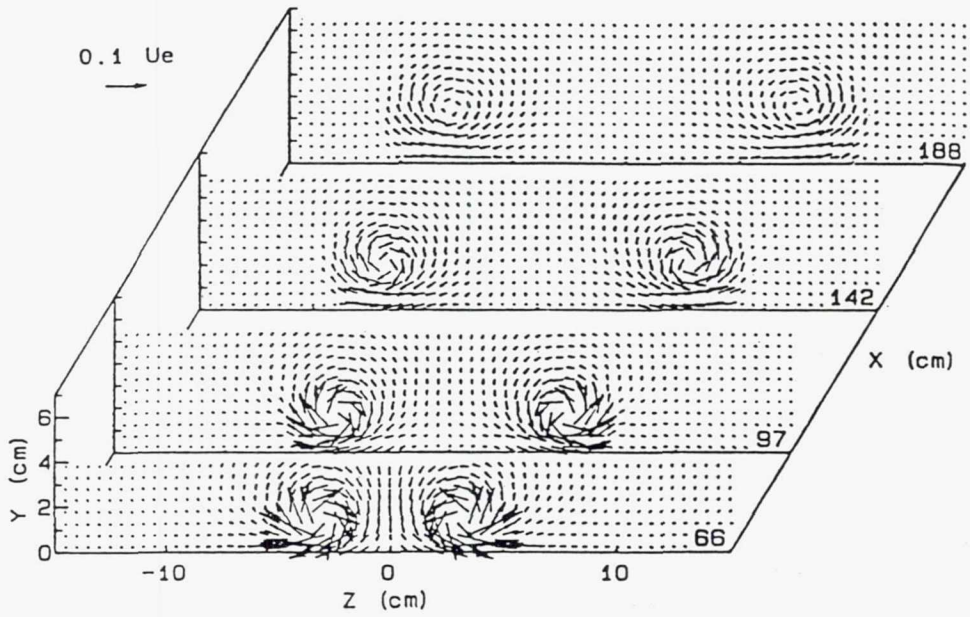

Figure 5.26a - The secondary velocity field at four crossplane locations for the downflow pair of vortices observed in the Stanford study. From Pauley and Eaton (1988).

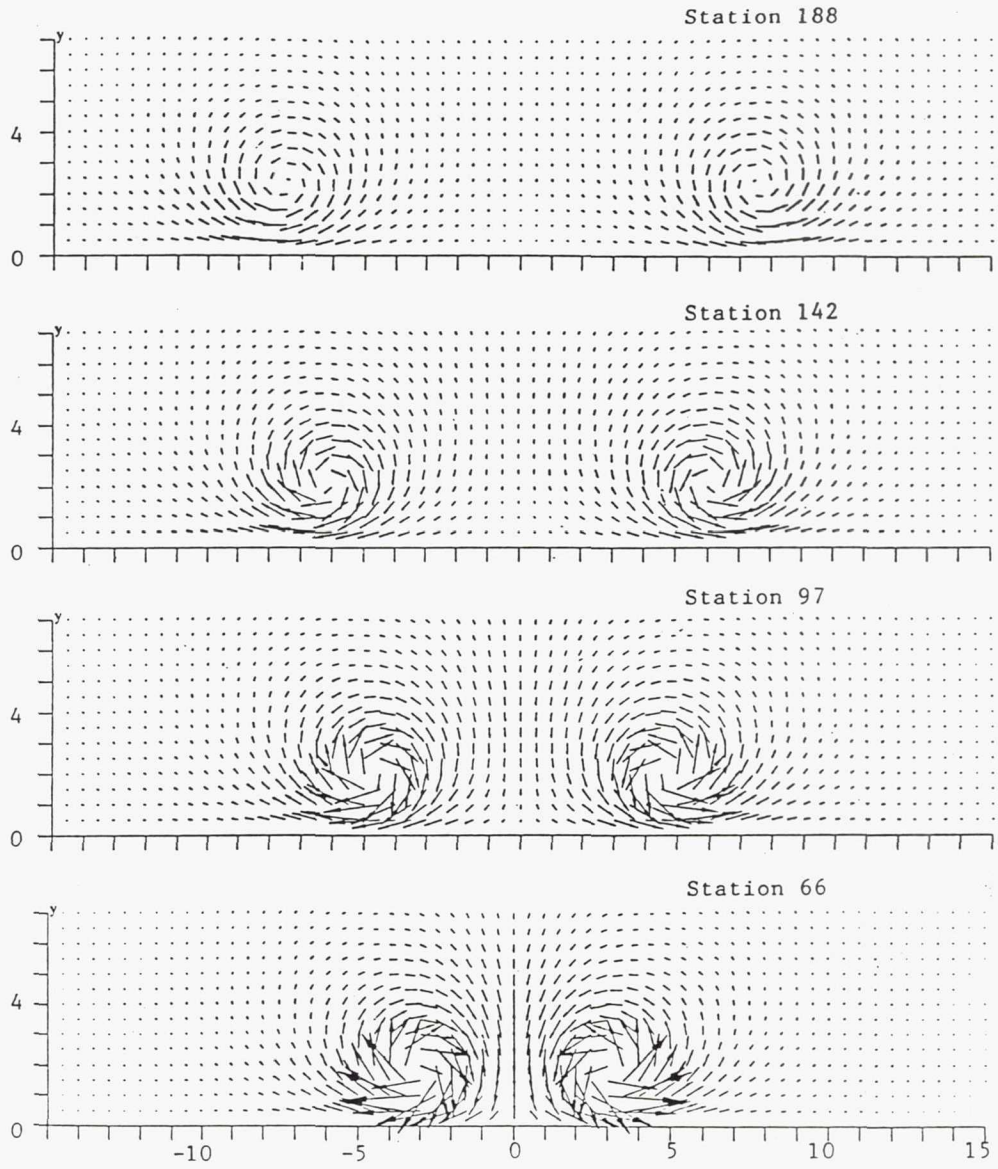

Figure 5.26b - The corresponding secondary velocity field generated by the model program using the initial upstream conditions for the case of the downflow pair of embedded vortices as presented by Pauley and Eaton (1988).

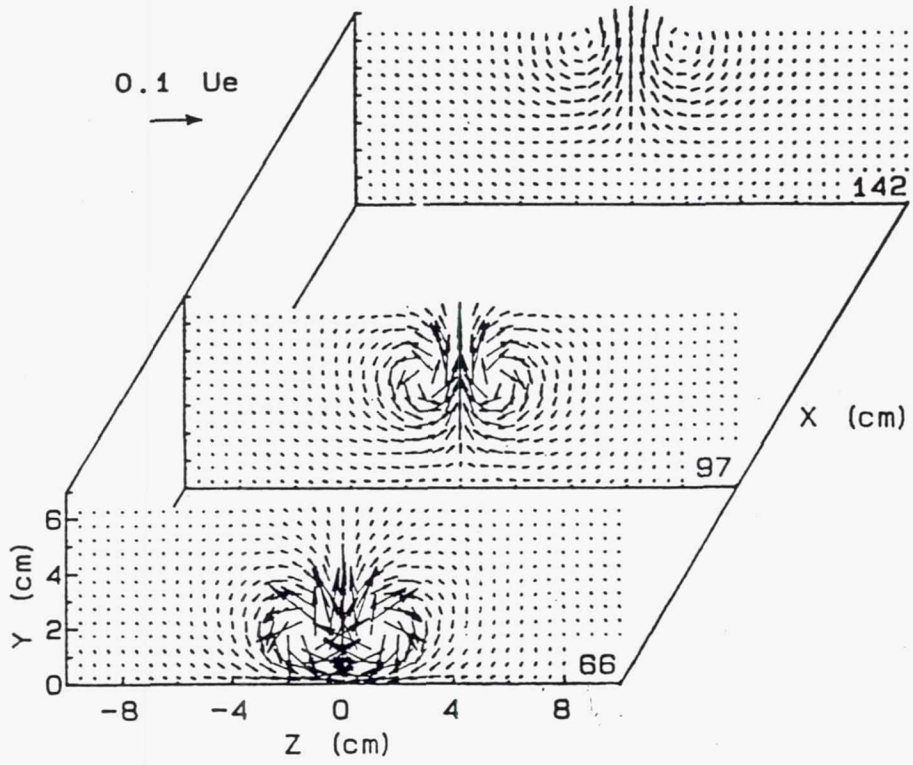

Figure 5.27a - The secondary velocity field at four crossplane locations for the upflow pair of vortices observed in the Stanford study. From Pauley and Eaton (1988).

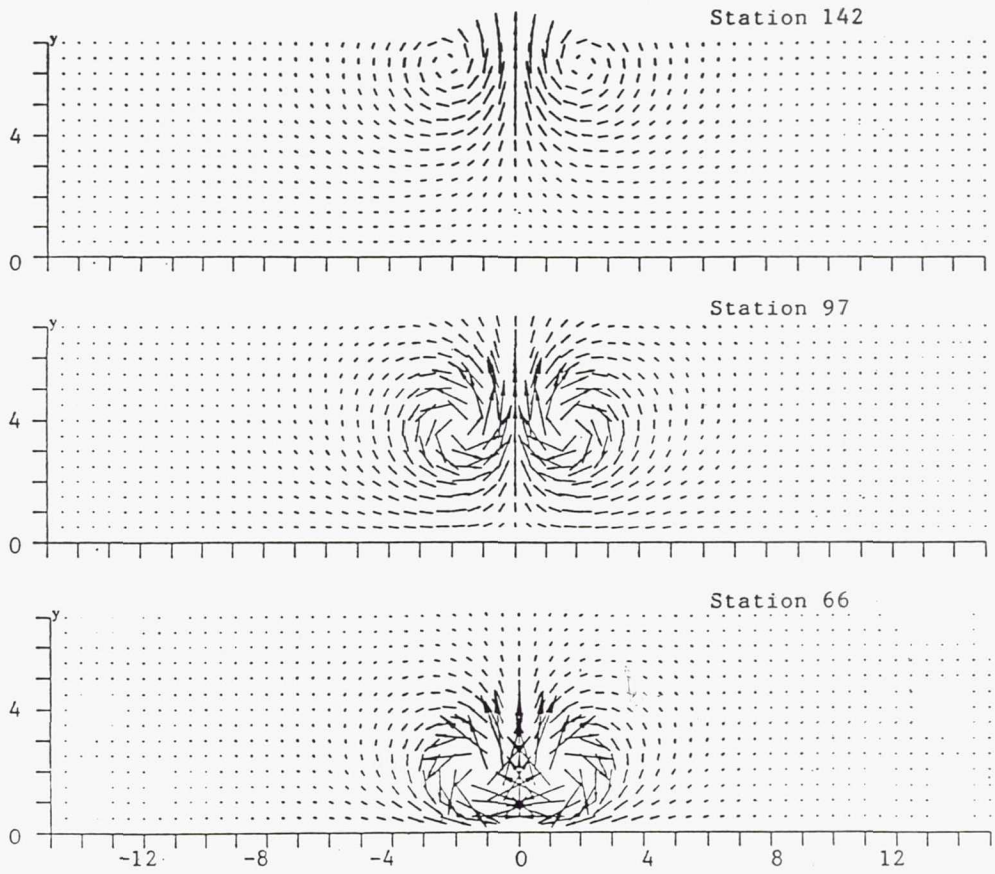

Figure 5.27b - The corresponding secondary velocity field generated by the model program using the initial upstream conditions for the case of the upflow pair of embedded vortices as presented by Pauley and Eaton (1988).

Chapter 6

Conclusions and Recommendations

6.1 Summary

6.1.1 Experimental Results

Embedded vortex array structure and development is examined for arrays of counter-rotating vortices produced by an equally spaced spanwise row of vortex generators. Structure of the array is examined in the crossplane; developmental trends are inferred from the crossplane structure at two streamwise locations.

The experimental description of embedded vortex array structure in the crossplane at Station 74 reveals the following :

- The vortices are highly concentrated, with small circular cores, and large core secondary velocities.

- The vortex arrays consist of counter-rotating cores nearly identical in shape and structure to the single embedded vortex at Station 74. The streamwise vorticity profiles of the cores are not noticably affected by close neighboring vortices.

Vortex trajectories are inferred from the relative displacement of vortex core to generator tip location in the crossplane. While this displacement is only slight at Station 74, the results indicate that the wall exerts the primary influence here. The vortex array with an initial spacing ratio of 2.0 also exhibits the influence of vortex to vortex interaction on the vortex trajectories.

The experimental description of embedded vortex array structure in the crossplane at Station 150 reveals the following :

- Compared to the vortex core structure exhibited at Station 74, the vortex cores at Station 150 are large and diffuse. Peak streamwise vorticity is 5 to 10 percent of the upstream values, and core secondary velocities are small.

- The vortex arrays consist of counter-rotating cores in a variety of elliptical shapes. The shape distortions result from convection of the streamwise vorticity by the secondary flow field. Vortex to wall and vortex to vortex interactions strongly modify this flow field and are largely responsible for the shapes observed.

The developmental trends inferred from the experimental results at both crossplanes depend strongly on the spacing between embedded vortices. It is here where some new insights are found :

- Vortex trajectories are determined by the convective effects of wall and neighboring vortices. Large spacings produce vortices which travel along the wall to form upflow pairs at the downstream measurement station. As the initial spacing ratio of the generators is decreased the strength of the upflow pairing is increased and displacement

of the upflow pairs from the wall becomes more pronounced at the downstream station. *This trend does not continue through to the smallest spacings examined.* At a spacing ratio of 3.0 the motion of the upflow pair away from the wall is hindered by the nearby presence of the other upflow pair in the array. At a spacing ratio of 2.0 the array at Station 150 ceases to be a summation of upflow pairs. The interior vortices form a downflow pair held in close confinement to the wall by the motion of the exterior vortices.

- The downstream values of peak streamwise vorticity indicate that the decay of this quantity depends partly on the proximity of neighboring vortices. Decay is enhanced with increased neighbor proximity.

- The decay of vortex circulation for vortices in arrays produced with large initial spacings is similar in extent to that exhibited by the single embedded vortex. The effects of wall friction are assumed to be responsible. For vortices in arrays produced with intermediate initial spacings motion away from the wall decreases the circulation losses somewhat. Large losses in circulation occur for vortices produced at spacing ratios of 2.0 and 3.0. The vortices in these arrays are no closer to the wall than the single embedded vortex. This leads us to conclude that *wall friction effects alone cannot explain the large losses in circulation occurring for vortices in these arrays.*

It is often assumed that equally spaced arrays of vortex generators set in a counter-rotating configuration produce vortices which tend to lift out of the boundary layer quickly, thereby reducing or eliminating the benefits of vortical mixing on the boundary layer. While this is true for intermediate values of the spacing ratio, it does not hold true for tighter spacings. Tight arrays of counter-rotating vortices are confined to the vicinity of the boundary layer. Increased mixing performance may result simply because the number of embedded

vortices per unit span length is increased. The downstream distance to which this beneficial mixing performance is achieved will be limited due to the rapid attenuation of individual vortex strength. In many applications, such as on airfoils or in diffusers, there is no need to maximize this distance; rather, the important requirement is that separation is avoided at certain critical locations. Tight arrays of vortex generators mounted just upstream of such locations may then provide the greatest mixing benefits.

6.1.2 Modelling Results

The structure of the Oseen vortex compares well to the structure of embedded vortices provided the vortex descriptors are matched between the two.

The structure of the embedded vortices at the upstream station provides the closest comparison to the Oseen vortex model. Here the variance between the two is less than 5 percent over the measurement domain, except in the regions of vortex upwash. In the upwash regions the variance peaks at about 40 percent.

At the downstream station the variance is considerably higher in the upwash regions, but is still quite good everywhere else; being generally within 10 to 15 percent near the vortex core and downwash regions.

At the end of Chapter 1 the question was asked : "What assumptions about the physical processes involved in embedded vortex array development are necessary to obtain a working model which convincingly reproduces the downstream data observed in this study ?". The previous chapter has outlined these assumptions in some detail. It must be kept in mind that these assumptions are obtained within the limitations of the model used, namely that the model itself is based on the structure of the two dimensional Oseen vortex. That the model is fundamentally two dimensional implies immediately that only certain aspects of the data can be reproduced directly. In this case it is the secondary velocity and vorticity

fields of the embedded arrays. The streamwise velocity field and interaction of vortices with the boundary layer cannot be modelled by this approach. Before discussing the implications of this and the limitations of the model in general, lets review the developmental trends the model does reproduce well and consider again the physical assumptions needed to obtain this performance.

The model reproduces the vortex trajectories observed in Chapter 4 and in the Stanford papers. The main assumption needed here is a convection process; secondary velocities generated in the crossplane by each vortex convect neighbors in the crossplane as the flow develops downstream. The convection due to the presence of the wall is modelled through the use of image vortices. In reviewing the data it is observed that the larger spacing ratios produce upflow pairs that tend to lift out of the boundary layer as the flow develops downstream. At close spacing ratios the trajectories become more complex; the vortices are observed in close proximity holding "equilibrium" positions, moving neither away from nor further into the boundary layer. The model reproduces the full range of trajectory behavior observed and so this convection mechanism is understood to be a dominating influence on the downstream development of vortex trajectories.

The model reproduces the slow decay of vortex circulation observed in both Chapter 4 and the Stanford papers. In the Stanford papers it was assumed that wall friction effects alone accounted for this decay. When this assumption alone was included in the model the circulation decay behavior of the larger spacing ratio arrays could be correctly modelled. The level of performance obtained in these cases results, in part, from the model's ability to closely reproduce the near wall secondary velocity structure. The model closely mimics this field over the range of spacing ratios covered, from 2.0 through 7.0. Thus when it was seen that the extensive circulation losses observed at spacing ratios of 2.0 and 3.0 were not reproduced by this version of the model, an additional loss mechanism (besides

wall friction) was postulated. The most probable mechanism, based on the evidence, is an additional opposing torque applied by gradients in the turbulent stress field generated by the "collision" of counter-rotating vortex cores. A review of the data will show that the spacing ratio 2.0 and 3.0 test cases produce arrays in which the vortex cores grow and develop in close proximity. At the downstream station the outer boundaries of the vortex cores (represented by the contour lines of the vorticity field) are apparently fused together indicating that some merging or cancelling process is occurring between the counter-rotating neighbors. Is this a manifestation of the action of the turbulent stress field ? The mean flow data collected here cannot provide the direct evidence to answer this question. An additional mechanism can be formulated, however, to represent these losses in an indirect way. This additional mechanism is based on the model's ability to represent the major features of the streamwise vorticity field of an embedded array. Circulation losses (in addition to those due to the before mentioned wall friction effects) are taken to be proportional to the vorticity gradient between counter-rotating vortex cores. Thus when the cores are widely separated, wall friction effects alone determine the streamwise development of circulation; and when cores are close together an additional cancellation process is implemented. This version of the model reproduces the whole range of observed circulation decay.

The decay of peak vorticity cannot be directly tied to any aspect of the mean flow field in the crossplane. It is closely tied to the turbulent nature of the vortex core and so a model based on the mean flow properties in the crossplane cannot account for, from any physical principles, the development of peak streamwise vorticity. A curve fit to the observed behavior of peak vorticity decay was employed in the model, with an adjustable decay rate parameter and boundary constraints imposed by the data. To provide correct trajectory and circulation behavior the decay rate parameter must be adjusted with initial spacing conditions providing another tie in to observations; namely that the peak vorticity of the

vortex cores decays faster when these cores are nearer to each other. This effect, termed "spreading", was first developed in the Stanford studies.

Although the model is fairly easy to construct and implement it is limited in the types of flow structure it can represent. The limitations of this quasi-three dimensional Oseen model arise from basic elements of its structure. For instance, the model does not reproduce the streamwise velocity field of the vortex embedded in a boundary layer because this field is fundamentally three dimensional while the model itself is two dimensional. There are instances where such flow structure is important. In the calculation of trajectories, for example, it is important to know the velocity at which the core is convected downstream. In this instance, the model borrows a correlation (from Batchelor (1964)) between the strength of the vortex and the size of the streamwise velocity deficit to refine an estimate of the core streamwise convective velocity. This, of course, is is only a single point (per core) in the crossplane. No further details of interaction between the boundary layer and vortices can be gleaned from the model.

Although there are many aspects of embedded vortex array structure and development which the model does not satisfactorily address it does provide reasonable approximations to the trajectories and gross structural streamwise development of arrays of counter-rotating vortices of a general composition. This should assist designers with the most basic questions of where the vortices go, the extent to which they interact, and the resulting persistance of their effects with downstream development. That this can be accomplished with a minimum of computational effort is a testament to the remarkable concurrence between the structure of embedded vortices and the Oseen model.

6.2 Recommendation for Further Study

The idea that vortices holding together in close proximity "feed" on one another due to the turbulent nature of the core structures needs further examination. The mean flow modelling procedure employed here is a crude technique which is able to reproduce the gross features of downstream structure. The particular loss mechanism responsible will only be revealed through a detailed examination of the turbulent stress field occurring between embedded vortices in close proximity. Part of the difficulty here is maintaining a developing pair of counter-rotating vortices inside a boundary layer region. This is demonstrated by the results of the Pauley and Eaton (1988) study. A downflow pair immediately splits apart. The interaction between vortices is quickly attenuated. An upflow pair interacts in close proximity, but quickly lifts out of the boundary layer region. If the measurement grid is kept near the wall, the interaction between vortices is not captured properly. A solution, suggested by the present study, is to use closely spaced pairs of counter-rotating vortices (refer to the structure revealed in the spacing ratio 2.0 test case, Figures 4.17a-c). Another approach could consider the detailed mean flow and turbulence structure of co-rotating vortex pairs. This is also a case where individual vortices come into close proximity. Instead of a cancellation process, a *merging* process occurs and since the vortices in the pair quickly lose their individual identity a number of downstream measurement stations would be needed. The connection between cancellation effects occurring between counter-rotating vortices and merging effects occurring between co-rotating vortices would be of primary interest, for on these results, perhaps, a truly general model of vortex interaction and development could be constructed.

Appendix : Calibration of the Five Hole Probe

The calibration procedure employed for the five hole probe originates from the work of Treaster and Yocum (1979) and follows quite closely the procedure outlined by Pauley and Eaton (1988). Figure A.1 diagrams the probe tip, coordinate system, and numbering convention for pressure ports on the probe tip. The five measured probe pressures are used in four dimensionless pressure coefficients to define the probe response to flow angle and velocity magnitude. The four dimensionless pressure coefficients are :

$$
\begin{aligned}
C_{p,p} = \frac{P_4 - P_5}{P_1 - \overline{P}} &= \frac{\Delta P_4 - \Delta P_5}{\Delta P_1 - \overline{\Delta P}}, \\
C_{p,y} = \frac{P_2 - P_3}{P_1 - \overline{P}} &= \frac{\Delta P_2 - \Delta P_3}{\Delta P_1 - \overline{\Delta P}}, \\
C_{p,s} = \frac{\overline{P} - P_s}{P_1 - \overline{P}} &= \frac{\overline{\Delta P} - (P_s - P_{ref})}{\Delta P_1 - \overline{\Delta P}}, \\
C_{p,t} = \frac{P_1 - P_t}{P_1 - \overline{P}} &= \frac{\Delta P_1 - (P_t - P_{ref})}{\Delta P_1 - \overline{\Delta P}}.
\end{aligned}
$$

where P_s and P_t are the local static and total pressures, respectively, and $\Delta P_i = P_i - P_{ref}$ are the measured port pressures P_i relative to a fixed reference pressure. Also :

$$\begin{aligned} \overline{P} &= (P_2 + P_3 + P_4 + P_5)/4, \\ \overline{\Delta P} &= (\Delta P_2 + \Delta P_3 + \Delta P_4 + \Delta P_5)/4. \end{aligned}$$

Represent the probe response to flow angle and velocity magnitude as follows :

$$\begin{aligned} \text{pitch angle } \alpha_p &= \alpha_p(C_{p,p}, C_{p,y}), \\ \text{yaw angle } \beta_p &= \beta_p(C_{p,p}, C_{p,y}), \\ C_{p,s} &= C_{p,s}(\alpha, \beta), \\ C_{p,t} &= C_{p,t}(\alpha, \beta). \end{aligned}$$

The measured flow angles of pitch (α_p) and yaw (β_p) observed in this study were found to fall within the range of $\pm 20°$. Following the procedure outlined by Pauley and Eaton (1988) the probe response functions for flow angle were simplified. For flow angles within $\pm 20°$ the pitch is independant of yaw angle and vice-versa. Assuming probe symmetry the uncoupled functions are as follows :

$$\begin{aligned} \alpha_p(C_{p,p}) &= (C_{p,p} - A_1)\left[A_2 - A_3\left|C_{p,p} - A_1\right| + A_4(C_{p,p} - A_1)\right], \\ \beta_p(C_{p,y}) &= (C_{p,y} - B_1)\left[B_2 - B_3\left|C_{p,y} - B_1\right| + B_4(C_{p,y} - B_1)\right]. \end{aligned}$$

The coefficients A_i and B_i were found through a least squares fit to the calibration data. The curvatures present in the pitch and yaw functions are meant to account for asymmetries in the geometry of the probe tip. However, the coefficients on the second order terms generating

these curvatures are quite small indicating a high degree of probe symmetry.

The functional form used to represent the total pressure coefficient "horseshoe" response to flow angle is borrowed from Pauley and Eaton (1988) :

$$C_{p,t} = 1 - D_1(1 - D_2 |\alpha|^{5/2})(1 - D_2 |\beta|^{5/2}),$$

where the coefficients D_i are determined from a least squares fit to the calibration data.

At each crossplane subsequent to about Station 66 the variation in wall static pressure was negligible. The local wall static pressure (known from spanwise rows of taps on the splitter plate surface) may be used as a reference pressure. The static pressure coefficient thus may be computed directly from the measured pressures on the probe ports :

$$C_{p,s} = \frac{\overline{\Delta P}}{\Delta P_1 - \overline{\Delta P}}.$$

Following Treaster and Yocum (1979) :

$$\left|\vec{V}\right| = \sqrt{\left(\frac{2}{\rho}\right)(\Delta P_1 - \overline{\Delta P})(1 + C_{p,s} - C_{p,t})},$$

where $\left|\vec{V}\right|$ is the magnitude of the local velocity vector. The components of the vector are :

$$\begin{aligned} \text{Streamwise} : u &= \left|\vec{V}\right| \cos\alpha_p \cos\beta_p, \\ \text{Normal} : v &= \left|\vec{V}\right| \sin\alpha_p \cos\beta_p, \\ \text{Spanwise} : w &= \left|\vec{V}\right| \sin\beta_p. \end{aligned}$$

When the tip of the five hole probe is near the wall the steep boundary layer velocity gradient will impose a pressure differential between upper and lower pressure ports (port

nos. 5 and 4). This pressure differential is an erroneous indication of flow pitch and must be corrected for. In general, a streamwise velocity gradient along either the normal or spanwise coordinates could cause an erroneous pitch or yaw measurement. These measurements are easily corrected for, however, by the following scheme outlined by Westphal, Pauley, and Eaton (1985). The procedure is to find a constant Y_c such that :

$$v = v_{5HP} + Y_c \frac{\partial u}{\partial y},$$
$$w = w_{5HP} + Y_c \frac{\partial u}{\partial z}.$$

Probe symmetry (pitch and yaw port pairs) is assumed. The constant Y_c is found by a calibration procedure using both the boundary layer probe and the five hole probe at Stations 74 and 150 in the absence of embedded vortices. In the equation for v above we may calculate $\partial u/\partial y$ from the data by the finite difference scheme discussed in Chapter 4 since measurements of the streamwise velocity u are unaffected by this gradient error. v_{5HP}, the normal velocity recorded by the five hole probe over the flat plate (and subject to gradient error), is also a known quantity. What we need to know to determine Y_c is what v *should* be at each position y in the measured profile. As noted in Chapter 4, the boundary layer probe verified the two dimensional structure of the turbulent flat plate boundary layer. $v(y)$ may then be calculated from the equations representing this structure at both Stations 74 and 150 (see White (1974) Chapter 6, for example). In Figure A.2 we see $v(y)$ plotted out at Station 150. Also plotted out is the v profile recorded by the five hole probe at Station 150 in the absence of embedded vortices at $z = 0.0$ cms (v_{5HP}). By equating the v velocity measured for the first point above the wall to the expected value of v at this y location we find that $Y_c = 0.0119$ meters. Repeating the process for the other 29 profiles recorded at regular spanwise intervals at Station 150 we obtain an average value; $\overline{Y_c} = 0.0122$ meters.

The corrected v profile using $Y_c = 0.0122$ is indicated on Figure A.2. Since the behavior of the corrected profile is now as expected near the wall, no further wall effects on the probe measurements are suspected. The calibration procedure is repeated at Station 74 and produces similar results.

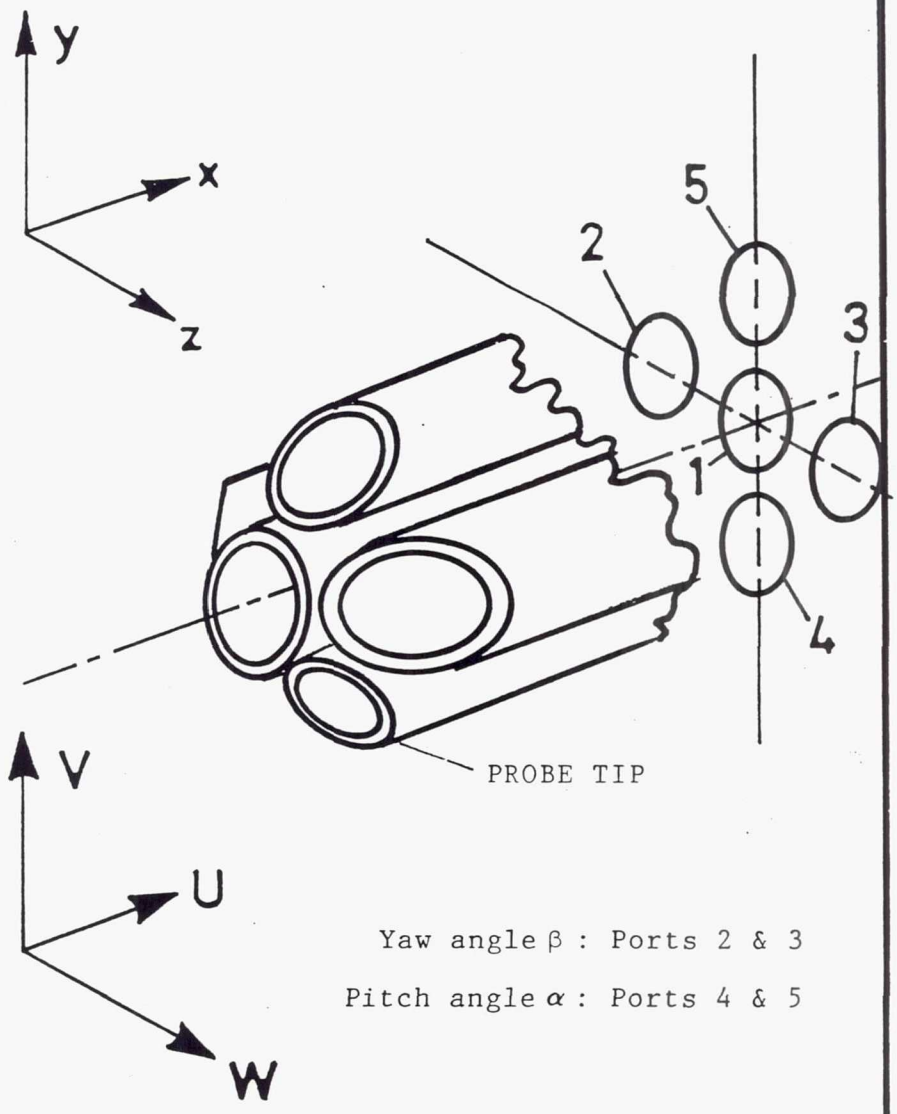

FIGURE A.1 - Probe tip pressure port numbering convention.

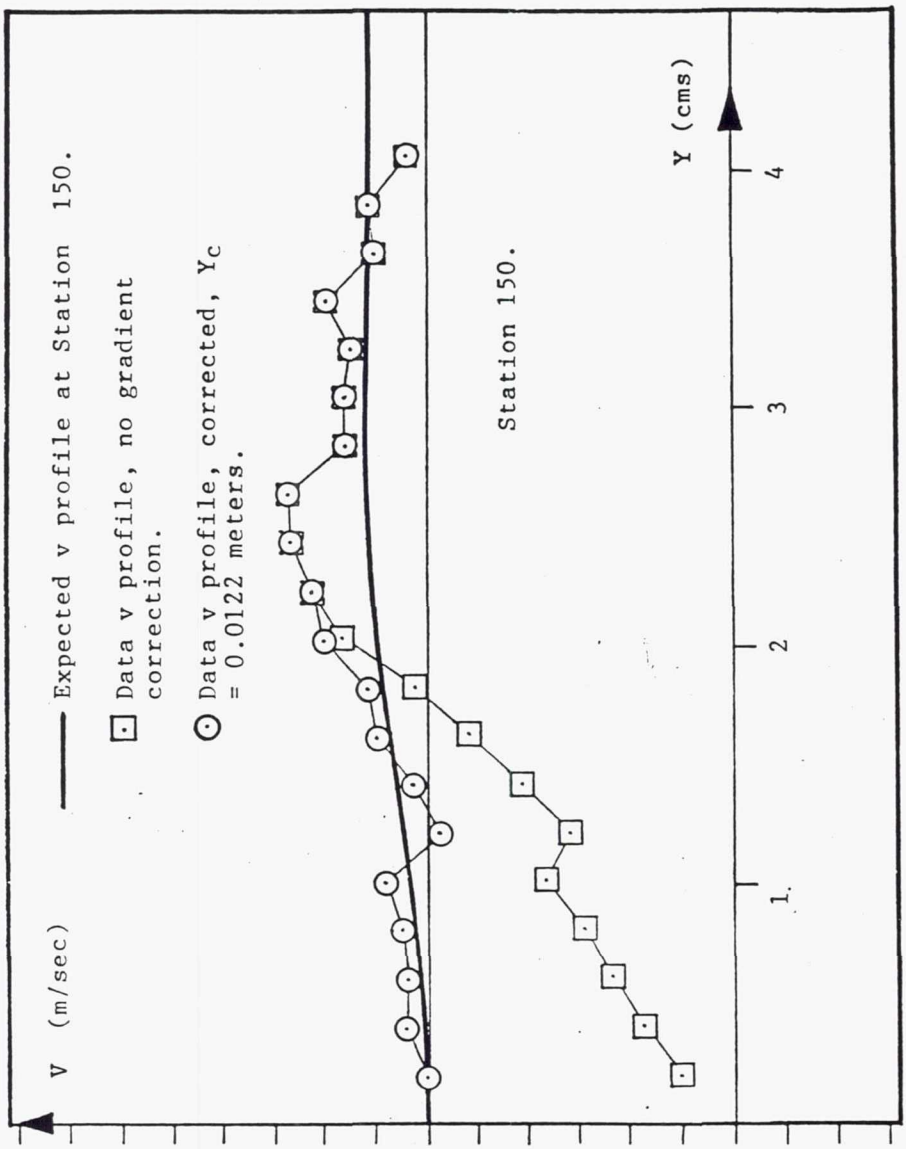

FIGURE A.2 - Application of the gradient correction procedure to probe v velocity profile at Station 150.

References

Batchelor, G.K. 1964. "Axial Flow in Trailing Line Vortices," *J. Fluid Mech.*, Vol. 20, pp. 645-658.

Brown, A.C. 1968. "Subsonic Diffusers Designed Integrally with Vortex Generators," *J. Aircraft,* Vol. 5, pp. 221-229

Burley, R.R. and D.E. Harrington 1987. "Experimental Evaluation of Honeycomb/Screen Configurations and Short Contraction Section for NASA Lewis Research Center's Altitude Wind Tunnel," NASA TP 2692

Coles, D.E. 1968. Proc.: Computation of Turbulent Boundary Layers-AFOSRIFP-Stanford Conference, Vol. II.

Eckert, E.R.G. and R.M. Drake, Jr. 1972. *Analysis of Heat and Mass Transfer*, McGraw-Hill, New York.

Eibeck, P.A. 1985. "An Experimental Investigation of the Heat-Transfer Effects of a Longitudinal Vortex Embedded in a Turbulent Boundary Layer," Rept. MD-48, Thermosciences Div., Dept. Mech. Engr., Stanford Univ.

Harrington, D.E., R.R. Burley and R.R Corban 1986. "Experimental Evaluation of Wall Mach Number Distributions of the Octagonal Test Section Proposed for NASA Lewis Research Center's Altitude Wind Tunnel," NASA TP 2666

Hippensteele, S.A., L.M. Russell and F.S. Stepka 1981. "Evaluation of a Method for Heat Transfer Measurements and Thermal Visualization Using a Composite of a Heater Element and Liquid Crystals," NASA TM 81639

Hoffman, E.R. and P.N. Joubert 1963. "Turbulent Line Vortices," *J. Fluid Mech.*, Vol. 16, pp. 395-411

Iversen, J.D. 1976. "Correlation of Turbulent Trailing Vortex Decay Data," *J. Aircraft,* Vol. 13, No. 5.

Johnston, J.P. and M. Nishi 1990. "Vortex Generator Jets-Means for Flow Separation Control," *AIAA Journal*, Vol. 28 No. 6, pp. 989-994.

Kays, W.M. and M.E. Crawford 1980. *Convective Heat and Mass Transfer*, McGraw-Hill, New York.

McCormick, B.W., J.L. Tangler and H.E. Sherrieb 1968. "Structure of Trailing Vortices," *J. Aircraft*, Vol. 5, no. 3, pp. 260-267.

Owen, P.R. 1970. "The Decay of a Turbulent Trailing Vortex," *Aeronautical Quarterly*, Vol. XXI, pp. 69-78.

Pauley, W.R. and J.K. Eaton 1988. "The Fluid Dynamics and Heat Transfer Effects of Streamwise Vortices Embedded in a Turbulent Boundary Layer," Rept. MD-51, Thermosciences Div., Dept. Mech. Engr., Stanford Univ.

Pearcy, H.H. 1961. "Shock-Induced Separation and Its Prevention by Design and Boundary Layer Control," Part IV, *Boundary Layer and Flow Control*, (G.V. Lachmann, ed.)

Phillips, W.R.C. and J.A.H. Graham 1984. "Reynolds-stress measurements in a turbulent trailing vortex," *J. Fluid Mech.* Vol. 147, pp. 353-371.

Rao, D.M. and S.C. Mehrotra 1983. "Flat-Plate Drag Measurements with Vortex Generators in a Turbulent Boundary Layer," NASA-CR-172125

Russell, C.M.B., T.V. Jones and G.H. Lee 1982. "Heat Transfer Enhancement Using Vortex Generators," Proc. 7th Intl. Conf. on Heat Transfer, Munich, W. Germany, Vol. 3, pp. 283-288.

Sankaran, L. and D.A. Russell 1990. "A Numerical Study of Longitudinal Vortex Interaction with a Boundary Layer," AIAA 21st Fluid Dyn., Plasma Dyn. and Lasers Conf. 90-1630.

Schlichting, H. 1979. *Boundary-Layer Theory*, McGraw-Hill, New York.

Schubauer, G.B. and W.G. Spangenberg 1960. "Forced Mixing in Boundary Layers," *J. Fluid Mech.*, Vol. 8, pp. 10-31.

Shabaka, I.M.M.A., R.D. Mehta and P. Bradshaw 1984. "Longitudinal Vortices Imbedded in Turbulent Boundary Layers. Part 1. Single Vortex," *J. Fluid Mech.*, Vol. 155, pp. 37-57.

Singh, P.I. 1974. "The Structure and Stability of a Vortex," Ph.D. Dissertation, University of Colorado, Boulder.

Spangler, J.G. and C.S. Wells Jr. 1964. "Effects of Spiral Longitudinal Vortices on Turbulent Boundary Layer Skin Friction," NASA CR-145

Squire, H.H. 1965. "The Growth of a Vortex in Turbulent Flow," *Aero. Quarterly*, Vol. 16, pp. 302-306.

Taylor, H.D. 1950. "Retractable Vortex Generators," UAC Research Dept., Report M-15355-3.

Taylor, H.D. and R.M. Grose 1954. "Theoretical and Experimental Investigation of Various Types of Vortex Generators," Report R-15362-5, United Aircraft Corporation Research Dept.

Treaster, A.L. and A.M. Yocum 1979. "The Calibration and Application of Five-Hole Probes," *ISA Trans.*, Vol. 18, pp. 23-34.

Turk, A.Y. and G.H. Junkhan 1986. "Heat Transfer Enhancement Downstream of Vortex Generators on a Flat Plate," Proc. Eighth Intl. Heat Transfer Conf., Vol. 6, pp. 2903-2908, San Francisco

Uberoi, M.S. 1977. "Proper equation for angular momentum of trailing vortices," *Phys. of Fluids*, Vol. 20, pg. 1785.

Uberoi, M.S. 1978. "Mechanisms of Decay of Laminar and Turbulent Vortices," *J. Fluid Mech.*, Vol. 90, pp. 241-255.

Westphal, R.V., J.K. Eaton and W.R. Pauley 1985. "Interaction Between a Vortex and a Turbulent Boundary Layer in a Streamwise Pressure Gradient," Proc. Fifth Symposium on Turbulent Shear Flows, Ithaca, N.Y.

Westphal, R.V., W.R. Pauley and J.K. Eaton 1987. "Interaction Between a Vortex and a Turbulent Boundary Layer, Part 1: Mean Flow

Evolution and Turbulence Properties," NASA TM 88361

White, F.M. 1974. *Viscous Fluid Flow*, McGraw-Hill, New York.

REPORT DOCUMENTATION PAGE

Form Approved
OMB No. 0704-0188

1. AGENCY USE ONLY (*Leave blank*)	2. REPORT DATE	3. REPORT TYPE AND DATES COVERED
	September 1991	Technical Memorandum

4. TITLE AND SUBTITLE

The Structure and Development of Streamwise Vortex Arrays Embedded in a Turbulent Boundary Layer

5. FUNDING NUMBERS

WU-505-62-52
G-NAG3-520

6. AUTHOR(S)

Bruce J. Wendt, Isaac Greber, and Warren R. Hingst

7. PERFORMING ORGANIZATION NAME(S) AND ADDRESS(ES)

National Aeronautics and Space Administration
Lewis Research Center
Cleveland, Ohio 44135-3191

8. PERFORMING ORGANIZATION REPORT NUMBER

E-6523

9. SPONSORING/MONITORING AGENCY NAMES(S) AND ADDRESS(ES)

National Aeronautics and Space Administration
Washington, D.C. 20546-0001

10. SPONSORING/MONITORING AGENCY REPORT NUMBER

NASA TM-105211

11. SUPPLEMENTARY NOTES

Bruce J. Wendt and Isaac Greber, Case Western Reserve University, Cleveland, Ohio 44106; Warren R. Hingst, NASA Lewis Research Center. This report was submitted by Bruce J. Wendt as a thesis in partial fulfillment of the requirements for the degree Doctor of Philosophy to Case Western Reserve University. Responsible person, Warren R. Hingst, (216) 433-5923.

12a. DISTRIBUTION/AVAILABILITY STATEMENT

Unclassified - Unlimited
Subject Category 02

12b. DISTRIBUTION CODE

13. ABSTRACT ***(Maximum 200 words)***

An investigation of the structure and development of streamwise vortices embedded in a turbulent boundary layer was conducted in the test facility CW-22 at NASA Lewis Research Center. The vortices were generated by a single spanwise row of rectangular vortex generator blades. A single embedded vortex was examined, as well as arrays of embedded counter-rotating vortices produced by equally spaced vortex generators. Measurements of the secondary velocity field in the crossplane provided the basis for characterization of vortex structure. Vortex structure was characterized by four descriptors. The center of each vortex core was located at the spanwise and normal position of peak streamwise vorticity. Vortex concentration was characterized by the magnitude of the peak streamwise vorticity, and the vortex strength by its circulation. Measurements of the secondary velocity field were conducted at two crossplane locations to examine the streamwise development of the vortex arrays. Large initial spacings of the vortex generators produced pairs of strong vortices which tended to move away from the wall region while smaller spacings produced tight arrays of weak vortices close to the wall. The crossplane structure of embedded vortices is observed to be very similar to that exhibited by the two dimensional Oseen vortex with matching descriptors. Quantitative comparisons are established. A model of vortex interaction and development is constructed using the experimental results. The model is based on the structure of the Oseen vortex. Vortex trajectories are successfully modelled by including the convective effects of neighbors, and images to represent the wall. The streamwise decay of circulation is successfully modelled for the single vortex, and for large initial spacings, by accounting for the effects of wall friction. An additional mechanism associated with the turbulent stress field in the near vicinity of the vortex cores is postulated to explain the large losses in circulation obtained for the smaller initial spacings. The streamwise decay of vortex circulation at the smaller spacings is successfully modelled by summing wall friction losses and "proximity" losses. These proximity losses are found to be proportional to the gradient in streamwise vorticity occurring between an embedded vortex and its adjacent counter-rotating neighbors.

14. SUBJECT TERMS	15. NUMBER OF PAGES
Vortices; Vortex generators; Oseen approximation	318
	16. PRICE CODE A14

17. SECURITY CLASSIFICATION OF REPORT	18. SECURITY CLASSIFICATION OF THIS PAGE	19. SECURITY CLASSIFICATION OF ABSTRACT	20. LIMITATION OF ABSTRACT
Unclassified	Unclassified	Unclassified	